Design and electrophysiological characterization of rhodopsin-based optogenetic tools

Entwicklung und elektrophysiologische Charakterisierung von rhodopsinbasierten, optogenetischen Werkzeugen

DISSERTATION

zur Erlangung des akademischen Grades
doctor rerum naturalium (Dr. rer. nat)
im Fach Biophysik

eingereicht an der Mathematisch-Naturwissenschaftlichen Fakultät I
der Humboldt Universität zu Berlin

von Diplom-Biophysikerin Franziska Schneider

Präsident der Humboldt-Universität zu Berlin:
Professor Dr. Jan-Hendrik Olbertz

Dekan der Mathematisch-Naturwissenschaftlichen Fakultät:
Professor Stefan Hecht (PhD)

Gutachter/innen:
1. Professor Dr. Peter Hegemann
2. Professor Dr. Franz Bartl
3. Professor Dr. Dr. h. c. Edda Klipp

Tag der mündlichen Prüfung: 21. März 2014

Contents

List of Tables

List of Figures

1. Abstract

Channelrhodopsins (ChRs) are light-activated cation channels functioning as primary photoreceptors in green algae. In the emerging field of optogenetics, ChRs are used to depolarize neuronal membranes, thus allowing for light-induced action-potential firing. The blue light-activated *Chlamydomonas* channelrhodopsin 2 (C2) and high-efficiency mutants such as C2 H134R represent the most commonly used depolarizing optogenetic tools. Complementary to ChRs, green to yellow light-activated proton and chloride pumps originating from archea enable neuronal inhibition by membrane hyperpolarization. The present work combines basic electrophysiological characterization of ChRs with their optimization for optogenetic application. Moreover, it describes the design of an optogenetic tool that allows for light-induced acidification of synaptic vesicles.

In order to perform multi-color optogenetic experiments, a high-performance ChR that exhibits a red-shifted activation maximum when compared to C2 was developed. By combining the two N-terminal transmembrane helices of *Chlamydomonas* channelrhodopsin 1 (C1) with the latter five from *Volvox* channelrhodopsin 1 (V1), the C1V1 chimera was created. C1V1 is not only activated with green light showing peak activation at 536 nm, but also shows excellent membrane targeting and high photocurrents when being expressed in mammalian cells. Hence, C1V1 can be used for light-induced action-potential firing with activation wavelengths up to 620 nm. Key residues of the C1V1 retinal-binding pocket were mutated to fine-tune its spectral and kinetic properties. The mutants C1V1 S220G and C1V1 L221T display blue- and red-shifted action spectra with peak activation at 524 nm and 542 nm, respectively. Additionally, C1V1 E122T E162T constitutes a fast-cycling ChR that exhibits sixfold accelerated channel-closing kinetics compared to C1V1. Together, expression of selected C2 and C1V1 mutants in distinct cellular populations allows for selective activation using blue and yellow light.

Based on structural models for C2 and C1V1, residues potentially involved in channel gating and cation binding were identified. Inner gate residues such as C2 H134 are shown to influence cytosolic cation release and are necessary for the characteristic inward rectification found in ChRs. Central gate residues include C2 S63 and C2 N258 that determine cation selectivity and competition, and affect the equilibrium between the two predicted open channel conformations. An enzyme-kinetic model was used to quantitatively dissect photocurrents into the contribution of different competing cations. Being applied to electrophysiological data for C2, C2 L132C T159C (Catch+) and C1V1, the model offers insights into voltage dependency of cation transport, cation competition and differential selectivities of the two open conformations. The model is also suitable to predict current amplitudes at ionic conditions that were not experimentally tested. The here presented data does not only reveal basic principles underlying cation selectivity in ChRs, but also facilitates choosing the optimal ChR variant for a certain optogenetic application.

Finally, pHoenix - a light-activated proton pump targeted to synaptic vesicles - was designed. Being expressed in hippocampal neurons, pHoenix colocalizes with vesicular glutamate transporters and specifically acidifies synaptic vesicles following green light application. pHoenix was successfully used to analyze the energetics of synaptic neuro-

transmitter uptake and to examine postsynaptic electric responses that depend on the filling state of synaptic vesicles. pHoenix represents the first optogenetic actuator that allows for specific manipulation of presynaptic processes with light.

2. Zusammenfassung

Kanalrhodopsine sind lichtaktivierte Kationenkanäle, welche als primäre Fotorezeptoren in Grünalgen dienen. Im aufstrebenden Forschungsfeld der Optogenetik werden Kanalrhodopsine für die Depolarisierung neuronaler Membranen verwendet. Dabei ermöglichen Kanalrhodopsine das licht-induzierte Auslösen von Aktionspotentialen. Das mit blauem Licht aktivierte Kanalrhodopsin-2 (C2) und verbesserte Mutanten wie C2 H134R stellen die am häufigsten zur Depolarisierung angewandten optogenetischen Werkzeuge dar. In komplementärer Weise zu Kanalrhodopsinen werden lichtaktivierbare Protonen- und Chloridpumpen aus Archaebakterien zur neuronalen Inhibierung durch Hyperpolarisation verwendet. Die vorliegende Arbeit kombiniert die grundlegende, elektrophysiologische Charakterisierung von Kanalrhodopsinen mit ihrer Optimierung für optogenetische Anwendungen. Des Weiteren wird die Entwicklung eines optogenetischen Werkzeuges, welches lichtinduzierte Ansäuerung von synaptischen Vesikeln ermöglicht, beschrieben.

Um optogenetische Experimente mit verschiedenen Anregungswellenlängen möglich zu machen, wurde ein optimales Kanalrhodopsin mit im Vergleich zu C2 rotverschobener Aktivierung entwickelt. Durch Kombination der zwei N-terminalen Transmembranhelizes von *Chlamydomonas* Kanalrhodopsin 1 (C1) mit den letzten fünf Helizes von *Volvox* Kanalrhodopsin 1, entstand die Chimäre C1V1. C1V1 wird nicht nur mit grünem Licht mit maximaler Aktivierung bei 536 nm angeregt, sondern zeichnet sich auch durch exzellente Membranständigkeit und hohe Fotoströme in Säugetierzellen aus. Folglich, kann C1V1 für das Auslösen von Aktionspotentialen mit Licht der Wellenlängen bis maximal 620 nm benutzt werden. Entscheidende Aminosäuren der C1V1 Retinalbindungstasche wurden für die Feinabstimmung der spektralen und kinetischen Eigenschaften der Chimäre mutiert. Die Mutanten C1V1 S220G und C1V1 L221T weisen blau- und rotverschobene Aktionsspektren mit Maxima bei 524 nm und 542 nm auf. Als Ergänzung stellt C1V1 E122T E162T eine C1V1 Variante dar, welche sich durch einen sechsfach schnelleren Fotozyklus im Vergleich zu C1V1 auszeichnet. Die Expression von ausgewählten C2 und C1V1 Mutanten in verschiedenen zellulären Populationen ermöglicht die selektive Aktivierung dieser mit blauem und gelbem Licht.

Basierend auf Strukturmodellen für C2 und C1V1 wurden Aminosäuren, die potentiell an Kanalöffnung und Kationenbindung beteiligt sind, identifiziert. Für Aminosäuren wie C2 H134, die die Kanalpore an der zytosolischen Seite begrenzen, wurde eine Beteiligung an der intrazellulären Kationenfreisetzung nachgewiesen. Außerdem wurde gezeigt, dass diese Aminosäuren essentiell für die typische Einwärtsgleichrichtung der Kanalrhodopsine sind. Aminosäuren des zentralen Porenbereichs wie C2 S63 und C2 N258 bestimmen dagegen Kationenselektivität und -konkurrenz und beeinflussen das Gleichgewicht zwischen den zwei vorhergesagten offenen Kanalzuständen. Ein enzymkinetisches Modell wurde verwendet, um die Fotoströme in die Bestandteile der verschiedenen, konkurrierenden Kationen zu zerlegen. Das Modell wurde zur Beschreibung der elektrophysiologischen Daten von C2, C2 L132C T159C und C1V1 benutzt und gibt Einblicke in die Spannungsabhängigkeit des Kationentransports, in Kationenkompetition und in die verschiedenen Selektivitäten der beiden offenen Zustände. Zusätzlich ist das Modell dazu geeignet, Fotostromamplituden für Bedingungen vorauszusagen, welche nicht experi-

mentell untersucht wurden. Die hier präsentierten Daten legen nicht nur grundlegende Prinzipien der Kationenselektivität von Kanalrhodopsinen offen, sondern unterstützen auch die Auswahl einer passenden Kanalrhodopsinvariante für unterschiedliche optogenetische Anwendungen.

Der letzte Teil der Arbeit beschäftigt sich mit der Konstruktion und Charakterisierung von pHoenix, einer licht-aktivierten Protonenpumpe gekoppelt an synaptische Signalsequenzen. In Neuronen des Hippocampus kolokalisiert pHoenix mit vesikulären Glutamattransportern und säuert synaptische Vesikel an, sobald es mit grünem Licht aktiviert wird. pHoenix konnte erfolgreich zur Untersuchung der treibenden Kräfte für die Neurotransmitteraufnahme in Vesikel sowie zur Analyse von postsynaptischen, elektrischen Antworten in Abhängigkeit des vesikulären Füllstands verwendet werden. pHoenix stellt das erste optogenetische Werkzeug da, welches die spezifische Aktivierung von präsynaptischen Prozessen mit Licht erlaubt.

3. Introduction

Light is the universal energy source that enables energy-consuming processes in all kingdoms of life. Photoautotrophic organisms use the light energy delivered by the sun to synthesize high-energy organic compounds. In the process of oxygenic photosynthesis, the absorption of photons enables the production of sugars and molecular oxygen from carbon dioxide and water. Reversely, cellular respiration provides metabolic energy by oxidation of carbohydrates in both photoautotrophic and photoheterotrophic species. Most plants, algae and cyanobacteria perform photosynthesis and have developed highly specialized organelles to optimize light-energy conversion. In order to maximize the efficiency of light harvesting, photosynthetic organisms employ further photosensitive molecules, so-called photoreceptors. These photoreceptors detect color and intensity of the incident light, thereby allowing to correspondingly adjust photosynthesis and developmental steps [1]. Moreover, motile photosynthetic organisms such as flagellated algae use photoperception for optimal orientation towards the respective light source. Photoreceptors are not restricted to plants, algae and cyanobacteria, but are also found in bacteria, fungi and animals. In the vertebrate kingdom, photoreception is mainly used for spacial orientation which is commonly referred to as "vision". In the following, mechanisms of photoreception and the involved molecules are introduced.

3.1. Photoreceptors

Photoreceptors are photosensitive proteins that absorb light in the visible range (380 nm to 740 nm), the part of the sun's electromagnetic spectrum that the earth's atmosphere is most permissive to [2]. Since neither the peptide backbone nor amino acid side chains show considerable absorption of visible light, photoreceptors bind additional organic compounds called chromophores. All known chromophores exhibit delocalized electrons distributed across conjugated π-electron systems [3] allowing for visible light perception. Based on protein sequence similarities and the nature of the applied chromophore seven distinct classes of sensory photoreceptors have been identified. These include rhodopsins, xanthopsins, light-oxygen-voltage (LOV) sensors, blue-light sensors using flavine adenine dinucleotide (BLUF), cryptochromes, phytochromes and the most recently found cyanobacteriochromes [4, 3, 5]. Distinct photoreceptor classes show different primary photochemical reactions that usually lead to conformational changes in the protein structure and are eventually forwarded to the respective effector domains. While photoreactions are triggered by isomerization around double bonds in rhodopsins, xanthopsins, phytochromes and cyanobacteriochromes, LOV sensors are activated by the formation or rupture of a covalent bond and electron transfer starts photoreactions in BLUF proteins and cryptochromes [3, 6, 7]. Also, different mechanisms of signal transduction have been evolved. The most simple photoreceptors are constituted of a single domain that directly mediates both sensory and effector functions (e.g. microbial ion pumps and channelrhodopsins). In contrast, many photoreceptors display a modular architecture linking mainly N-terminal sensor domains to one or more C-terminal effector domains. In nature, diverse and complex combinations of sensors and effectors are present, which include proteins with several different sensor domains. Representatives of

photoreceptor class	chromophore	examples	occurrence
rhodopsins (Rs)	retinal	vertebrate Rs, invertebrate Rs, microbial Rs	animals, plants, algae, cyanobacteria, archea, proteobacteria
xanthopsins	coumaric acid	photoactive yellow protein (PYP)	archea
LOV proteins	flavin nucleotide cofactor	phototropin, neocrome, aureochrome	plants, algae, bacteria
BLUF proteins	FAD	AppA, photoactivated adenyl cyclases	protists, proteobacteria, cyanobacteria
cryptochromes	flavin nucleotide cofactor, pterin	*Arabidopsis* cryptochrome 1-3	animals, plants, algae, cyanobacteria
phytochromes	tetrapyrrole	phytochrome 1, bacteriophyto-chromes	plants, proteobacteria, cyanobacteria
cyanobacterio-chromes	tetrapyrrole (bilin)	SyPixJ1, SyCcaS, SyCikA	cyanobacteria

Table 3.1.: Seven photoreceptor classes with respective chromophores. Note that cryptochromes bind a second chromophore belonging to the group of pterins, that is not directly involved in the primary photoreaction. For each class several examples are presented in the third column and the last column depicts the kingdoms of life where representatives of each group have been identified.

modular-built photoreceptors are found in all photoreceptor classes. The third mechanism of signal transduction is the activation of secondary proteins by the photoreceptors. Using this mechanism, many copies of effector proteins can be activated by one receptor molecule, thereby allowing for signal amplification. One of the best-known examples is visual rhodopsin that belongs to the G-protein-coupled receptor family. An overview of the seven visible light-absorbing photoreceptor classes is given in Table 3.1.

3.2. Vision in phototactic algae

Most photoreceptors presented in this work originate from green algae belonging to the family of volvocaceae. These algae are unicellular or colonial biflagellates. The interplay of photoreceptors and the two flagellas enables the algae to perform phototaxis according to the ambient light quality. In the following, photoreception in two prominent representatives of volvocaceae, *Chlamydomonas reinhardtii* and *Volvox carteri*, is shortly summarized.

3.2.1. Chlamydomonas reinhardtii

Chlamydomonas reinhardtii is a species of unicellular, green algae that possesses a cell wall and a chloroplast. Moreover, it uses a specialized organelle for light detection, the so-called "eyespot" [8]. The eyespot consists of two or more layers of pigmented granules that function as quarter-wave stack antennas [9]. Reflection and positive interference intensifies blue light shining perpedicularly on the surface of the eyespot. In contrast, light

coming from other directions will be attenuated by the antenna. The photoreceptors are located in the plasma membrane at the surface of the eyespot, thereby sensing different light inputs depending on the orientation of the cell related to the incident light. The eyespot itself is placed such that it precedes the beating plane of the flagella by approximately 30° during rotational swimming [1]. The direction-modulated signal allows the algae to adjust plane, frequency and three-dimensional pattern of the flagellar beating [1]. The ability to perform both photophobic responses and positive phototaxis suggested the involvement of at least two different photoreceptors. Foster *et al.* showed that the photoresponses were mediated by retinal-binding rhodopsin proteins [10]. Subsequently, the first rhodopsin, namely Chlamyopsin 1 (Cop1), was purified from the eyespot and its protein sequence was determined [11, 12]. Sequence comparisons revealed homology to invertebrate rhodopsins including the conserved loop responsible for G-protein binding [13, 14, 15]. However, experiments failed to prove its employment in phototaxis [14]. Also, the Cop2 protein, an alternatively spliced variant of the cop1 gene, was only expressed at very low levels in the eyespot and was therefore excluded to be the primary photoreceptor [14].

Only when a *Chlamydomonas* cDNA database was available, two additional opsin-coding genes were identified [16, 17, 18, 19]. Nagel and coworkers heterologously expressed the rhodopsins coded by the cop3 and cop4 genes in *Xenopus* oocytes and recorded light-activated currents in two-electrode voltage-clamp measurements [17, 18]. The measured photocurrents may account for the currents earlier detected by electrical recordings on cell-wall deficient *Chlamydomonas* cells [20]. Due to channel characteristics of the light-induced currents, the gene products were named channelrhodopsin 1 (C1) and channelrhodopsin 2 (C2) [17, 18]. Moreover, Sineshchekov *et al.* used an RNA interference approach to show that the two rhodopsins are responsible for photoresponses in *Chlamydomonas* in vivo [16]. They proposed that C1 would mediate the fast photoresponse at high light levels and C2 would cause slower responses at lower light intensities. Since the fast photoresponses are Ca^{2+}-driven currents that are more or less insensitive to pH changes [21], the involvement of a secondary Ca^{2+} channel was proposed [22, 23]. This Ca^{2+} channel could be either activated by membrane depolarization or by direct interaction with the C-terminal intracellular domains of channelrhodopsins. Although the sequence of a putative interaction partner has been suggested, the interplay of channelrhodopsins and secondary channels remains to be investigated. Recent advances in gene targeting in *Chlamydomonas* will allow for the creation of knock-out variants that will provide further understanding of the mechanisms underlying phototaxis [24, 25]. Structure and function of channelrhodopsins (ChRs) are described in detail in section 3.4.

The *Chlamydomonas* genome contains four additional opsin genes. cop5, cop6 and cop7 code for microbial rhodopsins with long C-terminal extensions. The N-terminal microbial rhodopsin genes are followed by genes potentially being translated into a histidine kinase, a response regulator and an effector protein, e.g. a nucleotide cyclase [1, 26]. Only recently, the rhodopsin part of histidine kinase rhodopsin 1 encoded by the cop5

photoreceptor group	representatives	protein structure	putative functions
invertebrate rhodopsins	Cop1, Cop2 , Vop1	rhodopsin domain, G-protein binding	possibly involved in phototaxis regulation and PSI assembly
channel-rhodopsins (ChRs)	C1 (cop3), C2 (cop4), V1, V2	microbial rhodopsin with C-terminal cytosolic domain	photoreceptors responsible for phototaxis
histidine kinase rhodopsins (HKRs)	HKR1 (cop5), Cop6, Cop7, Cop8, Vop5, Vop6	microbial rhodopsin linked to HK, RR and effector protein; Cop8: N-terminal K^+ channel	HKR1: UVA receptor potentially involved in photoadaptation
phototropins (phots)	*Chlamydomonas* phot, *Volvox* phot	2 LOV domains and a S/T kinase	regulation of development, chemotaxis, photosynthesis, phototaxis
cryptochromes	*Chlamydomonas* CPH1, aCRY, *Volvox* cryptochrome	photolyase-related domain and C-terminal extension	control of metabolism, cell cycle, circadian clock

Table 3.2.: Overview of photoreceptors in *volvocaceae*. Rhodopsins were categorized into three groups based on sequence and structural homologies. For each group the reported representatives and their structural composition is given. The right column displays selected functional roles in the algae. Abbreviations are used as follows: cop- *Chlamydomonas* opsin, vop- *Volvox* opsin, C1 and C2- channelrhodopsins from *Chlamydomonas*, V1 and V2- channelrhodopsins from *Volvox*, PSI- photosystem I, HKR1- histidine kinase rhodopsin 1, HK- histidine kinase, RR- response regulator, S/T- serine/threonine, CPH- *Chlamydomonas* photolyase homolog

gene was purified and shown to be a bistable receptor sensitive to UVA and blue light [27]. Luck *et al.* propose that histidine kinase rhodopsin 1 is involved in the adaptation of photoresponses in the presence of UVA radiation. Even more complex, the cop8 gene combines a putative potassium channel with a microbial rhodopsin and down-stream effector proteins. But, while expression of the the cop5 and cop6 genes in the algae has been verified by PCR (personal communication Meike Luck), no such information has been reported for cop7 and cop8. Therefore, expression pattern, structure and function of the cop7 and cop8 gene products remain highly speculative.

Apart from rhodopsins, *Chlamydomonas* expresses a phototropin that consists of two LOV domains and a C-terminal kinase. Phototropin was shown to control developmental processes, chlorophyll and carotenoid biosynthesis as well as chemotaxis [28, 29, 30, 31] in *Chlamydomonas*. A recent knock-out study demonstrates that phototropin regulates the size of the eyespot and the expression level of channelrhodopsin 1 in the algae [32]. Additionally, the *Chlamydomonas* genome codes for at least two cryptochromes (CPH1 and aCRY) and a DASH protein sensitive to blue and red light [33, 34]. The animal-like cryptochromes (aCRYs) control expression of a number of different genes, thereby controlling chlorophyll and carotenoid biosynthesis, nitrogen metabolism and the pro-

duction of light-harvesting complexes [34]. Furthermore, cryptochromes control the cell cycle and are part of the circadian clock [34]. In summary, photoreception in *Chlamydomonas* is mediated by the complex interplay of many different photoreceptors. While at least ten distinct photoreceptor genes are found in the *Chlamydomonas reinhardti* genome, the expression pattern as well as the functional role of several proteins remain to be investigated.

3.2.2. Volvox carteri

Volvox carteri is a colony-forming biflagellate and a model organism for the development of multicellularity [35]. The single somatic cells resemble the *Chlamydomonas* cells featuring an eyespot, a chloroplast and two flagellas. Light-induced photocurrents are restricted to the eyespot [22] and have been assigned to the primary photoreceptors *Volvox* channelrhodopsin 1 (V1) and *Volvox* channelrhodopsin 2 (V2) [36, 37, 38]. In addition, an animal-like rhodopsin - the gene product of the vop1 gene - has been reported to control the organism's phototactic behaviour [39]. Moreover, two genes encoding for histidine-kinase rhodopsins (vop5 and vop6), a phototropin gene and a cryptochrome gene were identified in a *Volvox carteri* genome project [40, 26]. All presented photoreceptors in volvocaceae, their structures and potential functions are summarized in Table 3.2.

3.3. Microbial rhodopsins

Rhodopsins are classified into two distinct classes [41]. Type I rhodopsins, also referred to as microbial rhodopsins, bind all-*trans* retinal and are found in bacteria, algae, archea and fungi. This group comprises sensory rhodopsins, channelrhodopsins and ion-pumping rhodopsins with its prominent representatives bacteriorhodopsin, proteorhodopsin and halorhodopsin. Type II rhodopsins are G-protein coupled receptors binding 11-*cis* retinal and imply the visual rhodopsins of higher animals. Moreover, type II rhodopsins are represented by non-visual vertebrate rhodopsins including pinopsin, vertebrate ancient rhodopsin, melanopsin, peropsin and encaphalopsin that are suggested to be involved in circadian entrainment, body pigmentation, detection of ambient light, seasonsal adaptation and phototaxis (for a review see [41]). In the following, a closer insight into structure and activation mechanism of selected microbial rhodopsins is presented.

All microbial rhodopsins are membrane proteins consisting of seven characteristic helices featuring amino acid sequence homology of 25 % or higher. The retinal chromophore is bound via a conserved lysine residue in helix seven, thus forming a Schiff base (see Figure 3.1A for bacteriorhodopsin model structure). Photon absorption induces an isomerization of the all-*trans* retinal to a 13-*cis* configuration by double-bond rotation (Figure 3.1B). While resulting Schiff base reorientation and/or deprotonation is involved in ion transport in ion-pumping rhodopsins, retinal isomerization is followed by major conformational changes in sensory rhodopsins and channelrhodopsins. In sensory rhodopsins

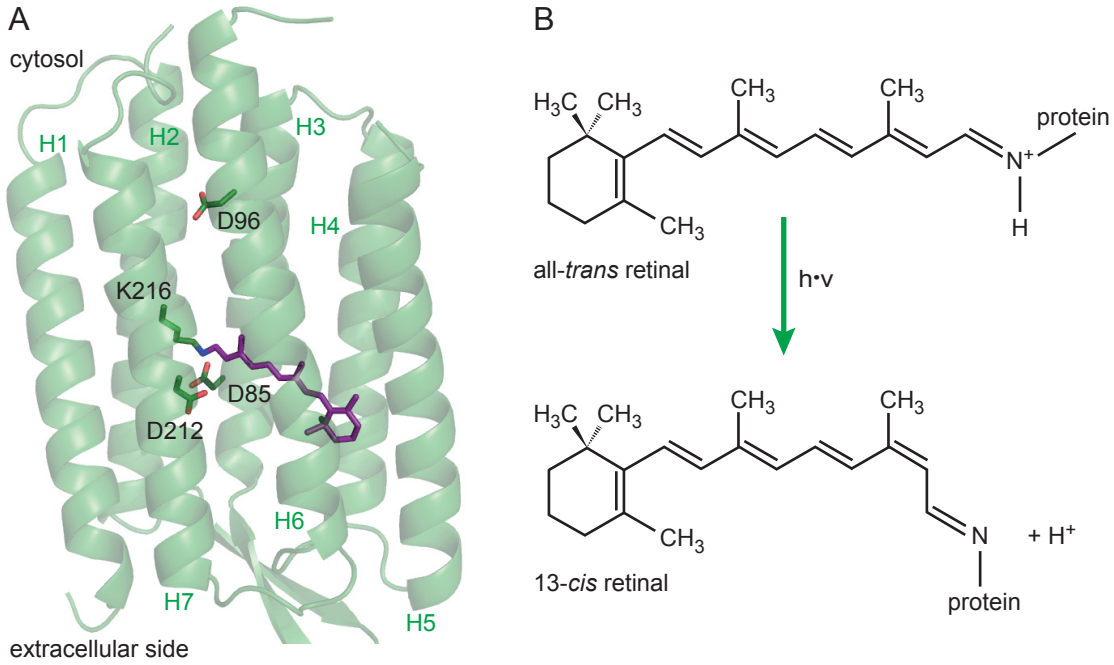

Figure 3.1.: Structural characteristics of microbial rhodopsins. **A** Crystal structure of a bacteriorhodopsin photointermediate (L-state, 2NTU) showing the typical seven transmembrane helices and the retinal chromophore covalently linked to K216 in helix seven [42]. The Schiff base is stabilized by the counterion complex comprising D85, D212 and a water molecule [43, 44, 45]. D85 and D212 are involved in primary proton uptake from the Schiff base and D96 depicts the primary proton donor for reprotonation from the cytosolic side [46, 47, 48]. **B** In microbial rhodopsins photon absorption triggers retinal isomerization from the all-*trans* to the 13-*cis* isoform [49]. Retinal isomerization induces transient deprotonation of the Schiff base nitrogen.

the conformational changes cause rearrangements of the bound transducer molecule by helix-helix interactions [50].

3.3.1. Proton-pumping rhodopsins

Archaeal bacteriorhodopsins [51] and the more recently discovered proteorhodopsins [52] and xanthorhodopsins [53] use the absorbed photoenergy to actively pump protons from the cytosol to the extracellular side. The resulting proton gradient drives the energy-consuming processes in the cell. Here, the proton-pumping mechanism is exemplarily described for bacteriorhodopsin (BR) which constitutes one of the best studied membrane proteins. Since the different transport steps and the corresponding protein conformations change the retinal environment, UV-vis absorption spectroscopy is well-suited to follow the reaction cycle also referred to as photocycle [54]. BR in its dark-adapted state is activated by green light of about 560 nm [51] triggering isomerization of all-*trans* retinal to the 13-*cis*, 15-*anti* configuration [49] (Figure 3.1B). Rapid retinal isomerization is followed by the J, K and L states [54] that exhibit distinct retinal and Schiff-base orientations. Both K and L state are high-energy intermediates featuring bent retinal configurations [55]. Consecutively, the Schiff-base proton is transferred to the primary proton acceptor D85 [46, 47] via a connecting water molecule (water 402), thereby forming the M1 state. Schiff-base deprotonation decreases the effective size of the delocalized electron system resulting in a characteristic blue-shifted absorption spectrum of the M

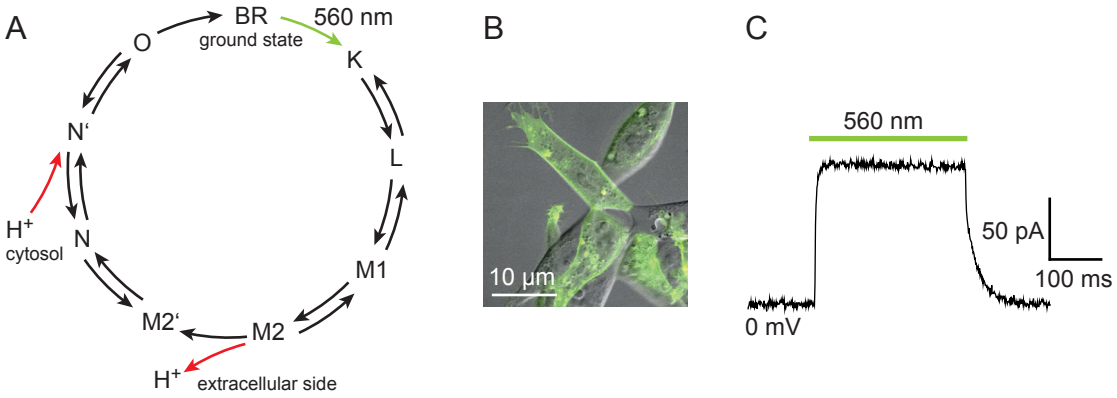

Figure 3.2.: Upon photon absorption microbial proton pumps transport protons from the cytosol to the extracellular side of the membrane. **A** BR photocycle with the K, L, M, N and O photointermediates after Lanyi, 2004 [55]. Light absorption triggering retinal isomerization is shown in green and proton release and uptake is depicted by red arrows. **B** Confocal fluorescence image showing HEK 293 cells transiently expressing the proton pump C_vRh [26] that is linked to the green fluorescent protein eGFP. The image was recorded by Arend Vogt in our group. **C** Exemplary macroscopic current trace of C_vRh measured in a whole-cell voltage clamp recording on a HEK cell.

states. Sequentially, a proton is released to the extracellular side via the proton release group constituted by E194, E204 and bound water molecules [56, 57, 55]. At the same time, the Schiff base reorientates to the cytoplasmic side (M1 → M2) and the pK_a of D85 increases (M2 → M2') [55]. Next, the Schiff base is reprotonated from D96 via several water molecules forming the N intermediate [46, 58]. Finally, D96 is reprotonated by a cytosolic proton, the retinal thermally reisomerizes (N → 0) and the initial state is recovered [59].

The overall reaction cycle results in outward transport of one proton per absorbed photon. The duration of one complete cycle is in the range of 15 ms [60]. During continueous high illumination, BR molecules may start the next reaction cycle as soon as they reach the ground state and absorb another photon. Macroscopic photocurrents can be measured by electrical recordings on *Xenopus* oocytes or cultured animal cells that heterologously express the respective proton pump [61]. Figure 3.2B shows human embryonic kidney (HEK) cells transiently expressing the BR-like proton pump from the green algae *Chlorella vulgaris* (C_vRh). Upon green light activation a characteristic outward current can be detected in whole-cell voltage-clamp recordings (Figure 3.2C).

While BR and related pumps such as C_vRh favorably absorb green light of 560 nm (personal communication with Arend Vogt), proteorhodopsins and xanthorhodopsins exhibit action spectra with shifted maxima. Proteorhodopsin action spectra are tuned according to the habitat of the bacteria, thus proteorhodopsins isolated from marine surface bacteria belong to the class of green-light absorbing proteorhodopsins (maximal absorption at 525 nm) and proteorhodopsins from deeper water levels belong to the blue-light absorbing proteorhodopsins (maximal absorption at 490 nm) [62, 63]. The two classes are distinguished by the amino acid at position 105 (E105 vs L105) and several other amino acids are involved in additional fine-tuning of the spectrum [63, 64]. Color-shifted proteorhodopsin variants are an excellent example for the influence of the protein environment on the π-electron system and thus the absorption properties of the

retinal. In general, retinal absorption depends on the conformation of the retinal (e.g. planarity), electrical interactions of the Schiff base with the counterion complex and other electrostatical interactions that either stabilize or destabilize the ground state or the excited state [65].

Xanthorhdopsins employ a different strategy to shift their spectrum. By binding a second chromophore, salinixanthin, xanthorhodopsin is also able to absorb blue light with spectral peaks at 457 nm, 487 nm and 521 nm, thereby complementing its retinal absorption at 565 nm [53]. The energy absorbed by salinixanthin is transferred to the retinal with an efficiency of 40 % [53]. Altogether, action spectra of retinal-binding proteins can be altered by tuning the residues of the retinal-binding pocket or by energy transfer from a second chromophore.

3.3.2. Halorhodopsins

Halorhodopsins (HRs) are inward-directed chloride pumps originating from Archea [66, 67]. They are activated by yellow light with maximal absorption at 580 nm. While their overall structure resembles the BR structure, some structural and mechanistic differences to BR account for chloride transport. The counterion complex is conserved for R108 (BR R82), D238 (BR D212), but the primary proton acceptor in BR (D85) is replaced by T111 in HR. This difference allows for chloride binding on the extracellular side of the Schiff base in dark-adapted HR. Early in the HR photocycle, the Schiff base orientates to the cytoplasmic side (K state) and the chloride ion is transported to the cytosolic release side (L states). Subsequently, the chloride ion is intracellularly released, the retinal thermally reisomerizes and the Schiff base adopts its original orientation (L $\rightarrow$ O). Finally, a chloride ion is bound to the extracellularly exposed transport side (O $\rightarrow$ N transition) and the initial protein conformation is reestablished [68, 69]. Notably, the HR photocycle does not include an intermediate with an unprotonated Schiff base (M state). Macroscopic photocurrents measured on cells expressing HR show similar time courses than BR currents with apparent ”outward currents” reflecting chloride influx [70, 71].

3.4. Channelrhodopsins

Channelrhodopsins (ChRs) are light-activated cation channels that constitute the primary photoreceptors of green algae (see section 3.2). The first identified ChRs originate from *Chlamydomonas reinhardtii* (C1 and C2) [16, 17, 18, 19] and *Volvox carterii* (V1 and V2) [36, 37, 38]. Only recently, genomic analysis revealed a variety of ChR genes in other algae species including *Mesostigma viride*, *Chlamydomonas augustae*, *Chlamydomonas yellowstonensis*, *Dunalliella salina*, *Pleodorina starii* and *Pyramimonas gelidicola* [72, 73, 26]. The following section deals with common structural and mechanistic principles of ChRs and focusses on C2 representing the best characterized ChR variant.

3.4.1. Structure

Channelrhodopsins consist of a N-terminal rhodopsin domain (amino acids 1-315 in C2) followed by an intracellular signaling domain (amino acids 316-737 in C2) [18] possibly involved in protein-protein interactions or eyespot targeting in the algae. Early studies showed that the rhodopsin domain is sufficient for channel activity [17, 18]. Therefore, in most studies truncated versions only expressing the rhodopsin part are used. Frequently, a fluorescent marker protein such as the green fluorescent protein (GFP) is C-terminally fused to the rhodopsin part, thereby replacing the original intracellular domain.

Figure 3.3 shows an amino-acid alignment comparing the C1, V1, C2 and BR sequences [74]. The ChR sequences exhibit 15 % to 20 % sequence homology when compared to other microbial rhodopsins [17] such as BR. Conserved residues are especially found in the retinal-binding pocket [17] whereas homology is lowest in helices one and two [75]. ChR sequences contain the retinal-binding lysine in helix seven (K257 in C2). Moreover, the conterion complex consists of E123 and D253 in C2 corresponding to D85 and D212 in BR. However, in *Dunaniella* ChR (DChR) one of the counterion charges is replaced by a neutral alanine without disrupting the channel function [26]. The primary proton donor in BR (D96) is replaced by histidine, alanine or lysine residues in ChRs (H134 in C2) [18, 72, 76]. Interestingly, ChR sequences feature a number of charged residues in helix two, that appear with a seven-helix periodicity (see amino acids highlighted in red in Figure 3.3) [75]. The side chains of these residues are supposed to face to the inside of the protein and to be involved in ion binding/transport [75]. But, in the phylogenetically more distant *Mesostigma* ChR (MChR) only three out of six charges are conserved.

Early structural models were obtained by homology modeling using the available crystal structures for BR and *Anabena* sensory rhodopsin as templates. These models were well-suited to describe the retinal binding pocket of ChRs but were underdetermined for the first two helices and the loop regions. Only recently, direct structural informations were gained from experiments on ChR crystals. First, Müller and coworkers solved the C2 structure at 6 Å by electron microscopy [77]. This first structure confirmed that ChRs form dimers as had been earlier concluded from biochemical studies. Furthermore, it showed the existence of seven transmembrane helices with helices three and four being located at the dimer interface [77]. However, the resolution was too low to position single amino acids.

Only in 2012, Kato *et al.* published the X-ray structure of a dark-adapted ChR at 2.3 Å [74]. They crystallized the C1C2 chimera consisting of the first five helices of C1 and the last two helices of C2 that had been previously described by others [78, 79, 80]. The high-resolution structure shows dimers built of cysteine-brigded protomers. Respective disulphide bonds are formed by C66, C73 and C75 (C27, C34 and C36 in C2) located N-terminally of the first helix (Figure 3.4A) [74]. When compared to BR, the C1C2 structure differs in the conformations of helices one, two and seven which are proposed to be involved in cation channeling [74]. Also, the amino acids of the counterion complex are differentially localized. In the closed channel conformation distances between the Schiff-base nitrogen and the carboxy groups of E162 and D292 (E123 and D253 in C2)

```
C1    MSRRPWLLALALAVALAAGSAGASTGSDATVPVATQDGPDYVFHRAHERMLFQTSYTLENN 61
V1    ---------------MDYPVARSLIVR-------------------------YPTDLGN 19
C2    ---------------MDYGGALSAVG--------------------RELLFVTNPVVVN- 24
BR    ------------------------------------------------------------

                              TM1                                TM2
C1    GSVICIPNNGQCFCLAWLKSNGTNAEKLAANILQWITFALSALCLMFYGYQTWK--STCGW 120
V1    GTVCMPRG--QCYCEGWLRSRGTSIEKTIAITLQWVVFALSVACLGWYAYQAWR--ATCGW 76
C2    GSVLVPED--QCYCAGWIESRGTNGAQTASNVLQWLAAGFSILLLMFYAYQTWK--STCGW 81
BR    ----------------QAQITGRP-EWIWLALGTALMGLGTLYFLVKGMGVSDPDAKKFYA 45

                                        TM3
C1    EEIYVATIEMIKFIIEYFHEFDEPAVIYS-SNGNKTVWLRYAEWLLTCPVILIHLSNLTGL 180
V1    EEVYVALIEMMKSIIEAFHEFDSPATLWL-SSGNGVVWMRYGEWLLTCPVLLIHLSNLTGL 136
C2    EEIYVCAIEMVKVILEFFFEFKNPSMLYL-ATGHRVQWLRYAEWLLTCPVILIHLSNLTGL 141
BR    ITTLVPAIAFTMYLSMLL--GYGLTMVPFGGEQNPIYWARYADWLFTTPLLLLDLALLV-- 101

           TM4                          TM5
C1    ANDYNKRTMGLLVSDIGTIVWGTTAALS-K-GYVRVIFFLMGLCYGIYTFFNAAKVYIEAY 239
V1    KDDYSKRTMGLLVSDVGCIVWGATSAMC-T-GWTKILFFLISLSYGMYTYFHAAKVYIEAF 195
C2    SNDYSRRTMGLLVSDIGTIVWGATSAMA-T-GYVKVIFFCLGLCYGANTFFHAAKAYIEGY 200
BR    D-ADQGTILALVGADGIMIGTGLVGALTKVYS-YRFVWWAISTAAMLYILYVLFFGFTSKA 161

            TM6                                  TM7
C1    HTVPKGICRDLVRYLAWLYFCSWAMFPVLFLLGPEGFGHINQFNSAIAHAILDLASKNAWS 300
V1    HTVPKGICRELVRVMAWTFFVAWGMFPVLFLLGTEGFGHISPYGSAIGHSILDLIAKNMWG 256
C2    HTVPKGRCRQVVTGMAWLFFVSWGMFPILFILGPEGFGVLSVYGSTVGHTIIDLMSKNCWG 261
BR    ESMRP-EVASTFKVLRNVTVVLWSAYPVVWLIGSEGAGIVPLNIETLLFMVLDVSAKVGFG 221

C1    MMGHFLRVKIHEHILLYGDIRKKQKVNVAGQEMEVETMVHEEDDET-------------- 346
V1    VLGNYLRVKIHEHILLYGDIRKKQKITIAGQEMEVETLVAEEEDDTVKQSTAKYASRPRT 316
C2    LLGHYLRVLIHEHILIHGDIRKTTKLNIGGTEIEVETLVEDEAEAGAV------------ 309
BR    LILLRS-RAIFGEAEAPEPSAGDGAAATSD----------------------------- 250
```

Figure 3.3.: Amino acid alignment based on the crystal structure of a ChR chimera by Kato et al. [74]. The sequences of the channelrhodopsins C1, V1 and C2 are aligned to the BR sequence. Helical structures (corresponding to the Kato structure) are colored in light blue, β-sheet-like motifs are depicted in yellow. Characteristic charged residues in helix 2 are highlighted in red color, other important ChR residues are colored in purple. Additionally, proton donor, proton acceptor, Schiff base lysine and counterion complex residues in BR and their corresponding residues in ChRs are shown in dark green.

are 3.4 Å and 3.0 Å [74]. In contrast to BR, the nearest water molecule in C1C2 is more distal (4.4 Å) than the respective carboxy groups. Moreover, theoretical calculations of pKa values propose that E162 is protonated and D292 is deprotonated in the dark suggesting that D292 functions as proton acceptor in C1C2 [74]. Kato *et al.* describe an electronegative pore between helices one, two, three and seven with major contributions from negative charged residues of helix two (Figure 3.4B). On the extracellular side a water-filled vestibule with a diameter of 8 Å is framed by polar residues including K154, K209 and R213 at the surface and R159, Y160, E274 and S284 further in the

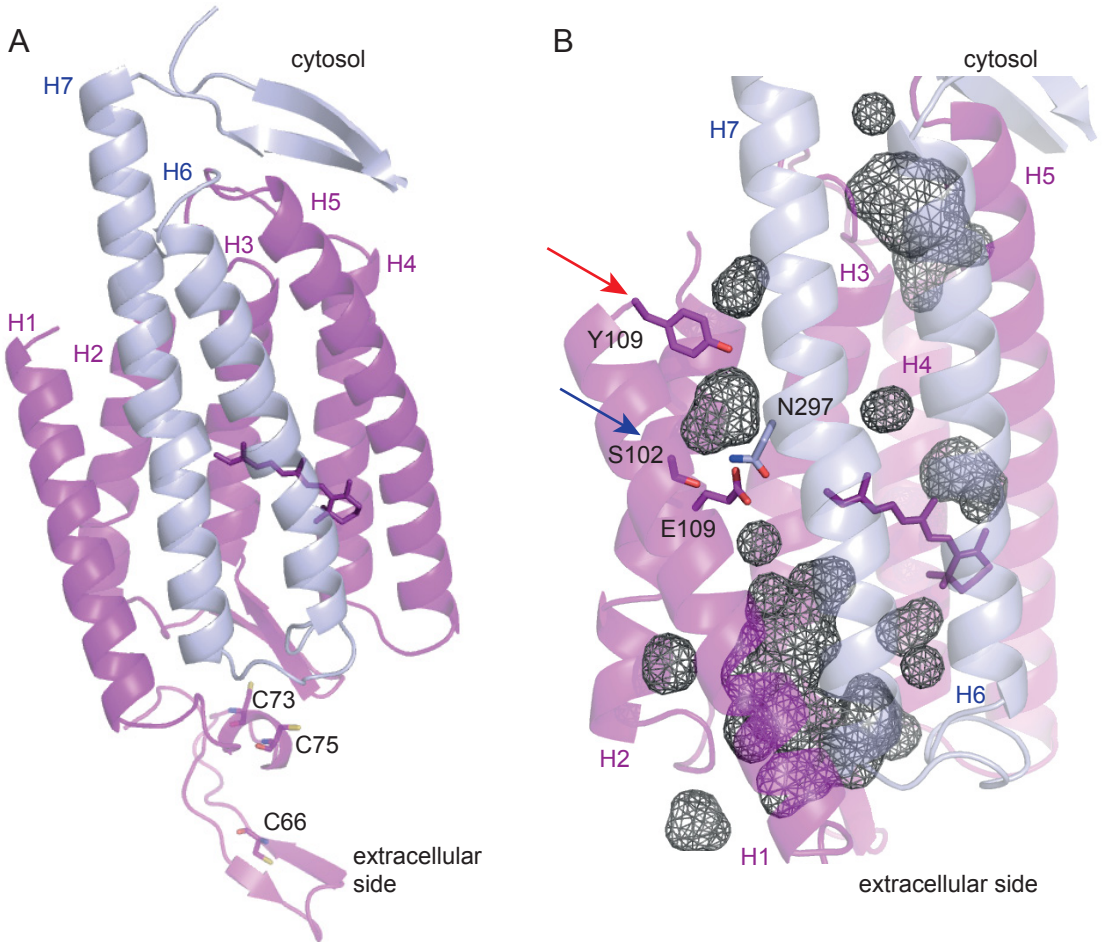

Figure 3.4.: Structural model of the C1C2 chimera after Kato *et al.* [74] (pdb:3UG9). The structure depicts dark-adapted C1C2, thus the channel adopts a closed conformation. The first five helices originating from C1 are shown in pink and the last two helices from C2 are colored in light blue. The all-*trans* retinal is highlighted in magenta. **A** Presentation of the entire protein including loop regions. The N-terminal cysteine residues that built disulphide brigdes with the other protomer are labeled. **B** Closer view on the transmembrane region. Cavities within the protein are depicted by grey wireframes. The potential channel is framed by helices one, two, three and seven. The large cavity located extracellularly of the Schiff base is blocked by two potential gates, the central gate (blue arrow) and the inner gate (red arrow).

vestibule (C2 R115, T170, K174 and C2 R120, Y121, E235, S245, respectively) [74]. Additional twelve polar amino acids are located at the inner end of the vestibule. Close to the retinal Schiff base the potential channel is blocked by S102, E129 and N297 (S63, E90 and N258 in C2) that are interconnected by several hydrogen bonds and directly interact with the counterions (Figure 3.4B blue arrow). A second constriction is given by the side chain of Y109 (C2 Y70) at the intracellular protein surface [74] (Figure 3.4B red arrow). Taken together, in the closed channel conformation cations may bind to the hydrophilic extracellular side of the channel, but are hindered to pass to the intracellular side by several residues. Notably, the Kato structure was available only after most of the experiments presented in this thesis were started. A structural model depicting the C1C2 structure and all amino acids relevant for this thesis, as well as the corresponding residues in related ChRs is depicted on the fold-out on the very last page A.1.

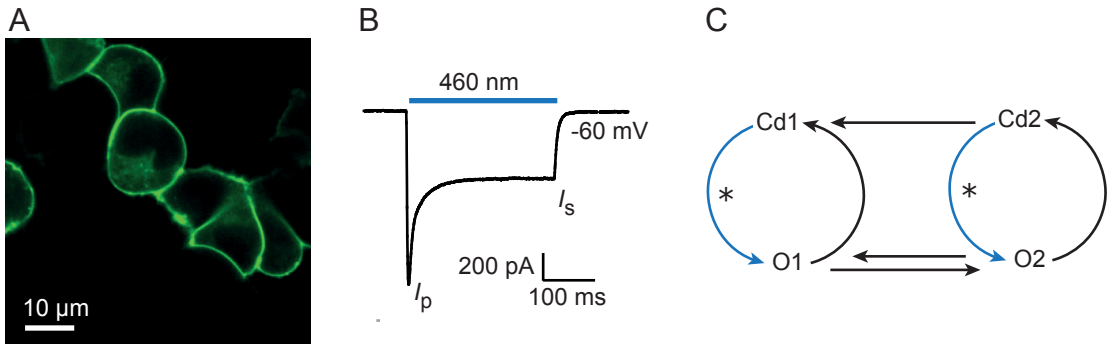

Figure 3.5.: Electrophysiological characterization of C2. **A** Green fluorescence of HEK cells transiently expressing C2-eGFP. The fusion protein is targeted to the plasma membrane. **B** Photocurrent of C2 recorded by whole-cell voltage-clamp measurement at −60 mV. The blue bar depicts the time of illumination at 460 nm. The current trace exhibits a characteristic peak current I_p that inactivates to a stationary current level I_s. **C** A four-state model with two open states O1 and O2 and two closed states Cd1 and Cd2 describes the electrophysiological properties of ChRs. O1 and O2 show distinct ion selectivities and their equilibrium is influenced by the applied electrochemical gradient and the quality of the activating light [84, 36, 85, 86].

3.4.2. Photocurrent properties

In order to examine light-induced ChR currents, ChRs are expressed in cultured adherent cells e.g. human embryonic kidney (HEK) cells (Figure 3.5A). The expression level and the ratio of membrane targeted protein thereby depend on the respective ChR variant and correlate with their photocurrent amplitudes. In HEK cells both C2 and V2 show high expression levels. In contrast, membrane expression of V1 and C1 are weak resulting in low photocurrent amplitudes (see Table 3.3).

ChR-expressing cells allow for current measurements by whole-cell voltage clamp recordings [81, 82]. Since single channel conductance is in the order of 40 fS at high Na^+ concentrations and −60 mV (C2) [83], measurements of single-channel opening and closing is not possible using classical electrophysiological methods. The measured photocurrents represent averages over many activated ChR molecules.

Figure 3.5B depicts a typical photocurrent trace for C2 measured at −60 mV. When activated by high-intensity blue light for 300 ms the inward-directed photocurrent comprises a high peak current I_p that is reached within 200 µs or even faster [18]. I_p gradually decreases to a stationary current level I_s. The transition from I_p to I_s is commonly referred to as inactivation and results from channel desensitization as well as from different conductances of I_p and I_s. After the light is turned off, the current level decays biexponentially to baseline level with effective time constants of 10 ms to 20 ms for C2 depending on extra- and intracellular pH. When a second activating light pulse is applied after a short dark period, the initial peak current amplitude is not reached. Only after a recovery period the initial current amplitude is regained [18, 84, 36]. The corresponding recovery kinetics are accelerated at negative voltages and low pH [18]. Degree of inactivation and kinetic parameters differ significantly between different ChRs and strongly depend on experimental conditions such as light quality, voltage and pH. Table 3.3 compares some kinetic parameters of selected ChRs.

Photocurrents result from transport of diverse cations including protons, monovalent

ChR	expression level in HEK cells	λ_{max} /nm pH 4	pH 7.5	inactivation /% $(1 - I_s/I_p)$	effective τ_{off} /ms pH 7.5
C1	+	500	470	32	23
C2	++++	460	460	72	21
V1	++	535	500 (pH 9)	38	77
V2	++++	465	465	/	25*

Table 3.3.: Comparison of basic properties of selected ChRs in HEK cells. The expression level is a qualitative measure for the amount of protein targeted to the HEK cell membrane and is reflected by photocurrent sizes [87]. Maxima of action spectra are compared at two different pH values [37, 38, 79, 88, 87]. Inactivation relates the stationary current size after 300 ms illumination to the peak current size [87]. Effective τ_{off} values represent the time point when the current has decreased to 1/e of I_s and combines the time constants of the biexponential decay after 300 ms of illumination [87]. *For V2 the fast decay component after continuous illumination that was determined for a V1V2 chimera in *Xenopus* oocytes is given as a reference value [36].

and divalent cations. Current amplitudes and direction depend on the applied electrochemical gradient indicating passive ion flux. The following order of decreasing relative conductances has been described for C1, C2, V1 and V2: $p(H^+) >> p(Li^+) > p(Na^+) > p(K^+) > p(Ca^+)$ [18, 36, 37, 80, 79, 86]. The relative proton conductance has been estimated to be between 10^5 and 10^6 times higher than the corresponding Na^+ conductivity [18, 80]. In contrast, K^+ conductivity is in the same order of magnitude than Na^+ conductivity with $p(K^+)/p(Na^+) \approx 0.4 - 0.5$ [18, 80]. Conductance of Ca^{2+} has been indirectly shown by activation of Ca^{2+}-activated Cl^- channels in *Xenopus* oocytes and directly by Ca^{2+} imaging using the fluorescent Ca^{2+} indicator Fura-2 [18, 80, 87]. The relative Ca^{2+} conductivity has been estimated to be 12 % of the respective Na^+ conductivity from changes in reversal potentials [80]. Small ion conductivities of other divalent cations such as Sr^{2+} and Ba^{2+} have been reported whereas Zn^{2+} and Mg^{2+} transport has not been detected [18]. But, under physiological conditions only protons, K^+, Na^+, Ca^{2+} and possibly Mg^{2+} contribute to the currents. Notably, the *Dunaniella* ChR is highly selective for protons and other conductances have not been detected for this ChR [26].

Berndt, Prigge *et al.* were the first who explicitly discrimated between C2 conductivity of the initial current and C2 conductivity of the stationary current. They determined the initial current I_0 by linear extrapolation of I_p to $t = 0$ of illumination (see Figure 4.1B in the methods part for details). By quantification of conductances from reversal potentials they determined higher relative proton selectivities for I_s than for I_0. In contrast, the relative Ca^{2+} conductivity was reduced for I_s when compared to I_0. To account for the different selectivities of I_0 and I_s, the biexponential current decay after light application and the pH-dependent recovery kinetics, two open states O1 and O2 and two closed states Cd1 and Cd2 have been proposed [84, 36, 85, 86]. The reaction scheme combining these four states is presented in Figure 3.5C. Dark-adapted ChR molecules populate the Cd1 state and are transformed to the first open state O1 following the first light activation. Therefore, the initial current I_0 is only mediated by conductances via O1. During prolonged illumination an equilibrium between the two open states is established. I_s is thus fed by conductances of both O1 and O2. After light is turned off, both closed

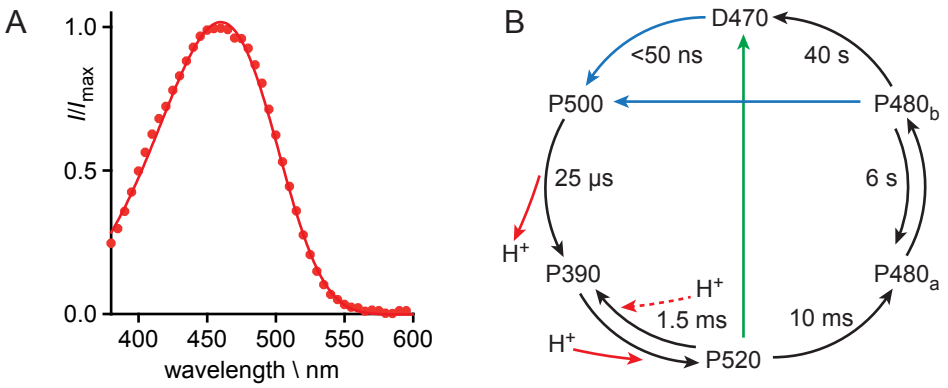

Figure 3.6.: Action spectrum and photocycle of C2. **A** Normalized action spectrum of C2 as recorded in HEK 293 cells. Maximal activation occurs at (460 ± 1) nm. **B** C2 photocycle model with the dark-adapted D470 state that undergoes as number of photointermediates after photon absorption. The conducting state appears on the time scale of the P390 and P520 photointermediates. The cycle can be shortcut by activation of the P520 intermediate by green light. The photocycle can also be triggered by blue-light activation of the $P480_b$-state. Red arrows indicate proton release and proton uptake. The model was adapted after Ritter *et al.* [89].

states are present. The recovery kinetics describes the transition from molecules in Cd2 to Cd1. All four states represent distinct ChR conformations, but direct structural information is only available for dark-adapted C1C2, presumably representing the Cd1 state.

3.4.3. Activation and photocycle models

Figure 3.6A shows the action spectrum of C2 using 10 ms actinic light pulses. The spectrum is bathochromically shifted when compared to the absorption of free retinal (opsin shift). It shows a characteristic maximum at $\approx$ 460 nm with a spectral half-bandwidth of $\approx$ 100 nm. Similar to proteorhodopsins, natural-occuring ChRs also feature color-tuned absorption. Whereas C1, C2 and V2 are maximally activated by blue light of 470 nm, 460 nm and 465 nm, V1 shows red-shifted activation at 535 nm (see Table 3.3) [37, 38, 79, 87]. The C1 action spectrum is pH-dependent and shifts to 500 nm at acidic pH [79]. In V1, the pH-dependent equilibrium displays higher pK_a values than in C1. Hence, at neutral pH V1 mostly adopts the red-shifted form with a minor shoulder peaking at $\approx$ 480 nm [88, 38].

As in other microbial rhodopsins photon absorption triggers retinal isomerization in ChRs. Subsequently, the activated protein undergoes a series of photointermediates that have been intensively studied by various spectroscopic techniques including UV-vis, IR, and Raman measurements on purified ChRs reconstituted in detergent solution or lipid vesicles. Figure 3.6B illustrates a simple photocycle model for C2 after Ritter *et al.* [89]. Blue-light absorption of dark-adapted C2 (D470) is followed by the conversion to the first red-shifted photointermediate P500 [89]. This early intermediate occurs on a sub-nanosecond timescale and is characterized by a non-planar retinal conformation coupled to major rearrangements of the protein backbone [89, 90, 91]. Next, the retinal Schiff base is deprotonated yielding the blue-shifted P390 state [92, 89]. The primary proton acceptor is most likely C2 D253, because the side chain of the corresponding

residue in C1C2 (D292) is closest to the Schiff-base nitrogen [74, 91]. The P390 state is in equilibrium with the P520 state exhibiting a reprotonated Schiff base [92, 89]. Reprotonation may occur from D156 close to the retinylene chain [91]. While there is general consensus about P520 being a conducting state, the involvement of P390 in ion conductance remains controversal [93]. IR measurements suggest the opening of the channel pore during a late P390 substate [91]. Channel closure goes along with the transition from the P520 state to the non-conducting P480 states that biphasically revert to the ground state [89]. Major conformational reorientations occur only in these late P480 states in the second-time range. Interestingly, E90 is deprotonated in at least one P480 substate and a transient hydrogen bond to N258 might be involved in channel closure [94, 91]. There are several light-induced cross reactions in the photocycle. For C2 wt a transition from the conducting P520 state to the ground state is triggered by green light absorption [89]. Moreover, upon UV absorption the P390 state can be photoconverted to a late photocycle intermediate as has been reported for the slow C2 mutant C128T [95, 93]. Slow-cycling mutants are well-suited to study photocycle reactions due to their highly prolonged occupancy of certain photointermediate states.

Retinal extraction and Raman measurements indicate a mixture of retinal isoforms even for dark-adapted C2 (C128T) that has never been illuminated before. Dark-adapted C2 exhibited between 22 % to 40 % 13-*cis* and 60 % to 78 % all-*trans* retinal [95, 96, 97]. The 13-*cis* to all-*trans* ratio increases upon illumination depending on the color and duration of light application [95, 97]. Also, minor amounts of 11-*cis* and 9-*cis* isoforms appear. Combining the retinal extraction experiments with IR spectroscopy, Ritter *et al.* concluded that multiple retinal isomerization occur in parallel during the photocycle. While all-*trans*, 15-anti as well as 13-*cis*, 15-*syn* retinal stabilize a saltbrigde between the Schiff base and the counterion complex - thereby favoring closed channel conformations - 13-*cis*, 15-*anti* and all-*trans*, 15-*syn* retinal could evoke the formation of the conducting states [95, 97]. Moreover, it has been suggested that the Cd1 state of the electrophysiological reaction scheme corresponds to the D470 state incorporating all-*trans*, 15-anti retinal that converts to the O1 state (P520 with 13-*cis*, 15-*anti*) upon light absorption. In line, D470 incorporating 13-*cis*, 15-*syn* and P520 featuring all-*trans*, 15-*syn* may represent the Cd2 and O2 states. The transition between the two cycles with the conversion of *cis*, *anti* to *trans*, *syn* might happen during late P480 photocycle intermediates [97]. The photocycle model presented by Ritter *et al.* explains both electrophysiological and spectroscopic findings on a molecular basis.

3.4.4. Selected channelrhodopsin variants

The following section deals with selected ChR variants that are not only interesting for deciphering the ChR mechanism, but are also relevant for ChR applications (see section 3.5.2). In general, variants have been created by site-directed mutagenesis (see Figure A.1 for positions of mutated residues) and by the chimera approach combining helices from different ChRs [78, 79, 80]. Recently, the genomic search for new ChRs extended the palette of available variants.

ChETA mutations: The residue corresponding to the primary proton acceptor BR D85 is C2 E123 belonging to the counterion complex [18]. Replacement of E123 to A, Q and T increases the I_p/I_s ratio and leads to faster τ_{off} values in the range of 5 ms (laser activation in *Xenopus* oocytes) to 15 ms (continuous illumination in HEK cells) [98, 87]. Moreover, the on-kinetics of E123T are accelerated by a factor of two when compared to wt C2 [98]. Interestingly, E123T exhibits a reduced voltage-dependency of the kinetics, allowing for fast photocycling even at depolarized membrane voltages [99]. As a consequence, the "ChETA" term stands for "ChR2-E123T accelerated", but can be equally applied for E123A and for combination mutants [98]. As expected from structural considerations, charge exchange in the counterion complex destabilizes the positively charged Schiff base of the dark state thereby red-shifting the ChR activation maximum. A closer insight into action spectra of ChETA mutants is given in sections 5.1.3 and 5.2.1. In addition to kinetic and spectral effects, E123 is also crucial for ion selectivity and E123A has been reported to exhibit enhanced proton selectivity [100]. A possible explanation is given by the close vicinity of E123 to the central gate residues allowing for direct interactions [74].

C2 H134: Mutations at position H173 in C1 -the corresponding residue to the BR proton donor D96- were already introduced by Nagel *et al.* [17]. Replacement by a negatively charged aspartate yielded unfunctional C1, whereas C1 H173R and H173Y were functional. Therefore, it was concluded that H173 does not act as proton donor in C1 [17]. Moreover, the corresponding mutant C2 H134R was tested in oocytes and HEK cells and was reported to exhibit reduced inactivation resulting in higher stationary photocurrents [101, 80]. Low inactivation usually is accompanied by decelerated kinetics. Lin *et al.* reported between 33 % and 60 % slower on-kinetics and between 32 % and 34 % slower channel closure with overall $\tau_{off} = 18$ ms for C2 H134R in their system. In the C1C2 structure H173 points towards the potential intracellular channel pore and might be part of the inner gate close to Y109 (see Figure 3.4) [74]. Accordingly, C2 H134 does not only influence channel kinetics, but also plays a role in ion selectivity. Both C2 H134R and H134S display a high competition between proton and Na^+ transport. At acidic pH Na^+-mediated currents are strongly inhibited by external protons in these mutants [100]. Taken together, C2 H134R and related mutations are useful due to their enhanced stationary photocurrents. The involvement of H134 in ion selectivity and channel gating needs to be investigated in more detail.

Step-Function Opsins (SFOs): C2 C128 and C2 D156 were identified to strongly influence channel on- and off-kinetics. When C128 is replaced by alanine, serine and theonine τ_{off} values are 51 s, 106 s and 2 s after prolonged illumination in *Xenopus* oocytes [102]. Similarly, D156A displays slow off-kinetics with time constants of $\tau_{off1} = 30$ s and $\tau_{off2} > 10$ min [103]. In BR and related proton pumps one charge is transported per absorbed photon. In contrast, the number of charges transported in ChRs depends on the opening time of single channels after photon absorption. Thus, the number of charges per photon are highly increased in SFOs displaying three to four orders of mag-

nitude longer opening times. This goes along with a higher light sensitivity of the SFO variants. The light sensitivity of ChRs is generally defined as the light intensity that accounts for half-saturating photocurrents. Both C128A and C128S show more than 300 times enhanced light sensitivity when responding to short light pulses [102].

Since the open state of C2 C128T is present on timescales easiliy accessible by spectroscopy, this mutant has been used to characterize the open states. In C2 C128T the P390 state and the P520 state can be converted to a late non-conducting photocycle intermediate, supposedly P480, by UV and green light absorption, respectively [95]. Also, in electrical measurements photocurrent decay after light off can be accelerated by UV or visible illumination [102, 87]. Triggering the backreaction by green light results in accelerated channel closure in both C2 C128A and C2 C128S, but photocurrents do not reach baseline level due to simultaneous activation of the dark state D470. Although driving the backreaction with yellow light is not as effective as with green light resulting in slower channel closing rates, yellow light does not activate SFOs and is thus best suited to diminish SFO photocurrents [102]. Alternating blue and yellow light pulses allow for bi-stable on and off-switching of SFOs. The SFO photocycle includes an additional branch appearing after prolonged light activation [95]. The corresponding photoproducts P380 and P353 were suggested to bind retroretinal [95] or to implie transiently hydrolysed retinal [104]. The ”branching” photoproducts are non-conducting and stable over minutes, thereby reducing the SFO photocurrents during prolonged illumination.

Since C128 and D156 mutants exhibit similar light responses, a direct interaction of the two residues e.g. by hydrogen bonding was suggested [103, 105]. Notably, the corresponding residues in BR, T90 and D115 form a interhelical hydrogen bond [106]. However, in the C1C2 structure side chain atoms of C167 and D195 are more than 4 Å apart and C167 is orientated towards the retinal [74]. Recent structural calculations by Watanabe *et al.* suggest indirect interaction of C2 C128 and D156 via an interjacent water molecule [107]. Nevertheless, they provide evidence for a direct hydrogen bond between the two residues in the C128T mutant [107]. Both kinds of interactions might be interrupted in the double mutant C2 C128S D156A that does not exhibit channel closure even 30 min after light activation (stable SFO, also SSFO) [108]. As mentioned above, D156 is a potential candidate for the primary proton donor in C2 [91]. The underlying mechanism and the interacting residues remain to be determined.

C2 T159C: C2 T159, a residue in close vicinity to D156, has been mutated to cysteine, the corresponding residue in V1 (see Figure 3.3). When expressed in *Xenopus* oocytes, C2 T159C displays more than ten-fold increased stationary photocurrent amplitudes compared to wt C2 [99]. In HEK cells, photocurrents were three-fold increased in our hands [87]. Slower off-kinetics of the single mutant can be compensated by additional introduction of the E123T mutation that leads to fast closure in the range of only 8 ms [99]. The double mutant C2 E123T T159C also features favorable properties such as red-shifted absorption and voltage-indendence of the kinetics [99]. Ullrich *et al.* showed that T159C exhibits superb retinal binding affinity providing higher protein stability,

especially in the case of low retinal concentrations [109].

C2 L132C "Catch": The "Calcium-transporting ChR" (Catch) has been generated by mutation of C2 L132 to cysteine. The mutant displays 2.5-fold higher photocurrents in HEK cells without altered single channel conductance [110]. Therefore, the enhanced currents are considered to be caused by the slower off-kinetics and a slightly higher expression level of the mutant. The decelerated kinetics imply a decreased inactivation which is only $(10 \pm 6)\,\%$ in our hands [87]. Moreover, the relative Ca^{2+} conductivity of the mutant is increased by a factor of 1.6 compared to the wt [110]. Expressed in hippocoampal neurons, Catch has been described to enhance the intracellular surface potential, thereby depolarizing the membrane. In addition, Catch-mediated Ca^{2+} influx activates neuronal BK channels [110]. In the C1C2 chimera the corresponding L171 is located close to H173 (C2 H134), but faces away from the inner gate towards helices four and five [74]. Thus, the molecular basis of the role of C2 L132 in ion selectivity is not understood.

Chimeric ChRs Chimeric ChRs combine helices from different ChRs with the aim of unifying their properties such as expression level, photocurrent kinetics and absorption. Due to wrong sequence information in the *Volvox* cDNA database, the first characterized *Volvox* ChR was inadvertently composed of the first two helices of V1 and the latter five from V2 [36, 38]. This V1V2 2-5 chimera exhibits V2-like properties, but shows a characteristic proton-induced 10 nm red-shift that is not seen in wt V2 [38].

In 2009 three groups systematically created chimeric proteins of C1 and C2 and analyzed the influence of selected helices [78, 79, 80]. All presented chimera possess the N-terminal part of C1, while the C-terminal helices are replaced by the corresponding C2 helices. Notably, ChR chimera comprising N-terminal parts of V2 and C2 were found to be unfunctional [88]. First, the different C1C2 chimera were tested for membrane targeting in different host systems. Wang *et al.* showed that chimera comprising the last five, four or three helices of C2, namely C1C2 2-5, C1C2 3-4 and C1C2 4-3, show superior membrane expression compared to both C1 and C2 in HEK cells [78]. Moreover, C1C2 3-4 and C1C2 5-2 display twofold higher photocurrents than C2 [78, 80]. C1C2 5-2 is of special interest, because it combines high photocurrents with low inactivation of $\approx 30\,\%$ [78, 79, 80]. The C1C2 5-2 chimera - also referred to as "ChEF" or simply "C1C2" - retains the pH-dependent spectral shift described for C1 [79, 88]. The exchange of C1C2 E87 by non-protonable glutamine stabilizes the red-shifted form even at neutral pH, exhibiting maximal absorption at 515 nm [79]. Since E87 is situated at the extracellular side of helix one, distant from the retinal binding pocket, the nature of this longe-range interaction is not clear [74]. Lin *et al.* replaced I170, a residue next to the Catch position and close to the inner gate, to valine. The resulting "ChIEF" mutant displays strongly accelerated off-kinetics with τ_{off} between 10 ms and 12 ms depending on the duration of the activating light pulse [80]. More recently, the Yawo group presented a similar chimera that consists of C1 with replacement of helix six as well as the second half of helix seven by the corresponding C2 sequences. This so-called "channelrhodopsin-green

receiver" (ChRGR) also exhibits high photocurrents evoked by green-light together with low inactivation and relatively fast off-kinetics (≈ 4 ms under their test conditions) [111]. In summary, the chimera approach is useful to understand the molecular determinants of ChR properties [78] and allows for creation of enhanced ChR variants with high potential for applications.

3.5. Optogenetic toolbox

Optogenetics is a fast-evolving method that combines genetic approaches with optical technologies for manipulation and visualization of cellular processes. The "optogenetics" -term was first applied by Deisseroth *et al.* for optical experiments on specifically "targeted neurons and proteins [...] within intact, living neural circuits" [112]. A broader definition given by Miesenböck implies any type of "genetically targeted groups of cells [...], often in the intact animal" as potential target for optical observation and manipulation [113].

Application of optogenetics demands for photosensitive proteins, strategies to deliver the respective genes into the cells of interest, technical means for targeted illumination and readout systems to monitor the light-induced effects [114]. Gene delivery employs transfection, viral transduction and the use of transgenic animals [114]. Illumination strategies use modern microscopy techniques in combination with different light sources such as LEDs and lasers. The present work focusses on the optimization of protein-based optogenetic tools that will be introduced in the following.

3.5.1. Overview

Optogenetic tools can be subdivided into the group of sensor proteins and the group of "optogenetic actuators", the latter comprising all proteins that influence cellular activity following light application. Sensors imply mostly fluorescent proteins that alter their fluorescent behavior upon changes in cellular properties. Sensor proteins might respond to changes in membrane voltage and pH or sense the concentration of ions, neurotransmitters or metabolites. Relevant tools for pH sensing are presented in section 3.5.4.

Complementary to the sensors, the diverse group of actuators implies photoreceptors involved in enzymatic processes or signal transduction and proteins that alter membrane properties such as voltage and electrochemical gradient. Representatives of the first group include natural and modified light-activated membrane receptors that bind specific G-proteins, thereby activating different signaling pathways [115, 116, 117]. Moreover, this group also comprises soluble photoreceptors e.g. LOV domains that couple to effectors including DNA binding proteins and enzymes. These modular systems allow for diverse manipulation of cellular activity [118, 119, 120]. Photoinduced protein dimerization has been used to study protein-protein interactions and for spatiotemporal protein recruitment [121, 122, 123, 124, 125]. The group is supplemented by naturally occuring light-activated enzymes e.g. the photoactivated adenylate cyclases that pro-

duce the common second messenger cAMP [126, 127]. The second group is constituted of microbial rhodopsins. Their use for membrane hyperpolarization/ depolarization is described in detail in the following sections.

3.5.2. Membrane depolarization

Back in 1988, Khorana *et al.* showed that heterologously-expressed bovine rhodopsin triggers light-induced inward currents in *Xenopus* oocytes [128]. The rhodopsin currents were small and were not suitable to induce sustained membrane depolarization. First attempts to depolarize plasmamembranes in order to trigger action potentials (APs) were performed by Zemelman *et al.* that coexpressed the *Drosophila* rhodopsin NinaE with arrestin-2 and the α-subunit of the cognate heterotrimeric G-protein [115]. Light induced currents showed a characteristic peak after several seconds followed by inactivation within $\approx 30\,\mathrm{s}$ [115]. In hippocampal neurons, currents could reliably evoke action potentials, but the three-component system did not establish itself as a neuroscientific tool due to difficult handling and poor time resolution.

Heterologously-expressed ChR allows for light-induced membrane depolarization by proton, Na^+ and Ca^{2+} influx [18]. In 2005, Boyden *et al.* showed that C2-induced depolarization is sufficient to drive action potential firing in cultured hippocampal neurons [129]. They used short blue-light pulses that precisely induced action potentials at frequencies up to 30 Hz. Moreover, they showed that supplementation of retinal is not necessary, thus the retinal concentration in the cells and the medium is sufficient for C2 functioning. In the following, C2 was used to elicit action potentials in acute brain slices [130] where it was employed to induce synaptic plasticity and to map neuronal circuits [131, 132]. Moreover, C2 activation triggered behavioral responses in chicken embryos [133], in *C. elegans* [101] and in *Drosophila* larvae [134]. Subsequently, the first C2-expressing transgenic mouseline was available [135]. Already in 2006, Bi *et al.* showed that C2 activation in inner retinal neurons restores vision in mice suffering from retina degeneration [136]. Other potentially clinical applications imply the treatment of Parkinson's disease [137] and restoration of hearing impairments [138]. Apart from neuronal activation C2-mediated membrane depolarization has been applied to other excitable cell types such as cardiomyocytes in zebrafish and mice [139, 140].

Although C2 has been successfully applied in many optogenetic experiments, it bears several limitations. C2 exhibits a high degree of inactivation that was partially overcome by introduction of the H134R mutation [101]. Since C2 H134R exhibits higher stationary currents it allows for more robust depolarization especially to prolonged light pulses [101, 80] and has therefore become the most commonly used depolarizing tool. Introduction of the ChETA mutations allows for very fast spiking with high precision [98]. The reduced photocurrent sizes of the fast-cycling mutant can be counterbalanced by additional introduction of T159C that greatly enhances protein stability and thus expression level in neuronal cells [99]. Similar to the C2 E123T T159C variant the ChIEF hybrid combines good expression and fast off-kinetics. In addition, ChIEF features low inactivation [80]. Complementary to the fast-cycling mutants the SFO variants allow for

long-time depolarization that can be switched on and off by single blue and yellow light pulses [102, 108].

While ChR variants with variable kinetics and high expression levels are now available, the fine-tuning of other parameters such as absorption maximum and ion selectivity is more difficult. Color-tuned ChRs would be useful for several reasons. First of all, both scattering and absorption of blue light in brain tissue is stronger than for red light [141]. Typically, brain tissue features minimal absorption between 600 nm and 700 nm due to overlapping spectra of water, fatty components, heme and other pigments [142]. Thus, red light penetrates deeper into tissue and shows less side effects such as local tissue heating. Second, more advanced optogenetic experiments combining different actuators or sensors demand for ChRs with distinct action spectra from the widely used C2. Although V1 shows maximal activation at 535 nm and was shown to elicit action potentials following orange light stimuli (589 nm), its employment has been limited due to its low expression and poor membrane targeting in mammalian cells [37, 88]. Color-tuned ChRs might be engineered by the chimera approach, by site-directed mutagenesis of the retinal binding pocket and by search for new ChR genes in genomic databases [78, 79, 80, 74, 98, 88, 72, 73, 26].

ChRs display low ion selectivity by conducting all kinds of small cations. Nevertheless, an optimal ChR would be highly-selective for one defined substrate e.g. a Na^+-selective ChR would be used for depolarization, a Ca^{2+}-selective ChR for synaptic activation and a K^+-selective one for AP inhibition. Several C2 point mutations have been described to alter ion selectivity. The Catch mutant exhibits 1.6-fold higher Ca^{2+} selectivity and E123A has been reported to feature higher relative proton conductance [110, 100]. However, highly-selective C2 variants are not at hand for cations other than protons. The design of such variants demands for a thorough study of the channel pore and its putative selectivity filter. Interestingly, DChR1 is a purely proton-selective variant, but has not been tested for neuronal expression due to its low expression level in *Xenopus* oocytes and HEK cells [26].

3.5.3. Membrane hyperpolarization

Contrarily to ChRs, activation of microbial proton and chloride pumps can hyperpolarize neuronal membranes, thereby reducing the probability of AP firing. In 2007, two groups applied the light-driven chloride pump from *Natronomonas pharaonis* (N_pHR) to optically inhibit neuronal activity with milli-second temporal precision [143, 70]. N_pHR was functionally applied in acute brain slices and its activation in muscle or neuronal cells elicited specific behaviors in worms *in vivo* [70]. Moreover, N_pHR was successfully combined with C2 using blue and yellow activating light [143, 70]. Following the first descriptions, N_pHR was used in many studies *in vitro* and *in vivo* including experiments on zebrafish, rodents and non-human primates [144, 145, 146, 147]. Clinically-relevant studies included Parkinson's and epilepsy models as well as vision restoration experiments in rodents [137, 148, 149, 150].

Proton pumps can also serve for neuronal silencing. In a screen for potential neuronal

silencers Chow *et al.* identified two suitable proton pumps with distinct action spectra [151]. Archaerhodopsin-3 from *Halorubrum sodomense* (Arch) enables effective hyperpolarization following yellow-green activation and is complemented by the proton pump from the fungus *Leptosphaeria maculans* (Mac) exhibiting maximal activation with blue-green light [151]. In cultured neurons, internal pH changes due to Arch activation were smaller than 0.2 pH units and were estimated to be in the range of physiological pH deviations [151]. Subsequently, the archaerhodopsin from the *Halorubrum* strain TP009 (ArchT) was reported to exhibit a three-fold enhanced light sensitivity when compared to Arch [152]. Therefore, ArchT might allow for more effective inhibition, especially in *in vivo* experiments. Mac and Arch variants offer an alternative way for membrane hyperpolarization whenenver N_pHR is not suited [153], e.g. when alteration of the cytosolic/extracellular chloride concentration causes unwanted side effects.

3.5.4. pH sensing

Many fluorescent sensors exhibit a modular architecture coupling one or more sensor domains to a circular-permutated fluorescent protein or a FRET pair. Upon binding of the respective substrate to the sensor domain, a conformational change is transduced to the respective FP, thereby changing its excitation or emission spectrum.

In contrast, pH imaging uses the intrinsique pH sensitivity of GFP derivatives. Wt GFP exhibits two excitation maxima at 395 nm and 475 nm which correspond to the two protonation states of Y66 of the GFP chromophore [154, 155, 156]. Miesenböck *et al.* screened for GFP mutants with enhanced pH sensitivity and found two optimized variants. Ecliptic pHluorin contains six amino acid replacements and reduces its fluorescence excitation at 395 nm by a factor of ≈ 7 when the pH is lowered from pH 7.5 to pH 5.5 [156]. Ratiometric pHluorin (nine mutations) shows fluorescence reduction at 395 nm going along with fluorescence increase at 475 nm following pH reduction, thereby allowing for ratiometric pH determination [156]. Since both variants reversibly change their excitation spectra within < 20 ms and feature pK_a values between 6.5 and 7.2 [156], they are suited to detect changes in cytosolic pH and allow for distinction between different cellular compartments. A brighter version of ecliptic pHluorin - so-called superecliptic pHluorin - was obtained by introduction of two additional point mutations and exhibited a characteristic pK_a of 7.1 [157]. Complementary, the T-Sapphire variant of GFP exhibits enhanced protein folding, a single excitation maximum at 399 nm and a pK_a of 4.9 [158]. Thus, this variant is suitable for detection of pH changes in acidic compartments such as lysosomes.

In order to allow for multi-color imaging GFP-variants with distinct fluorescence spectra are demanded. Screening of mutant libaries and genomic searches for new FPs yielded many fluorescent protein variants that cover the entire visible range from blue to near-infrared emission (for a review see [159]). Red-fluorescent proteins (RFPs) are especially suited for combination with GFPs or with blue-light activated ChRs. pHRed is a ratiometric, pH-sensitive RFP that was developed by mutagenesis of the FP mKeima [160]. Excitation at 440 nm and 585 nm enables ratiometric pH determination with an apparent

pK_a of 6.5 [160]. pHRed has been applied to visualize cytosolic and mitochondrial pH alterations [160]. An alternative pH-sensitive RFP is represented by the mStrawberry-derivative pHTomato. This single wavelength indicator is maximally excited at 550 nm and strongly reduces its fluorescence upon acidification featuring a pK_a of 7.8 [161]. pHTomato has been applied in combination with the green-fluorescent Ca^{2+} indicator GCamp3 and the channelrhodopsins C2 and V1 [161]. Both pHRed and pHTomato can be activated by two-photon absorption and extend the palette of available pH indicators [160, 161].

3.5.5. Targeting of optogenetic tools

Effective use of optogenetic tools requires their targeting to the cells of interest and expression in the respective cellular compartment. Cellular targeting is accomplished by different transfection methods e.g. viral delivery, lipofection or electroporation in combination with cell-type specific promotors [162]. Conditional gene expression using the Cre-Lox system and transgenic animals represent alternative ways of targeting as extensively described for C2 [163, 164]. Activity-dependent expression using immediate early gene promotors and retrograde neuronal labeling are examples of further sophisticated targeting concepts [131]. While a variety of systems for cell-type specific expression are available, only few examples for subcellular targeting of optogenetic tools have been reported.

Surface expression of microbial rhodopsins: Photocurrents of microbial pumps and channelrhodopsins directly correlate with the amount of protein targeted to the plasma membrane. Gradinaru *et al.* systematically tested targeting sequences for enhancing the surface expression of N_pHR. N-terminal fusion of the signal peptide of the nicotinic acetylcholine receptor in combination with the C-terminal ER export signal from a vertebrate potassium channel yielded improved surface expression [137]. Correspondingly, the resulting enhanced N_pHR ($eN_pHR2.0$) exhibited two-fold higher photocurrents in hippocampal neurons [137]. C-terminal fusion of the trafficking signal from Kir2.1 further enhanced plasmamembrane targeting in the "state of the art" chloride pump $eN_pHR3.0$ [165]. This variant features up to 20-fold higher currents than the initial N_pHR thereby allowing for membrane hyperpolarization of more than 100 mV at moderate light intensities [165]. All three targeting sequences have also been applied to optimize membrane expression level of the green-absorbing channelrhodopsin V1, but only with moderate success [88, 108].

Targeting to neuronal compartments: Subcellular neural activation enables the investigation of local depolarization independent of global AP firing. By C-terminal fusion of the myosin-Va binding domain (MBD) of melanophylin to C2, C2 was preferentially localized in the somatodendritic region and was excluded from the axon [166]. Photoexcitability of axons expressing C2-MBD was reduced by a factor of six when compared to axons expressing untargeted C2 [166]. In another study C2 was targeted to the

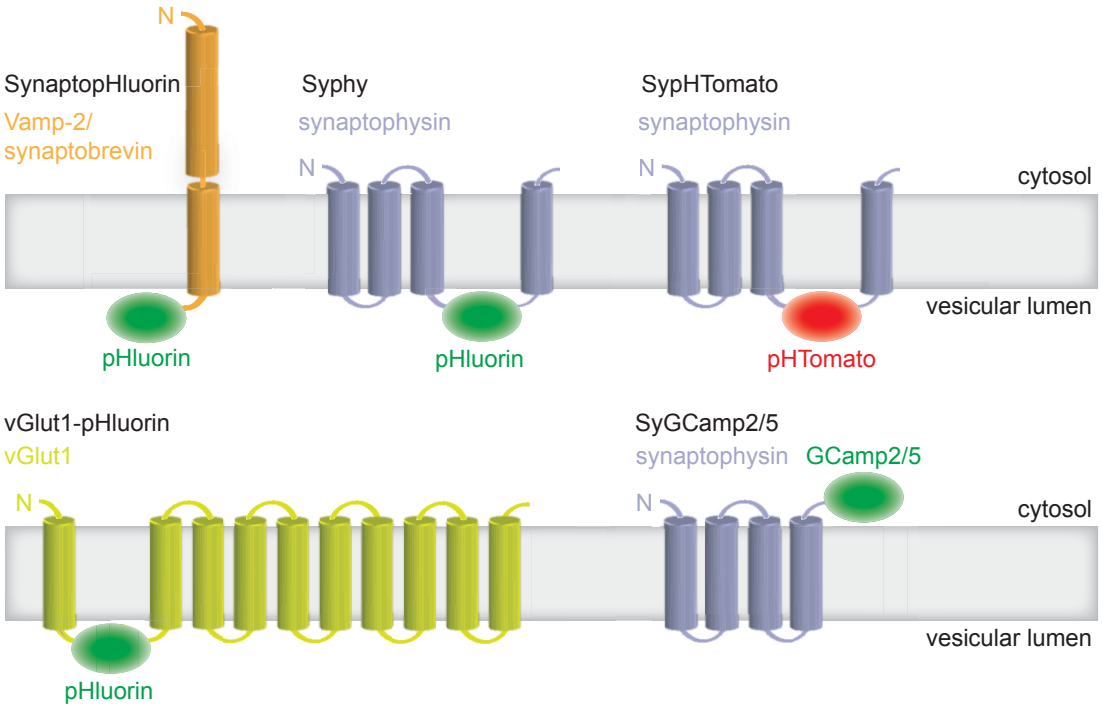

Figure 3.7.: Overview of available sensor proteins targeted to synaptic vesicles. The original synaptopHluorin was obtained by C-terminal fusion of pHLuorin to Vamp2/synaptobrevin [156]. Syphy, SypHTomato and SyGCamp represent fusion proteins with synaptophysin [172, 161, 173, 174]. VGlut1-pHluorin combines vesicular targeting with cell-type specificity [175].

postsynaptic side of glutamatergic synapses by C-terminal fusion of the PDZ binding motif ETQV involved in NMDA receptor clustering [167]. Postsynaptically targeted C2 retained its ability to trigger action potentials in hippocampal neurons. C-terminal addition of the ankyrinG-binding loop of voltage-gated sodium channels localized C2 to the axon initial segment (AIS) [168]. In cultured hippocampal neurons the AIS-targeted C2 generated low photocurrents and was only able to trigger APs when voltage-gated K^+ channels were blocked [168]. The same targeting strategy was applied to localize C2 to a specialized AIS-like structure in axonless amacrine cells of the mouse retina [169]. Targeting of C2 or N_pHR to the axonal membrane used N-terminal fusion to the ankyrinG polypeptide and was combined with dendritic targeting of the respective other actuator (N_pHR or C2) by fusion with the postsynaptic density 95 (PSD-95) targeting motif [170]. In ganglion cells the described spacial separation of C2 and N_pHR enabled differential spatial and spectral photosensitivity, thereby generating center-surround antagonistic receptive fields [170]. In brain slices and in vivo 3D laser-scanning photostimulation might offer an alternative way to activate subcellular compartments without targeting of the respective optogenetic tool [132, 171].

Targeting to synaptic vesicles: To study the processes underlying synaptic transmission, optogenetic tools directly targeted to synaptic vesicles are of great interest (see Figure 3.7). Ecliptic pHluorin has been targeted to the lumen of presynaptic vesicles by N-terminal fusion to VAMP-2/synaptobrevin, thereby allowing for vesicular pH determination [156]. The resulting synaptopHluorin has been successfully applied to study

kinetics of vesicular recycling and vesicular acidification [176, 177]. An improved version of synaptic pHluorin (Syphy) has been generated by introduction of super-ecliptic pHluorin into the second lumenal loop of synaptophysin [172] and has been used to study vesicle retrieval, synaptic plasticity and synapse development [178, 179, 180]. The same molecular design was applicable for synaptic targeting of pHTomato [161]. SypHTomato enabled combinational application with both GCamp3 and V1 [161]. A synaptic pH indicator specific for glutamatergic neurons has been created by fusing super-ecliptic pHluorin into the first lumenal loop of the vesicular glutamate transporter VGlut1 [175].

Complementary to synaptic pH markers, synaptoGCamp2 - a synaptic Ca^{2+} indicator - has been obtained by fusion with synaptophysin and applied to evaluate the impact of Ca^{2+} on synaptic strength [173, 179]. Accordingly, one of the latest versions of green-fluorescent Ca^{2+} indicators, namely GCamp5, has been successfully targeted to the synapse [174]. Although diverse synaptic sensors are available (Figure 3.7), presynaptic targeting of optogenetic actuators has not yet been reported.

3.6. Synaptic processes

Chemical synapses constitute key structures involved in neuronal communication and represent potential targets for subcellular application of optogenetics. In the following, the basic processes underlying synaptic transmission are introduced.

Chemical synapses are junctions between two cellular membranes, usually the axonal membrane of a neuron (presynaptic cell) and the dendritic membrane of a second neuron (postsynaptic cell) where directional communication via neurotransmitter release and reception takes place. At the presynaptic membrane neurotransmitter-containing vesicles are docked to the so-called active zone (Figure 3.8 - 1). Vis-à-vis, at the postsynaptic membrane specific neurotransmitter receptors are clustered. According to their function receptors are classified into ionotropic receptors constituting ion channels, and metabotropic receptors that activate intracellular signaling cascades by G-protein coupling. Signaling from the presynaptic to the postsynaptic cell involves the following steps (see Figure 3.8): Upon arrival of an action potential at the presynaptic terminal, voltage-gated Ca^{2+} channels mediate Ca^{2+} influx. The local increase in Ca^{2+} concentration is sensed by synaptotagmins and complexins and causes conformational changes in the SNARE-complexes of docked vesicles thereby triggering vesicle exocytosis (as reviewed in [181]). Similarly, double C2 domain (Doc2) proteins are high-affinity Ca^{2+} sensors involved in spontaneous vesicle fusion [182]. Neurotransmitters are released into the synaptic cleft and bind to specific postsynaptic receptors. Opening of postsynaptic ion channels induces hyperpolarization (inhibitory postsynaptic currents) or depolarization (excitatory postsynaptic currents) of the postsynaptic membrane depending on the nature of neurotransmitters and receptors. Activated metabotropic receptors mediate slower cellular responses by activation/inhibition of important signaling proteins including phospholipase C, protein kinase C, adenylyl cyclases and phosphodiesterases, or by modulating activity of ionotropic receptors [183]. Neurotransmitter removal occurs via diffusion, enzymatic digestion and neurotransmitter reuptake by presynaptic or glial

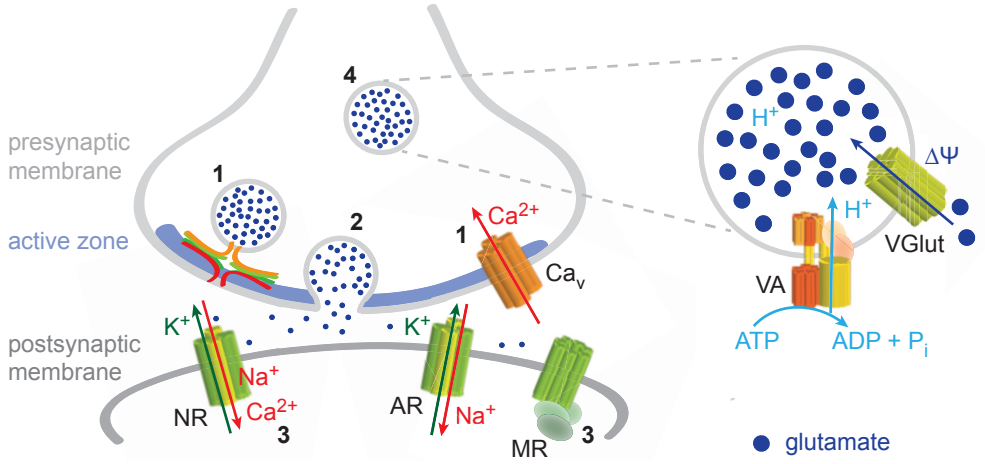

Figure 3.8.: Basic steps in synaptic transmission (modified after [184]). **1** Upon arrival of an action potential at the presynaptic terminal, voltage-gated Ca^{2+} channels mediate Ca^{2+} influx. **2** The increase in the presynaptic Ca^{2+} concentration triggers membrane fusion of docked and primed vesicles (**1**) of the active zone. Neurotransmitters e.g. glutamate are released into the synaptic cleft. **3** Neurotransmitter binding to postsynaptic ionotropic receptors initiates postsynaptic currents. In the case of glutamate, depolarizing, thus excitatory post-synaptic currents (EPSCs) are initiated. Neurotransmitters also activate metabotropic postsynaptic receptors that regulate postsynaptic signaling cascades e.g. by G-protein activation. Finally, neurotransmitters are removed from the synaptic cleft by diffusion, enzymatic digestion and/or neurotransmitter reuptake. Synaptic vesicles are recycled from the presynaptic plasma membrane. **4** Vesicular ATPases acidify newly formed vesicles and the resulting electrochemical gradient is used for glutamate uptake via vesicular glutamate transporters. Docking and priming of vesicles may allow for another fusion event. Ca_v - voltage-gated Ca^{2+} channel, NR - NMDA receptor, AR - AMPA receptor, MR - metabotropic glutamate receptor, VA - V-type ATPase, VGlut - vesicular glutamate transporter.

transporters. Afterwards, presynaptic vesicles are recycled, filled with neurotransmitters and potentially docked again to the active zone.

3.6.1. Recycling of presynaptic vesicles

Synaptic vesicles are recycled from the presynaptic membrane by at least three different mechanisms (reviewed in [185]). Clathrin-mediated endocytosis in combination with fast uncoating constitutes the most common way of vesicle retrieval [186, 187]. After burst of exocytic activity bulk endocytosis produces large vacuoles that are subsequently converted to synaptic vesicles by a yet undeciphered mechanism [188]. The third way of vesicle internalization - also referred to as kiss-and-run - includes a transient membrane-vesicle fusion that allows for direct recycling of the vesicle without vesicular collapse [189]. Independent of the regeneration pathway, the resulting vesicles are homogeneous in size and feature a defined composition of synaptic proteins [185]. While synaptic proteins such as synaptotagmin and synaptophysin occur in several tens of copies per vesicle, only a dozen copies of neurotransmitter transporters and one or two copies of the vacuolar-type ATPase (V-type ATPase) are present in a single vesicle [190]. Synaptic V-type ATPases hydrolyze ATP to pump protons into synaptic vesicles, thereby acidifying synaptic vesicles (Figure 3.8). The resulting proton motive force is used by specialized transporters for neurotransmitter uptake. The uptake of glutamate - the most commonly used excitatory neurotransmitter in the central nervous system - is mediated by

glutamate transporters such as the mammalian isoforms VGlut1, VGlut2 and VGlut3 [191, 192, 193, 194]. VGlut-mediated glutamate uniport is driven by both the electrical gradient over the vesicular membrane and δpH [195]. Moreover, glutamate transport is enhanced by intravesicular chloride and is inhibited by high cytosolic chloride concentrations [196]. Other neurotransmitter transporters employ different transport modes including proton-amine antiport (amines can be serotonin, adrenaline, noradorenaline, histamine or dopamine) and chloride-GABA synport [195]. In glutamatergic hippocampal synapses, the quantal size of excitatory postsynaptic currents (EPSCs) is unaltered even after prolonged high-frequency stimulation, suggesting that glutamate uptake is completed during vesicle recycling [197, 198]. While vesicle acidification was estimated to exhibit time constants between 0.5 s and 5 s in cell culture, glutamate uptake displays maximal rates in the range of 15 s [176, 198]. Thus, glutamate refilling is faster than recovery of EPSCs after vesicle depletion induced by high-frequency stimulation occuring within 40 s [199, 198].

3.6.2. Vesicle pools and release probability

At single synapses vesicles can be classified into two functional pools [200]. The recycling pool encompasses all vesicles that can be released following AP-induction [200, 180]. Out of these vesicles the ready-releasable subfraction is rapidly released upon sporadic firing and corresponds to vesicles docked to the active zone and primed for release, whereas the remainder is recruited only following sustained activity [201, 202, 200]. The size of the recycling pool directly correlates with the release probability of the individual synapse, thus the number of vesicles released following one AP [201, 180]. In contrast, the resting pool describes vesicles that do not participate in synaptic neurotransmitter release. The fractions of the relative pool sizes depend on the developmental stages of the neuronal tissue, the history of depolarizing events at the respective synapse as well as type and size of synapses [180]. Pool partioning represents an important mean to regulate synaptic strength at a level of individual synapses.

3.6.3. Motivation for presynaptic optogenetic manipulation

The presynaptic vesicle machinery plays a key role in maintenance and regulation of synaptic transmission at chemical synapses. It has been intensively investigated by biochemical studies, electron microscopy, fluorescence imaging and analysis of the corresponding postsynaptic electrical responses [203, 204, 205, 206, 156]. However, none of the available methods enables temporally precise manipulation of the individual steps in the vesicle cycle. Hence, biophysical studies analyzing the complex reaction sequences are difficult to perform. Optogenetic manipulation is especially well-suited to trigger reactions with high spatiotemporal resolution. Optogenetic activation of specific steps in the vesicle cycle e.g. vesicle acidification, neurotransmitter uptake, vesicle docking and priming or vesicle fusion may constitute a potent mean to analyze these processes. Light control in combination with the available read-out techniques may not only be used to temporally resolve the reaction sequences, but also to investigate the causalities

of the complex reaction network. Presynaptic optogenetic experiments may thus allow to analyze the energetic coupling of the underlying reactions e.g. what driving forces are essential for vesicular neurotransmitter uptake or vesicle fusion. Moreover, it may reveal molecular determinants for pool partioning and release propability at the level of individual vesicles. Hence, an optogenetic interrogation of selected presynaptic processes may facilitate to answer some open questions of synaptic information processing.

3.7. Objective of Research

The present study addresses three important questions of optogenetics. First, it deals with the design and characterization of a high-efficiency channelrhodopsin that features a distinct action spectrum when compared to the most commonly used optogenetic actuator C2. Second, principles of ion selectivity and gating in ChRs are aimed to be pointed out in both a qualitative and a quantitative manner. Third, the construction of an optogenetic tool that photoactivates synaptic vesicle acidification is pursued.

In order to allow for efficient *in vivo* applications of ChRs a red-shifted ChR with a high expression level would be favorable. A potent variant would enable combinational experiments with C2 and GFP-based sensory proteins (see section 3.5.2). Moreover, it may allow for deeper light penetration into the target tissue without increasing the intensity of the actinic light. Such a red-shifted variant could be either obtained by improved expression of the yellow-light absorbing V1 or by red-shifting the absorption maxima of available high-expressing ChRs by mutation of the retinal binding pocket. Alternatively, identification of new ChRs by screening genomic databases of green algae originating from different habitats may reveal potential candidate proteins. Here, several strategies for the optimization of a red-shifted ChR are followed. Resulting variants are analyzed for expression strength and photocurrent properties. Subsequently, both spectral and kinetic features are further fine-tuned offering potent candidates for two-color optogenetic experiments.

Although ChRs have been characterized for more than ten years, few information is available on the mechanisms that regulate ion selectivity of these channels. But, only a detailed comprehension of the underlying structural elements may allow for the design of cation-selective ChRs. In addition, knowlegde of the exact composition of ChR-mediated photocurrents is essential to evaluate results of diverse ChR applications. Here, key residues of the ion conduction pathway are systematically mutated and analyzed for cation selectivity. Based on homology modeling and the recently available C1C2 structure, two potential channel gates that may act as selectivity filters are identified and tested for their functional relevance. Apart from structural considerations, the present work aims at understanding the kinetic parameters that determine ion transport and ion competition. A special focus is laid on cation composition of the stationary photocurrent that has not yet been quantitatively analyzed. The creation of an ion transport model that quantitatively describes cation conductance of both early and late photocurrents would allow for a better choice of the best-suited ChR for a certain application.

Targeting of optogenetic actuators to subcellular domains enables the control of mem-

brane voltage and ion composition in specialized cellular compartments. Neurons are subdivided into compartments with distinct functions in information transmission. Out of these, the presynapse is a specialized region that converts temporal changes in membrane voltage into chemical signals detectable for postsynaptic cells. Based on targeting strategies applied for presynaptic sensors, the development of a presynaptic actuator is pursued in the present work. The biophysical properties of the resulting fusion proteins are analyzed by electrical recordings. Furthermore, the new tools are tested for subcellular localization in cultured hippocampal neurons and are used for preliminary experiments to monitor presynaptic processes. Eventually, subcellular optogenetics will extend the repertoire of cellular manipulation experiments, thereby increasing the specificity of optogenetic interventions.

Taken together, this study combines mechanistic analysis of optogenetic actuators with the design of new optogenetic tools, thus paving the way for broad applications of light-activated proteins.

4. Materials and methods

Gene synthesis together with standard molecular biology techniques allow for the creation of plasmids that code for the genes of the respective proteins of interest. Modified genes are generated by the use of molecular cloning and site-directed mutagenesis. Proteins are heterologously expressed in HEK 293 cells, Cos cells and cultured hippocampal neurons. Protein purification from Cos cells potentially enables spectroscopic analysis of the photoactivated proteins (see supplementary method in section A.2 for the respective purification protocol). Photocurrent properties of microbial rhodopsins are tested in electrophysiological measurements applying the whole-cell patch-clamp method in combination with complex illumination protocols. While electrical recordings on HEK 293 cells serve for the mechanistic analysis of rhodopsin characteristics, measurements on hippocampal neurons enable light-activated manipulation of neuron-specific behaviors. Recordings on self-projecting ("autaptic") neurons are applied to examine both spontaneous and evoked postsynaptic cellular responses. In order to investigate protein expression levels and localization, rhodopsin-coupled fluorescent proteins are visualized by fluorescence microscopy. Moreover, Fura-2 imaging allows for a comparative analysis of intracellular Ca^{2+} concentrations. Finally, an enzyme-kinetic algorithm is applied to quantitatively describe the data gained from ion-selectivity measurements.

4.1. Molecular biology

4.1.1. Reagents

The principal reagents used for *E. coli* culturing, DNA modification and plasmid preparation are summarized in Table 4.1.

reagent/ kit	source
components of *E. coli* media	Becton, Dickinson and Co. (Le pont de claix, France)
salts, sugars, antibiotics, other chemicals	Sigma Aldrich (Hamburg, Germany) or Carl Roth (Karlsruhe, Germany)
reprofast polymerase and reaction buffer	Genaxxon Biosciences (Ulm, Germany)
PfuTurbo DNA polymerase and DpnI enzyme	Agilent Technologies (Böblingen, Germany)
restriction enzymes, ligase and corresponding buffers	Fisher Scientific GmbH (Schwerte, Germany)
customized primers	Sigma Aldrich (Hamburg, Germany)
PureYield Plasmid Maxiprep System	Promega GmbH (Mannheim, Germany)
NucleoSpin Plasmid and NucleoSpin Gel and PCR clean-up kit	Macherey-Nagel GmbH (Düren, Germany)

Table 4.1.: Reagents used for molecular biology and their respective sources.

4.1.2. Buffers

Commonly used media and buffers applied for regeneration of competent *E. coli* are presented in Table 4.2.

solution	components and concentration	solvent	pH
LB medium	10 g l^{-1} tryptone; 5 g l^{-1} yeast extract; 10 g l^{-1} NaCl; only for plates: 15 g l^{-1} agar	ddH_2O	7.5 (NaOH)
SOB medium	20 g l^{-1} tryptone; 5.5 g l^{-1} yeast extract; 10 mM NaCl; 10 mM KCl; after autoclaving: 10 mM $MgCl_2$; 10 mM $MgSO_4$;	ddH_2O	/
TfbI	30 mM KAc; 50 mM $MnCl_2$; 100 mM KCl; 15 % glycerol	ddH_2O	5.8 (acetic acid)
TfbII	10 mM Mops; 75 mM $CaCl_2$; 10 mM KCl; 15 % glycerol	ddH_2O	7.0 (NaOH)

Table 4.2.: Composition of media and buffers employed for *E. coli* culturing. LB and SOB display growth media. TfbI and TfbII represent buffers for preparation of chemocompetent *E. coli* cells.

4.1.3. Genes and vectors

Table 4.3 presents all template genes used for cloning.

gene	vector	origin	references
Cop3 (C1)	peCFP-N1	Satoshi Tsunoda	[17]
Cop4 (hC2)	peCFP-N1	Matthias Prigge	[18]
Cop4 (hC2)	pmCherry-N1	Matthias Prigge	[18]
Cop4 (hC2)	pMT4	Katja Stehfest	[89]
hV1	peCFP-N1	self-made	[37]
hV1	pLenti	Karl Deisseroth (Stanford)	[37]
V2	peGFP-N1	Matthias Prigge	[38]
Arch3	peGFP-N1	addgene	[151]
C_vRh	pGEM	Suneel Kateriya (Delhi)	/
N_pHR	pGEM	Satoshi Tsunoda	[207]
β-SU ATPase	pUC57	synthesis (GeneScript)	[208, 209, 210]
Syphy	pLenti	Benjamin Rost (Charité)	[172]

Table 4.3.: List of genes used for all future constructs. The "h" indicates codon-optimization according to human codon usage.

To visualize protein expression, fluorescent marker proteins derived from the green fluorescent protein (GFP) from *Aequorea victoria* were C-terminally fused to microbial rhodopsins. In order to purify selected ChRs C-terminal affinity tags were employed (see Table 4.4). Commonly used DNA vectors are summarized in Table 4.5.

4.1.4. Competent E. coli

XL1-blue cells were used for the enrichment of regular DNA plasmids. When demethylated DNA was required the methylation-deficient *E. coli* strain JM-110 was utilized.

fluorescent marker or tag	application
eCFP	labeling of green-light activated ChRs
eGFP	labeling of light-activated pumps
eYFP	labeling of ChRs for neuronal expression
mCherry	labeling of blue-light activated ChRs
mKate	labeling of proton pumps in synapses
pHluorin	imaging of synaptic pH changes
1D4	protein purification from HEK or Cos cells

Table 4.4.: List of protein tags and their respective usage.

vector	promotor	resistence gene	application
peGFP-N1 and derivatives	CMV	kanamycin	HEK cell recordings
pMT4	AdMLP	ampicillin	protein purification from HEK or Cos cells
pLenti	hsynapsin	ampicillin	neuronal expression

Table 4.5.: List of commonly used vectors for expression of microbial rhodopsins in HEK 293 and Cos cells, and primary hippocampal neurons. CMV - cytomegalovirus promotor, AdMLP - adenovirus major late promotor, hsynapsin - human synapsin promotor.

In order to minimize recombination events in lentiviral constructs that exhibit long-terminal repeats, we used Stbl3 cells (Life Technologies GmbH, Darmstadt, Germany) for plasmid preparation.
Chemocompetent cells were prepared using the following protocol: A 50 ml preculture in SOB medium was inoculated from the respective *E. coli* glycerol stock. Cells were grown at 37 °C and 190 rpm overnight. The main culture was started at an OD_{578} of 0.05 in a 200 ml volume of SOB. Cells were harvested at a final density of 0.3-0.4. The cell suspension was transferred to falcon tubes and cells were pelleted by centrifugation at 4 °C and 3000×g for 7 min. Cells were resuspended in 15 ml of TfbI buffer on ice for 10 min. After a second centrifugation at 3000×g for 5 min and resuspension in 2 ml of TfbII 110 µl of cells were aliquoted in Eppendorf tubes and immediately shock frozen in liquid nitrogen. Competent cells were stored at −80 °C until they were used for transformation.

When a small amount of competent cells of a certain strain was sufficient, electrocompetent cells were used. Preparation of electrocompetent cells included the following steps. First, 5 ml of LB medium was inoculated from the respective *E. coli* cryostock and incubated at 37 °C and 190 rpm overnight. The next day 100 µl of the preculture were transferred to 5 ml fresh LB medium and cells were grown for another 2 h to 3 h. Cells were pelleted in 2 ml tubes at 8000×g and 4 °C for 30 s and washed three times with 10 % glycerol in ddH_2O. After the final washing step the supernatant was discarded and cells were stored at −80 °C or directly used for DNA transformation.

4.1.5. Transformation and DNA preparation

Transformation of DNA plasmids into chemocompetent *E. coli* was typically performed with the heatshock method [211]. *E. coli* cells were thawed on ice and mixed with a

0.1 M $CaCl_2$ solution in a 1:1 V/V ratio. Next, 0.5 µl of purified DNA or up to 8 µl of modified DNA was added and the cell- DNA suspension was incubated on ice for 15 min. Heat exposure at 42 °C for 2 min was followed by another 5 min incubation on ice. Then, 600 µl LB medium was added and samples were shaken at 37 °C and 700 rpm for 45 min. Cells were pelleted by centrifugation at 8000×g for 1 min, resuspended in 50 µl LB and plated on LB agar plates containing the corresponding antibiotic to select for plasmid-containing *E. coli* colonies. Antibiotic concentrations were 30 µg ml^{-1} and 100 µg ml^{-1} for kanamycin and ampicillin, respectively. Plates were incubated at 37 °C overnight.

DNA was transformed into electrocompetent *E. coli* using the following protocol: Cells were thawed on ice and mixed with 50 ng to 100 ng of plasmid DNA. After 1 min on ice the cell- DNA suspension was transferred to the electroshock cuvette and a short voltage pulse of 1500 V at 150 Ω was applied. Immediately, 500 µl of LB medium was added and cells were incubated at 37 °C and 700 rpm for 1 h. Then, cells were plated as described above.

The next day, colonies were selected for inoculation of 4 ml LB medium containing the corresponding antibiotic. Cells were grown at 37 °C and 190 rpm overnight. DNA was purified following the protocol of NucleoSpin Plasmid and DNA concentration was determined by absorbance measurement at 230 nm, 260 nm and 280 nm using a spectrophotometer (Eppendorf biophotometer plus, Hamburg, Germany). Purified DNA was stored at −20 °C. When large amounts of plasmid DNA were required, DNA was purified from 200 ml *E. coli* cultures using the PureYield Plasmid Maxiprep System.

4.1.6. DNA cloning

All wt proteins were cloned into the target vectors by PCR amplification followed by enzyme digestion and ligation. Chimeric ChRs were generated using overlapping PCR [212]. The standard PCR mixture is summarized in Table 4.6.
PCR was performed in a thermocycler (Biometra biomedizinische Analytik GmBH, Göttingen, Germany) applying the following temperature steps:

1. 2 min at 95 °C
2. 1 min at 95 °C
3. 30 s at 60 °C
4. 1 min kb^{-1} at 72 °C (30 repetitions of steps 2-4)
5. 2 min at 72 °C

DNA fragments amplified by PCR were then loaded on a 1 % to 1.5 % m/V agarose gel containing 0.5 µg ml^{-1} ethidium bromide. DNA fragments were separated by gel electrophoresis at 120 V for 30 min. DNA bands were visualized by ethidium bromide fluorescence and purified from the gel applying the standard protocol of NucleoSpin Gel and PCR clean-up. The obtained DNA concentration was determined by absorbance measurement at 230 nm, 260 nm and 280 nm using a spectrophotometer (Eppendorf biophotometer plus). The target vector and the PCR product were digested by compatible

step	volume	component	concentration
PCR	5 µl	Reprofast reaction buffer	10 x
	5 µl	dNTPs	2 µM
	2 µl	template plasmid	25 ng µl^{-1}
	5 µl	primer pair	10 µM
	1 µl	Reprofast polymerase	5 U µl^{-1}
	32 µl	ddH_2O	
enzyme	2 µl	Fast digest buffer	10 x
digestion	1.5 µg	vector DNA or PCR product	
	1 µl	restriction enzyme	10 U µl^{-1}
	1 µl	Fast AP[1]	1 U µl^{-1}
	to 20 µl	ddH_2O	
DNA	2 µl	ligation buffer	10 x
ligation	50 ng	vector DNA	
	x ng	PCR product (insert)	molecular ratio 3:1; insert:vector
	1 µl	T4 DNA ligase	5 Weiss U µl^{-1}
	to 20 µl	ddH_2O	

Table 4.6.: Standard preparations for basic steps in cloning including PCR, enzyme digestion and ligation of DNA fragments.

restriction enzymes for 30 min at 37 °C as summarized in Table 4.6. Enzymes were inactivated for 5 min at 80 °C. Next, vector digestion was verified by gel electrophoresis and all fragments were purified using the NucleoSpin Gel and PCR clean-up kit. The ligation mixture was prepared as listed in Table 4.6 and incubated for 1 h at room temperature. Finally, 8 µl of ligated DNA was transformed into competent *E. coli* and purified as described in 4.1.5. In order to validate correct ligation, 3 µl of each DNA sample was digested by the formerly used enzymes, separated by gel electrophoresis and visualized by ethidium bromide fluorescence. Positive DNA samples showed a characteristic band at the size of the introduced DNA segment. DNA sequences were checked by DNA sequencing services (Martin Meixner, Berlin; GATC Biotech AG, Konstanz or LGC genomics GmbH, Berlin, Germany).

4.1.7. Site-directed mutagenesis

Point mutations were introduced following the QuikChange protocol (Agilent Technologies, Böblingen, Germany). Therefore, a matching primer pair was rationally designed and T_m values were checked with the Gentle software. The PCR mixture was prepared as depicted in Table 4.7. Amplification of the mutated plasmid was performed in a thermocycler (Biometra biomedizinische Analytik GmBH, Göttingen, Germany) applying the following temperature steps:

1. 30 s at 95 °C
2. 30 s at 95 °C
3. 1 min at 55 °C
4. 12 min at 68 °C (30 repetitions of steps 2-4)
5. 10 min at 68 °C

[1]The Alkaline Phosphatase was only added to the enzyme digestion mixture of the target DNA vector.

volume	component	concentration
5 µl	Pfu reaction buffer	10 x
5 µl	dNTPs	2 µM
2 µl	template plasmid	40 ng μl^{-1}
1.25 µl	primer pair	10 µM
1 µl	PfuTurbo hotstart DNA Polymerase	5 U μl^{-1}
35.75 µl	ddH_2O	

Table 4.7.: Standard recipe for PCR in site-directed mutagenesis.

The PCR products were analyzed by gel electrophoresis and visualized by ethidium bromide fluorescence. Then, 0.5 µl of DpnI enzyme was added to 20 µl of amplified DNA. After incubation at 37 °C for 1 h, 8 µl DNA was directly transformed into *E. coli*. Plasmids were prepared as described in 4.1.5 and sequenced to confirm the respective mutations.

4.2. Cell culture

4.2.1. Materials and reagents

Sources of cell culture materials and reagents are given in Table 4.8.

material/ reagent/ kit	source
tissue culture flasks and dishes	TPP (Trasadingen , Switzerland)
cryotubes; roller flasks	Greiner Bio-One (Frickenhausen, Germany)
glass coversplips	Hecht Assistant (Sondheim, Germany)
HEK/Cos cell media and supplements	Biochrom AG (Berlin, Germany)
media used for neuronal culture	Gibco/Life Technologies GmbH
TripLE Express, Lipofectamine 2000, antibiotics	Life Technologies GmbH (Darmstadt, Germany)
Fugene HD	Promega GmbH (Mannheim, Germany)
other chemicals	Sigma Aldrich (Hamburg, Germany)
papain dissociation system	Worthington (Lakewood, NJ, USA)

Table 4.8.: Materials and reagents used for cell-culture experiments and their respective sources.

4.2.2. HEK 293 cells

HEK 293 cells were grown at 37 °C and 5 % CO_2 in a sterile incubator. The standard medium was Dulbecco's MEM with stable glutamine that was supplemented with 10 % fetal calf serum (FCS) and 100 µg ml^{-1} penicillin/streptomycin. Cells were grown in sterile tissue culture flasks with surface areas between 25 cm^2 and 175 cm^2 and splitted twice a week. For this purpose, cells were washed with PBS and treated with 20 µl/cm^2 of TrypLE Express (1x) at 37 °C for 3 min. The detached cells were resuspended in 3 ml medium and pelleted by centrifugation at 25×g for 3 min. The supernatant was discarded and cells were resuspended in 5 ml medium. The cell number was determined using a Neubauer chamber. 4×10^4 cells ml^{-1} medium were transferred to a new culture flask. Cells were passaged up to 30 times.

Freezing and unfreezing cycles: Low passage cells could be deep-frozen at −80 °C. Prior to freezing 2×10^6 cells in 1.5 ml freezing medium were aliquoted in cryotubes. In order to increase cell survival during freezing and thawing the freezing medium contained 20 % FCS and 10 % DMSO. Freezing was slowed down using a highly temperature-isolated container. In contrast, cells were thawed as rapid as possible. Cryotubes were heated up in a water bath at 37 °C, then transferred into 10 ml medium containing 20 % FCS and pelleted by centrifugation at 25×g for 3 min. The supernatant was discarded and cells were seeded into T25 flasks containing 5 ml medium with 20 % FCS.

Measurement preparation: In preparation for electrophysiological measurements and fluorescence imaging, two coverslips with a diameter of 15 mm were transferred into a 3 cm culture dish. Next 1.5×10^5 to 3×10^5 cells in 2 ml standard medium supplemented with 1 µM all-*trans* retinal were seeded into the dish. The following day cells were transfected using Fugene HD. Prior to transfection 250 µl of DMEM without additives was mixed with 6 µl transfection reagent and 2 ng plasmid DNA. The mixture was incubated at room temperature for 20 min and added drop by drop to the cells. Recordings were performed 24 h to 60 h after the transfection procedure.

Stable cell line: Measurements on wt C2 were performed with a stable HEK cell line expressing hC2-mVenus [103]. The cell line was maintained in standard medium supplemented with 50 µg ml^{-1} blasticidin and 200 µg ml^{-1} zeocin. Protein expression was induced by addition of 0.1 µM tetracyclin.

4.2.3. Neuronal cultures

Preparation of hippocampal mass cultures for simple testing of ChRs was established in the Hegemann laboratory. Protocols and know-how were supplied by Anke Schoenherr (AG Schmitz, Charité), Benjamin Rost (AG Rosenmund, Charité), Christian Herold (now Cramer group, UC Berkeley) and the Deisseroth group (Stanford University). Neurons on astrocyte microislands and hippocampal mass cultures for more sophisticated measurements were prepared in the group of Christian Rosenmund in the Charité Berlin. Required solutions for neuronal culturing are summarized in Table 4.9. A basic protocol for isolation and seeding of hippocampal neurons is briefly described below.

Mass cultures: Coverslips with a diameter of 13 mm were washed with HCl and ethanol, flamed and transferred to 24-well dishes. After addition of 3.7 µl coating solution coverslips were dried and UV light sterilized for 1 h. Next, 1 ml Neurobasal A medium was added and dishes were preequilibrated in the cell culture incubator. Alternatively, coverslips were coated with glia cells as described in [88]. Newborn BL-6 mice (day P0) were provided by the FEM of the Charité Berlin. Mice were decapitated, brains were removed and quickly transferred into ice-cold Earle's Balanced Salt Solution (EBSS). In the following, hippocampi were isolated, chopped into small pieces and collected in cold

solution	components and concentration	solvent
coating solution	0.02 % poly-D-lysine; 2 % collagen; 0.1 % acetic acid (17 mM)	ddH_2O
Neurobasal A medium	2 mM glutamax; 2 % B27 supplement; 100 µg ml^{-1} penicillin/streptomycin	Neurobasal A
growth-permissive stamp solution	0.1 mg ml^{-1} poly-D-lysine; 0.85 mg ml^{-1} collagen; 10 mM acetic acid	ddH_2O
astrocyte-growth medium	10 % FCS; 10 mM Glutamax; 0.2 % penicillin/streptomycin; 10 mM Hepes; 5 mM glucose; 2.5 µg ml^{-1} insulin	basal medium eagle

Table 4.9.: Solutions and media required for preparation of neuronal cultures.

EBSS. Next, neurons were isolated using the Papain Dissociation System and 5×10^4 to 2×10^5 of isolated cells were seeded per coversplip.

Autaptic cultures: Microdot autaptic cultures [213, 214, 215] were prepared by Annegret Felies in the group of Christian Rosenmund as described in [216]. Briefly, flamed coverslips with a diameter of 30 mm were coated with 0.15 % agarose and dried for 48 h. Then, coverslips were imprinted with microdots of the growth-permissive stamp solution using a custom-made stamp and sterilized with UV light. Astrocytes were isolated from mice cortices and separated by trypsin treatment (0.25 % for 10 min at 37 °C) and careful trituration. After trypsin removal astrocytes were plated at a final concentration of 4×10^4 cells cm^{-2} into T75 tissue flasks containing astrocyte growth medium. After seven days astrocytes could be passaged and 5×10^4 cells were seeded per microdoted coverslip. Seven days later astrocyte medium was replaced by Neurobasal A medium. Finally, 3×10^3 hippocampal neurons were seeded per coverslip [216].

DNA delivery: Neurons were transduced using lentiviral particles. Lentivirus production was performed by Bettina Brokowski in the Rosenmund group as described in [217, 218]. Neurons were transduced 24 h to 72 h post-seeding and measurements took place at days 14-18 of culturing. Alternatively, neurons were transfected using Lipofectamine 2000 according to the supplier's instruction manual.

4.3. Electrophysiology

Whole-cell patch clamp recordings [81, 82] on HEK 293 cells and hippocampal neurons were performed as earlier described [219, 88, 220, 216]. When the voltage-clamp modus is applied, the feedback circuitry of the patch-clamp amplifier enables the evaluation of the current that is needed to clamp the plasma-membrane voltage to a given value [81]. Membrane capacitance and resistance are compensated by additional correction circuits. By combining voltage-clamp measurements with temporally precise illumination pro-

tocols, light-induced current flow over the entire plasma membrane can be determined with millisecond-timing resolution. Different voltages and intra- and extracellular solutions are tested to analyze the photocurrent dependency on the applied electrochemical gradient. Similarly, illumination protocols testing different activation wavelengths and intensities are used to determine the light response of the respective photoreceptors. Inversely to voltage-clamp recordings, measurements in the current-clamp mode detect changes in the plasma membrane voltage in the presence of a given membrane current. These measurements are applied to analyze membrane depolarization or hyperpolarization following rhodopsin activation.

4.3.1. Measuring solutions

If not stated otherwise, all used chemicals were purchased from Sigma Aldrich (Hamburg, Germany) and Carl Roth (Karlsruhe, Germany). Salts used for preparation of measuring solutions exhibited a purity degree of 99 % or higher. External measuring solutions were freshly prepared once a week and stored at 4 °C. Internal solutions were aliquoted in Eppendorf tubes and kept frozen at −20 °C. For HEK cell recordings the final osmolarities were 320 mosm and 290 mosm for extracellular and intracellular solutions, respectively. The standard external and internal solutions were "high Na^+, pH 7.2". If not stated otherwise (e.g. action spectra, current amplitudes), the standard buffers were used. Composition of standard solutions is summarized in Table 4.10.

	component / mM						
name of solution	NaCl	KCl	CsCl	$CaCl_2$	$MgCl_2$	Hepes	EGTA
external standard solution "high Na^+, pH_e 7.2"	140	1	1	2	2	10	/
internal standard solution "high Na^+, pH_i 7.2"	110	1	1	2	2	10	10

Table 4.10.: Standard measuring solutions for HEK cell recordings.

In order to quantifiy cation selectivity of different ChRs NaCl in the standard external solution was replaced by salts of different monovalent and divalent cations (see Table 4.11). Conductivity of individual cations was determined at pH 9 and competition with protons was measured at pH 7.2. The internal solution "NMG, pH_i 9.0" contained only

	component / mM							
name of solution	NaCl	KCl	CsCl	$CaCl_2$	$MgCl_2$	NMG	Tris/ Hepes	EGTA
high Na^+, pH_e 9	140	1	1	2	2	/	10	/
NMG, pH_e 9/7.2	1	1	1	2	2	140	10	/
20 mM Ca^{2+}, pH_e 9	1	1	1	20	2	100	10	/
high Ca^{2+}, pH_e 9/7.2	1	1	1	70	2	/	10	/
20 mM Mg^{2+}, pH_e 9	1	1	1	2	20	100	10	/
high Mg^{2+}, pH_e 9	1	1	1	2	70	/	10	/
NMG pH_i 9 (internal)	1	1	1	2	2	110	10	10

Table 4.11.: Measuring solutions for cation selectivity experiments performed in HEK 293 cells.

minor amounts of cations to minimize outward directed currents. Additional experiments on HEK cells were dealing with Na^+ vs. H^+ competition. For these experiments, different internal and external Na^+ concentrations were tested at pH 9, 7.2 and 5. Furthermore, the influence of internal Mg^{2+} was analyzed and Cs^+ was tested as potentially conducted cation. The measuring solutions used in these experiments are summarized in Table 4.12.

	component / mM							
name of solution	NaCl	KCl	CsCl	$CaCl_2$	$MgCl_2$	NMG	pH buffer	EGTA
high Na^+, pH_e 5	125	1	1	2	2	/	10	/
NMG, pH_e 5	1	1	1	2	2	140	10	/
high Na^+, pH_i 5/9	95/110	1	1	2	2	/	10	10
NMG, pH_i 7.2	1	1	1	2	2	110	10	10
20 mM Mg^{2+}, pH_i 7.2	110	5	/	2	20	/	10	10
2 mM Mg^{2+}, pH_i 7.2	110	5	/	2	2	/	10	10
0.2 mM Mg^{2+}, pH_i 7.2	110	5	/	2	0.2	/	10	10
high Cs^+, pH_e 9	1	1	140	2	2	/	10	/

Table 4.12.: Additional measuring solutions used in HEK-cell experiments. The pH buffer was Tris-HCl at pH 9.0, Hepes at pH 7.2 and 5 mM trisodium citrate/ 5 mM citric acid at pH 5.0. In order to avoid Na^+ in the NMG, pH_e 5 solution, trisodium citrate was replaced by NMG.

For neuronal recordings measuring solutions mimicking physiological conditions were used. Osmolarity of external and internal solutions was adjusted to 300 mosm. During measurements cells were constantly perfused with external solution at a speed of 1 ml min^{-1} to 2 ml min^{-1} via a perfusion pencil with a diameter of 500 µm. A fast stepper in combination with a valvebank allowed for external solution exchange within 100 ms. 3 µM NBQX (Tocris, Ellisville, MO, USA) were applied to inhibit postsynaptic AMPA receptors. Composition of solutions is shown in table 4.13.

	component / mM						
name of solution	NaCl	KCl	$CaCl_2$	$MgCl_2$	glucose	Hepes	
NaCl, pH_e 7.3	140	2.4	2	4	10	10	
	K-gluconate	Na-GTP	Mg-ATP	Hepes	EGTA	CP	PCK U ml^{-1}
K-gluconate, pH_i 7.3	146	0.3	4	17.8	1	12	50

Table 4.13.: Standard measuring solutions for neuronal recordings. CP- creatine phosphate, PCK-phosphocreatine kinase.

4.3.2. Preparation

Pipettes: Patch pipettes were pulled from microhematocrit tubes (Karl Hecht, Germany) or borosilicate tubes with filament (Science Products, Germany) using a P-97 puller (Sutter Instruments, Novato, CA, USA). Pipettes for HEK cell measurements were fire-polished over a hot platinum wire. Prior to measurements pipettes were filled with the respective intracellular buffer.

Electrodes: AgCl coated Ag wires served as electrodes. Ag wires (AG-10T or AG-25T, Science Products, Germany) were cut, roughended with sandpaper and oxidized by application of 1V in 3 M KCl. Diameters of plain wire were 640 µm and 250 µm for bath and measuring electrodes, respectively. During measurements bath electrodes were connected with the bath solutions via agar bridges filled with 140 mM NaCl and 1 % agar.

HEK cells: Measuring chambers were custom-built by A. Laws (HU Berlin). Coverslips overgrown with HEK cells were removed from cell culture dishes, washed and transferred to the measuring chamber. The mounted chamber was quickly filled with the reference extracellular solution (high Na^+, pH_e 7.2).

Neurons: Coverslips were broken into four to eight pieces and individually transferred to the measurement chamber filled with standard external neuron buffer. V-type ATPases were inhibited by application of 1 µM bafilomycin (Sigma Aldrich) for 2 h to 5 h prior to measurements.

4.3.3. Electrical and optical equipment

Four different setups were used to perform electrical recordings. Setups 1 to 3 were mainly used for HEK cell recordings, but setup 2 could also be used for measurements on hippocampal neurons. Measurements on autaptic neurons were performed in the Rosenmund laboratory (Charité Berlin) on setup 4. Table 4.14 summarizes the main components of each setup. The individual setups were mounted on vibration-cushioned tables (Newport Spectra-Physics GmbH, Darmstadt, Germany). Faraday cages covered with black plastic foil served as electrical and optical shielding. All electrical devices were grounded. Water columns connected to the patch electrode served for application of positive and negative pressure to achieve the whole-cell configuration.

4.3.4. Light sources and delivery

Setup 1: A Polychrome V system served as major light source. Therein light from a 150 W Xenon Arc lamp is split into its constituent spectral colors using a galvanometer-driven diffraction grating and monochromatic light is selected via a bandwidth-adjustable slit. Wavelength, intensity and bandwidth were controlled via the TillVision software. When no wavelength was selected, the resting position of the polychrome was set at 720 nm. A UV/Vis quartz fiber connected the Polychrome with an optical bench coupled to the microscope. A fast shutter allowed for light triggering and prevented artifacts while the Polychrome was approaching the selected wavelength. In order to maintain equal photon flux at all wavelengths for action spectra recordings, a neutral filter wheel was installed by Jonas Wietek (Hegemann group, HU Berlin). An additional 75 W Xenon Arc lamp was used to study multi-photon processes. Wavelengths were selected via different bandpass filters, light onset was triggered using a shutter device and light was combined with the Polychrome light using a 70 %/30 % reflection/transmission mirror.

Setup 2: The Polychrome II differed from the Polychrome V in two aspects. First of all, it implied a 75 W Xenon Arc lamp yielding smaller light intensies. Second, wavelengths could be directly selected by voltage.

Setup 3: This setup used a 75 W Xenon Arc lamp combined with a shutter device. Wavelengths were selected by microscope-inherent excitation filters and dichroic mirrors.

Setup 4: A mercury vapor lamp connected to a shutter was directly attached to the microscope. Wavelengths were selected by excitation filters and dicroic mirrors in the microscope. In imaging experiments, a LED system containing LEDs with maximal activation at 405 nm, 470 nm, 510 nm and 588 nm was used. LED intensities were adjustable by an external control unit.

Photoreceptor activation and fluorescence intensity strongly depends on the intensity and wavelength of the applied light. Therefore, light intensities and lamp alignments were frequently controlled and optimized using an optometer (photodiode PD-93, control

component	setup 1 "Imaging"	setup 2 "Polychrome 2"	setup 3 "Ion selectivity"	setup 4 Charité
amplifier	EPC7 (HEKA)	ELC-03XS (npi)	Axopatch 200B (Molecular Dev.)	Multiclamp 700B (Molecular Devices)
DAC	Digidata 1440A (Molecular Devices)	Digidata 1440A	Digidata 1440A	Digidata 1440A
micro-manipulator	PatchStar (Scientifica)	PatchStar (Scientifica)	LM SM1 (Luigs and Neumann)	customized Piezo Jena Tritor 100 (Medizintechnische Labore der Charité)
inverted microscope	IX70 (Olympus)	Axiovert 100TV (Zeiss)	Axiovert 35 (Zeiss)	IX51 (Olympus)
light source	Polychrome V (TillPhotonics)	Polychrome II (TillPhotonics)	75W Xenon lamp (Osram)	mercury-vapor lamp
alternative light source	75W Xenon lamp (Osram)	n.a.	n.a.	p-E2 LED system (CoolLED)
shutter	VS25; LS3T2-NL-100 (Uniblitz)	n.a.	VS25 (Uniblitz)	VS25 (Uniblitz)
shutter driver	VCM-T132; VCM-D1 (Uniblitz)	n.a.	custom-built; (Dr. R. Arndt)	T132 Controler (Uniblitz)
b\w camera	AVT-BC-12 (AVT Horn)	EcoLine TV7002 (ABUS)	b\w camera (Grundig electronic)	n.a.
imaging camera	Imago CCD (TillPhotonics)	n.a.	n.a.	iXon 897 (Andor)
special equipment	circular filter NSND-3 (Newport)	n.a.	n.a.	perfusion ValveLink8.2 (AutoMate Scientific); stepper SF-77B (Warner)

Table 4.14.: Principal components of the different electrophysiology setups.

unit P9710 and correction filter PD-9304RW, all Gigahertz-Optik GmbH, Türkenfeld, Germany). Table 4.15 summarizes the most frequently used filter sets and the corresponding light intensities in the object plane. Diameters of illuminated areas were determined with an object micrometer. Setups 1-3 used 40x oil objectives with numerical apertures of 1.3 (Fluar and Achrostigmat, both Zeiss, Jena, Germany). Setup 4 implied a 20x fluorescent-optimized objective (Olympus, Hamburg, Germany).

4.3.5. Measuring protocols for HEK cells

Whole-cell recordings were performed in the voltage-clamp mode. Current signals were amplified with EPC7, ELC-03XS or Axopatch 200B and digitized with Digidata1440A. Data was sampled at 10 kHz to 50 kHz and filtered using a 2 kHz to 10 kHz low pass filter. pClamp10 was used to control electrical and optical devices. At setup 1 TillVision was used to trigger light sources.

setup	excitation filter or wavelength	dicroic mirror	emission filter	light power	excitation
1 (PV)	(380 ± 15) nm + extra mirror	493/574	BP512/630	33 mW/cm^2	Fura
1 (PV)	(440 ± 15) nm	493/574	BP512/630	430 mW/cm^2	eCFP
1 (PV)	(540 ± 15) nm	493/574	BP512/630	440 mW/cm^2	mCherry
1 (Xenon)	450 nm + extra mirror	493/574	BP512/630	66 mW/cm^2	C2
1 (Xenon)	540 nm + extra mirror	493/574	BP512/630	66 mW/cm^2	C1V1
1 (PV)	(510 ± 15) nm	440/520/590	BP465/537/623	490 mW/cm^2	eYFP
1 (PV)	(460 ± 15) nm	R30 %/T70 %	/	190 mW/cm^2	C2
1 (PV)	(460 ± 7) nm	R30 %/T70 %	/	57 mW/cm^2	C2
1 (PV)	(490 ± 15) nm	R30 %/T70 %	/	170 mW/cm^2	ChETA
1 (PV)	(490 ± 7) nm	R30 %/T70 %	/	54 mW/cm^2	ChETA
1 (PV)	(520 ± 15) nm	R30 %/T70 %	/	130 mW/cm^2	C1V1 S220G
1 (PV)	(520 ± 7) nm	R30 %/T70 %	/	43 mW/cm^2	C1V1 S220G
1 (PV)	(560 ± 15) nm	R30 %/T70 %	/	120 mW/cm^2	C1V1
1 (PV)	(560 ± 7) nm	R30 %/T70 %	/	37 mW/cm^2	C1V1
2 (PII)	(480 ± 15) nm	BS500	LP520	110 mW/cm^2	eGFP
2 (PII)	(520 ± 15) nm	BS543	BP550-650	87 mW/cm^2	mCherry
2 (PII)	(420 ± 15) nm	440/540	BP 464/547	78 mW/cm^2	eCFP
2 (PII)	(510 ± 15) nm	440/540	BP 464/547	80 mW/cm^2	eYFP
2 (PII)	(470 ± 15) nm	R80 %/T20 %	/	100 mW/cm^2	C2
2 (PII)	(470 ± 15) nm	R80 %/T20 %	/	100 mW/cm^2	C2
2 (PII)	(560 ± 15) nm	R80 %/T20 %	/	63 mW/cm^2	C1V1
3 (Xenon)	(470 ± 20) nm	BS510	LP520	171 mW/cm^2	C2
3 (Xenon)	(546 ± 15) nm	BS580	LP590	68 mW/cm^2	C1V1

Table 4.15.: Most frequently used light sources in combination with used filter sets and examples for common applications. PV- Polychrome V, PII- Polychrome II, BS- beamsplitter, BP- bandpass filter, LP- longpass filter.

In the following, important measuring protocols are described in detail.

Amplitude determination: Microbial rhodopsins were activated at the wavelength of maximal absorption for 300 ms. Applied voltages were −60 mV for ChRs and 0 mV or 40 mV for light-activated pumps. Amplitudes were measured at setup 1 using the polychrome V illumination system at 100 % and 7 nm.

Ion selectivity experiments: Current-voltage relationsships were recorded at setups 2 and 3. The time course of the applied voltage is summarized in Figure 4.1A. After baseline recording at 0 mV for about 100 ms a voltage ramp to −50 mV at a speed of $-250\,\mathrm{mV\,ms^{-1}}$ was applied. After a reverse ramp to 0 mV and another baseline recording for 100 ms, the measuring voltage varying between −60 mV and 40 mV in 20 mV steps was applied for 1 s. After 200 ms of equilibration at that voltage light was applied for 300 ms. Finally, the voltage was clamped again at 0 mV. Activation wavelengths corresponded to the maximal absorption of the respective rhodopsin. Intersweep duration was 20 s. All measurements started while applying the external standard solution (precontrol). Buffers were exchanged by careful pipetting. Buffer exchange was repeated four times and took approximately 60 s. If possible a postcontrol using standard conditions was realized.

Action spectra: Action spectra were recorded at −60 mV by light application for 10 ms using the Polychrome V system (setup 1). Spectra were recorded between 380 nm and 650 nm in 10 nm steps. Equal photon flux was adjusted to $7 \times 10^{23}\,\mathrm{s^{-1}m^{-2}}$ for all wavelengths using a neutral density filter wheel.

Inactivation spectra: Two-photon processes could be electrically adressed by inactivation spectra recordings on slow ChR mutants. Membrane voltage was clamped at

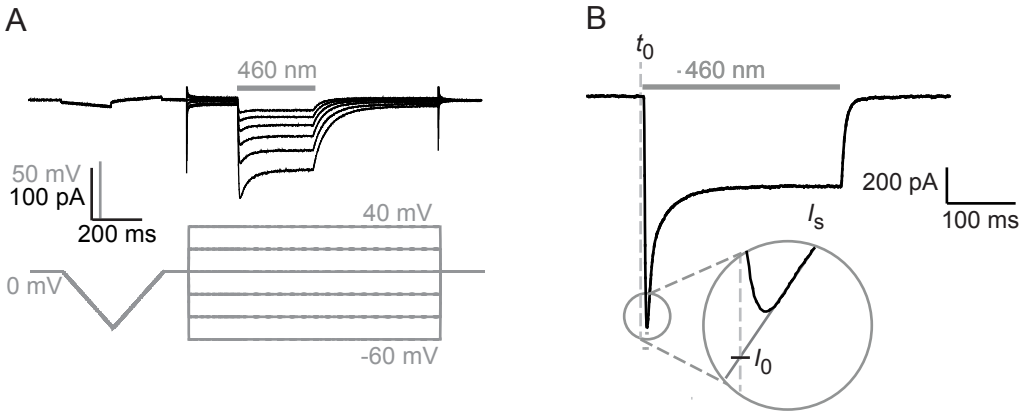

Figure 4.1.: Measuring protocol for IV curve and representative current trace
A- Schematic representation of measuring protocol for IV curves. Black traces represent exemplary photocurrents for C2 L132C T159C, grey lines represent voltage protocol and upper grey bar indicates the TTL pulse used to trigger the illumination shutter. **B**- Photocurrent trace of C2 wt at −60 mV. Both stationary current I_s and initial photocurrent I_0 are indicated.

−60 mV and mutants were activated by their peak absorption wavelength for 80 s using a shutter-controlled Xenon lamp (setup 1). After reaching a stationary current value additonal light flashes from the Polychrome V unit were applied for 1 s each. Light flashes covered the optical spectrum from 380 nm to 670 nm in 10 nm steps and were separated by 1 s pauses. Photon flux was adjusted to $7 \times 10^{23}\,\mathrm{s^{-1}m^{-2}}$ for all wavelengths.

4.3.6. Protocols for neuron measurements

Whole-cell voltage clamp measurements were performed using the ELC-03XS or Multiclamp 700B amplifiers and Digidata 1440A (setups 2 and 4). Data was sampled at 10 kHz with the pClamp10 software. Shutter and perfusion system were controlled via pClamp. Holding potential was −70 mV if not stated otherwise.

Measurements of excitatory postsynaptic currents (EPSCs): Action potentials were evoked by membrane depolarization to 0 mV for 1 ms. Stimulation frequency varied between 0.1 Hz and 1 Hz. Pump activation was achieved by illumination with 540 nm or 590 nm light for various durations. Light intensity could by reduced to 25 % or 50 % with neutral density filters. During paired-pulse measurements the second action potential was triggered 40 ms after the first action potential was evoked.

Recordings of miniature excitatory postsynaptic currents (mEPSCs): Prior to mEPSC recordings a baseline was recorded for 30 s by application of 3 µM 2,3-dihydroxy-6-nitro-7-sulfamoyl-benzoquinoxaline-2,3-dione (NBQX). NBQX inhibits kainate and AMPA receptors and is used to block synaptic transmission at glutamatergic synapses. In order to increase the signal to noise-ratio mEPSCs were recorded without resistance and capacitance compensation. Light was applied at an reduced intensity (25 %) for various durations.

4.4. Fluorescence microscopy

4.4.1. Ca^{2+} imaging

Preparation: Imaging was performed two days post-transfection. Therefore, medium in culture dishes was replaced by 2 ml fresh DMEM supplemented with 2 µM Fura-2-acetoxymethyl ester (Life Technologies GmbH, Darmstadt, Germany). After 30 min coverslips could be transferred to the measuring chamber. Standard solution used for Fura-2 imaging was "high Ca^{2+}, pH_e 7.2" (see table 4.11 for details).

Optics: Setup 1 (table 4.14) was used for Ca^{2+} imaging. Fura-2 was excited by 340 nm and 380 nm light provided by the Polychrome V unit. Light intensity was reduced to $3.3\,\mathrm{mWcm^{-2}}$ using a 10 % neutral density filter. ChR activation light was provided by a 75 W Xenon Arc lamp regulated via a fast shutter. Wavelengths were selected using bandpass filters at 450 nm and 560 nm yielding a light intensity of $66\,\mathrm{mWcm^{-2}}$ at both

wavelengths. An imago CCD camera (TillPhotonics, Gräfelfing, Germany) was used for fluorescence detection.

Software and protocol: All devices were controlled via the TillVision Software (TillPhotonics, Gräfelfing, Germany). At first, overview pictures of Fura-2 fluorescence and fluorescent proteins were taken. Next, isolated cells were chosen as regions of interest. Untransfected cells served as negative controls. Fura-2 fluorescence was scanned every 2 s for 500 ms. After baseline recording for 40 s, ChRs were activated for 10 s followed by fluorescence scanning for another 180 s. Time responses of mean fluorescence intensities were used for further analysis.

4.4.2. Confocal microscopy

Sample preparation: HEK cells were imaged two days post-transfection. Coverslips were carefully washed and placed upside-down onto glass slides with a thickness of 0.14 mm. A drop of PBS was added and preparations were sealed with nailpolish. Neuronal preparations were washed with PBS and fixated applying 4 % paraformaldehyde for 15 min. Berit Söhl-Kielczynski (Charité Berlin) performed immunofluorescence stainings using primary anti-Map2 antibody (chemicon AB5542 by Merck Millipore, Darmstadt, Germany) and primary anti-VGlut1 antibody (AB135302 by synaptic systems, Göttingen, Germany).

Recordings: All confocal microscopy pictures were taken in the group of Professor Andreas Herrmann (HU Berlin) with help from Dr. Thomas Korte. Images were taken on a confocal laser scanning microscope (FV1000 by Olympus, Hamburg, Germany) using a 60x water objective with a numerical aperture of 1.2. Fluorescence excitation was performed with diode lasers at 405 nm, 488 nm, 559 nm and 647 nm. Recordings were controlled with the Fluoview software (Olympus).

4.5. Data analysis

4.5.1. Software

Electrophysiological and imaging data were analyzed using Clampfit 10.2 (Molecular devices, Sunnyvale, CA, USA), TillVision (TillPhotonics, Gräfelfing, Germany) and FV10-ASW 2.0 Viewer (Olympus, Hamburg, Germany). Data from neuronal recordings were examined with Axograph X (AxoGraph Scientific, Sydney, Australia). Further analysis was performed with Microsoft Office Excel 2007 (Microsoft Corporation, Redmond, WA, USA), SigmaPlot 11.0 (Systat Software GmbH, Erkrath, Germany) and Adobe Illustrator CS5 (Adobe Systems, San Jose, CA, USA).

4.5.2. Data from recordings on HEK cells

All current traces were filtered using a 500 Hz Gaussian low pass filter and baseline correction was performed by current substraction before light onset.

Amplitude determination: Stationary currents I_s were extracted from mean currents after 300 ms illumination. Initial currents I_0 were determined by linear extrapolation to t_0 where t_0 corresponds to the time of TTL pulses initiating shutter opening (see Figure 4.1B for details).

Reversal potentials: A reversal potential describes the voltage where the inward and outward directed currents through an ion channel are equal in size - there is no net current flux.

$$I(E_{rev}) = I_{in} + I_{out} = 0 \tag{4.1}$$

Reversal potentials E_{rev} were determined from $I(E)$ measurements by linear extrapolation between the two voltages where the $I(E)$ plot intersects the current axis. When E_{rev} was greater than 40 mV, the extrapolation was performed by using data points at 20 mV and 40 mV. Reversal potentials could be compared with the Nernst potential for the respective cation [221].

$$E_{Nernst} = E^0 + \frac{RT}{z_E F} ln \frac{c(x)_i}{c(x)_e} \tag{4.2}$$

Action spectra: Peak photocurrents were determined at all wavelengths. When no neutral filter wheel was used, spectra were corrected by division with the respective photon count at each wavelength. Spectra were normalized to the peak current value. Maxima of averaged action spectra were determined by fitting a five-parametric Weibull function (see equation for details) with x_0 representing the wavelength of the maximum. The Weibull distribution is used instead of Gaussian or Lorentz distributions because it allows for the description of asymetrically shaped action spectra.

$$y = y_0 + a \left(\frac{c-1}{c}\right)^{\frac{1-c}{c}} \left[\frac{x-x0}{b} + \left(\frac{c-1}{c}\right)^{\frac{1}{c}}\right]^{c-1} exp^{\left[\frac{x-x0}{b} + \left(\frac{c-1}{c}\right)^{\frac{1}{c}}\right]} + \frac{c-1}{c} \tag{4.3}$$

Kinetic parameters: Kinetics of channel opening ("on-kinetics") and channel closing ("off-kinetics") were determined by fitting with mono- or biexponential curves. Inactivation describes the relaxation from I_0 to I_s with the time constant τ_{inact}. The extent of inactivation x_{inact} can be calculated according to equation 4.4 and τ_{inact} was determined under assumption of monoexponential decay.

$$x_{inact} = \frac{I_0 - I_s}{I_0} \tag{4.4}$$

4.5.3. Data from neuronal recordings

Data from neuronal recordings were mainly analyzed by Dr. Benjamin Rost (Charité Berlin).

EPSCs and paired pulse ratio: Peak amplitudes of EPSCs were determined at each time point. For assignment of kinetic parameters in experiments using bafilomycin,

baseline EPSC values before light onset were substracted and EPSC amplitudes were normalized to their maximal value. Light-induced EPSC kinetics were monoexponentially fitted. Paired pulse ratios were determined from two subsequent EPSC amplitudes using the following formula:

$$R_{PP} = \frac{I_{EPSC2}}{I_{EPSC1}} \tag{4.5}$$

mEPSC determination: Current traces were prefiltered using a 1 kHz low-pass filter. Baseline noise was determined using the traces recorded in NBQX. mEPSCs were detected using a template with variable amplitude and specific kinetic parameters. Frequency and amplitude of EPSCs were further analyzed.

4.5.4. Analysis of Fura-2 imaging data

For each region of interest the mean fluorescence intensity at 380 nm was analyzed in time. Fluorescence values were normalized to the intensity before light onset yielding F/F_0 and $\Delta F/F_0$.

4.5.5. Statistics

All graphs show mean values with respective standard errors. In order to test for significant differences between two sample groups, a Student's t-test was performed. Significant differences were marked with stars: $*\ p \leq 0.05$; $**\ p \leq 0.01$ and $***\ p \leq 0.001$.

4.5.6. Enzyme-kinetic model

Complete datasets from ion selectivity measurements were used for computation. Datasets were selected based on the consistency between pre- and postcontrol at standard conditions (high Na^+, pH_e 7.2). All current values were normalized on the initial current I_0 at -60 mV at standard condition and adjusted to amplitude drifts between pre- and postcontrol under assumption of a linear drift in time. All model calculation were performed by Professor Dietrich Gradmann. The model algorithm can be found in the Appendix.

5. Results

5.1. Color-tuning in ChRs

Multi-color optogenetics demands a palette of optogenetic actuators with well-separated action spectra. Therefore, it would be useful to have both blue-shifted ChR variants as well as enhanced ChRs that are activated by yellow or red light. Here, two approaches were followed in order to gain ChRs with shifted action spectra. First, site-directed mutagenesis was performed on C2 with the aim of introducing a hypsochromic shift. Second, the chimera approach [78, 80, 79] was applied to create a well-expressing ChR with yellow absorption. The resulting C1V1 chimera - originally introduced by Matthias Prigge - was subjected to further fine-tuning by additional mutagenesis. All constructs were expressed in HEK 293 cells and tested in whole-cell patch clamp experiments. Most importantly, action spectra were recorded and compared to the respective wt spectra.

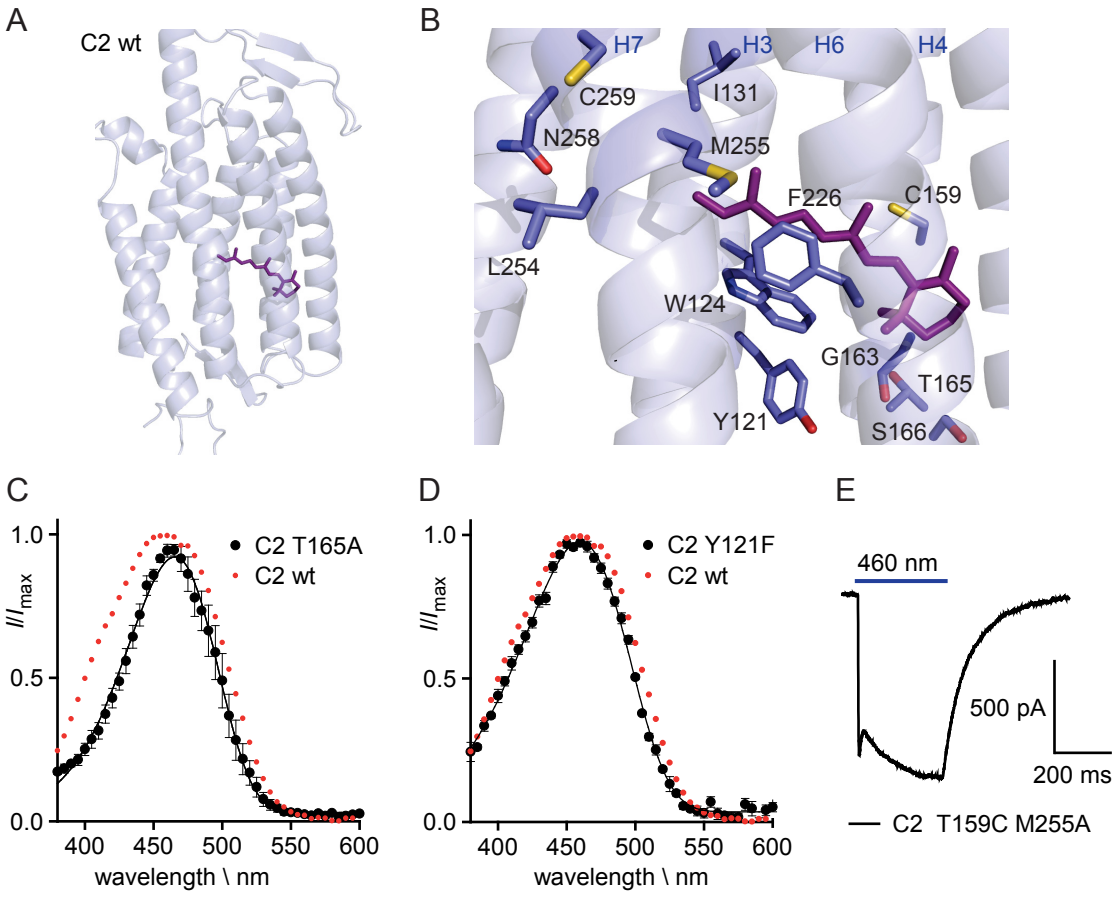

Figure 5.1.: Characterization of C2 mutants. **A** Structural model of C2 T159C based on the X-ray crystal structure by Kato *et al.* [74]. The retinal chromophore ist shown in magenta. **B** Closer insight into the retinal binding pocket of C2. The side chains of the amino acids that were mutated for color-tuning are highlighted in blue. The aromatic residues Y121, W124 and F226 (helices three and six) are in close vicinity to the polyene chain of the retinal, whereas G163 (main chain shown), T165 and S166 (helix four) interact with the β-ionone ring. I131 of helix three and L254, M255, N258 and C259 of helix seven are positioned close to the retinal-Schiff base. Originally, mutants were designed without knowlegde of the Kato structure. **C** and **D** Action spectra of C2 T165A and Y121F in comparison to wt C2. The spectrum of C2 T165A shows a slight bathochromic shift (6 nm) when compared to the wt. **E** Representative current trace of C2 T159C M255A. The double mutant displays high photocurrents with slow off-kinetics. Interestingly, the stationary current even exceeds the initial current level at high light intensities (100 % and 15 nm). For a current trace for wt C2 recorded at identical conditions see Figure 3.5B.

5.1.1. C2 mutants

Twelve mutations that potentially blueshift the C2 absorption were rationally designed. The first round of mutations was based on work by Kim *et al.* (2008) on proteorhodopsin [222]. Kim and coworkers identified twelve proteorhodopsin mutants that exhibited hypsochromically shifted absorption spectra. Out of the responsible residues, four amino acids are conserved in C2. The corresponding exchanges were introduced in C2, yielding Y121F, W124G, G163D and F226N. Additionally, phenylalanine at postion 226 was also replaced by tyrosin (F226Y) since the corresponding mutation in V1 (F221Y) had been reported to introduce a 10 nm blue-shift [88]. While the three aromatic residues (Y121, W124 and F226) are close to the polyene chain, G163 is interacting with the β- ionone ring. Because the polarity of residues, that interact with the ring system, has a strong influence on absorption properties [65], the neighboring polar amino acids T165 and S166 were exchanged by non-polar alanines. In the following, four mutations were introduced close to the retinal Schiff base in helix 7. Since the exchanged amino acids are too distant to directly interact with T159, these mutations were tested on the background of the well-performing C2 T159C. Last, I131 was replaced by leucine and valine (I131L and I131V). The corresponding mutation in C1C2, C1C2 L170V, which is also referred to as "ChIEF", was reported to blue-shift the C1C2 spectrum [80]. The positions of the exchanged residues in respect to the retinal chromophore are depicted in Figure 5.1B.

All mutants were transiently expressed in HEK 293 cells and tested for functionality. C2 W124G, G163D and F226N did not show any photocurrents while the other mutants exhibited peak currents between 200 pA and 2000 pA (see Table 5.1 for details). Subsequently, action spectra were recorded. Spectral Maxima of all mutants are summarized in Table 5.1 and exemplary spectra for C2 T165A and C2 Y121F are shown in Figure

mutant	λ_{max} / nm	I_p / pA	τ_{off} / ms
C2 wt	460 ± 1	760 ± 140*	17 ± 2
C2 Y121F	460 ± 1	210 ± 40	16 ± 7
C2 W124G	no current detectable		
C2 I131L	461 ± 1	510 ± 100	20 ± 2
C2 I131V	462 ± 1	200 ± 40	16 ± 4
C2 G163D	no current detectable		
C2 T165A	466 ± 1	780 ± 150	19 ± 4
C2 S166A	465 ± 1	310 ± 80	22 ± 2
C2 F226Y	461 ± 1	290 ± 80	59 ± 9
C2 F226N	no current detectable		
C2 T159C	463 ± 1*	2340 ± 390*	18 ± 2
C2 T159C M255A	462 ± 1	600 ± 130	57 ± 4
C2 T159C L254F M255F	462 ± 1	2000 ± 290	260 ± 50
C2 T159C L254Y M255Y	461 ± 1	/	140 ± 30
C2 T159C N258S C259A	460 ± 1	/	49 ± 3

Table 5.1.: Comparison of C2 mutants for color-shift. Action spectra of C2 T165A and S166A are red-shifted by 6 nm and 5 nm, respectively. Several mutants show considerably decelerated off-kinetics, this is most pronounced for the triple mutants C2 T159C L254F M255F and C2 T159C L254Y M255Y. Stars indicate values that were taken from [87] and were determined together with Dr. Matthias Prigge.

5.1C and D. Against expectation, none of the C2 mutants showed a blue-shifted action spectrum. Instead, action spectra of C2 T165A and S165A were slightly red-shifted. This may suggest the replacement of threonine and serine by a water molecule in the respective mutants. Off-kinetics were determined by monoexponential fitting of current traces after the 10 ms light pulse. C2 F226Y as well as all four mutations in the seventh helix induced decelerated off-kinetics indicating a reduced rate in late photocycle processes such as structural rearrangements and reprotonation. Interestingly, C2 T159C M255A shows a very low inactivation (Figure 5.1E). At high light intensities the stationary photocurrent even exceeds the early peak current. Taken together, the generation of a blue-shifted C2 mutant was not successful by the mutagenesis approach presented here.

5.1.2. C1V1

The chimera approach was initally applied to combine the kinetic properties of C1 with the higher expression level of C2 yielding different C1C2 chimera (see section 3.4.4) [78, 80, 79]. Our group extended the approach to V1 and V2 [87, 88]. The major aim was to generate a ChR with an action spectrum similar to V1 (or further red-shifted), but with high photocurrents comparable to those of C2 or V2. Combinations of V1 and V2 helices only moderately increased the V1 expression level [87, 88]. But, these experiments indicated that helix six and seven are crucial to maintain the absorption maximum of V1. Consequently, Matthias Prigge designed chimera that combined N-terminal helices of C1 and C-terminal helices of V1. The best variant consisted of the first two helices of

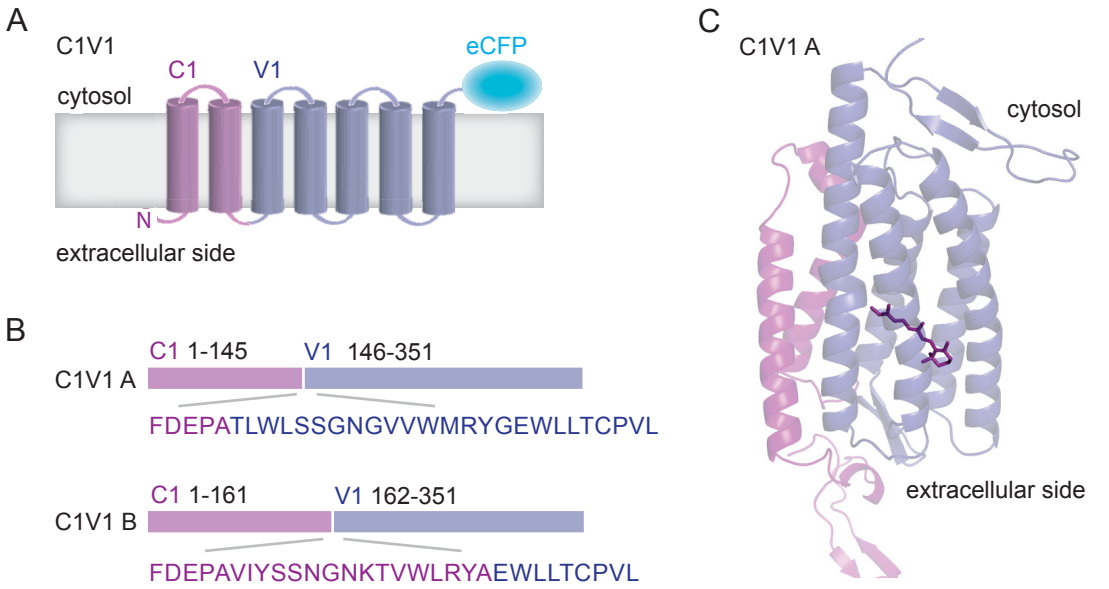

Figure 5.2.: Design of the C1V1 chimera. **A** C1V1 is composed of the two N-terminal helices of *Chlamydomonas* ChR1 (C1) and the subsequent five helices of *Volvox* ChR1 (V1). In most experiments the enhanced cyan fluorescent protein (eCFP) was C-termially fused to C1V1. **B** There are two C1V1 variants, namely C1V1 A and C1V1 B, that differ in their linker region between helices two and three. While C1V1 A consists of the first 145 amino acids of C1 and amino acids 146 to 351 of V1, the N-terminal C1 part is extended in C1V1 B comprising amino acids 1 to 161 from C1 [87, 108]. **C** Structural model of C1V1 based on the crystal structure of the C1C2 chimera (pdb:3UG9) [74].

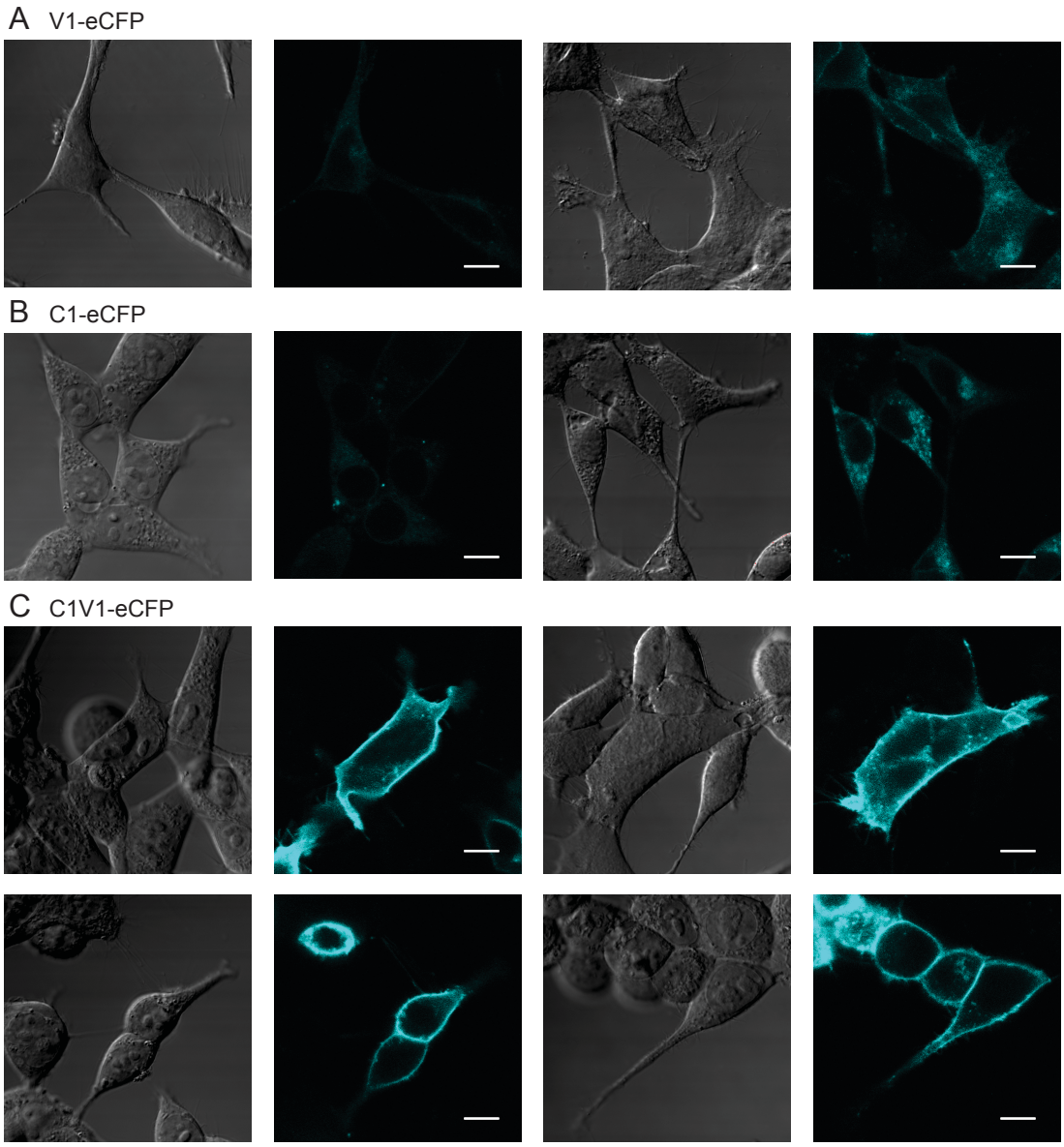

Figure 5.3.: Comparison of expression level of V1 (**A**), C1 (**B**) and C1V1 A (**C**) in HEK293 cells. Confocal images show cells using differential interference contrast (DIC) in comparison to the respective eCFP fluorescence. All images were recorded using the same laser power and detector voltage. The white scale bars correspond to 10 µm.

C1 and the adjacent five helices of V1. This variant was called C1V1 A (see Figure 5.2A for details). A chimera with a similar helix composition was presented by Ofer Yizhar (Weizmann Institute, Israel). Subsequently, this variant was named C1V1 B. C1V1 A and C1V1 B differ in the linker region between helices two and three. The amino acid sequences of the respective linkers are depicted in Figure 5.2B. Since C1V1 A was developed in our group, most experiments shown here were performed using C1V1 A, but should be valid for C1V1 B as well.

A fusion protein of C1V1 and eCFP was expressed in HEK 293 cells. The fluorescence tag allowed for the localization and quantification of C1V1. Figure 5.3 shows confocal fluorescence images of HEK cells expressing C1V1-eCFP and the parental proteins C1 and V1. C1V1 exhibits high levels of expressed protein and very good membrane target-

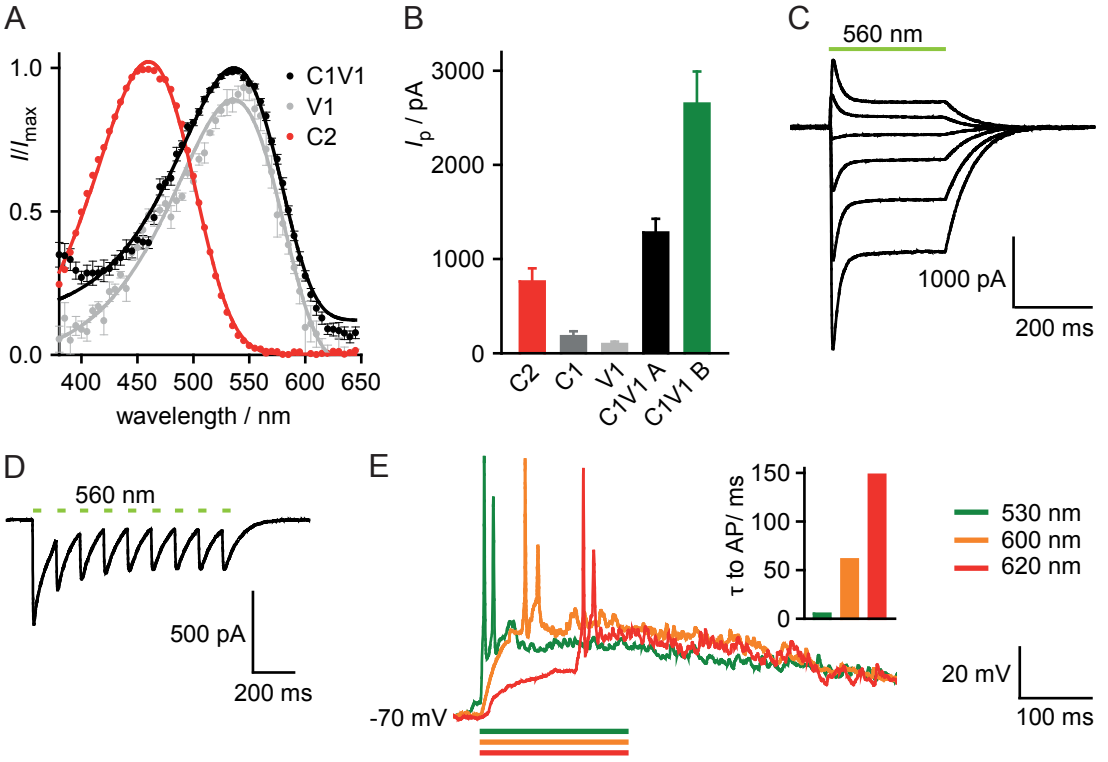

Figure 5.4.: Basic characterization of C1V1. **A** Action spectra of C1V1, V1 and C2. Both C1V1 and V1 show maximal activation 536 nm. **B** Amplitudes of peak currents I_p of C1V1 variants and wt ChRs. ChRs were activated at 460 nm, 490 nm and 560 nm. **C** and **D** Current responses of C1V1 A to prolonged illumination at different voltages (−60 mV to 40 mV) and to repetitive short flashes (10 ms at 10 Hz) applying −60 mV. HEK cell measurements were performed at standard conditions. **E** C1V1-A can trigger action potentials in hippocampal neurons. Light application for 200 ms provokes a substantial depolarization which increases network activity. The time to the first action potential depends on the wavelength of the applied light and was 5 ms, 61 ms and 148 ms at 530 nm, 600 nm and 620 nm for the shown cell, respectively.

ing. Moreover, C1V1 shows an enhanced membrane expression when compared to both C1 and V1. In the following, C1V1 was characterized by whole-cell patch-clamp recordings in order to analyze action spectra and photocurrent properties. When activated by green light C1V1 shows ChR-characteristic photocurrents with an early peak current that relaxes to a stationary current of reduced amplitude. Amplitude and direction of the photocurrent depend on the applied membrane voltage (Figure 5.4C). Action spectra of C2, C1V1 and V1 are depicted in Figure 5.4A. While C2 shows maximal activation at 460 nm, action spectra of C1V1 and V1 peak at 536 nm. Spectra of C1V1 and V1 exhibit a pH-dependent shoulder at around 480 nm (data not shown) [88]. Furthermore, peak-current amplitudes of the two C1V1 variants were analyzed and compared to wt ChRs. At −60 mV both C1V1 A and C1V1 B show robustly high current amplitudes of (1280 ± 150) pA and (2650 ± 340) pA, respectively. C1V1 current amplitudes do not only exceed C1 and V1 photocurrents, but are also larger than currents measured for C2 ($P = 0.025$ for C1V1 A and $P < 0.001$ for C1V1 B). Since C1V1 shows a lower degree of inactivation than C2 ((36 ± 3) % vs (72 ± 16) %) [87], the difference in stationary photocurrent amplitudes would be even more pronounced. Figure 5.4D shows a photocurrent trace of C1V1 following repetitive activation for 10 ms at 10 Hz. The trace does not only

show the photocurrent decline to a stationary level after four or more light pulses, but also displays the relatively slow off-kinetics of C1V1. The time constant of the closing reaction of C1V1 after a 10 ms light pulse was determined to be (110 ± 10) ms. Next, C1V1 was functionally expressed in hippocampal neurons. C1V1 activation induces a prolonged membrane depolarization and action potentials can be evoked using light of 530 nm, 600 nm and 620 nm. Nevertheless, the delay time to the first action potential strongly depends on the used wavelength (Figure 5.4E). In summary, C1V1 shows high expression levels in HEK cell membranes which is reflected by its high photocurrents. Being maximally activated by green light, C1V1 retains the absorption properties of V1 and can trigger action potentials in neurons at wavelength beyond 600 nm. When compared to other ChRs, C1V1 exhibits relatively slow off-kinetics.

5.1.3. C1V1 mutants

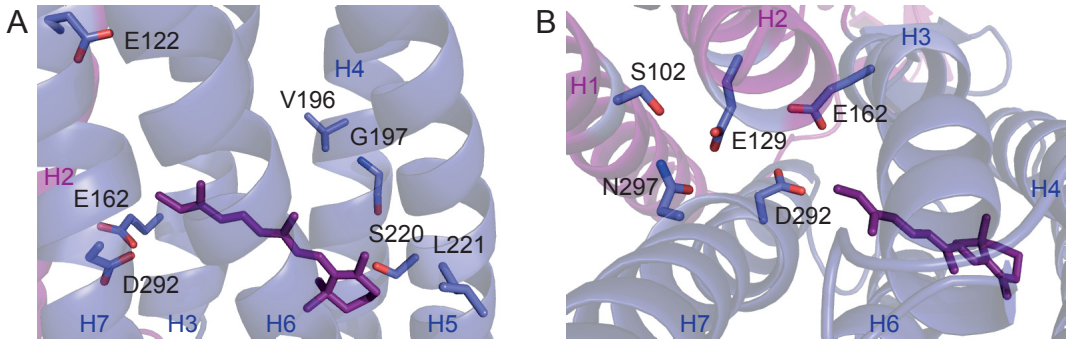

Figure 5.5.: Closer insights into the C1V1 structural model. The model is based on the C1C2 X-ray structure (pdb:3UG9)[74]. **A** Side chains of relevant C1V1 positions that were mutated to fine-tune C1V1 properties. For G197 the peptide backbone is depicted. While E162 and D292 are part of the counterion complex, E122 is an important residue of the inner gate. V196, G197, G220 and L221 are in close vicinity to the polyene chain and the β-ionone ring of the retinal (colored in magenta). **B** Central gate residues and counterion complex of C1V1 as seen from the extracellular side. Mutations of selected central gate residues are described in section 5.2.3.

In order to optimize and fine-tune the C1V1 properties a large screen of mutants was performed in collaboration with Matthias Prigge. More than 100 single and double mutants were tested for expression level, action spectrum and kinetic parameters. The information gained from the mutant experiments did not only give rise to new variants, but also revealed information about the molecular mechanism of C1V1. Here, only a selection of six relevant mutants is presented.

In C1V1, the counterion complex comprises the conserved residues E162 and D292. Replacement of C1V1 E162 yields functional mutants. It has been previously shown that mutation of the corresponding E123 position in C2 shifts the absorption spectrum, accelerates the photocycle and alters the ion selectivity [98][100]. The so-called ChETA mutation E162T was introduced in C1V1. In addition, E122 (corresponding to E83 in C2) - a residue of the "inner gate" that indirectly interacts with the active site [223][74] - was also mutated to threonine. Furthermore, G196 and V197 of helix four and S220 and L221 of helix five were mutated. These residues are in contact to the polyene chain and the β-ionone ring of the retinal chromophore. The vicinity of G196 and V197 to

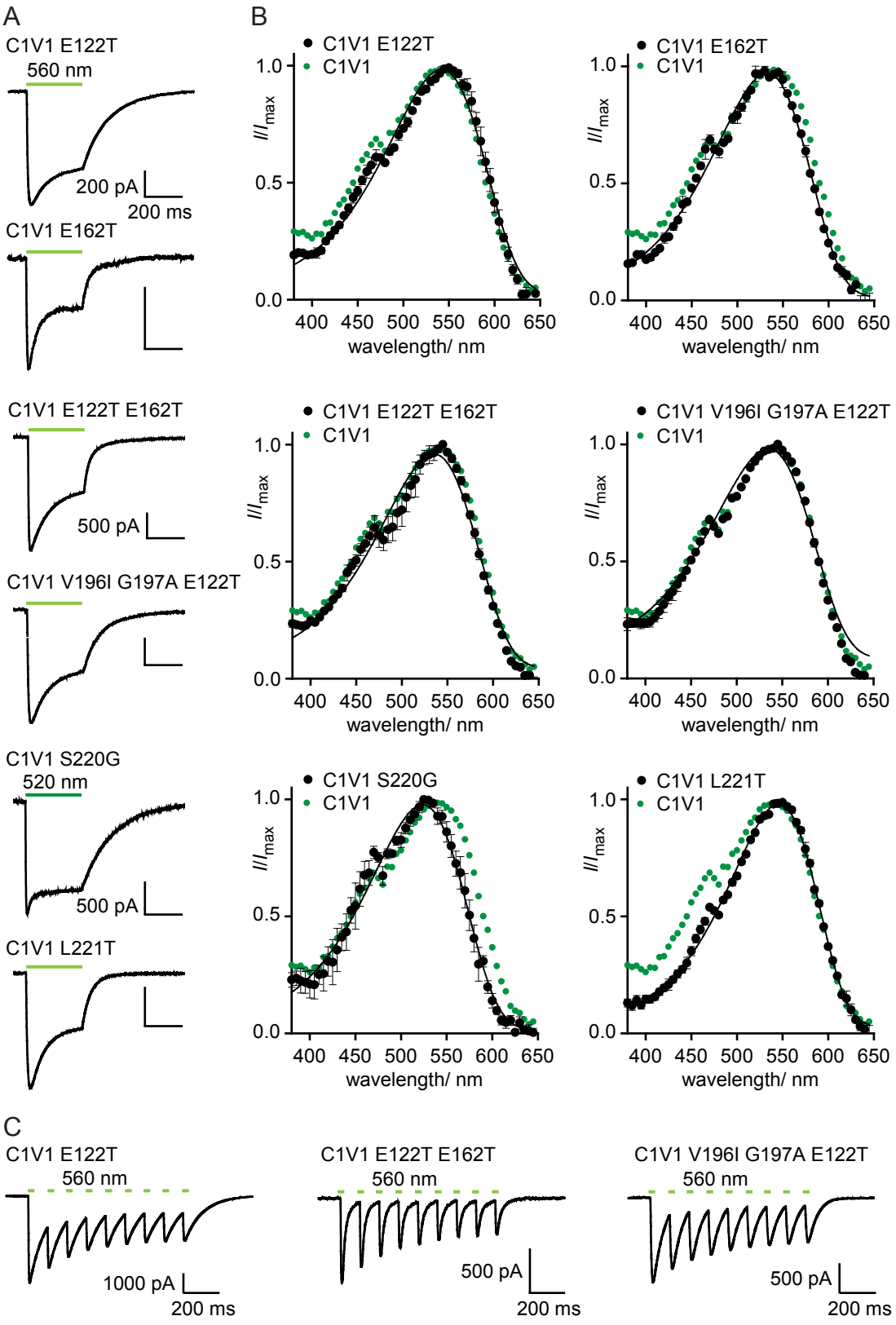

Figure 5.6.: Further fine-tuning of C1V1 by mutagenesis. **A** Representative current traces of selected C1V1 mutants at −60 mV and standard conditions. If not stated otherwise the scalebars correspond to 200 pA and 200 ms. Notably, the mutants show varying degrees of inactivation and altered kinetics. **B** Action spectra of the six mutants. C1V1 S220G exhibits a blue-shifted activation maximum while C1V1 L221T is the most red-shifted variant. All mutant spectra show a shoulder at about 480 nm. **C** Repetitive stimulation (10 ms at 10 Hz) of three mutants. C1V1 E122T E162T is the fastest C1V1 mutant.

mutant	λ_{max} / nm	I_p / pA	τ_{off} / ms
C1V1	536 ± 1	1280 ± 150	110 ± 10
C1V1 E122T	542 ± 1	1020 ± 120	100 ± 10
C1V1 E162T	532 ± 1	680 ± 110	34 ± 4
C1V1 E122T E162T	535 ± 1	1190 ± 230	19 ± 1
C1V1 E122T V196I G197A	535 ± 1	1300 ± 190	65 ± 4
C1V1 S220G	524 ± 1	1580 ± 350	110 ± 20
C1V1 L221T	542 ± 1	490 ± 100	46 ± 3

Table 5.2.: Comparison of basic parameters of selected C1V1 mutants. Action spectra of C1V1 E122T and C1V1 L221T show the most pronounced red-shift while C1V1 S220G is significantly blue-shifted. C1V1 E122T E162T exhibits the fastest off-kinetics. Amplitudes of most mutants are similar to C1V1, only C1V1 E162T and C1V1 L221T show reduced current sizes. M.P. equally contributed to all amplitude determination experiments.

C198 (corresponding to T159 in C2) may suggest an kinetic effect of the introduced mutations. S220G has been found to red-shift the C1C2 action spectrum [88]. The neighboring residue L221 may also affect the absorption properties of the chromophore.

The mutants were tested in patch-clamp recordings on HEK cells. Whereas most mutants exhibit current amplitudes comparable to C1V1, introduction of E162T and L221T leads to reduction in current size (Table 5.2). Representative current traces are illustrated in Figure 5.6A. C1V1 E122T and C1V1 S220G display similar kinetic parameters to C1V1 (see also Table 5.2). Interestingly, the relatively slow off-kinetics correlate with the low degree of inactivation. All other mutants show accelerated off-kinetics. The fastest C1V1 mutant is the C1V1 E122T E162T double mutant that features a characteristic τ_{off} value of (19 ± 1) ms. The different off-kinetics result in distinct responses to repetitive light stimuli, as is displayed in Figure 5.6C. In the following, action spectra were determined (Figure 5.6B) and compared to C1V1. While the ChETA mutation only marginally blue-shifts the absorption, E122T causes a 6 nm bathochromic shift. The same shift is achieved by the L221T mutation that introduces a polar residue close to the ring system. But, combination of E122T and L221T does not further red-shift the absorption (data not shown). By removal of the polar S220 next to L221, the C1V1 spectrum is hypsochromically shifted by 12 nm. The other mutations do not affect the action spectrum. Maxima of action spectra, current amplitudes and τ_{off} values for the presented mutants are summarized in Table 5.2. Perspectives of the presented mutants for optogenetic applications are given in the discussion section 6.1.

5.2. Gating and ion selectivity in ChRs

The following section deals with characteristic structural motifs of ChRs. These include the conserved charged residues of helix two and the two gates - the inner and the central gate - that were identified by Kato *et al.* [74]. In the end, a more general model of ion selectivity will be presented. The model allows for quantification of ion contribution to both early and stationary currents for different ChR variants.

5.2.1. Conserved polar and charged residues

While helices three to seven are highly conserved among ChRs (more than 47 % for all ChRs in the protein databank) and other microbial rhodopsins (24 % to 30 %), helices one and two of ChRs differ from other rhodopsins and exhibit characteristic sequence patterns (see section 3.4.1). Both helices show a number of polar amino acids that exhibit a seven amino-acid periodicity and were suggested to point into the protein interior [75]. In the second helix, a high number of charged residues is present [223]. Since charged residues are uncommon in the membrane-spanning domains of proteins, these residues were proposed to be implied in channel function. In C2 the charged residues in the second helix are E82, E83, E90, K93, E97, E101 and K103 (see Figure 5.7A). K103 is not conserved among ChRs and is not included in the present study. Additionally, E82 and E90 were intensively analyzed by Jonas Wietek and André Berndt in our group and are not examined here [220, 100, 94]. Between E83 and E90 another polar amino acid is found in the sequence, namely C87. Here, these charged and polar amino acids were exchanged by site-directed mutagenesis and current amplitudes as well as action spectra were determined. E123 was included in the study due to its close proximity to second helix residues. All mutations were tested on the C2 T159C background that promotes protein stability, retinal binding and exhibits increased current sizes [99, 109].

Figure 5.8A illustrates typical current traces of the tested single mutants at −60 mV.

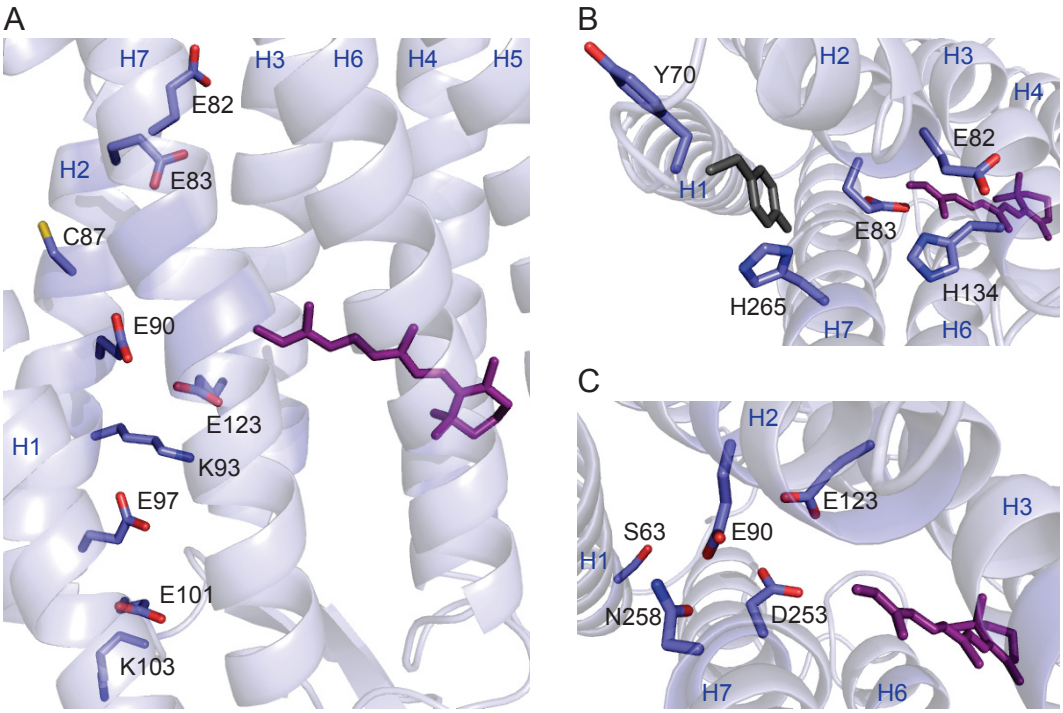

Figure 5.7.: Characteristic structural motifs in C2. All C2 model structures are based on the C1C2 X-ray structure (pdb:3UG9)[74]. The all-*trans* retinal is highlighted in magenta. **A** Conserved polar and charged residues of the second helix. All side chains point to the protein interior. **B** Important residues of the proposed inner gate. While Y109 is orientated towards the inner gate in the C1C2 structure (here shown in grey), the side chain of the corresponding Y70 points into the opposite direction in the C2 model. **C** Residues of the proposed central gate and the counterion complex. Both **B** and **C** depict views from the intracellular side to the active site.

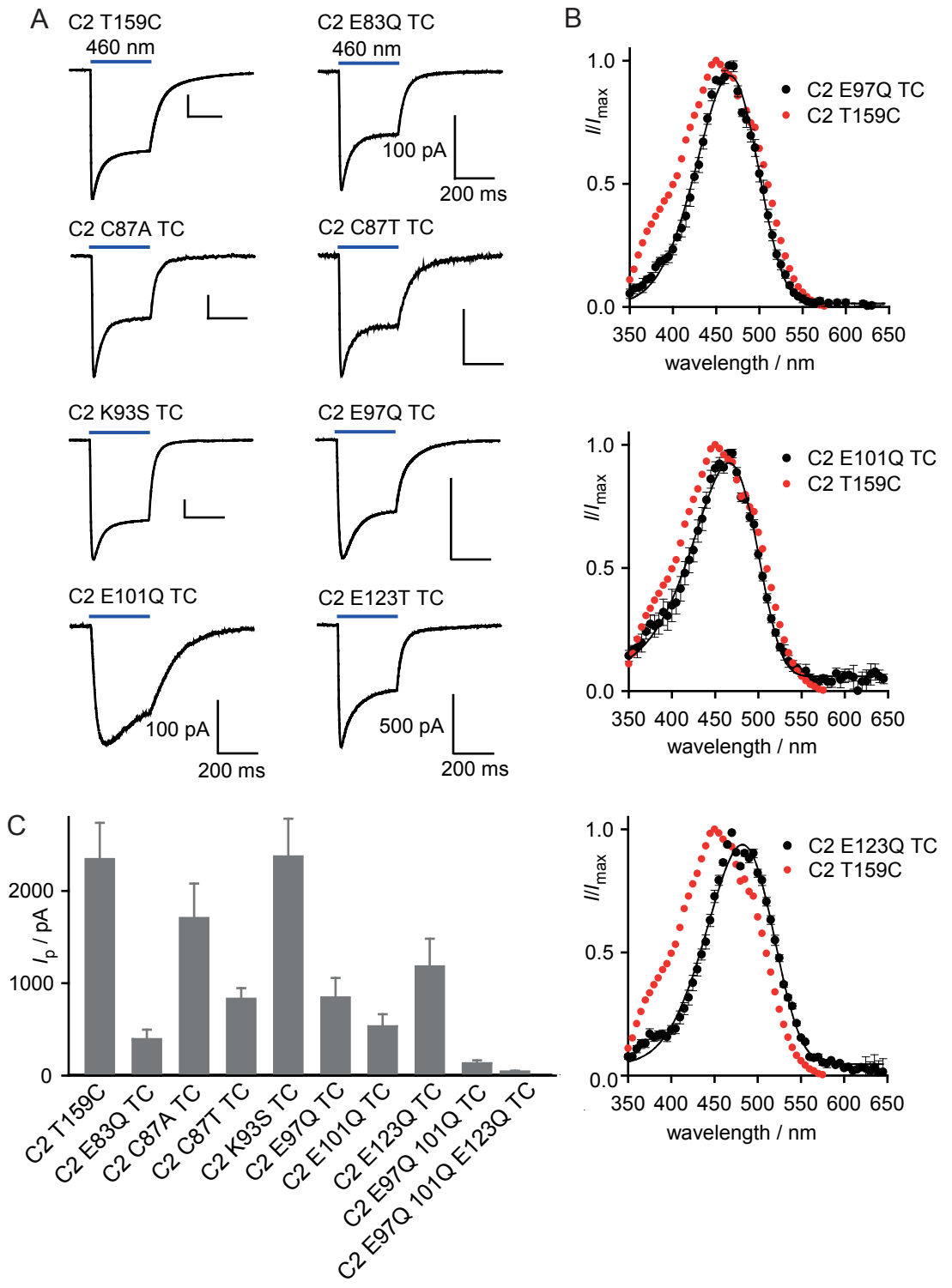

Figure 5.8.: Replacement of characteristic polar and charged C2 residues. **A** Representative current traces of C2 T159C and seven selected mutants at standard conditions and −60 mV. If not stated otherwise, vertical scalebars correspond to 500 pA and horizontal scale bars correspond to 200 ms. Notably, C2 E123Q T159C shows accelerated off-kinetics while inactivation and off-kinetics are retarded in C2 E101Q T159C. **B** Action spectra of three selected mutants in comparison to C2 T159C. Spectral maxima are (466 ± 1) nm, (466 ± 1) nm and (482 ± 2) nm for C2 E97Q T159C, C2 E101Q T159C and C2 E123Q T159C, respectively. **C** Average peak currents at −60 mV for C2 variants with single, double or triple replacement of polar or charged amino acids.

All mutants are functional and exhibit ChR-characteristic photocurrents. While C2 E123Q T159C shows the fastest off-kinetics, inactivation and channel closure are decelerated in C2 E101Q T159C. Peak-current amplitudes for each variant are presented in Figure 5.8C. Except for C2 K93S T159C the introduced mutations reduce the average current sizes. This might be caused by decreased protein stability or reduction of cation conductance. Moreover, there is a cooperative effect. Single mutations reduce the currents by a factor of six or less, whereas the tested double and triple mutations reduce the currents by a factor of 18 and 55, respectively. Since expression of the triple mutant is still observable by fluorescence imaging (data not shown), the drastic reduction in current amplitude might result from reduced cation conductance. Action spectra were recorded for the tested mutants. Figure 5.8B illustrates the influence of single glutamate removals on the respective action spectra. Introduction of E97Q or E101Q red-shifts the C2 T159C action spectrum to (466 ± 1) nm, but the double mutant does not display any further spectral shift (not shown). Notably, the spectrum of C2 E123Q T159C is bathochromically shifted by 22 nm confirming the direct interaction of this residue with the Schiff base. In contrast, C2 E83Q T159C does not alter the C2 spectrum and shows maximal activation at (460 ± 1) nm (Jonas Wietek, personal communication).

5.2.2. Inner gate

Based on the C1C2 crystal structure Kato and coworkers proposed two gates that block the ion conducting pathway in the closed channel conformation [74]. The central gate blocks the extracellular entrance channel and is located close the counterion complex. The inner gate is orientated towards the intracellular side and might be implied in cation release. Kato *et al.* considered Y109 (C2 Y70) to be the essential residue of the inner gate. Here, the neighboring residues in C2 E82, E83, H134 and H265 are regarded to be part of the inner gate as well (see Figure 5.7B for positions in the C2 structure). Moreover, the C2 structural model orientates Y70 to the lipid phase rather than into the protein interior, which renders its involvement in C2 gating rather unlikely. E82, E83, H134 and H265 have been previously described to alter protein folding and stability, ChR kinetics, ion selectivity and color-tuning [17, 223, 100, 75, 87]. Furthermore, spectral effects and ion selectivity of Y70, E82 and E83 were recently investigated by Jonas Wietek. In the following, the influence of mutations at position H134 is further analyzed. Thereby, special focus is placed on ion selectivity. The experiments were designed based on previous studies by André Berndt.

The mutations H134R, H134N and H134S were introduced in C2 and mutants were analyzed by patch-clamp recordings on HEK 293 cells. Figure 5.9A illustrates peak-current amplitudes of the three mutants applying standard conditions. When compared to wt C2, current sizes were reduced by a factor of 2.5, 3 and 11 for H134R, H134N and H134S, respectively. Notably, the H134R mutant has been described to induce higher stationary photocurrents in oocytes and HEK cells [101]. This discrepancy might be partly explained by the lower inactivation of C2 H134R (32 %) in comparison to wt C2 (72 %) [80][87]. Action spectra and pH dependency of C2 H134R are very similar to the

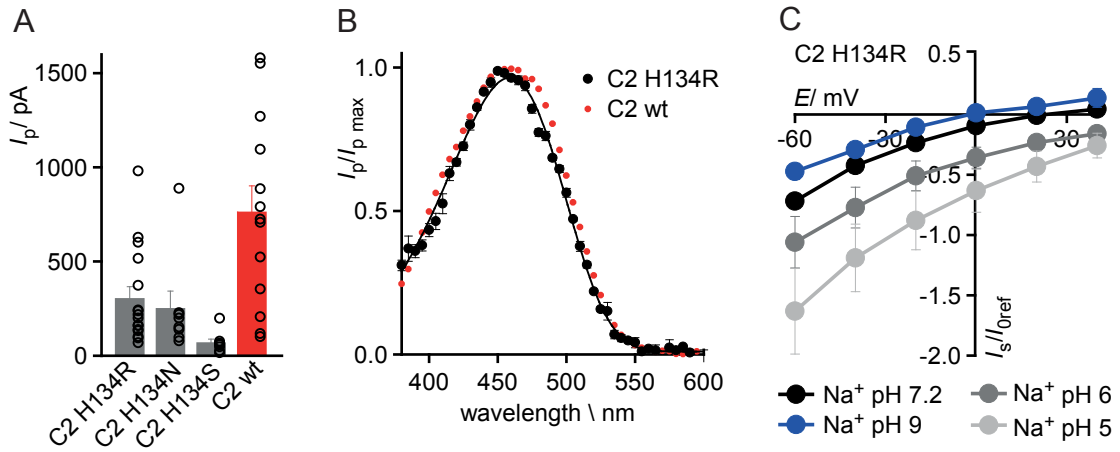

Figure 5.9.: Influence of mutations at position H134 in C2. **A** Comparison of current amplitudes of three selected mutants at standard conditions and −60 mV. **B** Action spectra of C2 H134R and wt C2. **C** pH dependency of C2 H134R. IV plot is shown for the stationary current I_s.

wt properties (Figure 5.9B and C). André Berndt reported an altered proton and Na^+ dependence for H134N [224]. In consequence, the cation conductance of this mutant was examined in more detail. As seen from the individual current traces at three extracellular conditions (Figure 5.10A), C2 H134N does not only show reduced inactivation at high Na^+, pH_e 7.2 (black traces). Strikingly, inactivation almost totally disappears at high Na^+, pH_e 9.0 and negative voltages (blue traces). At this specific condition the stationary current even exceeds the initial current. Moreover, the stationary current at high Na^+, pH_e 9.0 is higher than the stationary current at high Na^+, pH_e 7.2 (Figure 5.10B and C). In contrast, amplitudes of Ca^{2+}-mediated inward currents are unaffected by the H134N mutation (red lines/symbols in Figure 5.10A-C). At all presented conditions the reversal potentials of C2 H134N are more positive than the respective reversal potentials of wt C2. The difference in reversal potentials is most pronounced at Na^+, pH_e 9.0 ($p < 0.001$) indicating a higher Na^+ conductivity of H134N in the abscence of protons. To further evaluate competition of Na^+ with protons the extra- and intracellular pH dependency of the mutant was evaluated.

Figure 5.11 shows selectivity measurements of the mutant at internal high Na^+, pH_i 9.0. This condition was chosen because it creates a driving force for inward proton transport whereas Na^+ transport is still possible in both directions. In the presence of external Na^+, reversal potentials are comparable between wt and mutant (Figure 5.11A; C). In contrast, the shape of the IV plots exhibits significant differences. While currents increase with the proton concentration in wt C2, addition of protons leads to reduced currents in C2 H134N at negative voltages leading to intersection of the pH-dependent IV curves for the mutant (Figure 5.11A, blue arrows). This is also illustrated in the bar chart that compares amplitudes at −60 mV (Figure 5.11B). In the abscence of external Na^+ and at moderate proton concentrations, the reversal potentials of H134N are negatively shifted compared to wt C2 (Figure 5.11D red arrows; F). This is most obvious at external NMG, pH_e 9.0 ($p = 0.004$) suggesting outward-directed Na^+ transport. Furthermore, inward currents are lower and outward currents are much higher for the mutant than in

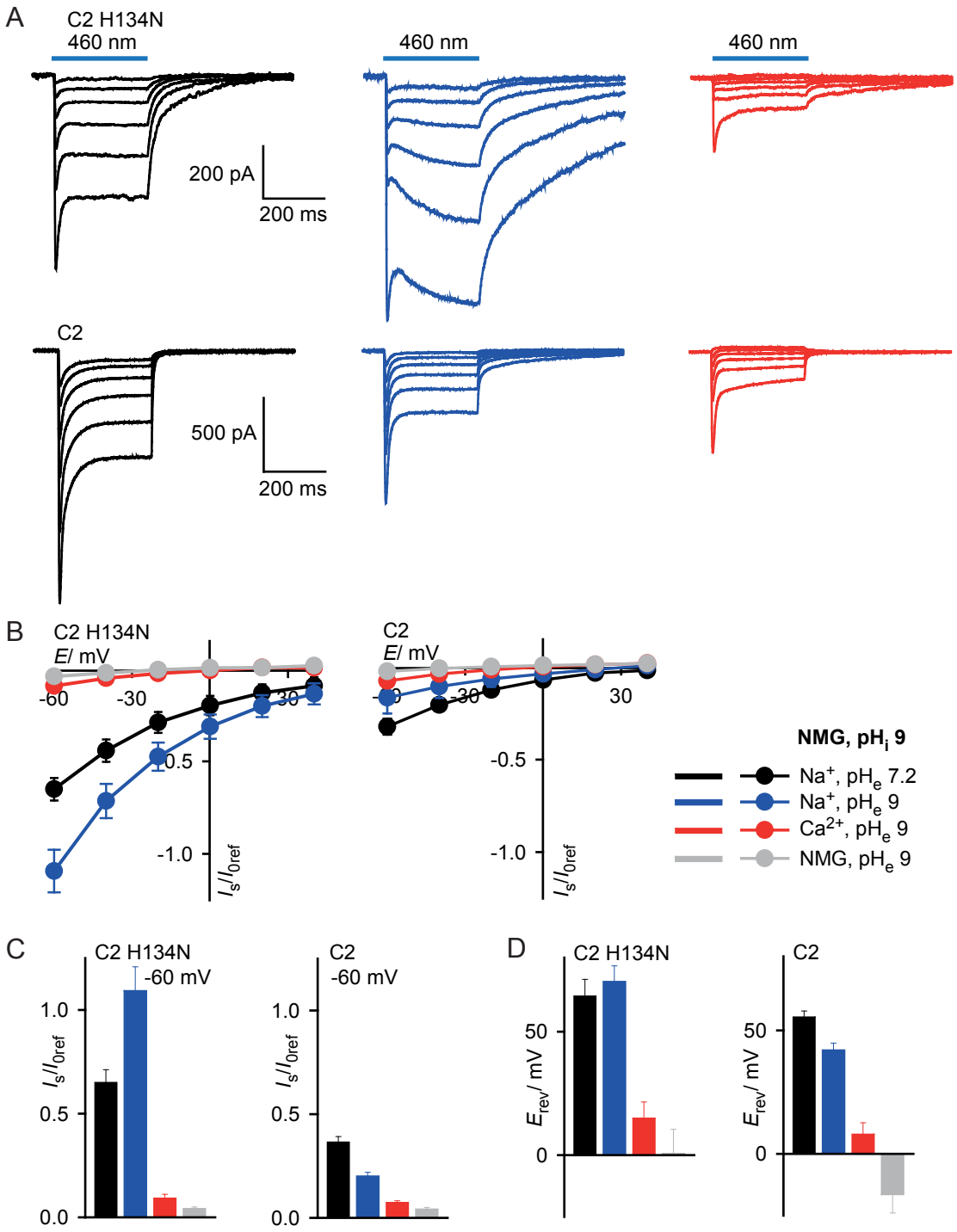

Figure 5.10.: Cation selectivity of C2 H134N in comparison to wt C2. The intracellular solution contained NMG, pH_i 9. **A** Representative current traces at three selected conditions for C2 H134N (upper row) and C2 (lower row). Applied voltages were varied between −60 mV and 40 mV in 20 mV steps. **B** Current-voltage relationsships of stationary photocurrents at varying external conditions. **C** and **D** Corresponding current amplitudes at −60 mV and calculated reversal potentials.

wt C2 (Figure 5.11D blue arrow; E). Taken together, these experiments suggest a high competition of protons and Na^+ as well as a reduced inward rectification of the mutant.

Next, selectivity measurements at internal acidic pH were performed (high Na^+, pH_i 5.0). This condition promotes both Na^+ and proton-mediated outward currents. As expected all reversal potentials are more negative at internal acidic pH than at internal

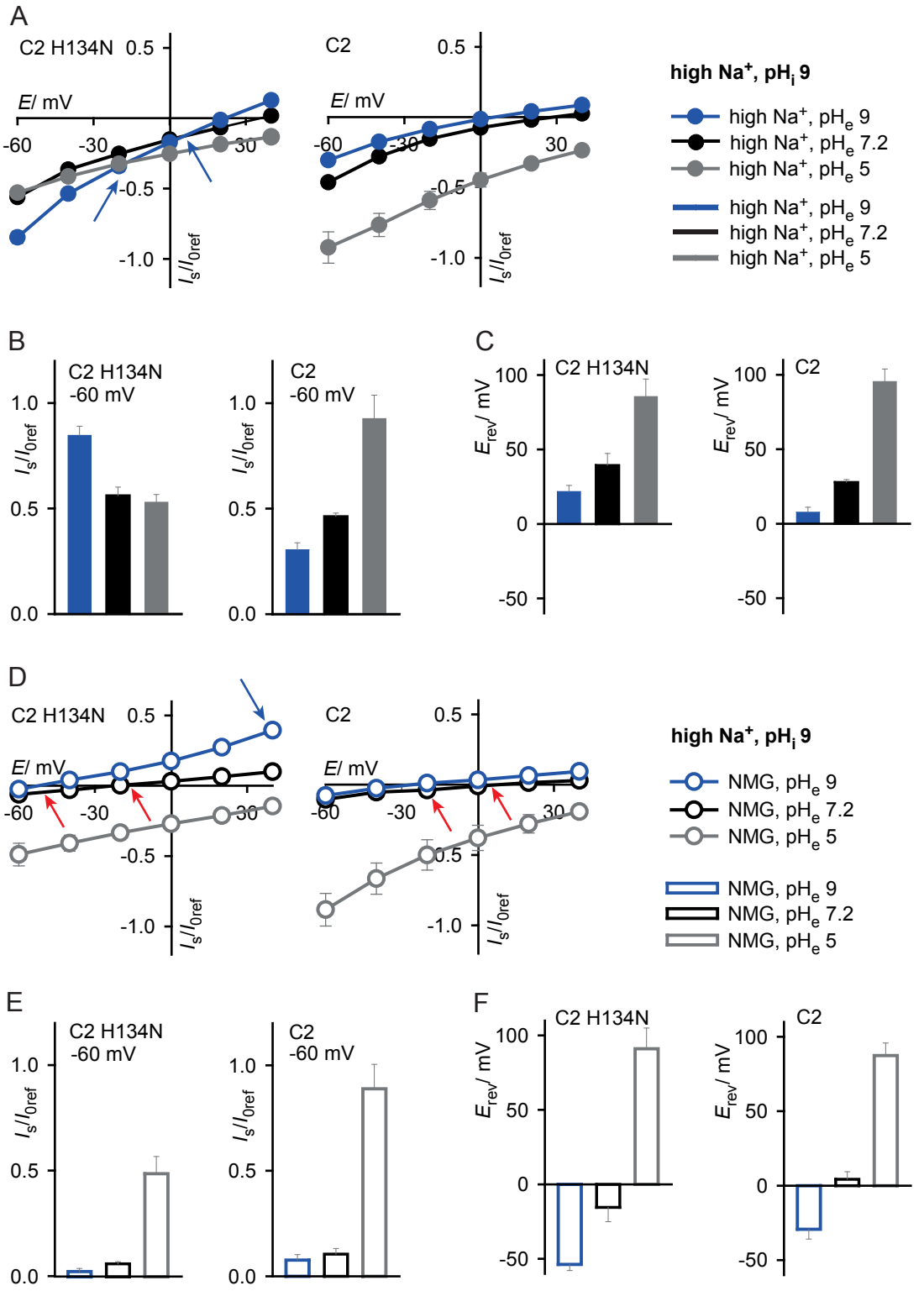

Figure 5.11.: Quantification of H^+ and Na^+ conductivity of C2 H134N and wt C2 at internal high Na^+ pH_i 9.0. Maila Reh contributed to wt reference measurements. **A** Current-voltage relationsships at external high Na^+ at three different pH values. **B** and **C** Corresponding current amplitudes at −60 mV and reversal potentials. **D** I-V curves at external high NMG, pH_e 5, 7.2 and 9. External Na^+ is reduced to 1 mM in order to reduce inward-directed Na^+ currents. **E** and **F** Respective current amplitudes at −60 mV and reversal potentials.

alkaline pH, both in C2 H134N and wt C2 (compare Figure 5.11C; F to Figure 5.12C; F). In the presence of external Na^+ H134N displays considerable outward currents at

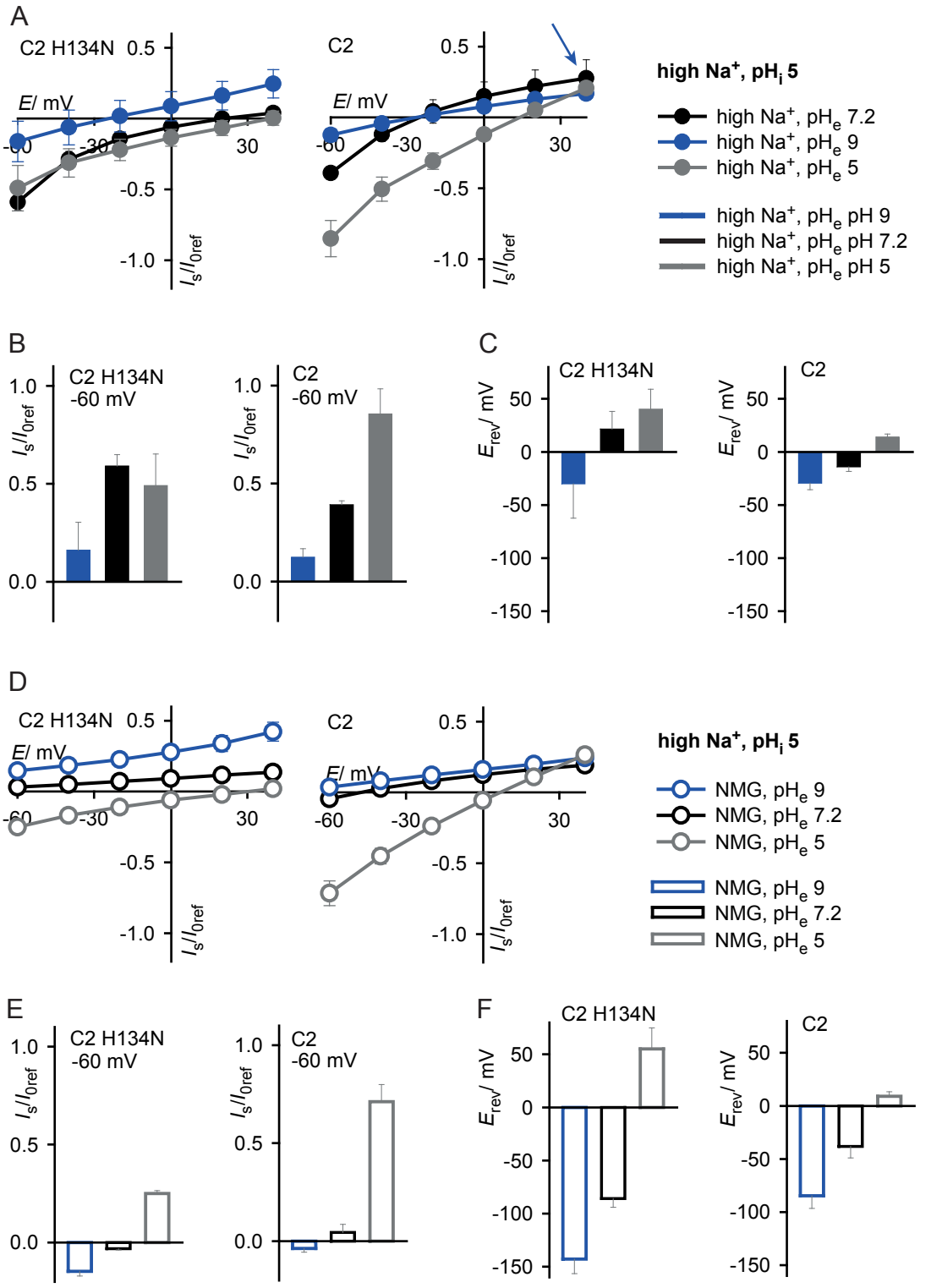

Figure 5.12.: Quantification of H^+ and Na^+ conductivity of C2 H134N and wt C2 at internal high Na^+ pH_i 5.0. Maila Reh contributed to wt reference measurements. **A** Current-voltage relationsships at external high Na^+ at three different pH values. **B** and **C** Corresponding current amplitudes at −60 mV and reversal potentials. **D** I-V curves at external high NMG, pH_e 5, 7.2 and 9. External Na^+ is reduced to 1 mM in order to reduce inward-directed Na^+ currents. **E** and **F** Respective current amplitudes at −60 mV and reversal potentials.

pH_e 9.0, but not at pH_e 7.2 and pH_e 5.0. In contrast, C2 shows outward currents at all pH values when positive voltages are applied (Figure 5.12A, indicated by blue arrow).

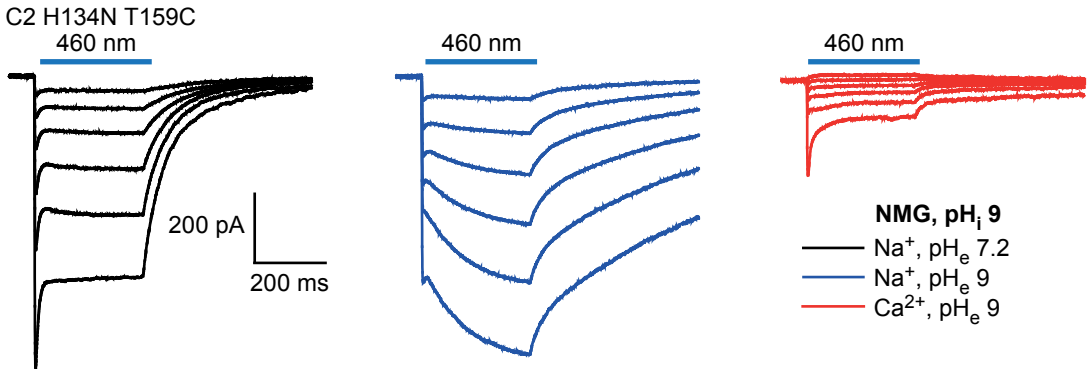

Figure 5.13.: Representative current traces for C2 H134N T159C at three selected external conditions. Internal solution was NMG, pH_i 9. Applied voltages were varied between −60 mV and 40 mV in 20 mV steps.

This might suggest an inhibition of outward currents by external protons in the mutant. Again, inward-directed Na^+ currents are smaller at pH_e 5.0 than at pH_e 7.2 (Figure 5.12A; B) indicating high competition of the two ions. In the abscence of external Na^+, both C2 and H134N show outward currents at pH_e 9 and pH_e 7.2 and inward currents at pH_e 5.0 applying negative voltages (Figure 5.12D). But outward currents are higher in the mutant (pH_e 9) and inward currents are higher in wt C2 (pH_e 5) as can be seen from Figure 5.12D and E. This finding again supports a higher Na^+ conductivity and a lower inward rectification of the mutant. Considering all experiments, one can conclude the following mutant properties. C2 H134N shows high stationary photocurrents, especially at low external pH. External protons seem to block both inward and outward Na^+-mediated currents. This can be explained by strong proton binding, but a relatively slow proton transport rate. Moreover, ChR-characteristic inward rectification is reduced in the mutant. In order to apply C2 H134N for membrane depolarization, a higher expression level would be preferable. Hence, the C2 H134N was combined with the T159C mutation. The double mutant shows C2 T159C-characteristic membrane targeting, but exhibits an ion selectivity pattern very similar to the H134N mutant. Figure 5.13 depicts current traces for the double mutant at three external conditions (please compare to Figure 5.10A). Besides slightly decelerated off-kinetics, photocurrents resemble the ones measured for the single mutant. Taken together, C2 H134N T159C shows advantageous expression properties and exhibits similar cation selectivity when compared to C2 H134N.

5.2.3. Central gate

The central gate is located in close proximity to the counterion complex and contains residues of helix one, two and seven [74]. In C2, the involved residues are S63, E90 and N258 (see Figure 5.7C). E90 has been intensively studied by several groups and was shown to determine ion selectivity and current amplitude [223, 100, 225, 94]. S63 and N258 were first proposed to be involved in ion selectivity by a bioinformatic approach that modeled the ion-conducting pathway of C2 [226]. Plazzo *et al.* described an increased Ca^{2+} conductivity for the mutants C2 S63D and C2 N258D. In contrast, Kato and

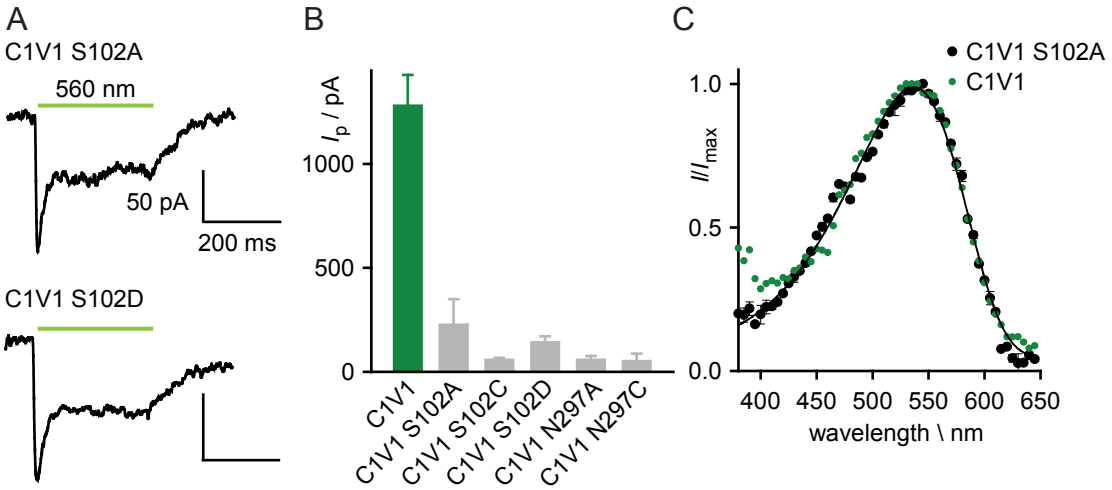

Figure 5.14.: Replacement of central gate residues in C1V1. **A** Current traces of C1V1 S102A and S102D at −60 mV and 100 % light intensity. The scalebars depict 50 pA and 200 ms. **B** Peak current amplitudes I_p of selected central gate mutants. Measurements were performed at −60 mV and 100 % light intensity. C1V1 N297D does not display any photocurrents (not shown). **C** Action spectrum of C1V1 S102A in comparison to C1V1. The spectrum peaks at (537 ± 1) nm.

coworkers reported an increased Ca^{2+} conductivity for the corresponding C1C2 mutant N258D, but reduced Ca^{2+} currents for the corresponding C1C2 mutant S102D (see blue arrow in Figure 3.4 for central gate position in C1C2). In addition, Kato *et al.* described decelerated off-kinetics for both aspartate exchanges. In my experiments, C2 S63 and N258 were mutated to alanine and aspartate. The mutations were introduced on the C2 T159C background. Furthermore, the corresponding residues in C1V1, S102 and N297, were mutated to alanine, cysteine and aspartate (see Figure 5.5B for C1V1 central gate). All mutants were expressed in HEK293 cells and tested for functionality.

All C1V1-based central gate mutants exhibit photocurrents of reduced amplitude that resemble C1V1 photocurrents (Figure 5.14A; B). Exchanges of S102 reduce current sizes by a factor of 5.6 or more, whereas exchanges of N297 result in very low currents that are more than 22 times smaller than C1V1 currents. C1V1 N297D did not show any photocurrents under the tested conditions. Exchange of serine by alanine induces the smallest reduction which might be explained by the replacement of serine by a water molecule in the alanine mutant. Figure 5.14C depicts the action spectrum of the C1V1 S102A mutant that is not shifted when compared to C1V1. The low current levels of the C1V1 central gate mutants restrict their use for both mechanistic studies and optogenetic applications, thus the mutants are not further analyzed.

Next, replacements of S63 and N258 in C2 T159C were investigated. All tested mutants exhibit reduced photocurrent amplitudes and the decrease is more pronounced for the mutations at postion N258 (5.15B) than for the mutations at postion S63. But current amplitudes of all mutants are larger than the respective C1V1 mutants. Notably, C2 T159C N258A shows a lower degree of inactivation when compared to C2 T159C (Figure 5.15A). Both C2 TC N258A and C2 TC N258D exhibit three- to four-fold slower off-kinetics than C2 T159C. Additionally, inactivation kinetics of C2 S63A T159C and C2 S63D T159C are biphasic with a dominant, fast component. Action spectra of C2

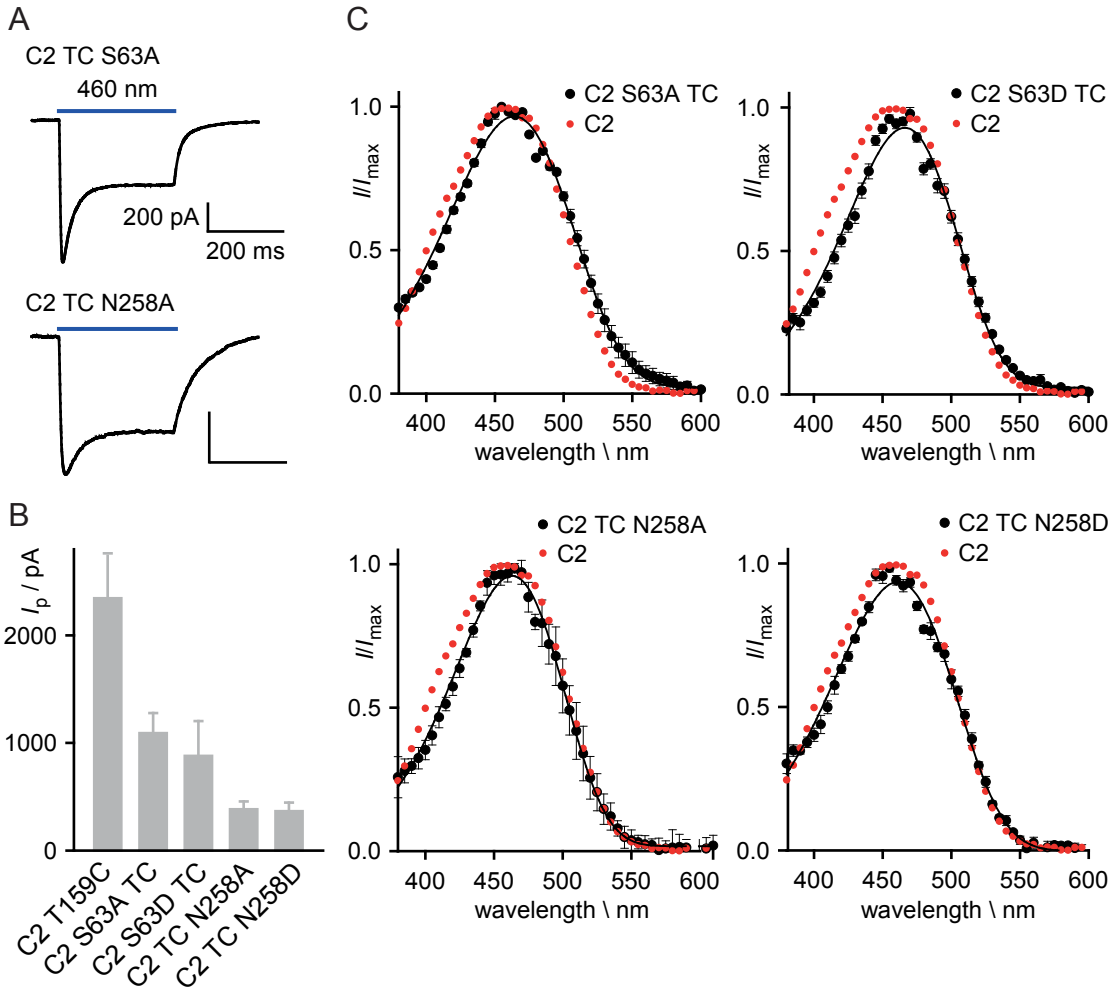

Figure 5.15.: Replacement of central gate residues in C2. **A** Current traces of C2 S63A T159C and C2 T159C N258A. The scalebars depict 200 pA and 200 ms. Current traces of C2 S63D TC and C2 TC N258D are presented in Figure 5.16. **B** and **C** Peak current amplitudes I_p and action spectra of the four investigated C2 mutants. All measurements were performed at −60 mV using standard buffer conditions.

S63A T159C, C2 S63D T159C and C2 N258A T159C are bathochromically shifted by 4 nm, 6 nm and 3 nm, respectively. These shifts confirm the proximity of S63 and N258 to the chromophore, but also show that the central gate residues have less influence on the absorption than the direct counterion residues such as E123. The basic parameters of all tested central gate mutants is summarized in Table 5.3.

In order to get a deeper understanding of the involvement of the central gate residues in ion binding and transport, ion selectivity of C2 T159C S63D and C2 T159C N258D was investigated in more detail. Figure 5.16A compares current traces of C2 T159C, C2 S63D T159C and C2 T159C N258D. At high Na^+, pH_e 7.2 (black traces), the three variants exhibit inward currents at all tested voltages. All variants show smaller currents at high Ca^{2+}, pH_e 9.0 (red traces). But, the reduction is strongest for C2 T159C and least pronounced for C2 T159C S63D pointing out a higher Ca^{2+} conductivity of the two double mutants. Subsequently, IV plots were analyzed (Figure 5.16B). C2 T159C exhibits the highest currents at high Na^+, pH_e 7.2, followed by high Na^+, pH_e 9 and high Ca^{2+}, pH_e 9. Only at a negative voltage of −60 mV, the Na^+-mediated inward currents

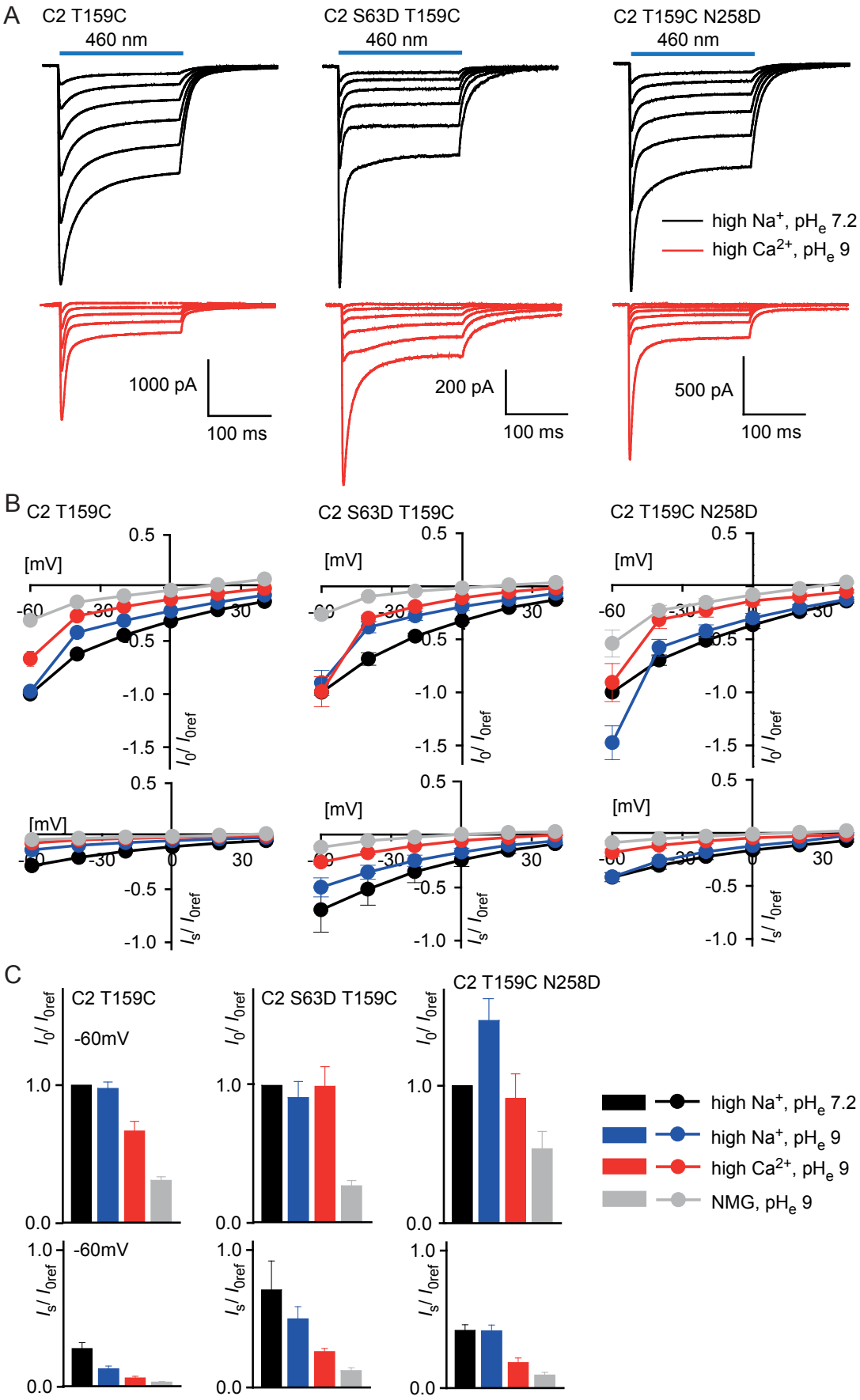

Figure 5.16.: Ion selectivity of central gate mutants. Internal solution was NMG pH_i 9. **A**- Representative current traces of C2 T159C, C2 S63D T159C and C2 T159C N258D at two different extracellular buffer conditions. Voltage was varied from −60 mV to 40 mV in 20 mV steps. **B** Normalized current-voltage relationships at four different external conditions. **C** Corresponding current amplitudes at −60 mV.

mutant	λ_{max} / nm	I_p / pA	τ_{off} / ms
C1V1	536 ± 30	1280 ± 150	110 ± 10
C1V1 S102A	537 ± 1	230 ± 120	130 ± 20
C1V1 S102C	/	58 ± 10	/
C1V1 S102D	/	140 ± 30	/
C1V1 N297A	/	58 ± 18	/
C1V1 N297C	/	51 ± 35	/
C1V1 N297D	no current detectable		
C2 T159C	460 ± 1	2340 ± 390	18 ± 2
C2 T159C S63A	464 ± 1	1090 ± 190	25 ± 2
C2 T159C S63D	466 ± 1	880 ± 320	27 ± 3
C2 T159C N258A	463 ± 1	380 ± 70	61 ± 8
C2 T159C N258D	461 ± 1	370 ± 80	67 ± 9

Table 5.3.: Comparison of central gate mutants to C1V1A and C2 T159C. All mutants exhibit reduced amplitudes, while action spectra are only slightly affected. Notably, C2 TC N258A and C2 TC N258D show more than threefold decelerated off-kinetics when compared to C2 T159C. Matthias Prigge contributed to values determined for C1V1A and C2 T159C.

at pH_e 7.2 and pH_e 9 are almost unity (Figure 5.16C). Stationary currents are more than three-fold reduced in C2 T159C. Two major differences are apparent when comparing C2 S63D T159C to C2 T159C. First, the Ca^{2+}-mediated initial currents at negative voltages exhibit similar amplitudes than the Na^+- and proton-driven currents. Second, relative stationary currents are more than twofold higher in C2 S63D T159C at all tested conditions. C2 T159C N258D shows a slightly different behavior. In this mutant the initial Na^+ currents at pH_e 9 are higher than the corresponding initial curents at pH_e 7.2 indicating an inhibition of Na^+ currents at neutral pH. Whereas Ca^{2+} influx at high Ca^{2+}, pH_e 9 is comparable in size to Na^+ influx at standard conditions, there is an considerably high influx even at NMG, pH_e 9 (grey lines and bars). Since the NMG buffer contains 2 mM Ca^{2+}, the current is most likely also mediated by Ca^{2+}. This finding implies a high affinity for Ca^{2+} binding in C2 T159C N258D. The stationary currents of C2 T159C N258D are intermediate in size. In summary, C2 S63D T159C shows

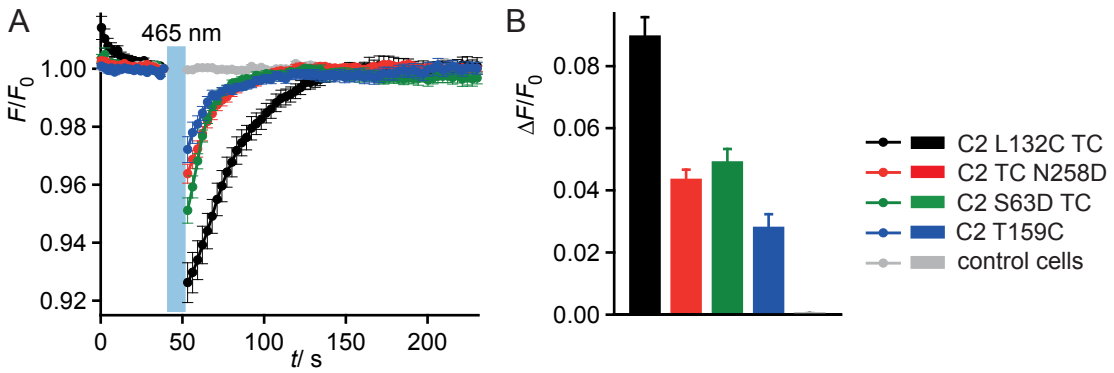

Figure 5.17.: Ca^{2+} conductance of selected C2 mutants analyzed by Fura-2 fluorescence. **A** Time-dependent fluorescence of HEK cells loaded with Fura-2 AM. ChRs were activated at 460 nm for 10 s (light blue bar). The external solution contained 70 mM Ca^{2+}, pH_e 7.2. **B** Relative change in fluorescence directly after light activation. Cells expressing C2 L132C TC (Catch+) were used as a positive control, untransfected cells were imaged as a negative control.

increased Ca^{2+} conductivity especially for the initial currents and more than twofold enhanced stationary currents. C2 T159C N258D displays high Ca^{2+} transport even at low Ca^{2+} concentrations and inhibition of Na^+-mediated photocurrents by external protons.

Since Ca^{2+} currents are superimposed by proton currents at neutral pH, evaluation of Ca^{2+} conductivity at neutral pH is difficult from electrical recordings. In order to overcome this problem, Fura-2 imaging was performed. This allows for direct measurements of Ca^{2+} concentration changes in HEK cells. Cells expressing different C2 variants were incubated with 2 µM Fura-2 acetomethylester for 30 min. After a consecutive washing step, time-dependent changes in Fura-2 fluorescence were imaged at 380 nm. Figure 5.17A compares the Ca^{2+} influx into HEK cells expressing four different C2 mutants. ChRs were activated by illumination at 450 nm for 10 s. The external solution contained high Ca^{2+}, pH_e 7.2. After illumination all ChR-expressing cells showed an decrease in fluorescence intensity. The fluorescence change was highest in C2 L132C T159C (Catch+) that served as a positive control. Moreover, the fluorescence change was significantly increased for C2 S63D T159C and C2 T159C N258D when compared to C2 T159C ($p = 0.001$ and $p = 0.005$, Figure 5.17B). In conclusion, the two central gate mutants C2 S63D T159C and C2 T159C N258D show an increased Ca^{2+} conductitvity under prolonged illumination. This effect is apparent even in the presence of competing protons. The presented data confirms the computational and experimental data of Plazzo *et al.* [226].

5.2.4. Ion selectivity

In the following, general aspects of ion selectivity were investigated. At first, the influence of internal Mg^{2+} was analyzed for C2. Subsequently, the different conductivities of the initial current I_0 and the stationary current I_s were described in detail. For this purpose, three model ChRs, namely C2, C1V1 A and C2 L132C T159C were chosen. C1V1 A has been found to exhibit an increased Ca^{2+} selectivity [87] and constitutes the best-expressing green-activated variant so far. C2 L132C T159C (Catch+) combines the Ca^{2+}-selective L132C mutation [110] with the stabilizing T159C mutation [99, 109]. Being expressed in HEK 293 cells the double mutant shows the highest photocurrents of all reported ChRs (see Figure 6.2 and Table 6.1). The three ChRs were tested for conductivity of protons, Na^+, Ca^{2+} and Mg^{2+}. In the end, the data was used to dissect currents into contributions of all competing ions. For that purpose, a general enzyme-kinetic algorithm was applied. All model calculations were performed by Professor Dietrich Gradmann.

In order to further understand inward rectification in ChRs, the influence of internal Mg^{2+} was tested. Mg^{2+} had been shown to cause inward rectification in potassium channels [227]. Furthermore, it causes complete photocurrent inhibition in *Chlamydomonas* cells [228]. Figure 5.18 compares Na^+-mediated inward currents at three different internal Mg^{2+} concentrations. Both current traces and IV plots precisely overlay for 0.2 mM, 2 mM and 20 mM Mg^{2+}. In addition, both absolute current amplitudes and reversal

potentials are very similar between the tested concentrations (Figure 5.18C; D). These findings demonstrate that internal Mg^{2+} can be ruled out as a possible source for inward rectification in ChRs [100].

Next, cation selectivities of the initial current I_0 and the stationary current I_s were analyzed. Therefore, photocurrents were measured for various cation concentrations at pH_e 9.0. All used buffers are summarized in Table 4.11. I_0 and I_s display different selectivities which are reflected by different current sizes and reversal potentials for the early and late currents. Figure 5.19 depicts current traces of C2 at conditions close to reversal potentials. At the presented conditions, I_0 is inward-directed while I_s reflects cation outward flux. I_0 and I_s differ in their respective reversal potentials by more than 20 mV. This example illustrates the necessity to independently analyze I_0 and I_s.

Earlier studies distinguished between three ion species; namely protons, monovalent cations and divalent cations [86, 100]. This treatment subsumes similar binding and transport rates for both Na^+ and K^+ as well as Mg^{2+} and Ca^{2+}. Here, Mg^{2+} and Ca^{2+} are treated independently. Our data suggests major differences in Mg^{2+} and Ca^{2+} conductance of different ChRs. Figure 5.20 shows the quantification of Mg^{2+} conductance for C2, C1V1 and C2 L132C T159C. IV relationships were recorded at 2 mM, 20 mM and 70 mM external Mg^{2+}. All tested ChR variants exhibit relatively low currents at all tested Mg^{2+} concentrations. Interestingly, C2 current amplitudes at −60 mV decrease with increasing Mg^{2+} concentrations (Figure 5.20A, see orange arrow 1 and Figure 5.20B, orange circle 1). A similar effect is seen at positive voltages

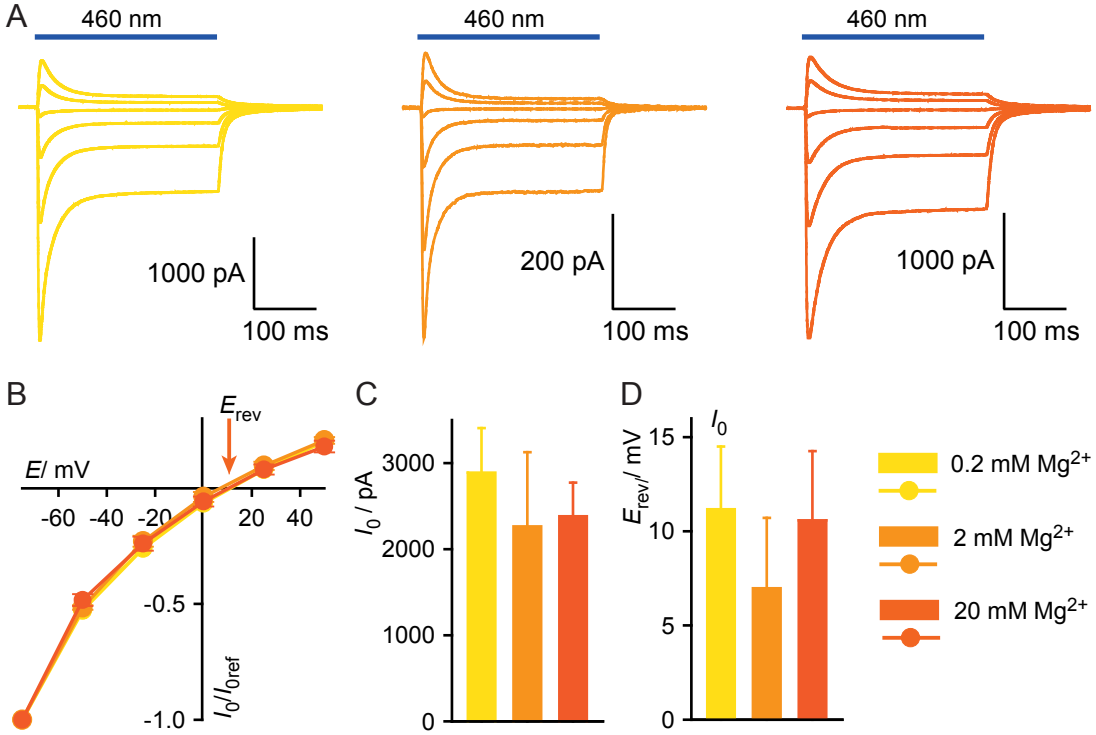

Figure 5.18.: Influence of the internal Mg^{2+} concentration on C2 photocurrents. **A** Current traces of C2 at an internal Mg^{2+} concentration of 0.2 mM, 2 mM and 20 mM. Voltages were varied from −75 mV to 50 mV. **B** Corresponding IV plot of initial current I_0. **C** and **D** Average current sizes of I_0 at −75 mV and reversal potentials E_{rev} for the three conditions.

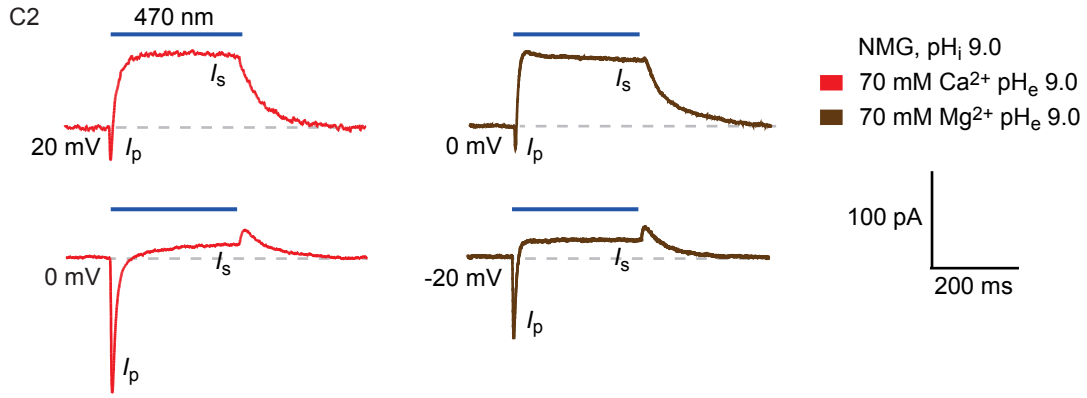

Figure 5.19.: Different selectivities of peak current I_p and stationary current I_s of C2. At specific electrochemical gradients I_p and I_s have opposite signs. This feature is most obvious at internal and external pH 9.0.

(Figure 5.20A, orange arrow 2). For C1V1 and C2 L132C T159C current inhibition by external Mg^{2+} is less pronounced, but apparent. In contrast, reversal potentials of C2 and C1V1 increase with the Mg^{2+} concentration indicating Mg^{2+} transport (Figure 5.20A, grey and brown arrows/3 and Figure 5.20C, orange circle/3). In C2 L132C T159C the external Mg^{2+} concentration does not influence reversal potentials. This finding might be explained in two different ways. Either the Mg^{2+} selectivity of C2 L132C T159C is very low and thus Mg^{2+} is not transported by the double mutant, or Mg^{2+} transport saturates at low Mg^{2+} concentrations due to strong binding. The second explanation is strengthened by the relatively high C2 L132C T159C currents, even at 2 mM Mg^{2+}. In summary, Mg^{2+} is transported by different ChR variants, but high external Mg^{2+} concentrations have an inhibitory effect. The role of Mg^{2+} will be further discussed based on the results from the model calculations.

In the following, the influence of external Ca^{2+} was investigated. Figure 5.21 compares current traces of C2, C1V1 and C2 L132C T159C at standard conditions (high Na^+, pH_e 7.2, black lines) to recordings at high Ca^{2+}, pH_e 9.0 (red lines). At standard conditions the three ChR variants differ in their respective amount of inactivation and their kinetic parameters. While C2 shows high inactivation (72 %) and fast off-kinetics (17 ms), C2 L132C T159C inactivates less (only 2 % at high light intensities) and is strongly decelerated (244 ms) [87]. Current sizes at high Ca^{2+}, pH_e 9.0 differ significantly between the constructs. Whereas relative C2 currents are low for both I_0 and I_s, C1V1 exhibits high Ca^{2+}-driven currents, especially for I_0. Moreover, stationary current levels are comparable in size between C1V1 and C2 L132C T159C. Notably, both C2 and C1V1 currents change their direction upon application of positive voltages. On the other hand, C2 L132C T159C displays only inward currents at all tested voltages reflecting positively shifted reversal potentials. IV relationships at three different Ca^{2+} concentrations are depicted in Figure 5.22A. For all presented ChRs inward directed currents increase with increasing external Ca^{2+} (Figure 5.22B). Similarly, reversal potentials increase when the Ca^{2+} concentration is augmented. Nevertheless, some subtle differences are apparent between the ChR variants. In general, Ca^{2+}-mediated inward currents are small in C2

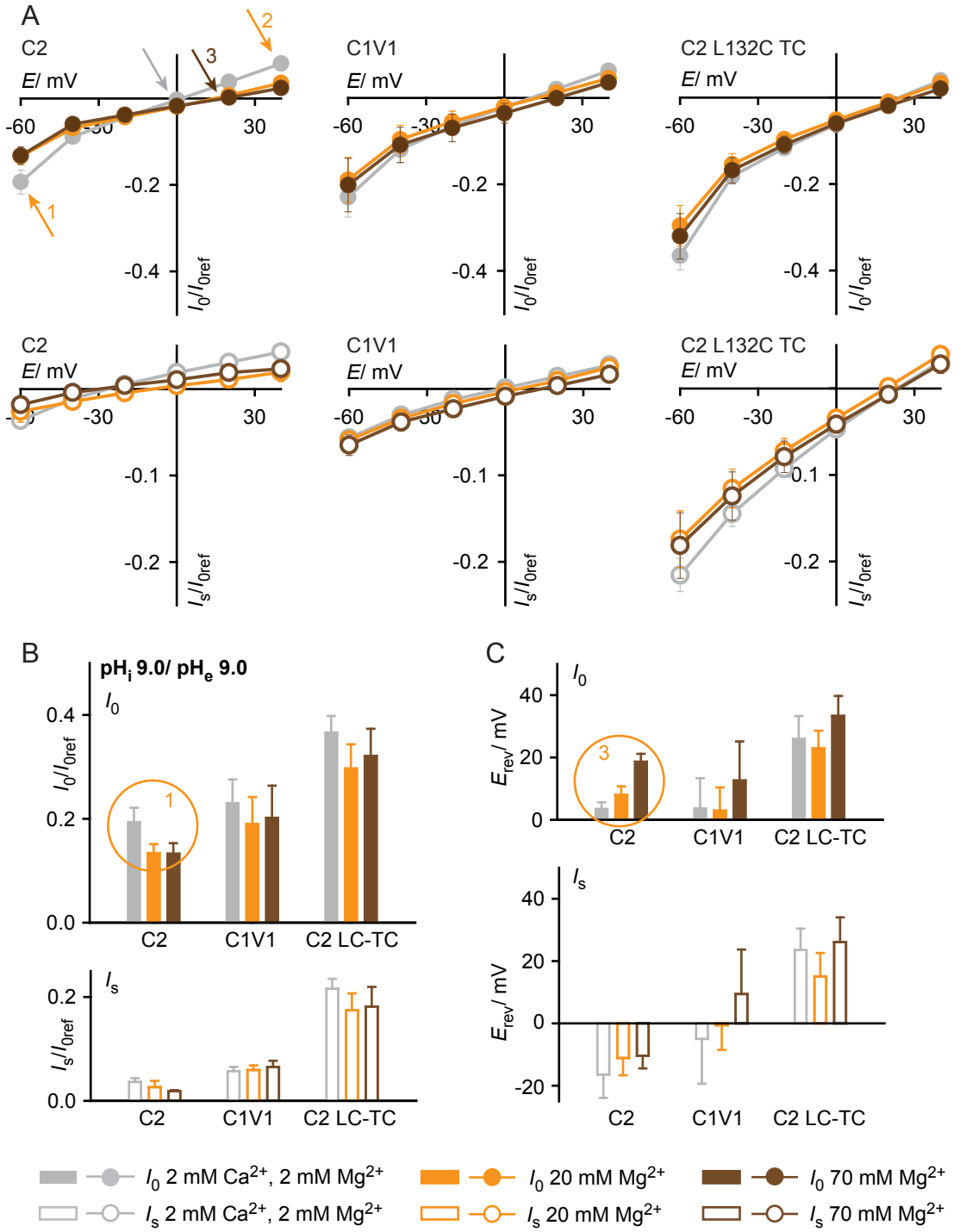

Figure 5.20.: Quantification of Mg^{2+} conductance of C2, C1V1 A and C2 L132C TC. Filled symbols represent initial currents I_0 and open symbols reflect stationary currents I_s. **A** Current-voltage relationssships at three different external Mg^{2+} concentrations. Orange arrows indicate current decrease upon increase in Mg^{2+} concentration. Grey and brown arrows point at the respective reversal potentials. **B** and **C** Average current amplitudes at −60 mV and reversal potentials for all constructs and conditions. The orange circle 1 exemplifies current reduction at −60 mV and the orange circle 3 indicates increasing reversal potentials. Based on the consistency between pre- and postcontrol the three to four best cells were chosen for each ChR. Reversal potentials were only determined for these cells.

and higher in C1V1 and C2 L132C T159C (Figure 5.22A, B). This goes along with less positive reversal potentials in C2, most obvious for I_s (Figure 5.22C). At 2 mM Ca^{2+}

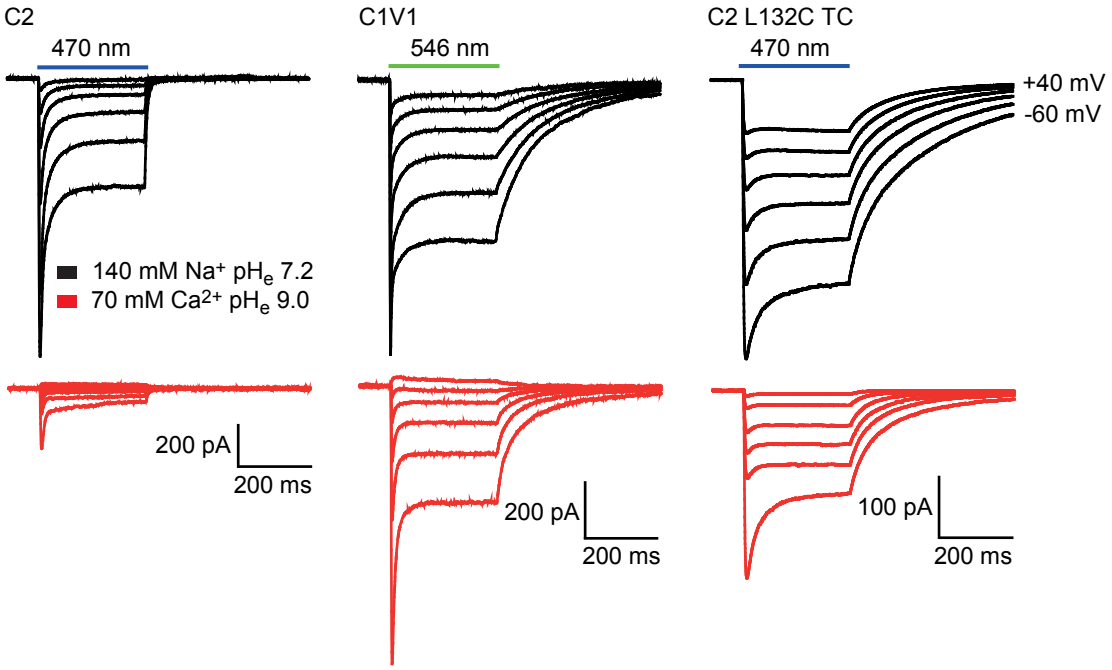

Figure 5.21.: Representative current traces of C2, C1V1 A and C2 L132C TC at 140 mM NMG, pH_i 9.0. The voltage was varied from −60 mV to 40 mV in 20 mV steps. Black traces show currents at high Na^+, pH_e 7.2 and red traces correspond to Ca^{2+}, pH_e 9.0.

C1V1 currents are similar to the C2 currents. But, C1V1 current amplitudes show a strong dependency on the external Ca^{2+} concentration (Figure 5.22B). When the external Ca^{2+} concentration is elevated from 2 mM to 70 mM, I_0 amplitudes increase by a factor of 3.4 for C1V1 and only by 1.9 for both other variants (−60 mV). Likewise, I_s amplitudes rise by a factor of 5.2, 2.1 and 1.6 for C1V1, C2 and C2 L132C T159C, respectively. C2 L132C T159C shows high current amplitudes even at low Ca^{2+} concentrations. In addition, reversal potentials are highest in C2 L132C T159C at all tested conditions. This might be explained by a strong Ca^{2+} transport even at low concentrations similar to the finding of a strong Mg^{2+} binding of the double mutant. An inhibitory effect of Ca^{2+} on transport of other ions, as was observed for Mg^{2+}, was not observed. The model calculations will give further insight into Ca^{2+} and Mg^{2+} transport of the three examined ChR variants.

5.2.5. Enzyme-kinetic model

For quantification of ion transport and competition a general enzyme-kinetic model was applied [230, 100]. This model considers the ChR molecule as an enzyme that reversibly binds substrates and can switch its orientation from the extracellular side to the intracellular side, thereby transporting the substrate (Figure 5.24A). The empty binding site reorientates depending on its apparent charge and the applied electrochemical gradient. The rate constants of empty binding-site reorientation are directly voltage-dependent by the following relationsship:

$$k_{ec} = k^0_{ec}\exp\left(\frac{z_E u}{2}\right),\ k_{ce} = k^0_{ce}\exp\left(\frac{-z_E u}{2}\right), \tag{5.1}$$

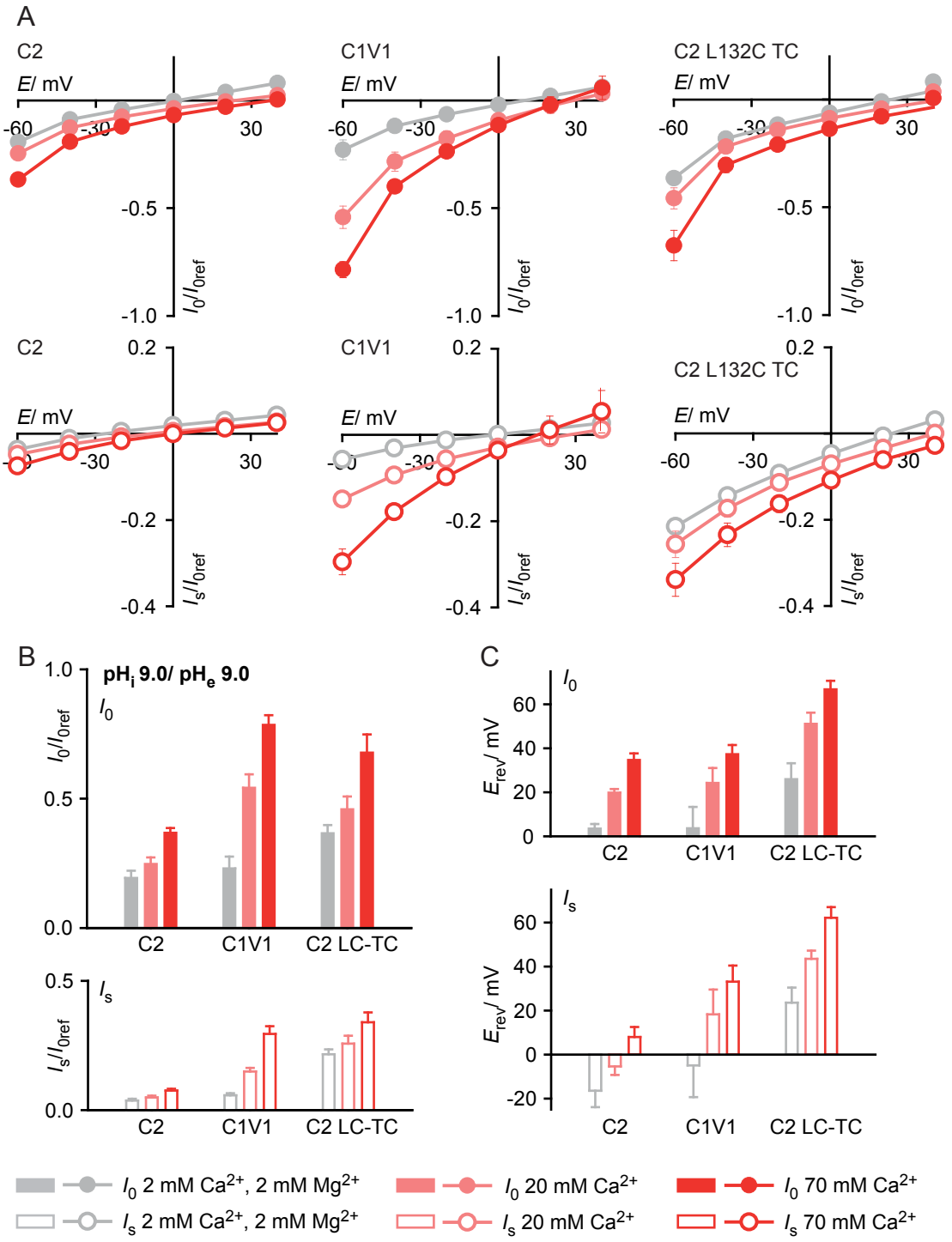

Figure 5.22.: Quantification of Ca^{2+} conductance of C2, C1V1 A and C2 L132C TC. Filled symbols represent initial currents I_0 and open symbols reflect stationary currents I_s. **A** Current-voltage relationsships at three different external Ca^{2+} concentrations. **B** and **C** Average current amplitudes at −60 mV and reversal potentials for all constructs and conditions. Based on the consistency between pre- and postcontrol the three to four best cells were chosen for each ChR. Reversal potentials were only determined for these cells.

with the reduced voltage u being $u = EF/RT$. k^0_{ec} and k^0_{ce} reflect the rate constants at $u = 0$ and z_E is the apparent charge number of the empty binding site. Here, only external substrate concentrations are considered. This allows unification of reversible

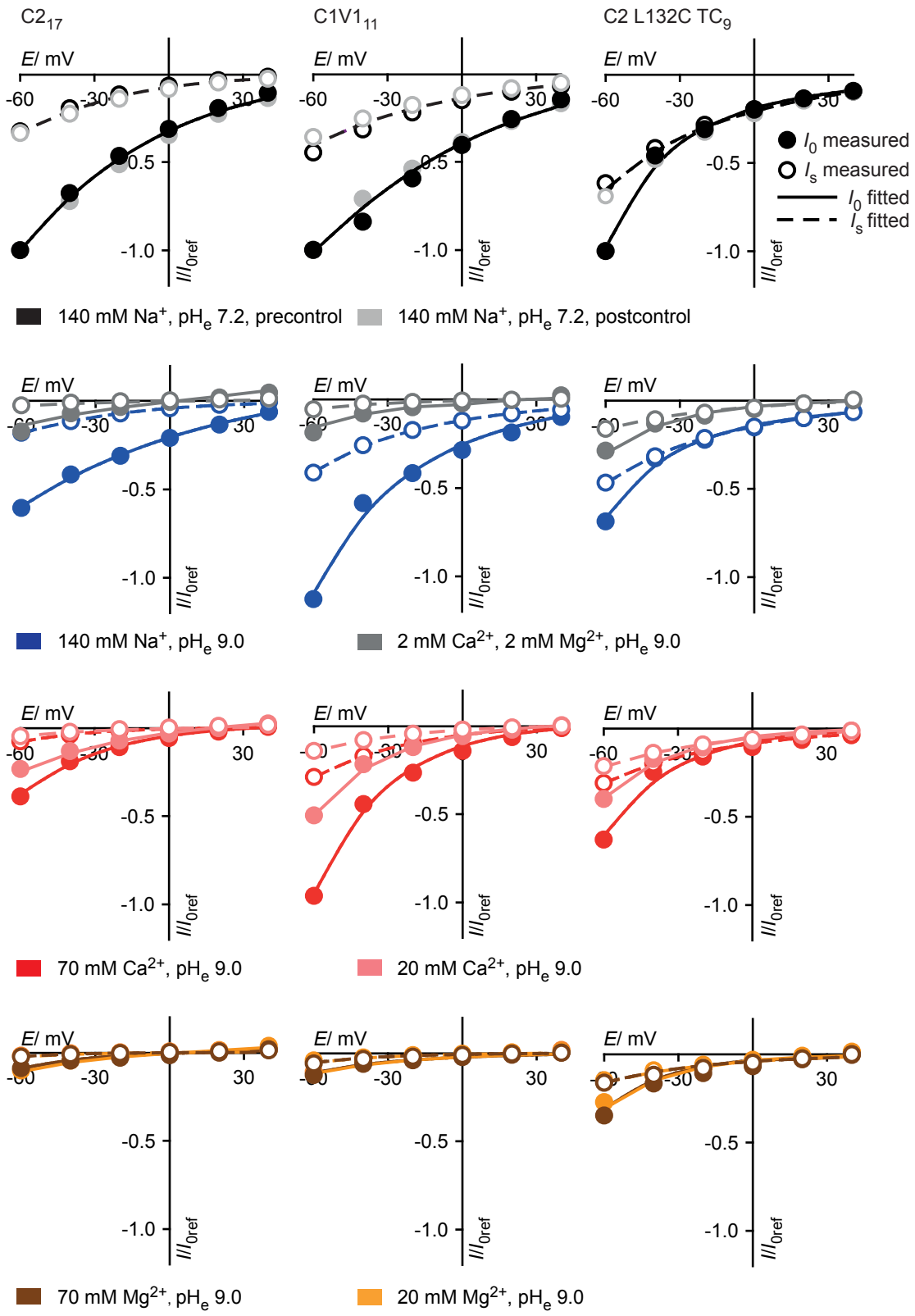

Figure 5.23.: Current-voltage relationships for selected cells expressing C2, C1V1 and C2 L132C TC. Internal solution was NMG, pH$_i$ 9.0. Solid circles represent measured initial currents I_0 and open symbols reflect stationary currents I_s. Solid and dashed lines correspond to the fitted curves using the enzyme-kinetic algorithm.

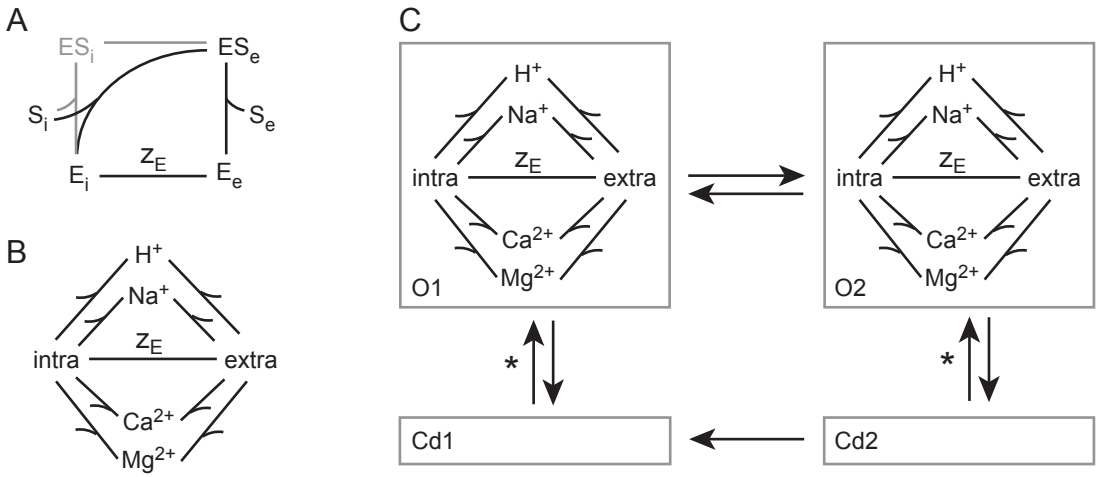

Figure 5.24.: Details of enzyme-kinetic model [229]. **A** Reaction scheme for binding of an ionic substrate S to a binding site E characterized by an apparent charge number z_{E}. Reorientation of ES results in effective ion translocation. Grey lines depict an explicit four-state model. Here, only external substrate concentrations are varied resulting in a simplified three-state model (black lines). **B** Corresponding reaction scheme considering external changes of protons, Na^+, Mg^{2+} and Ca^{2+}. The four substrates compete for binding and transport. **C** After prolonged illumination, ChRs adopt two different open conformations, the open states O1 and O2. Consequently, two distinct reaction schemes are present.

reorientation as well as cytoplasmic binding and debinding into one reversible step [229]. Hence, the number of free parameters per substrate is reduced by two. Cation transport is thus modeled by two reversible transport steps - the first reflecting substrate binding at the extracellular site and the second reflecting reorientation and cytoplasmic debinding - whereas the reduced voltage u is divided by the voltage-partioning coefficient d. Rate constants of cation transport and the voltage-partioning coefficient are iteratively determined using the following equations:

$$k_{cS} = k^0_{cS}\,[S]_c \exp\left(\frac{d(z_E + z_S)u}{2}\right), \tag{5.2}$$

$$k_{Sc} = k^0_{Sc} \exp\left(\frac{-d(z_E + z_S)u}{2}\right), \tag{5.3}$$

$$k_{Se} = k^0_{Se} \exp\left(\frac{(1-d)(z_E + z_S)u}{2}\right), \tag{5.4}$$

$$k_{eS} = k^0_{eS}\,[S]_e \exp\left(\frac{(d-1)(z_E + z_S)u}{2}\right). \tag{5.5}$$

The voltage partitioning coefficient d (for the cytoplasmic barrier) is treated as voltage- and substrate-dependent,

$$d = \frac{k_{Se} + k_{eS}}{k_{Se} + k_{eS} + k_{Sc} + k_{cS}}. \tag{5.6}$$

The current model differs from earlier studies by two extentions [229]. First, it considers four different substrates (protons, Na^+, Mg^{2+} and Ca^{2+}) that compete for binding and transport (Figure 5.24B). Second, it is the first study that describes ion selectivity of both I_0 and I_{s}. Under the assumption of an electrophysiological cycle considering two open states O1 and O2 as well as two closed states Cd1 and Cd2 (see Figure 3.5C), the

initial current I_0 - resulting from activation of dark-adapted molecules - is only mediated by ChRs in the first open state O1. In contrast, the stationary current I_s is composed of conductances of ChR molecules in both open states O1 and O2. The relative portion of molecules in either state thereby influences the overall selectivity of I_s. Consideration of two open states results in two distinct reaction schemes (Figure 5.24C). A detailed description of the model algorithm is found in the Appendix.

Current-voltage relationsships at seven extracellular conditions were used for the model calculations. Based on the consistency between pre- and postcontrol at standard conditions, three to four complete datasets were chosen for C2, C1V1 and C2 L132C T159C. The algorithm was independently applied to each dataset, yielding a set of kinetic parameters for each analyzed cell. Three tables summarizing all parameters can be found in the Appendix (Tables A.5, A.6 and A.7). Figure 5.23 depicts IV plots of three selected cells at all analyzed conditions. Measured datapoints (circles) are in good agreement with the model-retrieved curves (solid and dashed lines) supporting the choice of the model to sufficiently describe the data [229]. Black and grey symbols in the upper row reflect pre- and postcontrol. Since Mg^{2+} and Ca^{2+} measurements have been described in detail on the previous pages, only measurements in the presence of Na^+ and protons will be discussed here. At high Na^+, pH_e 7.2 I_0 currents exhibit similar IV courses for C2, C1V1 and C2 L132C T159C. In contrast, stationary currents are small for C2 and intermediate in size for C1V1. C2 L132C T159C displays little inactivation and I_0 and I_s are equal in size at $-20\,\mathrm{mV}$ and higher voltages. Elevation of extracellular pH to 9.0, thus taking away extracellular protons, decreases current sizes of C2 and C2 L132C T159C whereas shapes of IV curves are rather unaltered (Figure 5.23: blue symbols in second row). In C1V1 the effect is different. At most voltages I_s and I_0 are unaltered between pH_e 9.0 and pH_e 7.2. Moreover, at negative voltages I_0 amplitudes increase in the abscence of external protons suggesting inhibition of Na^+-mediated currents by protons. As described for Mg^{2+} and Ca^{2+} before, reversal potentials at the tested Na^+ and proton concentrations are lowest for C2 and highest for C2 L132C T159C.

Kinetic parameters allow for the dissection of inward currents into the contribution of different cations. The relative contribution depends on the applied electrochemical gradient, thus the membrane voltage and the external and internal ion concentrations, and differs for I_0 and I_s. Figure 5.25 depicts the ion contribution to I_0 and I_s at two different experimental conditions and application of $-60\,\mathrm{mV}$. The slender left bars represent I_0 that is only mediated by conductance through O1. The broader right bars reflects I_s being constituted by conductances of both O1 (dark color) and O2 (light color). Ion selectivity slightly differs between O1 and O2 and their portions do not only depend on the electrochemical gradient, but also on other experimental parameters such as the intensity of the actinic light. Since the internal solution contained NMG, pH_e 9.0 and the applied voltage was $-60\,\mathrm{mV}$ there was a high driving force for inward-directed ion transport. Moreover, the chosen conditions are far from thermodynamic equilibrium [229].

Of the three ChRs tested, C2 shows the highest degree of inactivation and inactivation

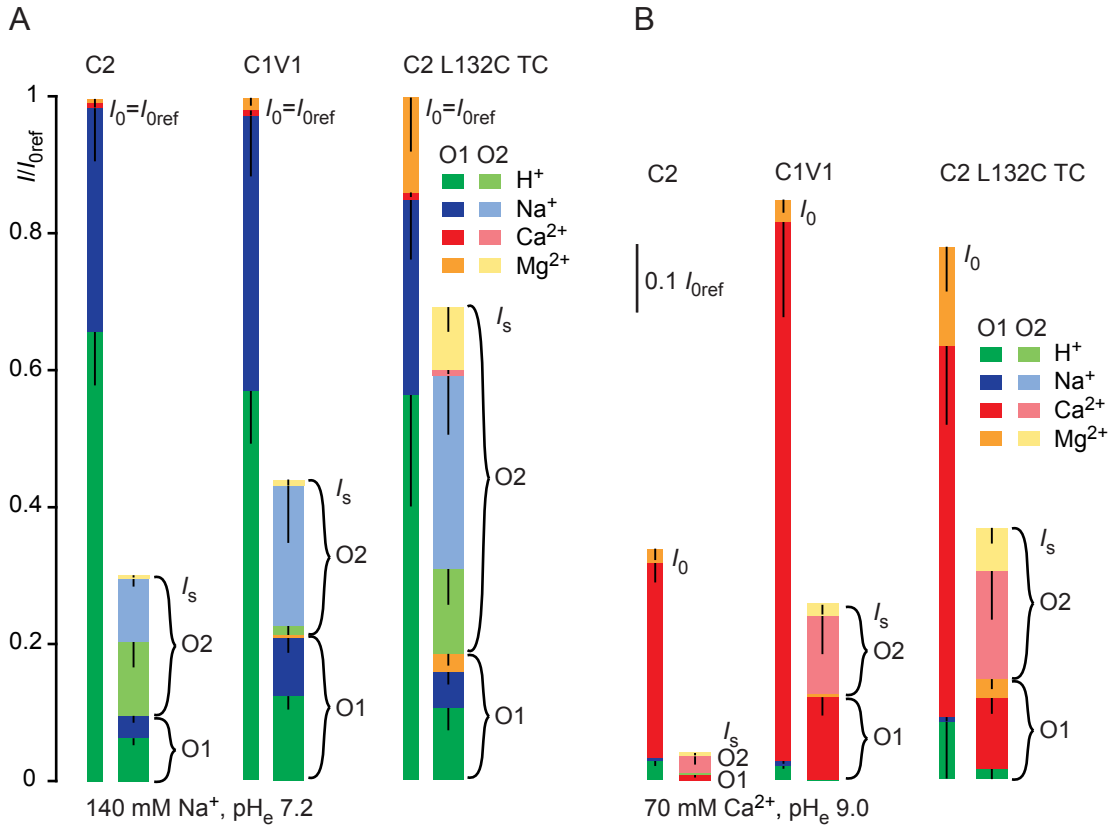

Figure 5.25.: Dissection of inward currents into contribution of different competing ion species for C2, C1V1 and C2 L132C TC. Internal solution was NMG, pH_i 9.0 and external solutions were 140 mM Na^+, pH_e 7.2 (**A**) and 70 mM Ca^{2+}, pH_e 9.0 (**B**). Slender bars in dark color represent initial currents I_0 that are only constituted by O1 conductance. Broad bars depict stationary currents I_s being composed of both O1 (dark color) and O2 (light color) conductance. Vertical solid lines represent standard errors of individual partial currents.

is strongly reduced for C2 L132C T159C. This may at least partially be explained by the high contribution of O2 to the stationary current in C2 L132C T159C. Notably, the double mutant shows considerably high Mg^{2+} influx (yellow and orange bars in Figure 5.25) even at low external Mg^{2+} concentration. At Na^+, pH_e 7.2 (Figure 5.25A) currents are mostly constituted by protons and Na^+. Interestingly, at this specific condition I_s exhibits a higher relative Na^+ conductance than I_0. The partial Na^+ contributions to I_0 are 33 %, 40 % and 29 % and the corresponding contributions to I_s are 40 %, 65 % and 48 % for C2, C1V1 and C2 L132C T159C, respectively. This increase is caused by a higher relative Na^+ conductance in the O2 state and goes along with a reduced relative proton conductance. At high Ca^{2+}, pH_e 9.0 (Figure 5.25B) currents are mainly carried by Ca^{2+}. Whereas relative cation contributions are similar between the different ChRs, the total current sizes show different tendencies. In C2 Ca^{2+}-mediated currents are small and inactivation is high (86 %). In the presence of high Ca^{2+} concentrations C1V1 displays high total current amplitudes, especially for I_0, that are only reduced by 15 % when compared to currents at high protons and high Na^+. Moreover, relative calcium contributions are highest in C1V1 for both I_0 (93 %) and I_s (89 %). C2 L132C T159C is also characterized by high Ca^{2+}-mediated currents, but inversely to C1V1 this effect is most pronounced for I_s. Therefore, C1V1 is best suited whenever short Ca^{2+}

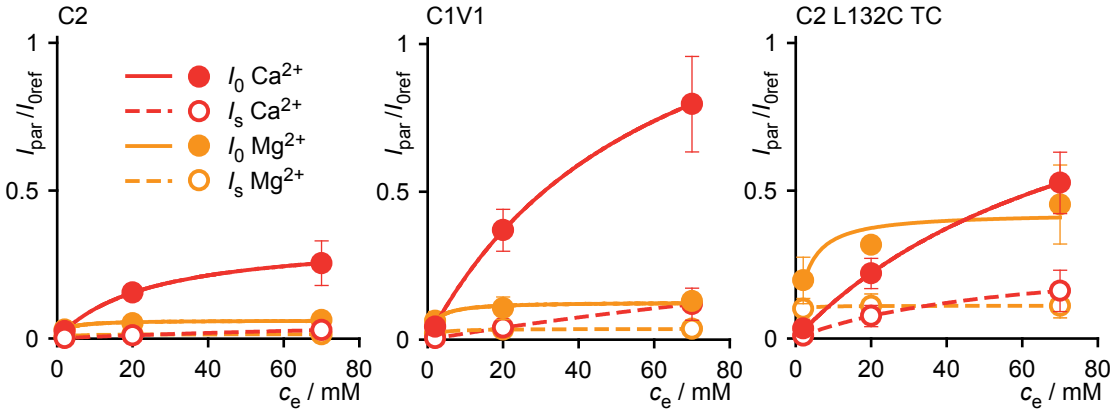

Figure 5.26.: Titration of partial currents I_{par} at different external Ca^{2+} and Mg^{2+} concentrations. Partial currents were calculated from $I(E)$ relationsships and plotted against the respective substrate concentration. Solid circles represent initial currents I_0 and open symbols reflect stationary currents I_s. Lines depict fits based on Michaelis-Menten kinetics.

influx is required whereas C2 L132C T159C provides the highest Ca^{2+} currents following long-term activation.

Next, the dependency of partial currents on the respective substrate concentration was explicitly evaluated for Ca^{2+} and Mg^{2+} (Figure 5.26). Current-substrate relationsships follow Michaelis-Menten kinetics (dashed and solid lines) supporting the enzyme-kinetic model. I_{max} and K_M values determined by application of the Michealis-Menten equation are summarized in Table 5.4. Some general conclusions can be drawn from the Ca^{2+} and Mg^{2+} titration. First, I_{max} values are higher for Ca^{2+} than for Mg^{2+} yielding higher partial Ca^{2+} currents at saturating Ca^{2+} concentrations. Second, half-saturating Mg^{2+} concentrations (K_M values) are lower than the corresponding Ca^{2+} concentrations suggesting stronger binding of external Mg^{2+}. Third, initial currents are characterized by higher I_{max} values, but not necessarily by stronger substrate binding. When comparing C2, C1V1 and C2 L132C T159C the following conclusions can be drawn. C2 displays the

	Ca^{2+} titration			
	initial current I_0		stationary current I_s	
	I_{max0}/ $\%I_{0ref}$	K_{M0}/ mM	I_{maxs}/ $\%I_{0ref}$	K_{Ms}/ mM
C2	34 ± 1	25 ± 1	9.3 ± 0.2	161 ± 5
C1V1	149 ± 4	61 ± 3	58 ± 2	270 ± 10
C2 L132C T159C	117 ± 9	90 ± 10	29 ± 1	57 ± 3

	Mg^{2+} titration			
	initial current I_0		stationary current I_s	
	I_{max0}/ $\%I_{0ref}$	K_{M0}/ mM	I_{maxs}/ $\%I_{0ref}$	K_{Ms}/ mM
C2	6.1 ± 0.4	2.3 ± 0.9	1.44 ± 0.02	2.4 ± 0.2
C1V1	13 ± 1	2.1 ± 0.9	3.66 ± 0.01	1.75 ± 0.01
C2 L132C T159C	43 ± 7	3 ± 2	11.1 ± 0.1	0.21 ± 0.01

Table 5.4.: Parameters of Ca^{2+} and Mg^{2+} titration gained by fitting to the Michaelis-Menten equation. I_{max}/I_{ref} represents the maximal amplitude of the partial current and K_M/ mM corresponds to the half-saturating substrate concentration.

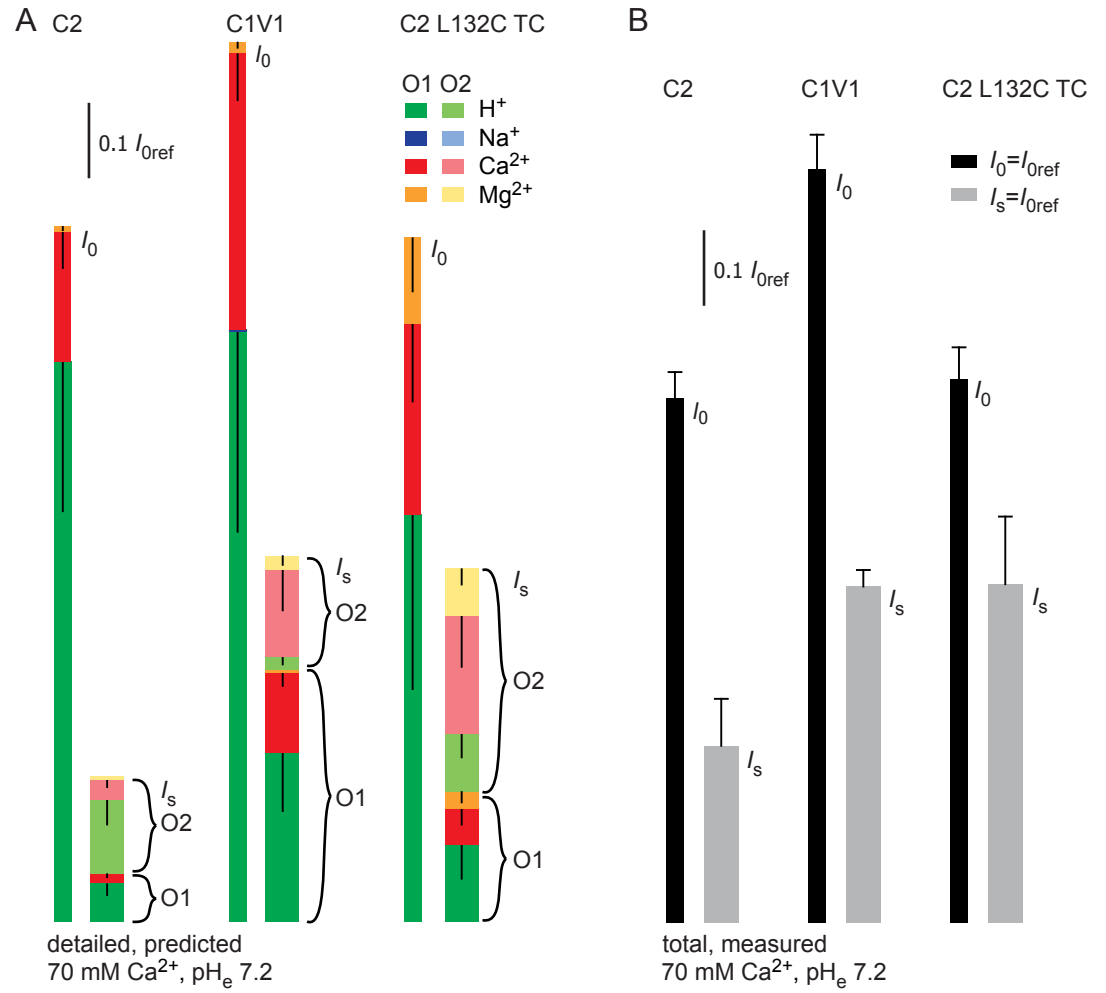

Figure 5.27.: Comparison of model-based current prediction to experimental values for C2, C1V1 and C2 L132C TC. **A** Predicted contribution of different ion species to I_0 and I_s at −60 mV, calculated for an internal solution of NMG, pH_i 9.0 and an external solution of 70 mM Ca^{2+}, pH_e 7.2. Slender bars in dark color represent initial currents I_0 that are only constituted by O1 conductance and broad bars depict stationary currents I_s being composed of both O1 (dark color) and O2 (light color) conductance. Vertical solid lines represent standard errors of individual partial currents. (**B**) Experimental confirmation of the total current amplitudes under the same conditions.

lowest maximal partial currents for both Ca^{2+} and Mg^{2+} indicating slow transport even at high concentrations of divalent cations. I_{max} values for Ca^{2+} transport are highest in C1V1, but these transport rates are only reached at unlikely high Ca^{2+} concentrations. In contrast, I_{max} values for Mg^{2+} transport can be reached at physiological Mg^{2+} concentrations. C2 L132C T159C exhibits highest maximal Mg^{2+} currents (I_{max} values). These are apparent even at low Mg^{2+} concentrations and when other competing ions are present (see Figure 5.25 and 5.27). Therefore, Mg^{2+} influx should be taken into account whenever C2 L132C T159C is used. Taken together, Ca^{2+} and Mg^{2+} differ in their respective binding and transport rates and should be treated as independent substrates [229].

The so-far presented partial currents were based on experimental data at the corresponding conditions. However, the enzyme-kinetic algorithm also allows for determination of current contributions at conditions that were not experimentally tested. Here,

current sizes and contributions at −60 mV were calculated for high Ca^{2+}, pH_e 7.2 (Figure 5.27A). At this condition protons and Ca^{2+} compete for inward transport. Initial currents are mainly mediated by protons with relative contributions of 80 %, 67 % and 59 % for C2, C1V1 and C2 L132C T159C. C1V1 and C2 L132C T159C also display considerable contributions of Ca^{2+} (32 % and 28 %). Interestingly, total currents of C1V1 at high Ca^{2+}, pH_e 7.2 are higher (117 %) than at high Na^+, pH_e 7.2 (100 %, compare Figure 5.25A to Figure 5.27A). The increased current is due to higher proton currents whereas partial Na^+ and Ca^{2+}-mediated currents are equal in size. This indicates a higher inhibition of proton currents by Na^+ than by Ca^{2+} in C1V1. The relative stationary currents at high Ca^{2+}, pH_e 7.2 are more than twice as high in C1V1 and C2 L123C T159C than in C2. In both variants I_s is mediated to a high extent by Ca^{2+} (50 % and 42 %). Therefore, both C1V1 and C2 L132C T159C are well suited for a sustained Ca^{2+} influx even in competition with external protons.

In the following, the predicted current sizes at high Ca^{2+}, pH_e 7.2 were experimentally verified (Figure 5.27B). Amplitudes of I_0 and I_s coincide well with the corresponding amplitudes predicted by the model. Also, differences between the tested ChR variants could be experimentally reproduced. In conclusion, the model is appropriate to predict current sizes and current contributions at untested experimental conditions. It should be applied to estimate cation influx prior to experiments and to avoid time-consuming ion selectivity experiments. Furthermore, the model allows a more detailed insight into general aspects of ion selectivity as well as variant-specific characteristics of ion competition.

One additional aspect will be analyzed here. In the case of competing Na^+ and protons, the model calculations yield higher proton contributions to I_0 than to I_s (Figure 5.25A). Inversely, Na^+ contributions to I_s exceed its contributions to I_0. The elevated Na^+ contribution to I_s is most pronounced in C1V1, where 65 % of I_s is mediated by Na^+ compared to 40 % for I_0. Accordingly, only 31 % of I_s current reflects proton transport in C1V1 at high Na^+, pH_e 7.2. Although less pronounced the tendency of reduced proton transport for I_s is also apparent in C2 and Catch+. At first glance, these findings seem to contradict the proposed "progressive proton selectivity" in time that was proposed for C2 by Berndt and Prigge *et al.* [86]. But, the earlier study was based on reversal potentials thus conditions close to thermodynamic equilibrium. In contrast, the current calculations were performed for high chemical gradients and a membrane voltage of −60 mV thereby representing conditions with a high driving force for inward cation transport. In order to understand the discrepancy $I(E)$ relationsships for C2 were measured at high external Na^+. Moreover, two external and two internal pH values (pH 7.2 and pH 9.0) were tested and reversal potentials were determined. Figure 5.28A, B illustrates the C2 $I(E)$ plot at pH_i 7.2 and two external pH. Reversal potentials for I_0 (filled circles in A) and I_s (open circles in B) are indicated by arrows. When the extracellular proton concentration is increased from pH_e 9.0 to pH_e 7.2 reversal potentials shift to more positive values as indicated by horizontal grey bars in Figure 5.28 A and B. The shift in reversal potentials (δE_{rev}) is significantly higher for I_s than I_0 at pH_i 7.2 (Figure 5.28C). This implies a

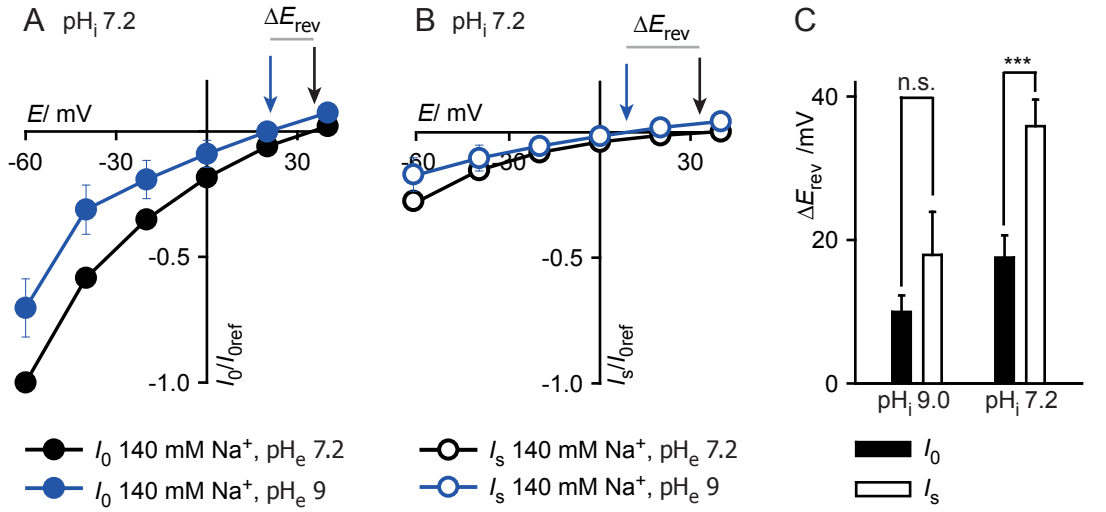

Figure 5.28.: Determination of proton selectivity of initial and stationary currents for C2. Filled circles and bars correspond to I_0 and open symbols reflect I_s. **A** and **B** $I(E)$ plots at pH_i 7.2 and varying external pH. Arrows indicate reversal potentials E_{rev} and grey bars shifts in E_{rev} when the external pH is reduced from pH 9.0 to pH 7.2. **C** Quantification of shift in E_{rev} between pH_e 9.0 and pH_e 7.2 at two internal pH. At pH_i 7.2 the shift is significally higher for I_s than for I_0.

higher proton selectivity of I_s and reproduces the results of Berndt and Prigge [86]. Thus, selectivities determined from reversal potentials differ from cation influx at high electrochemical driving forces where ion competition plays a more important role. Since living cells maintain membrane potentials far from equilibrium, reversal potentials may not be ideal to evaluate cation flux in ChRs. The here presented model presents an alternative way for the evaluation of ion selectivity and ion competition.

5.3. Optogenetic targeting of presynaptic vesicles

This section deals with the design and characterization of an optogenetic tool that enables synaptic vesicle acidification with light. The targeting strategy is based on synaptic proteins fused to different microbial rhodopsins and fluorescent indicators. The resulting fusion proteins were tested for functionality in HEK cells and hippocampal neurons. Moreover, the most promising construct was used to analyze some basic properties of presynaptic vesicle filling and fill-state dependent synaptic transmission.

All experiments presented in this section were planned and performed in close cooperation with Dr. Benjamin Rost (Charité Berlin). In most cases, datasets originate from both experimentators with equal contributions.

5.3.1. Construct design

In order to manipulate membrane potential and intravesicular pH of presynaptic vesicles by light, several constructs were created. All fusion proteins are based on the vesicular pH indicator Syphy [156, 172] which consists of the first three helices of synaptophysin followed by a pH-sensitive GFP derivative (superecliptic pHluorin) and is completed by the last helix of synaptophysin (as introduced in Figure 3.7). This arrangement places the pHluorin in the lumen of the vesicle and allows for intravesicular pH imaging.

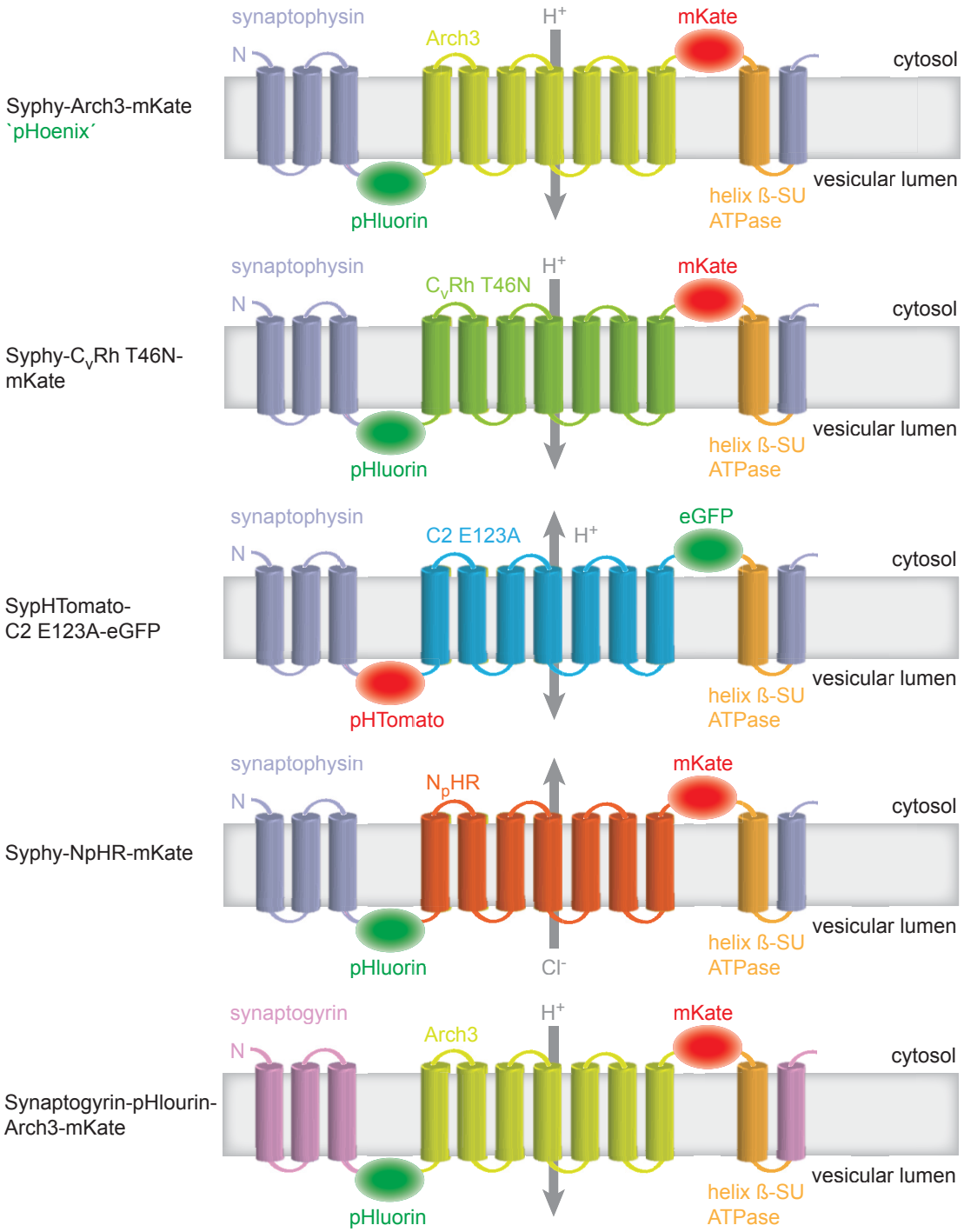

Figure 5.29.: Protein design of optogenetic actuators targeting presynaptic vesicles. All fusion proteins are based on the synaptic pH indicator Syphy [156, 172] which is coupled to the respective microbial rhodopsin. Arch3 and C_vRh T46N are used to pump protons into synaptic vesicles, C2 E123A TC to conduct protons in both directions and N_pHR to pump Cl^- out of vesicles. An additional intracellular fluorescent protein serves as pH-insensitive expression marker. In order to complete the synaptophysin an additional helix was introduced [208, 209, 210].

Here, the C-terminus of pHluorin was fused to the N-terminus of different microbial rhodopsins (Figure 5.29). Next, a second fluorescent protein was C-terminally added. This fluorescent marker can serve as a reference for expression levels and allows for ratiometric pH imaging as reported by others [180]. Moreover, it may enhance folding of

microbial rhodopsins and deliver the necessary flexibility of the protein [210]. Since wt ChRs exhibit large C-terminal intracellular domains, the fluorescent protein may mimic this structural element. To include the last helix of synaptophysin, an additional helix was necessary. Therefore, a helix of the rat gastric H^+, K^+-ATPase, that had been successfully used in combination with microbial rhodopsins in earlier studies [208, 209, 210], was placed after the second fluorescent protein. The fusion protein was terminated by the last helix of synaptophysin.

The following combinations of rhodopsins and fluorescent proteins were tested. First, the high-performing proton pumps Arch3 [151] and the C_vRh mutant C_vRh T46N [26] (personal communication of Suneel Kateriya, Satoshi Tsunoda and Arend Vogt) were used. In the context of the here presented fusion proteins proton pumps would potentially acidify vesicles. Fluorescent proteins were chosen such as the activating wavelength coincides with the excitation wavelength of the reference fluorescent protein whereas the pH-sensitive fluorescent protein could be independently activated. Thus, green-light activated proton pumps were combined with mKate2 and pHlourin. Syphy-Arch3-mKate2 was named "pHoenix" and this denomination will be used in the following. To reduce the pH gradient over the vesicular membrane the proton-selective C2 mutant E123A T159C was tested [100, 99]. The blue-light activated C2 mutant was combined with eGFP and the recently published red fluorescent pH-indicator pHTomato [161]. In order to distinguish between direct effects of membrane potential and effects of vesicular acidification, proton pumps were replaced by the light-activated chloride pump N_pHR [231, 70]. This arrangement should potentially alter the vesicular membrane voltage without affecting the intravesicular pH. Although N_pHR exhibits a red-shifted action spectrum compared to the proton pumps, N_pHR was fused to the same set of fluorescent proteins (mKate and pHluorin). Last, a pHoenix variant containing the nematode synaptogyrin as targeting protein was generated. Synaptogyrin-GFP fusions have been applied as synaptic marker in *C. elegans* [232]. Synaptogyrin-pHoenix is intended to be applied for light-driven vesicular acidification in *C. elegans*. Protein composition of all presented fusion proteins is displayed in Figure 5.29.

Proteins were expressed in HEK 293 cells and tested for functionality. For all constructs mKate or eGFP fluorescence was detectable, but fluorescence was mainly localized to internal membranes such as the endoplasmic reticulum (not shown). Current traces of four variants are depicted in Figure 5.30A indicating functionality of proton and chloride pumps. At symmetric buffer conditions and 0 mV light activation of pumps generates outward-directed proton currents or inward-directed chloride currents. In contrast, no photocurrents were detected for the C2-based protein. Quantification of maximal photocurrent amplitudes I_p yields very low values for all fusion proteins (Figure 5.30B). The amplitude reduction compared to untargeted proteins can be explained by the weak surface expression of the fusion proteins. C_vRh T46N-eGFP without targeting sequences served as a positive control for good membrane targeting and displays more than five-fold higher photocurrents than all pHoenix variants (Figure 5.30B).

Next, cultured hippocampal neurons were transduced with lentiviral particles deli-

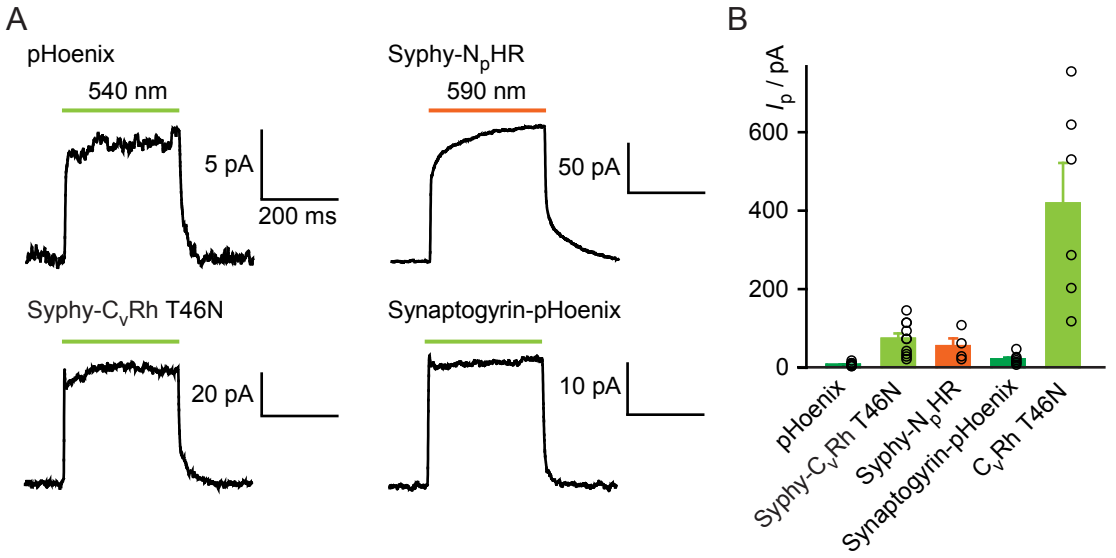

Figure 5.30.: Functionality test of fusion proteins in HEK 293 cells. **A** Current traces of pHoenix, Syphy-C_vRh T46N, Syphy-N_pHR and Synaptogyrin-pHoenix at 0 mV. Light application induces small positive currents that reflect proton-mediated outward currents in the case of the Arch3 and C_vRh-based proteins and Cl^--mediated inward currents for Syphy-N_pHR. **B** Peak current amplitudes of tested fusion proteins. C_vRh T46N serves as a positive control without synaptic targeting sequences. The C2-based construct did not display any light-induced currents, hence it is not included.

vering the pHoenix or the Arch3-eGFP gene, respectively. Neurons were stained against the cytosolic MAP2 kinase and the vesicular glutamate transporter 1 by immunocytochemistry. Fixed neuronal samples were visualized by confocal laser-scanning microscopy. Figure 5.31 compares Arch3-eGFP expression patterns to pHoenix localization at two different magnifications. Arch exhibits strong expression in plasma membranes that is not restricted to synapses (shown in green). On the contrary, pHoenix expression level is lower and pHoenix colocalizes with the synaptic vGlut1 protein as indicated by the white arrows in the bottom row images of Figure 5.31. Nevertheless, pHoenix expression in plasma membranes apart from synapses cannot be excluded from the images.

5.3.2. Light-activated vesicle filling

Autaptic hippocampal neurons were used to study synaptic transmitter release. Therefore, hippocampal neurons were seeded on microglia islands at low concentrations yielding single neurons per island that form autaptic connections. Neurons were transduced with lentivirus encoding pHoenix, Syphy-C_vRh T146N-mKate and Syphy-N_pHR-mKate. Two weeks later the influence of light activation of microbial pumps on synaptic release was analyzed by whole-cell electrical recordings. Action potentials were triggered by depolarization every 0.2 Hz and the successive excitatory postsynaptic currents (EPSCs) in glutamatergic neurons were recorded. Figure 5.32A shows the effect of light activation of pHoenix on normalized EPSC amplitudes. Upon continuous illumination EPSC amplitudes gradually increase until reaching a stationary level. At the end of light application amplitudes have increased by $(11 \pm 2)\,\%$ while amplitudes of untransduced cells are unaffected by light (Figure 5.32B). Despite higher photocurrent levels in HEK cells (Figure 5.30B) Syphy-C_vRh T146N-mKate and Syphy-N_pHR-mKate activation does not

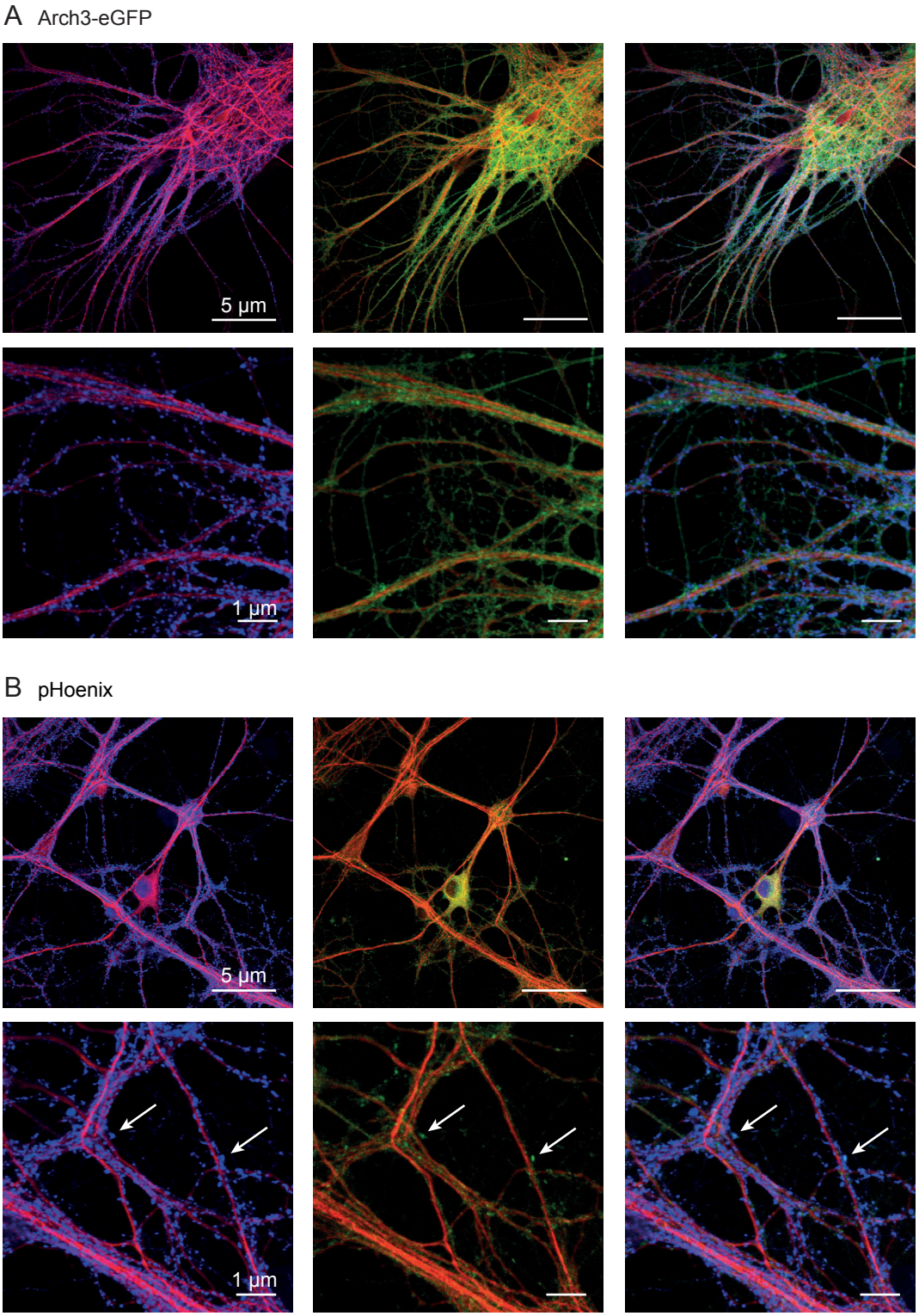

Figure 5.31.: Confocal images of fixated cultured neurons expressing Arch3-eGFP (**A**) or pHoenix (**B**). First and third row are overview images, while second and fourth row show additionally three-fold magnified dendrites. Neurons were stained against the vesicular glutamate transporter 1 (vGlut1) and the MAP2 kinase (MAP2K) by immunocytochemistry. Fluorescence of secondary antibodies was excited at 405 nm and 647 nm and fluorescence is shown here in blue (vGlut1) and red (MAP2K). eGFP and pHoenix fluorescence was excited at 488 nm and is presented here in light green. Left column shows VGlut1 and MAP2K and middle column depicts Arch3/phoenix and MAP2K localization. The last column combines all three channels. Arch3-eGFP fluorescence is brighter than pHoenix fluorescence and evenly distributes to all membranes. pHoenix is synaptically enriched and its fluorescence colocalizes with vGlut1 as indicated by the white arrows in the bottom row images. Scale bars correspond to 5 µm and 1 µm.

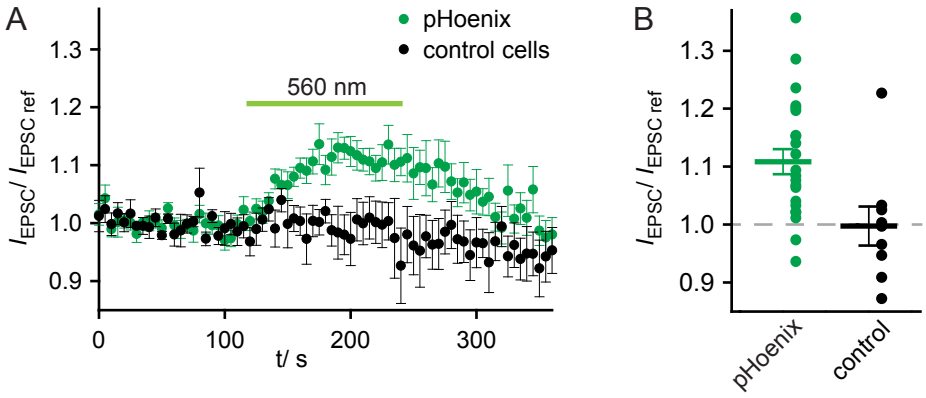

Figure 5.32.: Effect of pHoenix activation on EPSC amplitudes in glutamatergic neurons. Action potentials were triggered at 0.2 Hz. **A** Time-course of normalized EPSC amplitudes. EPSCs of pHoenix-expressing cells increase during continuous illumination (green symbols). Uninfected cells serve as a negative control and display unaltered EPSCs over time (black symbols). **B** Quantification of normalized EPSC amplitudes after 90 s to 115 s of illumination.

affect EPSC amplitudes (not shown). While these findings suggest unfunctionality of C_vRh in neurons as has been concluded from the abscence of somatic currents of untargeted C_vRh, the interpretation for N_pHR is more difficult and will be further discussed in section 6.3.3. Taken together, light-induced acidification of synaptic vesicles using pHoenix increases EPSC amplitudes of glutamatergic neurons. In contrast, EPSCs are unaffected by C_vRh and N_pHR activation.

Next, the effect of pHoenix activation on bafilomycin-treated neurons was investigated. Bafilomycin specifically inhibits V-Type ATPases [233, 234] and has been applied to block proton-transporting ATPases that acidify synaptic vesicles, thereby preventing neurotransmitter uptake [235, 236]. To deplete synaptic vesicles already filled with neurotransmitters, bafilomycin was applied for 2 h to 5 h prior to experiments. Figures 5.33A and B show the effect of pHoenix activation on the EPSCs of a glutamatergic, bafilomycin-treated neuron. While no EPSC is present at the beginning of illumination, application of green light for 2 min activates pHoenix, thereby rescueing EPSCs. In contrast, EPSC amplitudes of neurons expressing Arch-eGFP distributed over their plasmamembrane are not affected by green illumination (Figure 5.33B, C). These experiments support the idea that acidification of synaptic vesicles is necessary for vesicular neurotransmitter uptake in glutamatergic neurons. Next, EPSC amplitudes of untreated neurons were compared to pHoenix-rescued EPSCs of bafilomycin-treated neurons (Figure 5.33D, E). Amplitudes of rescued EPSCs do not significantly differ from those of untreated cells ($P = 0.53$) suggesting that continuous pHoenix activation in the light effectively compensates for ATPase inhibition. In the following, the influence of light intensity was further analyzed. Somatic currents of Arch-eGFP-expressing neurons are shown at three different light intensities in Figure 5.33F. Reduction of light intensity to 25 % ($\approx 600\,\mathrm{mWcm^{-2}}$) does not reduce current amplitudes of Arch3. Since pHoenix-driven somatic currents are hard to detect in neurons (Figure 5.33F), light dependence of somatic pHoenix currents was analyzed in HEK cells (Figure 5.33G). Again, current amplitudes are only slightly reduced at 25 % light intensity. Finally, pHoenix-mediated

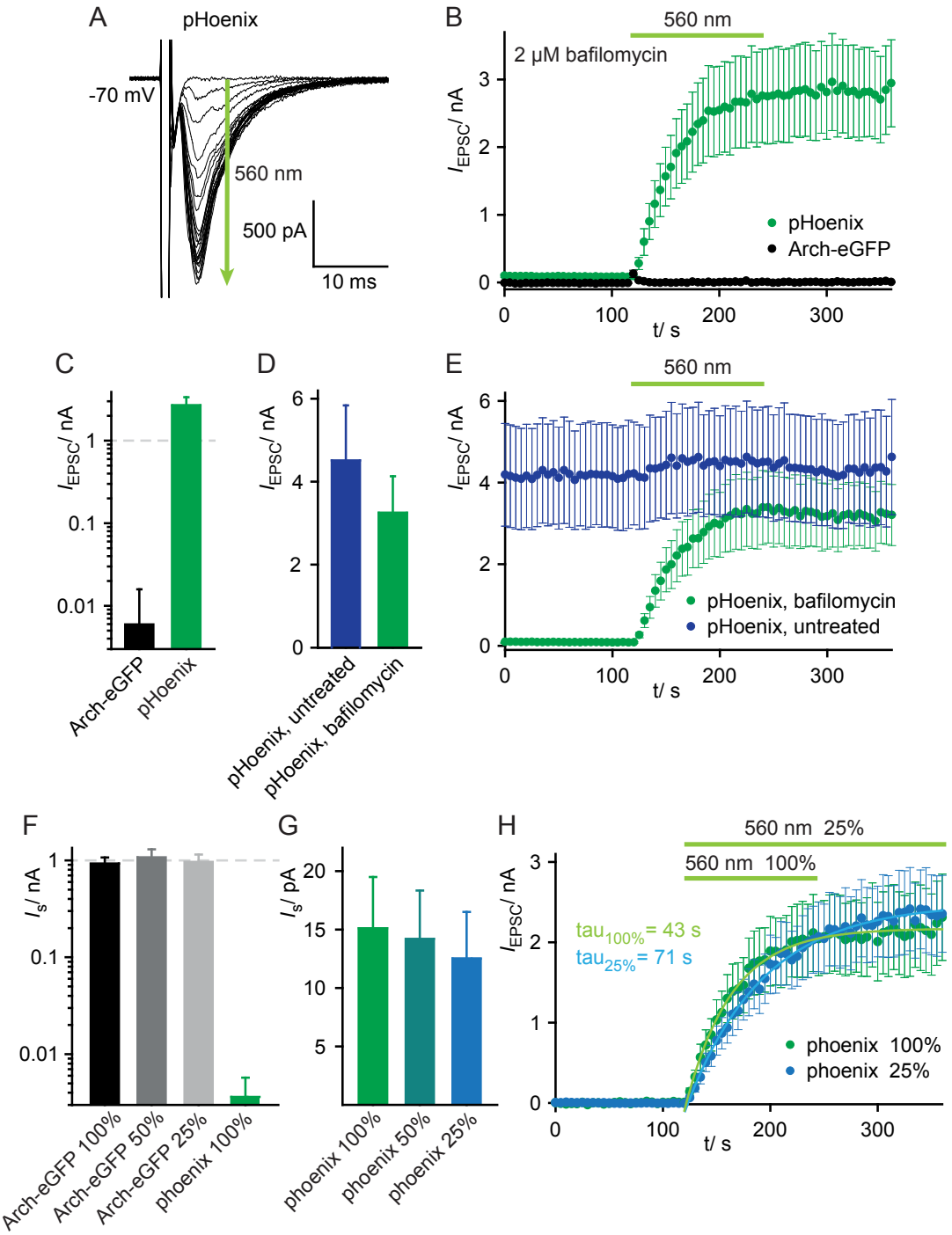

Figure 5.33.: pHoenix activation rescues EPSCs in glutamatergic, bafilomycin-treated neurons. Neurons were incubated with 1 µM bafilomycin for 2 h to 5 h prior to experiments. Action potentials were triggered at 0.2 Hz. **A** Current traces of pHoenix-expressing neuron during continuous illumination. At the beginning of light application, no EPSC is detectable. pHoenix activation gradually rescues EPSCs (green arrow). **B** Time-course of average EPSC amplitudes of pHoenix-expressing neurons vs Arch-eGFP-expressing cells. pHoenix and Arch were activated at 560 nm for 2 min. Arch activation does not rescue EPSCs. **C** Comparison of EPSC amplitudes after 90 s to 115 s of illumination for pHoenix- and Arch-expressing cells. Please note logarithmic scale (also in **F**). **D** and **E** After pHoenix activation for 2 min bafilomycin-treated cells exhibit EPSC amplitudes similar to the ones measured for non-treated cells. **D** depicts EPSC amplitudes after 90 s to 115 s of illumination and **E** shows corresponding time course. **F**, **G** and **H** Effect of light intensity on Arch and pHoenix activation. **F** Somatic currents of Arch and pHoenix in neurons. Arch-eGFP exhibits high currents that are uneffected by light intensity reduction to 25 %. pHoenix shows very low somatic currents. **G** Somatic currents of pHoenix in HEK293 cells. Amplitudes slightly decrease upon reduction of light intensity. **H** Time-course of EPSC amplitudes in pHoenix-expressing neurons that were activated at two different light intensities. Illumination at 25 % allowed for longer illumination without side effects. Kinetics of EPSC rescue were exponentially fitted with time constants of 43 ms and 71 ms for 100 % and 25 %, respectively.

EPSC rescue was compared at 100 % and 25 % light intensity (Figure 5.33H). In order to obtain time constants of EPSC-recovery kinetics, EPSCs were baseline-corrected for the period before illumination and curves were monoexponentially fitted from time points 120 s to 360 s. Notably, EPSC rescue is faster at 100 % light intensity (43 s) than at 25 % light intensity (71 s). Since EPSC amplitudes might not have reached their maximal value after illumination at 100 % for 60 s, the kinetic difference may at least partially be an artifact due to longer illumination time at 25 %. Most importantly, pHoenix activation at 25 % light intensity ($\approx 600\,\mathrm{mWcm^{-2}} \approx 1.7 \times 10^{22}$ photons $\mathrm{m^{-2}s^{-1}}$) seems sufficient to effectively rescue EPSCs in bafilomycin-treated neurons. Since reduction of light intensity prevents unwanted side effects such as heating, the following experiments used 25 % of activation light.

To further analyze the different filling states of synaptic vesicles, a protocol applying two consecutive intervals of green light was executed (30 s and 90 s, separated by 60 s), thereby rescueing EPSCs in bafilomycin-treated neurons. The time period between the two light applications is referred to as "intermediate" filling state and the minute following the second light application corresponds to the "full" state. At first, the time course of average EPSC amplitudes following the two-pulse protocol was recorded (Figure 5.34A). After the first light pulse, EPSC amplitudes remain constant at an intermediate level. Only during the second light pulse, EPSCs further increase until they reach a stationary level. Figure 5.34B, C quantifies changes in EPSC amplitudes for individual cells. All analyzed cells display increased EPSC amplitudes of the full state compared to the intermediate state resulting in an average increase by a factor of 2.5 ± 0.2. Second, the time course of the paired-pulse ratio (PPR) was investigated (Figure 5.34D, E, F). The PPR describes the ratio of amplitudes of two consecutive EPSCs and is an indirect measure for release probability. The PPRs exhibit a high variability, especially during the first light application when EPSCs are small (Figure 5.34D). Nevertheless, the temporal development of PPRS shows a trend. Out of twelve analyzed cells, nine exhibit a decreased PPR when comparing the full state to the intermediate state (Figure 5.34E). Also, the average PPR is decreased by (6.2 ± 2.8) % (Figure 5.34F) indicating a slightly higher release probability of the full state. More experiments will be necessary to validate this finding. Third, miniature excitatory postsynaptic currents (mEPSCs) reflecting spontaneous vesicle release were analyzed. Therefore, the two light-pulse protocol was applied to glutamatergic neurons without triggering of APs. Figure 5.34G displays exemplary current traces of the intermediate and the full state. Both traces show several events, representing mEPSCs. A characteristic mEPSC is presented in Figure 5.34H exhibiting the characteristic very fast onset in the submillisecond timescale and a slower off rate in the millisecond range. Next, mEPSC amplitude and frequency were compared between both states. All cells show higher average mEPSC amplitudes in the full state than in the intermediate state (Figure 5.34I). Moreover, mEPSC frequencies are enhanced for nine out of eleven analyzed cells (Figure 5.34J). When considering average changes mEPSC amplitudes and mEPSC frequencies are increased by factors of 1.32 ± 0.06 and 1.90 ± 0.28, respectively (Figure 5.34K). In summary, the full state displays higher EPSC

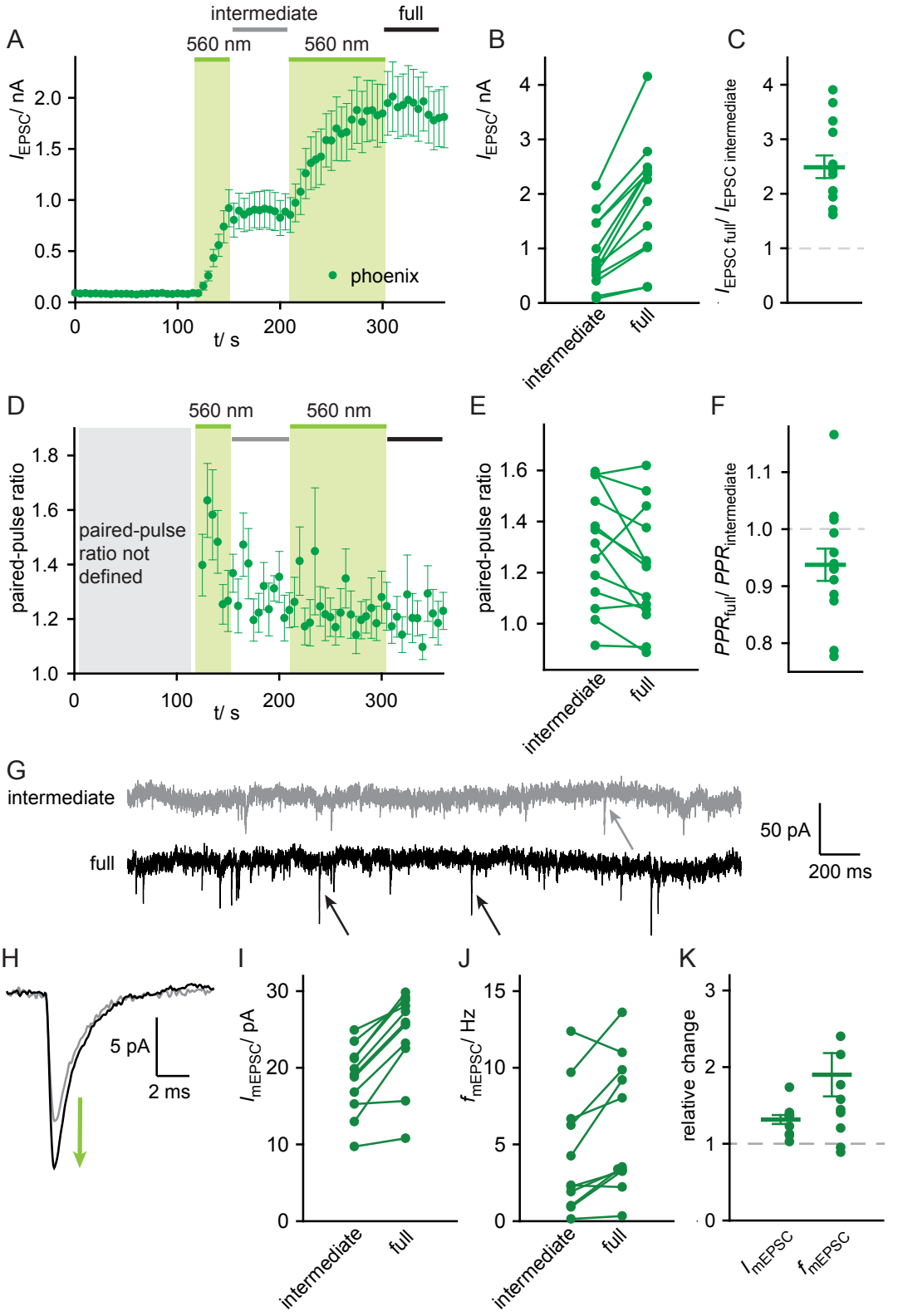

Figure 5.34.: Response of pHoenix-expressing neurons following two consecutive light intervals at 560 nm. Light pulses were 30 s and 90 s long and had an intensity of 25 %. Cells were incubated with 1 µM bafilomycin for at least 2 h prior to all experiments. **A** Time course of EPSC amplitudes. Time period in-between pulses is referred to as "intermediate" filling state and time after last pulse is referred to as "full" state. **B** Comparison of EPSC amplitudes of individual cells for intermediate and full state. **C** Corresponding relative changes. **D** Time course of paired-pulse ratios (PPR). **E** and **F** Comparison of PPR of individual cells for intermediate and full state and respective relative change. **G** Representative current traces showing miniature EPSCs (mEPSCs) for intermediate (grey trace) and full-filled vesicles (black trace). Selected mEPSCs are indicated by grey and black arrows. **H** Representative single events at both conditions. Full-filled vesicles display higher mEPSC amplitudes. **I** and **J** Comparison of mEPSC amplitude and mEPSC frequency of individual cells after first and second light pulse. **K** Quantification of relative changes in amplitude and frequency of single release events.

amplitudes going along with higher mEPSC amplitudes and mEPSC frequencies when compared to the intermediate filled state. Moreover, there is an indication of an increased release probability of the full state. These experiments show that pHoenix activation using more complex light protocols allows for the analysis of different filling states of synaptic vesicles.

Taken together, pHoenix constitutes a light-activated proton pump that preferentially targets to synaptic vesicle membranes. pHoenix activation in untreated autaptic neurons evokes (11 ± 2) %-enhanced excitatory postsynaptic currents. Moreover, pHoenix activation for 2 min can restore EPSCs in bafilomycin-treated neurons. First experiments also indicate that pHoenix might be useful to study correlations between different vesicular filling states and their respective postsynaptic responses.

6. Discussion

6.1. Towards multi-color optogenetics

Optogenetics is a powerful method to study cellular processes with high temporal and spatial precision. In order to perform complex combinational optogenetic experiments, both fluorescent sensors and actuators exhibiting distinct wavelengths of activation are essential.

Bright fluorescent proteins with excitation maxima ranging from 380 nm to 700 nm are now available [159, 237]. In GFP-like proteins the absorption is determined by post-translational modifications of the chromophore, the chromophore isomerization state and the chromophore environment [238]. Fine-tuning of the absorption by mutagenesis of the fluorescent proteins from the jellyfish *Aequorea victoria* and the reef coral *Discosoma sp.* yielded variants with emission spectra covering the entire visible range from blue to far-red [159, 237]. The palette of fluorescent proteins is furthermore extended by near-infrared fluorescent proteins being developed from bacterial phytochromes [239]. In fact, spectrally distinct sensors sensitive to diverse cellular parameters have been created. Prominent examples are the pH sensors pHluorin and pHTomato as well as the Ca^{2+}-sensitive GCamps and RCamps. FRET sensors that rely on the energy transfer between two FPs complement the repertoire of sensor proteins, thereby CFP and YFP derivatives represent the most commonly used FPs applied as FRET pairs.

Contrarily, the color palette of available optogenetic actuators is rather sparsely populated. Hyperpolarizing microbial pumps are activated by green, yellow or orange light and few variants have been successfully applied in neuronal cells (see section 3.5.3). Only very recently, a blue light-absorbing Arch variant exhibiting maximal activation at 500 nm was generated [240]. The Arch mutant was obtained by replacement of three residues within the retinal binding pocket. In the mutant the retinal favors an altered isomerization featuring a rotated β-ionone ring, thereby decreasing the effective size of the delocalized electron system [240]. Additional color-tuned hyperpolarizing tools e.g. a blue-absorbing chloride pump or a red-shifted proton pump would be of great interest for applications. In principle, the absorption of protein-embedded all-*trans* retinal can be tuned from 425 nm to 644 nm as has been shown in a study using human cellular retinol binding protein II [241]. But, optogenetic application requires reasonable protein stability and functionality of the respective rhodopsin. Since a single ion is transported per photocycle in microbial pumps, the number of transported charges directly correlates with the number of available pumps and the quantum efficiency of the primary photoreaction. Further mutational studies and/or genomic screens are thus necessary to provide new variants that allow for combinational experiments of both hyperpolarizing and depolarizing optogenetic tools.

6.1.1. Color-shifted ChR variants

High-efficiency ChRs are represented by C2 derivatives and C1C2 chimera that absorb blue and blue-green light only. In the present work we aimed to create potent ChRs with shifted action spectra. Generation of a blue-shifted C2 mutant failed for several reasons.

First, the retinal binding pocket is only partially conserved between ChRs and other microbial rhodopsins. Color-tuning has been intensively described for proteorhodopsins, but transfer of reported blue-shifted mutations to ChRs did not shift the absorption in the respective ChR mutants. The counterion complex in proteorhodopsins is composed of the R94, D97 and D227 and is stabilized by hydrogen bonding to H75 [242]. In contrast, the C1C2 counterion comprises E162, D292 (corresponding to C2 E123 and D253) and a near-by water molecule with D292 being closer to the Schiff-base nitrogen than E162 [74] (see Figure A.1 for positions in model structure). As a result, the Schiff base is stabilized by differentially arranged counterions in the two protein classes. Furthermore, the protein environment facing the retinal-polyene chain and the β-ionone ring are diversely tuned. Thus, the complexity of protein-retinal interactions in retinal proteins limits the transferability of color-tuning mutations between different protein classes. Even within the group of closely related ChRs, single amino acid exchanges may result in different phenotypes. For example, exchange of F226 by tyrosine induces a 10-nm blue-shift in V1, but the corresponding mutation does not affect the spectral characteristics of C2 [88]. Likewise, the C2 mutants I131V and I131L do not exhibit a spectral shift as reported for the ChIEF variant [80]. Interestingly, both the C2 T165A and the C2 S166A mutant show a bathochromically shifted activation maximum that can be explained by removal of polar side chains close to the ring system. Nevertheless, similar exchanges have also been reported to induce hypsochromic shifts due to bent retinal conformations disrupting retinal planarity [240]. Moreover, in the alanine mutants water molecules might replace the side chains of the more voluminous residues and the hydrogen network of the surrounding residues may reorientate. None of the mutations introduced in helix seven close to the counterion residue D253 affects the C2 action spectrum either. Taken together, no blue-shifted C2 variant was obtained by single mutagenesis. This may indicate that C2, V2 and related blue-light absorbing ChRs have already been optimized for low-wavelength absorption without affecting the channel function. Notably, most single mutants exhibit dramatically reduced C2 photocurrent sizes (see Table 5.1) which is due to less effective protein folding and reduced protein stability. The dramatic effect of an exchange in the retinal-binding pocket on protein stability and retinal binding has been extensively described for mutations at the C2 T159 position [109].

Next, the creation of a yellow-absorbing ChR with superior expression level compared to V1 was pursued. Early approaches of enhancing the V1 surface expression were performed by fusion with different targeting sequences. Introduction of an ER export signal and a signal peptide previously described to enhance N_pHR expression (see section 3.5.5) improved photocurrents by a factor of two [137, 88, 108]. Similarly, introduction of H129R, the corresponding residue to H134R in C2, resulted in two-fold higher transient currents [88]. Since the resulting V1 variants are not sufficiently well expressed to drive action potentials in neurons at moderate light intensities, the chimera approach was transferred to V1. First chimeric proteins were constituted of V1 with either one or two helices replaced by the corresponding C2 or V2 helices. Chimera featuring helices three and four of C2 or V2 (V1C2 223 and V1V2 223) exhibited up to two-fold enhanced

currents due to better membrane integration [88, 87]. While these chimera showed similar action spectra to V1 with an even red-shifted shoulder, exchange of helices six and seven (V1V2 52) resulted in a drastic blue-shift of the spectrum to ≈ 460 nm [88]. Thus, the last two V1 helices are crucial for its red-shifted activation. Accordingly, chimera combining two to five N-terminal helices of C2 and V2 with C-terminal V1 helices were tested [87, 88]. However, these combinations yielded througout unfunctional proteins. Next, Matthias Prigge designed chimera with a similar architecture to the previously described C1C2 chimera [78, 80, 79, 87]. The C1V1 52 chimera exhibits strongly improved membrane targeting, but features only small photocurrents [87]. In contrast, the C1V1 25 chimera that consists of the two N-terminal C1 helices and the latter five from V1 combines both excellent membrane targeting with stongly enhanced photocurrents (see Figures 5.3 and 5.4B). C1V1 25, also referred to as C1V1, retains the spectral characteristics of V1 and exhibits maximal activation at 536 nm. Consequently, it allows for sufficient membrane depolarization to drive action potentials in cultured hippocampal neurons even with red light activation at 620 nm (Figure 5.4E). Hence, C1V1 constitutes the first high-perfomance ChR that allows for neuronal activation with yellow light. In order to understand the superior expression level of C1V1 in comparison to C1, C2 and V1, several aspects should be taken into account. The N-terminus of C1 features 39 additional amino acids when compared to C2 (44 compared to V1). Out of these, residues 1-24 have been reported to be processed as a signal peptide [74]. Moreover, while the N-terminal sequences of C1, C2 and V1 feature one conserved glycosylation site, the C1 sequence contains an additional glycosylation site that just preceeds its first transmembrane helix (N82, G83, T84) [73]. Combination of the C1 N-terminus with C2 helices resulted in improved membrane targeting of five out of six chimera that were tested by the Yawo group [78]. Thus, the additional N-terminal amino acids found in the C1 sequence may provide better channel targeting, possibly via the signal peptide or the second glycosylation site. Furthermore, the C1V1 sequence features C198 at the corresponding position to T159 in C2. The C2 T159C mutation has been described to show three- to tenfold enhanced photocurrent amplitudes, probably caused by higher protein stability and improved retinal binding [99, 109]. A similar effect in C1V1 may explain its high photocurrents. Also, C198 may partially contribute to the more than three-fold decelerated off-kinetics that is found in both V1 and C1V1 when compared to C1 and C2.

Consecutively, C1V1 was further fine-tuned by site-directed mutagenesis (for mutated residues in C1V1 see Figure 5.5A). The mutational screen aimed for both blue- and red-shifted C1V1 variants as well as fast and slow mutants. Out of the tested mutants, two show significantly red-shifted absorption and might be better suited for combinational experiments with C2. The effect of the E122T mutation is rather unclear, since in both in the C1C2 X-ray structure as well as in the C1V1 homology model E122 constitutes a residue of the inner gate that is more than 8 Å away from the retinal chromophore and can thus only indirectly influence its absorption [74]. The red-shift seen in the L221T mutant can be explained by introduction of the electronegative oxygen of the tyrosine

close to the β-ionone ring of the retinal. While C1V1 E122T features similar kinetic parameters when compared to C1V1, C1V1 L221T shows 2.4-fold accelerated kinetics that go along along with 2.6-fold reduced photocurrents. Thus, C1V1 E122T is the best suited ChR featuring yellow-light absorption with moderate off-kinetics and C1V1 L221T might be best suited for fast depolarization with yellow light.

The mutational screen also revealed blue-shifted C1V1 mutants. The action spectrum of the corresponding ChETA mutant C1V1 E162T is slightly hypsochromically shifted to 532 nm. Notably, in DChR1 from *Dunaniella salina* the A178E mutant is maximally activated at 510 nm, whereas the spectrum of wt DChR1 that features a non-polar alanine at the ChETA position peaks at 475 nm [26]. Inversely, introduction of the ChETA mutation E123T in C2 induces a bathochromic shift of 22 nm (see section 5.2.1 for C2 mutant data and Figure A.1 in the Appendix for wt counterion residues). Taken together, the spectral effects of the ChETA replacements indicate that the counterion complex is differentially arranged in various ChRs and that the interaction of E162/A178 in C1V1/DChR1 with the Schiffbase might feature structural similarities. Besides the different color-shifts induced by ChETA replacements, both C2 and C1V1 ChETA mutants exhibit strongly accelerated off-kinetics. C1V1 E162T is the fastest C1V1 single mutant and features a characteristic τ_{off}-value of (34 ± 4) ms.

Even more pronounced than the blue-shift found in C1V1 E162T, maximal activation of C1V1 S220G is blue-shifted by 12 nm to 524 nm, whereas the mutant's kinetic parameters remain unaltered compared to C1V1. In C1C2 the inverse mutation G220S induces a 13 nm red-shift at neutral pH [88]. Interestingly, the residue at the corresponding position seems to divide microbial rhodopsins into a class of blue-absorbing and a class of green/yellow-activated proteins. While C1, C2, V2 and *Natronomonas pharaonis* sensory rhodopsin II (maximal activation at 497 nm) feature a glycine at the respective position, V1, BR, N_pHR and xanthorhodopsin from *Salinibacter ruber* (maximal activation at 560 nm) possess a conserved serine residue [74, 65, 53] (the corresponding residues are highlighted in light blue and green in the alignment of Figure 3.3). The only exception is given by MChR from *Mesostigma viride* that is activated by green light (531 nm) despite displaying a glycine residue [72]. Therefore, this position should be considered whenever searching for color-shifted microbial rhodopsins. Out of all C1V1 mutants C1V1 S220G is the most blue-shifted and constitutes a well-suited ChR for green-light induced depolarization with moderate kinetics.

In order to create a fast C1V1 variant, double and triple mutants were tested (see Figures 5.5A and 5.6). Combination of C1V1 E122T with G196I V197A lead to 35 % faster off-kinetics compared to the single mutant. Both G196 and V197 are neighboring residues of C198 - corresponding to C2 T159 - in the close vicinity of the β-polyene chain and might be involved in transduction of conformational changes of the retinal to the protein moiety. The fastest C1V1 mutant is C1V1 E122T E162T, that combines the red-shifted central gate mutant with the ChETA variant. C1V1 E122T E162T, which is also referred to as C1V1 ET ET, shows a typical τ_{off}-value of (19 ± 1) ms, while maintaining the high current amplitude of C1V1. Both C1V1 E122T G196I V197A and C1V1 E122T

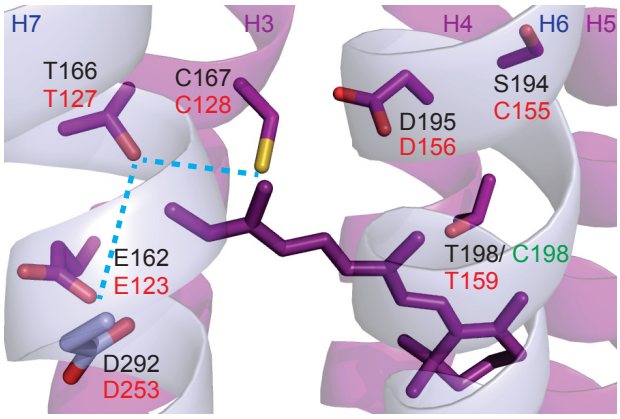

Figure 6.1.: Structural model depicting the active site and the DC-gate of C1C2 (pdb:3ug9) [74]. Respective C1C2 residues are labeled in black and the corresponding C2 residues are labeled in red. Numbering of C1V1 residues is equal to C1C2 residues. T198 in C1C2 is replaced by C198 in C1V1. C2 C128 is proposed to be hydrogen-bonded to C2 T127 that directly interacts with the deprotonated form of C2 E123 [107]. C2 C128 and C2 D156 are suggested to be hydrogen-bonded via an interjacent water molecule that fills the gap between the residues during MD simulations [107]. T159 may form an intrahelical hydrogen bond with the main chain of C2 S155, however this interaction is not visible in the C1C2 structure [107].

E162T display maximal activation at 535 nm similar to C1V1.

To complement the available ensemble of red-shifted ChRs, slow-cycling C1V1 variants were designed and characterized in close cooperation with Matthias Prigge (not shown in the results section). Combination of C1V1 E122T and C1V1 S220G with the corresponding SFO mutation C167S yielded two decelerated variants with characteristic τ_{off}-values of (4.2 ± 1.8) s and (4.7 ± 1.2) s [87]. In contrast, introduction of D195A (at the corresponding position to C2 D156) in the C1V1 background did not alter the photocycle kinetics ($\tau_{off} \approx 90$ ms) [87]. The reduced slow-down by introduction of mutations at position C167 (only 40-fold) and the abscence of an effect of D195 mutations may be due to altered interactions of the "DC-gate" residues in the presence of C198 (see Figure 6.1 for structural model). In C2 and C1C2, molecular dynamics simulations predict that C2 C128 and D156 are hydrogen-bonded via an interjacent water molecule [107]. Although in these simulations T159 does not directly interact with C128 or D156, it forms a hydrogen bond to the side chain of the neighboring S155 residue [107]. Thus, replacement of T159 by cysteine may lead to reorientation of the hydrogen bonding network, thereby strongly affecting the efficiency of coupling of the retinal isomeric states to the protein. Coupling of C2 C128 to the active site has recently been proposed to be mediated via a hydrogen bond between C128 and T127, whereas T127 directly interacts with the side chain of the counterion residue E123 (Figure 6.1) [107]. Experimental evidence for the importance of the residue at position T159 for the orientation of the DC-gate residues comes from experiments that combine C2 C128S with the T159C mutation. In the double mutant τ_{off}-values are in the range of 4 s compared to 106 s in the single SFO mutant (C2 C128S) [87]. For a further understanding of the proposed DC-gate residues, exchange of C1C2 T166, C167, D195 and T198 would be interesting, because structural information available for the chimera may facilitate interpretation of the mutant data.

C2-derived SFOs can be effectively deactivated with yellow light, but channel closure

is also triggered by UV light of 380 nm to 400 nm [102, 220, 87]. In contrast, inactivation experiments of C1V1 E122T C167S show efficient deactivation only with UV/blue light between 380 nm and 430 nm [220, 87]. Potentially triggered backreactions with yellow light are overlaid by C1V1 activation at these wavelengths. The spectral overlap of dark-adapted C1V1 and the C1V1 conducting state(s) is supported by recently measured C1V1 action spectra that exhibit broadening and an additional red-shifted peak following prolonged activation for 450 ms [243]. In V1, dark-adapted D540 is light-converted to the early photointermediate P600 (appearing on a similar timescale than P500 in C2) that preceeds the blue-shifted conducting state [38]. Due to spectral broadening the peak absorption of the V1 conducting state has not yet been assigned [38]. To understand the spectral characteristics of the underlying photocycle intermediates, time-resolved UV-vis absorption spectroscopy on purified C1V1 mutants is needed. In the present work, C1V1 was expressed in Cos cells and tested for purification by affinity chromatography via the 1D4-tag. Successful protein expression was shown by western blotting using the 1D4 antibody (not shown). However, purification of native C1V1 failed since the retinal chromophore was lost during the purification procedure. Very recently, C1V1 could be purified from HEK 293T cells by Benjamin Krause. Using a purification protocol from the Tom Sakmar Lab (Rockefeller University, New York), he obtained pure C1V1. Dark-adapted C1V1 exhibited peak absorption at 504 nm at neutral pH (personal communication with Benjamin Krause) and is thus slightly blue-shifted when compared to electrophysiological peak activation. Notably, absorption spectra of V1 are blue-shifted to ≈ 500 nm at both acidic pH and after prolonged illumination [38]. Future spectroscopic experiments will allow for identification of pH-dependent states and photointermediates of C1V1. Moreover, analysis of C1V1 mutants may reveal the functional role of single residues for color-tuning and channel kinetics. Last, UV-vis spectroscopy on C1V1 SFOs is crucial to understand the multi-photon processes that determine their step-function behavior and constitutes the basis for ratioanl design of experiments using combinations of C1V1- and C2-derived slow variants.

Using the chimera approach and further fine-tuning by mutagenesis, we created yellow-activated ChR variants that show excellent membrane targeting and high photocurrents in HEK cells. Action maxima of these variants range from (524 ± 1) nm to (542 ± 2) nm and kinetic variants featuring τ_{off}-values between (19 ± 1) ms and (4700 ± 1200) ms are available. In the following, the ensemble of blue to yellow-light activated ChRs is summarized and first applications that use C1V1 in combination with C2 variants are presented.

6.1.2. Combination of C1V1 variants with blue-light activated ChRs

The repertoire of available ChRs exhibiting high photocurrents in HEK cells is complemented by blue-light activated C2 variants. These comprise the Catch mutant (C2 L132C) and its combination with T159C (C2 L132C TC, Catch+) that are characterized by their positively shifted reversal potentials and extraordinarily high stationary currents (see section 5.2.4). For fast membrane depolarization, C2 T159C and combinations with the ChETA mutations are favorable. C2 T159C E123T does not only support rapid

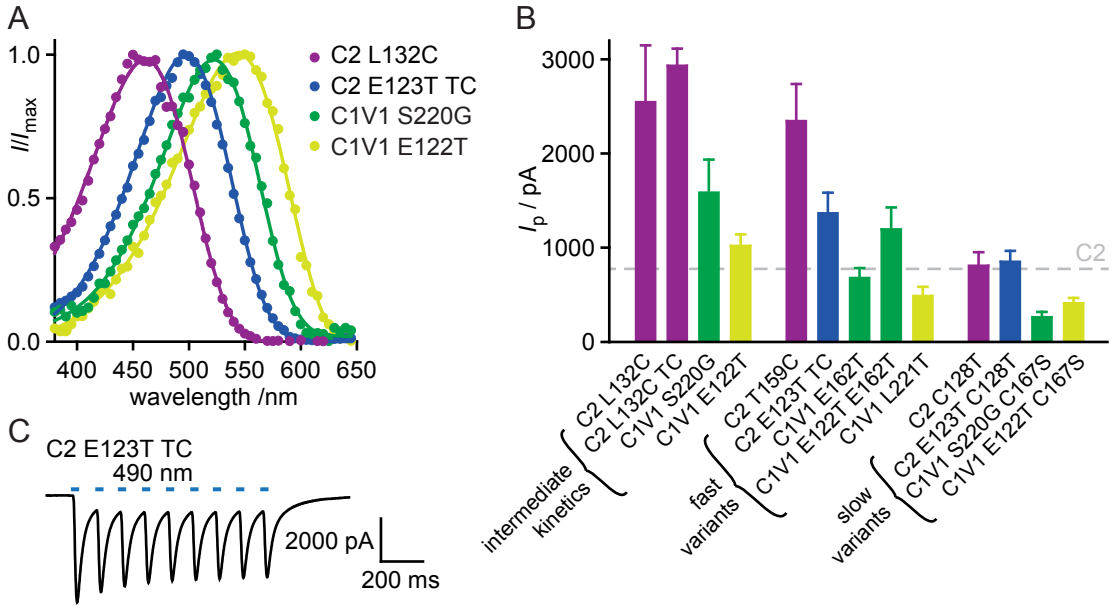

Figure 6.2.: Characteristics of available multi-color ChRs [87]. **A** Action spectra of four selected high-performance ChRs. Maximal activation occurs at (461 ± 1) nm, (492 ± 2) nm, (524 ± 1) nm and (542 ± 2) nm for C2 L132C, C2 E123T T159C, C1V1 S220G and C1V1 E122T, respectively. **B** Peak amplitudes for multi-color variants classified according to their photocycle kinetics. Horizontal grey lines indicates C2 current amplitude. Please note that C1V1-derived variants may exhibit greater amplitudes when using the C1V1 B background. **C** Current response to repetitive light trains for C2 E123T T159C. The double mutant combines very rapid kinetics with high photocurrents. For comparison to fast C1V1 variants see Figure 5.6.

channel opening/closing, but also features voltage-independent photocycle kinetics (Figure 6.2C). C2-derived SFOs imply C2 C128T and C2 E123T C128T that exhibit similar closing rates when compared to the C1V1-derived SFOs C1V1 C167S S220G and C1V1 E122T C167S. Interestingly, despite displaying the ChETA mutation C2 E123T C128T displays $\approx 70\,\%$ slower off-kinetics than the C2 C128T single mutant. Another potent blue-light activated SFO is the C2 L132C D156N double mutant characterized by its high light sensitivity (data not shown). Table 6.1 and Figure 6.2 summarize important characteristics of selected multi-color ChRs with high potential for applications.

Ofer Yizhar and Lief Fenno were the first to perform two-color optogenetic experiments with C1V1 and C2 variants. Using two different promotor systems they showed that C1V1 E122T E162T and C2 H134R activation independently drives action potential firing in cortical pyramidal and parvalbumin-expressing neurons following light pulses at 405 nm and 560 nm [108]. Moreover, they examined the combinational effect of C1V1 and C2 SSFO (C2 C128S D156A, ultraslow variant) on rhythmic activitiy in acute brain slices and showed independent axonal activation of two converging excitatory pathways [108]. At last, C1V1 E122T E162T expressed in excitatory neurons in combination with C2 SSFO expressed in inhibitory neurons were used to analyze the effect of the excitation/inhibition balance on cognitive and social functions in freely moving mice [108].

Similarly, Carrie Shilyansky coexpressed C1V1 E122T E162T with C2 L132C T159C (Catch+) in cultured hippocampal neurons [87]. At light intensities $< 1\,\mathrm{mW/mm^2}$ C1V1

mutant	λ_{max} / nm	I_p / pA	τ_{off} / ms
intermediate kinetics			
C2 L132C	461 ± 1	2550 ± 600	51 ± 5
C2 L132C T159C	460 ± 1	2930 ± 180	240 ± 30
C1V1 S220G	524 ± 1	1580 ± 350*	110 ± 20
C1V1 E122T	542 ± 1	1020 ± 120*	100 ± 10
fast kinetics			
C2 T159C	463 ± 1*	2340 ± 390*	18 ± 2
C2 T159C E123T	492 ± 2*	1360 ± 220*	7 ± 1*
C1V1 E162T	532 ± 1	680 ± 110*	34 ± 4
C1V1 E122T E162T	535 ± 1	1190 ± 230*	19 ± 1
C1V1 L221T	542 ± 1	490 ± 100	46 ± 3
slow kinetics			
C2 C128T	465 ± 6*	810 ± 140*	1400 ± 100*
C2 E123T C128T	485 ± 7*	850 ± 120*	2400 ± 800*
C1V1 S220G C167S	528 ± 4*	180 ± 60*	4700 ± 1200*
C1V1 E122T C167S	537 ± 5*	410 ± 60*	4200 ± 1800*

Table 6.1.: Overview of high-performance ChRs with activation maxima between 460 nm and 540 nm. Variants with fast, intermediate and slow kinetics are available. Values indicated by a star were determined with major contributions of Matthias Prigge. All other values were determined in the present work.

ET ET-expressing neurons could be independently activated from those neurons expressing Catch+ (see Figure 6.3A, B) [87]. However, using activation light of 8 mW/mm^2 or higher spiking probability following 405 nm light pulses was similar for both neuronal populations, whereas light activation at 560 nm remained specific for C1V1 ET ET-expressing cells [87]. Accordingly, light intensity is crucial for independent neuronal activation, especially at the blue edge of the respective action spectrum. Both Ofer Yizhar and Carrie Shilyansky showed that C1V1 can reliably elicit action potentials at 20 Hz and might be used for episodic stimulation at frequencies up to 50 Hz (see Figure 6.3 C) [108, 87].

Next, Karen Erbguth tested a variety of red-shifted ChRs for functional expression in *C. elegans* [244]. Out of the tested variants C1V1 ET ET exhibited the highest expression level both in body-wall muscles and neuronal cells. Green light activation of C1V1 ET ET in body-wall muscles induced muscle contractions going along with body-length reduction by 9 %. Contractions could be counteracted by UV light-induced activation of C2 H134R in GABAergic motor neurons. Nevertheless, purely independent activation of cells expressing C2 H134R and C1V1 ET ET was not possible using moderate light intensities. To minimize activation of C1V1 ET ET using UV light (400 nm) the high-efficiency variant C2 H134R T159C that displays an enhanced expression level and thus can be activated with lower light intensities was employed as a second actuator. By coexpression of C2 H134R TC in GABAergic motor neurons and C1V1 ET ET in cholinergic motor neurons body length could be independently regulated by application of either UV/blue or yellow light. Thus, C1V1 ET ET and C2 H134R TC are well-suited for two-color photostimulation and can be used to trigger opposing behaviors e.g. body contraction/ elongation in *C. elegans* in vivo.

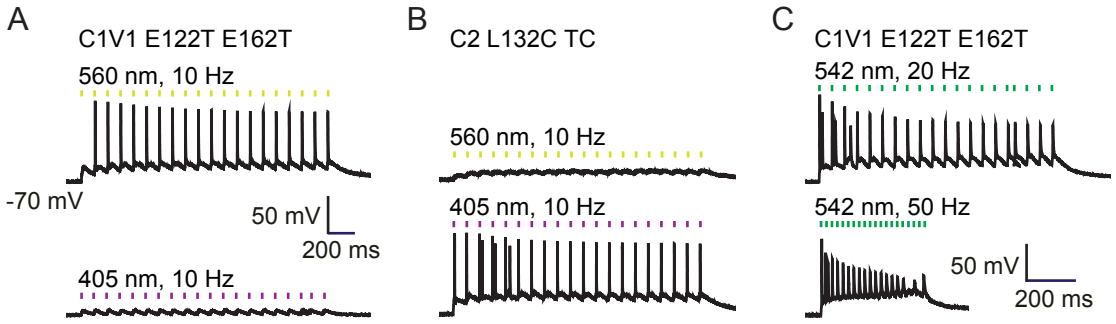

Figure 6.3.: Two-color activation of cultured hippocampal neurons [87]. All presented experiments were performed by Carrie Shilyansky (Deisseroth group, Stanford University). Light intensity was $0.875\,\mathrm{mW/mm^2}$. **A** In C1V1 ET ET-expressing cells action potentials are successfully triggered by 560 nm light pulses, but not by 405 nm light. **B** Inversely, APs are exclusively elicited at 405 nm in Catch+-expressing cells. **C** C1V1 ET ET activation can induce AP firing at frequencies up to 50 Hz.

In the following, C1V1 and C1V1 mutants were tested for two-photon activation with infrared light (1040 nm) [245]. Since C1V1 variants combine high two-photon cross-sections with large photocurrents and moderate off-kinetics, C1V1-mediated membrane depolarization outperforms depolarization via C2 H134R evoked with comparable two-photon activation protocols [245, 246]. Using the superior 3D resolution of two-photon stimulation, C1V1 E122T was successfully applied to selectively activate small dendritic regions and individual spines in brain slices [246]. Two-photon activation of C1V1 variants thus constitutes an effective method to induce membrane depolarization, thereby allowing for deeper tissue penetration than conventional one-photon ChR activation.

6.1.3. Perspective on color-tuning

Design of new ChRs by the chimera approach and additional site-directed mutagenesis generated a variety of high-performance ChRs that have been succesfully combined in two-color optogenetic experiments. Nevertheless, additional optogenetic actuators that display altered properties such as a further red-shifted activation or a faster photocycle may broaden the optogenetic horizon. Furthermore, expression level and functionality of the respective optogenetic tool strongly depends on the target-cell type and organism and thus the optimal ChR has to be elucidated prior to each application.

Using a similar strategy as for C1V1, John Y. Lin recently created the chimeric ChR "ReaChR" [247]. ReaChR is a V1-based ChR that features the N-terminus of C1, the sixth helix from V2 and the corresponding ChIEF mutation L171I [247]. Accordingly, ReaChR is maximally activated at ≈ 520 nm and is thus slightly blue-shifted when compared to V1 and C1V1 [247, 243]. Notably, ReaChR displays enhanced membrane trafficking in HEK cells [243] and shows superb expression in hippocampal slice cultures (personal communication with Thomas Oertner). Moreover, ReaChR purification from HEK 293T cells yields high amounts of pure protein (recent experiments by Benjamin Krause) and ReaChR should be considered as a potential target for spectroscopy and crystallization of a red-shifted ChR. Furthermore, site-directed mutagenesis of ReaChR may allow for creation of color-shifted and kinetically tuned variants with high potential for neuroscientific applications. Taken together, ReaChR constitutes a green-light ac-

tivated ChR with similar biophysical properties to C1V1, but with superior expression level in selected target systems.

By taking part in a recent algae genome project, Nathan Klapeotke and coworkers identified a number of new ChR sequences including opsin genes from *Chloromonas subdivisa*, *Chlamydomonas noctigama*, *Stigeoclonium helveticum*, *Neochlorosarcina sp.* and *Heterochlamydomonas inaequalis* [76]. When expressed in hippocampal neurons nine tested ChRs display inward-directed photocurrents with very different current amplitudes [76]. Out of these, two ChRs are of special interest for neuroscientific applications. The ChR of *Chlamydomonas noctigama*, which is also referred to as "Chrimson", shows maximal activation at $\approx$ 590 nm and represents the most red-shifted ChR identified so far [76]. Chrimson-mediated photocurrents are comparable in size to C2 currents, thereby being smaller than photocurrents of high-performance ChRs such as Catch+ or C1V1 [76]. A closer study of the retinal binding pocket of Chrimson may reveal the molecular determinants that cause the spectral shift. The responsible residues should be introduced into potent ChR variants such as C1V1 or ReaChR to combine both high expression level and orange absorption. The second interesting variant is given by the ChR of *Stigeoclonium helveticum*, so-called "Chronos", that represents a green-light activated ChR with ultrafast photocycle kinetics (τ_{off} <5 ms) [76]. Chronos displays large photocurrents and can be used to precisely elicit action potentials using 5 ms light pulses of 100 µW/mm^2 [76]. While both Chrimson and Chronos might be used for light-induced membrane depolarization, a closer look into their respective amino acid sequences will help to understand the molecular principles that determine ChR properties.

An alignment comparing the amino acid sequence of Chronos and Chrimson to the respective C2 sequence is shown in Figure 6.4. Both Chronos and Chrimson sequences contain characteristic conserved ChR residues including the glutamates in helix two, the Schiff-base lysine, the counterion asparagine (corresponding to C2 D253) and the leucine at the Catch position (C2 L132). However, several key residues are exchanged in their sequences (see red and blue arrows in Figure 6.4 for interesting exchanges). In Chrimson, the crucial inner gate histidine (C2 H134) is replaced by a lysine residue (Chrimson K176) which potentially results in distinct ion selectivity and inward rectification in the red-shifted ChR. Even more astonishing, the Chrimson sequence features a cysteine at position 198 (C2 D156) of the DC-gate. This residue has been proposed to be the primary proton donor in ChRs [91] which can be excluded in Chrimson. The neighboring M201 (corresponding to T159) may affect retinal binding and ion selectivity. The corresponding C2 T159M mutant displays small photocurrents with significantly shifted reversal potentials for both early and stationary photocurrents [224]. In respect to color-tuning it should be mentioned that Chrimson features a serine (S223) at the corresponding position to C1V1 S220 and two alanines (A207, A208) at the corresponding positions to C2 T165 and S166 close to the β-ionone ring of the retinal. Moreover, several aromatic residues of helix six are replaced by more polar tyrosine residues in Chrimson (Y259, Y261, Y268) including the corresponding residue to C2 F226. Homology modeling of the Chrimson retinal binding pocket may reveal further crucial residues for color-tuning.

Figure 6.4.: Amino-acid alignment of C2, Chronos and Chrimson. Helical structures (corresponding to the C1C2 structure) are colored in light blue, β-sheet-like motifs are depicted in yellow [74]. Characteristic charged residues in helix 2 are highlighted in red color, other important ChR residues are colored in purple. Additionally, corresponding residues to the BR proton donor (C2 E123), proton acceptor (C2 H134), Schiff-base lysine (C2 K257) and counterion residues (C2 D253) are shown in green. Blue and red arrows indicate interesting amino-acid exchanges in Chronos and Chrimson, respectively.

Taken together, Chrimson is not only interesting due to its extraordinarily red-shifted absorption, but should also be investigated in the context of channel gating (DC-gate, inner gate) and ion selectivity.

The sequence of the fast-cycling Chronos is characterized by a methionine residue at the ChETA position of the counterion complex (corresponding to C2 E123). In naturally occuring ChRs only glutamate and alanine residues had previously been found at the corresponding position [26]. Methionine replacements should be taken into account to produce fast-cycling mutants e.g. on the C2 T159C, C1V1 or ReaChR background. In addition, the corresponding residue to C2 T159 is occupied by a asparagine in Chronos, thus the kinetic effect of this replacement should also be investigated in more detail. Since Chronos belongs to the group of blue/green-light absorbing ChRs, it is only of minor interest for color-tuning projects.

Future color-tuning approaches should consider the ensemble of available ChR variants both as a theoretical and experimental basis. Bioinformatic sequence comparisons

together with molecular modeling of the retinal binding pocket of different ChRs will enable the identification of the molecular determinants involved in retinal-absorption tuning. A 3D structure of a red-shifted ChR variant would greatly facilitate the search for such structural elements. In addition to rational design, identification of new ChR genes in genomic screens may reveal ChRs with altered absorption properties.

6.2. Gating and ion selectivity in ChRs

Ion channels are an ubiquitous group of membrane proteins that selectively mediate ion flux via a membrane-spanning water-filled pore. Thereby, ion channels control the flow rate of individual ion species and precisely regulate opening and closing of the respective ion-permeation pathway (gating). Highly selective channels e.g. potassium or sodium channels contain so-called selectivity filters determining the kind of transported ions. These selectivity filters represent the narrowest part of the pathway and adopt conserved symmetrical structures that specifically bind one ion specie e.g. by mimicking the hydration shell of the respective ion [248]. Transitions between conductive and non-conducting states and vice versa are regulated by structurally distinct domains that sense external stimuli such as ligand-binding, deviations in membrane voltage, membrane distortion or protein-protein interactions. Upon signal detection, conformational changes are propagated from the sensor domain to the ion-permeation pathway. Channel gating may occur at the selectivity filter or at other specialized regions of the pathway.

Although selectively mediating cation fluxes in a temporally precise manner, channelrhodopsins differ from other ion channels in several respects. First of all, ChRs are directly regulated by light, therefore isomerization of the retinal chromophore triggers conformational changes involved in ChR gating. Second, despite functional dimerization of ChRs, ion permeation is assumed to take place in each monomeric subunit [74]. Thus, symmetrically ordered selectivity filters are unlikely to play a role in ChRs. When compared to other ion channels, ChRs feature a very low single channel conductance which has been estimated to be in the range of 40 fS to 90 fS for C2 by Feldbauer *et al.* and to be $\approx$ 1100 fS for C2, C1C2 and ChIEF (C1C2 V170I) by Lin *et al.* [83, 80]. But, the eyespot of green algae reflects a small compartment where few transported charges may dramatically influence both local membrane potential and ionic composition. Moreover, ChR-mediated depolarization may induce additional activation of secondary voltage-gated calcium channels that are present at low copy numbers in the eyespot, but exhibit higher single channel conductances, thereby allowing for signal amplification [22, 23]. Since single point mutations can induce channel activity in light-activated proton pumps [249, 250], ChRs may have evolved from microbial proton pumps ("leaky proton pumps"). In a recent publication, Sineshchekov and coworkers distinguish between naturally-occuring low-efficiency ChRs that display some residual proton-pumping activity and high-efficiency ChRs without detectable proton movement [251]. In the present work, structural elements that line the potential ion-permeation pathway of ChRs were mutated and the respective mutants were studied by whole-cell patch-clamp recordings. A special focus was laid on ion selectivity of selected mutants.

In addition, some general aspects of ChR photocurrents including inward rectification and ion competition were analyzed. Last, an enzyme-kinetic model was used to quantitatively describe cation flux of three prominent ChR variants.

6.2.1. The ion permeation pathway

ChR primary sequences contain a number of conserved charged and polar residues in helix two that appear with a 7-amino acid periodicity [75]. In C2, these are represented by five glutamates (E82, E83, E90, E97 and E101), one lysine (K93) and a cysteine residue (C87). Charged residues are unlikely to face towards the aliphatic lipid chains and are therefore thought to be orientated towards the protein interior. Replacement of the respective residues yields reduced photocurrents in all tested mutants except for the K93S mutant. Tested double and triple replacements result in 18- and 55-fold reduced photocurrents, respectively. Nevertheless, replacement of single glutamates still allows for cation transport, only with reduced efficiency. Together, these results indicate that the negatively charged glutamates and C87 are directly involved in cation binding and are thus part of the ion-permeation pathway. A recent MD simulation of the C2 structure suggests that charged residues of the second helix favor binding of water molecules [107]. Resultingly, the simulation does not only predict a continuous water distribution at the extracellular side of the central gate restriction, but also on the cytosolic side close to C2 E82, C2 E83, H134 and H265 [107]. In order to adress the interaction of the charged residues with the retinal, action spectra were analyzed. Out of the tested mutants C2 E97Q TC and C2 E101Q TC show slightly bathochromically shifted action spectra with peak activation at 466 nm. Accordingly, both potentially negatively charged glutamates influence the electrostatics of the retinal, possibly by stabilizing the protonated Schiff base. Combination of both glutamate exchanges does not further shift the action spectrum, suggesting that only one of the two glutamates is deprotonated at a time in wt C2. In comparison to the spectral shift of the ChETA mutant C2 E123Q TC, that is shifted by 22 nm when compared to wt C2, the spectral effects of the single mutants C2 E97Q TC and C2 E101Q TC are only minor, suggesting long-range interactions of the two residues with the retinal. Interestingly, replacement of E83 does not shift the action spectrum in C2, while exchange of the corresponding residue in C1V1 (E122) causes a 6 nm-shift (see section 6.1.1). Hence, the glutamates and especially E83/E122 might be differentially ordered in C2 and C1V1.

Based on the electrophysiological data and molecular dynamics simulations by Hiroshi Watanabe and Kai Welke (KIT Karlsruhe), two structural models of C2 were developed. Both models orientate the charged residues of helix two towards the protein interior and suggest the ion-conducting pore to be formed between helices two, three and seven [75]. The models differ in the arrangement of helix two, which is shifted to the intracellular side by two helical turns in model B [75]. Model A positions E90 in close proximity to the counterion complex and was later on confirmed by the C1C2 X-ray structure [75, 74]. In dark-adapted C1C2 the side chain of E129 (corresponding to C2 E90) is situated between the carboxylate groups of the counterion residues and the side chains of N297 (C2 N258)

and S102 (C2 S63) as depicted in Figure 5.7C for C2. Kato *et al.* suggest that C1C2 S102, E129 and N297 form a crucial constriction site for ion permeation and that these residues have to reorientate during conducting state formation in order to allow cation flux (central gate, see Figure 3.4B). Notably, in DChR1 the corresponding residue to C2 S63 is replaced by a cysteine (see Figure A.1) [107]. Together with replacement of the counterion glutamate by an alanine residue, this exchange might be crucial for the high proton selectivity found in DChR1 [26].

An additional constriction site was proposed to lie at the cytoplasmic protein surface with possible involvement of C1C2 Y109 (inner gate, see Figure 3.4B). Due to differential arrangement of the corresponding Y70 in C2, E82, E83 and H134 are considered to be part of the inner gate in C2 as well (see Figure 5.7A, B). Interestingly, recent structural simulations propose that C2 E82, E83, H134, H265 and R268 form a binding site for Na^+ in the dark-adapted C2 structure [107]. A second Na^+ binding site is suggested to consist of S52, E56 and E97 at the extracellular part of the ion permeation pathway [107]. The present work analyzes selected central and inner gate residues and validates their impact on gating and ion selectivity.

Most inner and central gate mutants allow open state formation, but all tested mutants exhibit lower photocurrents. For the mutations at position C2 H134, photocurrent sizes are reduced by factors of 2.5 to 11 depending on the type of replacement. Moreover, C2 Y70F TC mediates slightly reduced currents, whereas C2 Y70S TC only displays small currents in the range of 300 pA (personal communication with Jonas Wietek). Similarly, replacement of C2 S63 results in current reduction by a factor of 2.1 or more and N258 mutations evoke at least 6.2-fold reduced currents. In C1V1, the effect of central gate mutations is even more pronounced resulting in very low photocurrents of all tested mutants. C1V1 N297D does not exhibit light-induced currents in our hands. The observed current reductions could be accounted for by less effective (slower) cation transport at a single channel level, but could also result from a lower opening propability or faster channel closing kinetics. Since single-channel recordings on ChRs are not possible due to low single-channel conductance, this question cannot be unambiguously solved here. However, these mutations only moderately affect the average kinetics of channel opening and closing. The H134R mutant shows $\approx 24\,\%$ slower off-kinetics in HEK 293 cells [87]. While S63 replacements result in similar kinetic modulations, replacement of N258 decelerates the off-kinetics by up to a factor of 3.7. Again, effects are more pronounced for C2 N258 than for C2 S63. Mutational analysis of C2 Y70S TC also showed decelerated channel closing with an effective τ_{off}-value in the range of 400 ms (Jonas Wietek). But compared to the kinetic effects of the SFO mutations, the above mentioned alterations seem rather small. Upon retinal isomerization a conformational change is supposed to be translated from the active site - probably via the DC-gate and C2 T159 - to the ion-permeation pathway that opens towards the intracellular side (see Figure 6.1 for proposed hydrogen bonding between counterion and DC gate residues). This conformational change may involve reorientations of both central and inner gate residues. After all, our kinetic data supports only indirect involvement of the central and inner gate

residues in gating.

In contrast, all analyzed residues strongly influence ion selectivity in ChRs. Out of the inner gate residues, the H134N mutant was studied most intensively in the present report. Depending on the internal pH, C2 H134N displays positively shifted (pH_i = 9.0) or negatively shifted (pH_i = 5.0) reversal potentials when compared to C2. This finding may suggest a higher relative proton conductivity of the mutant. However, when considering the entire voltage range, protons (especially external protons) inhibit both inward and outward Na^+-mediated currents. The pronounced inhibition by external protons is interesting, because H134(N) is situated on the cytosolic side of the channel. Thus, proton release into the cytoplasm may be decelerated in the mutant. Moreover, inward rectification is diminished in C2 H134N (see Figures 5.11D and 5.12D). A similar effect is found by replacement of C2 Y70 (Jonas Wietek). Therefore, the inner gate might be responsible for the ChR-specific inward rectification. Also, C2 H134N changes the equilibrium between the two open states (see blue current traces in Figure 5.10A). At external Na^+, pH_e 9.0, the stationary current exceeds the initial current going along with strongly decelerated off-kinetics. Two possible explanations are at hand: On the one hand stationary illumination could lead to accumulation of the first open state O1 that features a high conductivity. On the other hand the second open state O2 might display an extraordinarily high Na^+ conductivity that is only apparent in abscence of competing protons and Ca^{2+} ions. Notably, C2 L132C (Catch) also exhibits very low inactivation, which is present at all analyzed conditions. L132 is located two residues apart from H134 on helix three, thereby facing away from the gate towards the active site. L132 may influence ion selectivity by deformation of helix three which in turn reorientates H134 of the inner gate. Taken together, H134 of the inner gate influences C2 ion selectivity with considerable effects on ion competition, inward rectification and the O1/O2 equilibrium.

Consecutively, C2 S63 and N258 of the central gate were analyzed for their impact on ion conductance. Both residues are in close proximity to the side chain of C2 E90, a residue whose exchange strongly influences cation selectivity [94, 224, 100]. By replacing S63 or N258 in C2 T159C by a negatively charged aspartate residue, the initial Ca^{2+} selectivities of the mutants are enhanced by 49 % and 36 %, respectively. Due to lower degrees of inactivation, stationary Ca^{2+} currents are even higher and are increased by 304 % and 186 % when compared to C2 T159C. C2 TC N258D displays high Ca^{2+} transport even at low Ca^{2+} concentrations, indicating a strong binding affinity in the double mutant. The increased Ca^{2+} transport is also apparent in the presence of competing protons as can be seen from Fura-2 measurements at neutral pH. In summary, the introduction of a second negative charge in the central gate region enhances binding and transport of divalent cations such as Ca^{2+}. In order to analyze this charge effect the transport efficiency of other divalent ions e.g. Mg^{2+} would be interesting. Notably, introduction of an aspartate residue does not only alter Ca^{2+} selectivity, but also effects inactivation and therefore the equilibrium between the two open states (most pronounced in C2 S63D TC) as well as competition of Na^+ and protons (C2 TC N258D).

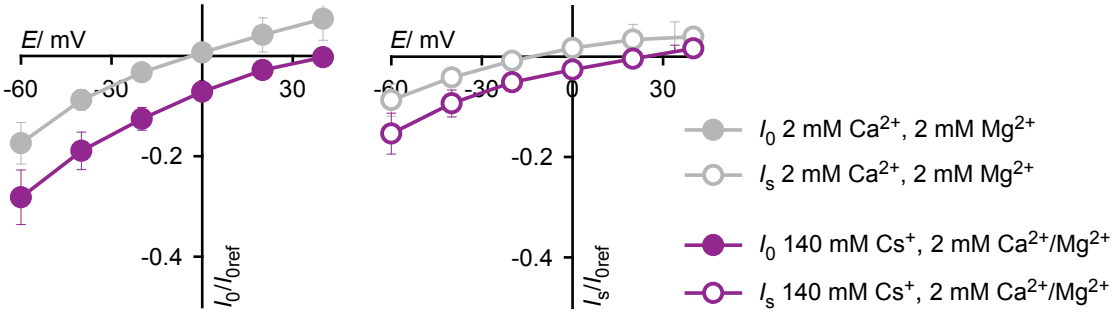

Figure 6.5.: Cs^+ selectivity of the initial current I_0 and stationary current I_s of C2. Addition of 140 mM Cs^+ positively shifted the respective reversal potentials by ≈ 40 mV.

Here, it was shown that selected inner and central gate residues play an important role in ion selectivity by determining the relative ratios between the conducted cations. Moreover, replacement of these residues partly abolishes the ChR-characteristic O1/O2 equilibrium that together with accumulation of late photocycle intermediates accounts for current inactivation. In addition, inner gate mutants cause reduced inward rectification. In order to obtain mutants with even more shifted selectivity ratios, inner and central gate mutations might be combined in a synergistic manner. But, multiple mutations often destabilize ChRs, leading to low photocurrent amplitudes. For example, creation of a highly selective Ca^{2+} mutant by combination of C2 TC N258D with the Catch mutation yielded an unfunctional triple mutant. While electrophysiological recordings provide complex functional data on the respective mutants, structural implications are difficult to gain. Future spectroscopic investigations may reveal specific amino acid interactions of the gating residues. Site-specific labeling with unnatural amino acids may allow for flexibility and distance measurements when comparing dark-adapted and light-adapted ChRs. But, a profound understanding of the ion conducting pathway can only be gained from an open-state ChR structure with atomic resolution. Furthermore, the positions of bound substrate cations are crucial to understand cation channeling. Since transport of heavier monovalent cations such as Cs^+ is comparable to Na^+ transport (see Figure 6.5), crystallization should be considered in the presence of these ions.

6.2.2. General aspects of ion selectivity

In the following, the presented experimental results are discussed with a special focus on cation conductance, inward rectification, contributions of the two open states as well as ion competition. Channelrhodopsins conduct different cations including protons, Li^+, Na^+, K^+, Ca^{2+} and guanidinium [18, 36, 37, 80, 79, 86]. Notably, C2 exhibits considerable Cs^+ conductivity as depicted in Figure 6.5. Hence, when using Cs^+ as a K^+ channel blocker in HEK 293 cells, this conductance should be taken into account. In the present work a symmetrical Cs^+ concentration of 1 mM was used in all ion selectivtity experiments. Because of similar transport rates for different monovalent cations, physiologically relevant monovalent cations (Na^+ and K^+) are commonly regarded as a single substrate [86, 100]. Likewise, divalent cations have been unified as one ion species.

But, the here presented ion selectivity experiments reveal very different Ca^{2+} and Mg^{2+} conductances. While addition of external Ca^{2+} results in higher inward photocurrents and positively shifted reversal potentials for C2, C1V1 and Catch+, the influence of Mg^{2+} is quite different. In C2, increase in the external Mg^{2+} concentration inhibits both outward and inward currents despite positively shifted reversal potentials. This effect can be explained by strong binding and slow transport of Mg^{2+} that prevents transport of protons and other cations as has earlier been reported for *Chlamydomonas* cells [228]. In C1V1 the inhibitory effect is less pronounced, whereas reversal potentials are also positively shifted upon external Mg^{2+} addition. Interestingly, variation of the external Mg^{2+} concentration between 2 mM and 70 mM does not significantly affect current sizes or reversal potentials in Catch+. This finding might be explained by strong Mg^{2+} binding even at low substrate concentrations.

In inward-rectifiying potassium channels cytosolic Mg^{2+} causes inward-rectification by blocking channel activity in a voltage-dependent manner. However, in ChRs variation of the internal Mg^{2+} concentration does not affect current sizes, reversal potentials and shapes of current-voltage relationships and Mg^{2+} can be excluded as the source for inward rectification. On the other hand, replacement of inner gate residues has been shown to cause more symmetrical IV curves. Possibly, inward rectification is caused by binding of a distinct cytosolic blocker at the inner gate or by voltage-dependent reorientation of the inner gate residues themselves.

ChR photocurrents are mediated by at least two distinct open conformations. Only by consideration of two open and two or more closed states one can sufficiently explain channel inactivation, biphasic off-kinetics and recovery kinetics of the peak current [84, 85]. Recently, it was suggested that the two open states differ in their respective retinal configurations [97]. Notably, the simultaneous presence of two open conformations may complicate the creation of homogeneous protein crystals necessary to solve an open state structure. Berndt, Prigge *et al.* showed that the initial photocurrent I_0, mediated by conductance via the first open state O1 only, and the stationary current I_s exhibit distinct ion selectivity patterns [86]. By analyzing reversal potentials of C2 they found a higher proton selectivity of I_s compared to I_0. In the present report, reversal potentials of I_0 and I_s are shown to differ by more than 20 mV at external high Mg^{2+}, pH_e 9 and external high Ca^{2+}, pH_e 9 (Figure 5.19). In C2, reversal potentials of I_0 are generally positively shifted compared to I_s. In order to quantify ion conductance via the two open states an enzyme-kinetic model was applied that allows for dissection of photocurrents into contributions by different cations. The used model considers four substates (protons, Na^+, Ca^{2+} and Mg^{2+}) that compete for external binding and transport to the cytosol. Furthermore, it is the first study that quantitatively describes current flux via both O1 and O2 using two distinct transport cycles. The model was successfully applied to reproduce current-voltage relationsships of C2, C1V1 and Catch+, three ChR variants displaying quite different ion selectivities (see Figure 5.23). Moreover, it allows for prediction of current sizes at ionic conditions that were not experimentally tested (Figure 5.27). The model data sufficiently describes the inactivation process that is caused by equilibration of

the O1/O2 ratio depending on the applied electrochemical gradient. But, the model does not consider other factors that determine O1/O2 equilibration e.g. the quality of the actinic light. Thus, quantitative model-retrieved data is only valid for a set of given experimental conditions. The here presented model bears another fundamental limitation. By consideration of inward fluxes only, three free parameters per substrate and open state have to be calculated. However, physiological cytosolic solutions contain high amounts of K^+ and considerable quantities of Na^+ and Mg^{2+} that will cause ChR-mediated efflux, especially at depolarizing voltages. To quantitatively describe cation efflux, the model has to be extended by eight additional kinetic parameters whose explicit calculation would require additional electrophysiological data.

Some general conclusions on ChR ion selectivity can be drawn from the calculated cation contributions. Notably, all presented current dissections depict conditions at −60 mV and are thus far from thermodynamic equilibrium. Accordingly, our data provides information that cannot be obtained from reversal potentials, which have been used to earlier describe ChR's ion selectivities. Based on our data the stationary current I_s is composed of contributions from both O1 and O2 that are comparable in size. Resulting from the different conductances of O1 and O2, the initial current I_0 features a higher proton selectivity than I_s. Inversely, both Na^+ and Ca^{2+}-mediated partial currents are higher for I_s. The discrepancy between the calculated partial currents and ion selectivities gained from reversal potentials (see Figure 5.28) is explained by voltage dependency of ion transport that is implemented in our model by a voltage-dependent reorientation of the empty and loaded binding site [86, 229]. This voltage dependency also accounts for the intersection of IV curves at different proton, Na^+ and Ca^{2+} concentrations (for example curves see Figure 5.16B). At pH_e 7.2, protons compete with Na^+ and Ca^{2+} for reversible binding and transport. In consequence, partial Na^+ and Ca^{2+}-mediated currents are smaller in the presence of external protons as is visualized for Ca^{2+} in Figures 5.25B and 5.27A. Interestingly, Mg^{2+}-mediated currents are unaffected by the external proton concentration. This finding might be explained by strong Mg^{2+} binding even in the presence of external protons. Titration of the substrate Mg^{2+} concentration reveals K_M values for Mg^{2+} transport in the low mM-range that correspond to physiological Mg^{2+} concentrations. Therefore, under physiological modulation Mg^{2+} shows a substantial contribution to both early and stationary ChR currents. The situtation for Ca^{2+} is quite different. Ca^{2+} does not only exhibit strong competition with proton and Na^+ transport, but it also displays unphysiologically high K_M values. Taken together, in the abscence of unlikely high external Ca^{2+} concentrations of 10 mM or higher, the contribution of Ca^{2+} ions to the total current will only be minor, even for the Ca^{2+}-permeative Catch(+) variant. Despite the above mentioned general principles of ion selectivity, each ChR variant exhibits distinct ratios between the different conducted ions that should be considered when choosing the appropriate ChR for a certain optogenetic experiment.

6.2.3. Application of ChR mutants with altered ion selectivity

Different optogenetic applications demand for light-activated ion channels with specific ion selectivities. ChRs are most commonly used to trigger action potentials. Thereby, ChRs mimic the threshold depolarization that inactivates K^+ channels and results in activation of voltage-gated Na^+ channels. This primary depolarization might be caused by an action potential in the neighboring membrane region or by opening of postsynaptic Na^+ and Ca^{2+} channels. For an optimal imitation of postsynaptic action potential initiation ChRs selective for Na^+ and Ca^{2+} would be favorable. Such variants would minimize the side effects of ChR-induced intracellular acidification. C2 H134N has been suggested to show enhanced Na^+ conductance [224]. But, the here presented data shows a complex inhibition of Na^+-mediated currents by external protons that may prevent application of the mutant at physiological pH_e. In order to quantify partial Na^+ and proton currents in H134N, model calculations on the electrophysiological data of the mutant would be helpful. Although not highly selective for Na^+ and/or Ca^{2+} neither, both C1V1 and Catch+ exhibit higher partial Na^+ and Ca^{2+} currents when compared to C2 wt. Thus, both variants provide "cleaner" membrane depolarization that should allow for fast action potential triggering when being combined with fast mutants (C1V1 E122T E162T or C2 E123T L132C T159C).

Many cellular processes are activated by transient elevation in the cytosolic Ca^{2+} concentration. One prominent example is the activation of neurotransmitter release upon presynaptic Ca^{2+} increase via voltage-gated Ca^{2+} channels. Both C2 S63D TC and C2 N258D TC exhibit enhanced Ca^{2+} permeability [226], especially when considering the stationary current I_s. This enhanced Ca^{2+} conductance is also apparent in the presence of competing protons at physiological pH_e. However, Catch+ mediates even higher light-induced Ca^{2+} influx, which can be accounted for by an combinational effect of both mutations (L132C and T159C) resulting in an high expression level, a low inactivation and an 1.6-fold higher Ca^{2+} selectivity [99, 110, 87]. Nevertheless, all mentioned mutants primarily conduct Na^+ and protons under physiological conditions.

The cytosolic pH level of $\approx$ pH 7.4 is strongly buffered by protonable amino acids such as histidine residues. In contrast, several intracellular organelles including lysosomes (pH 4.5-5.0), plant vacuoles (pH 5.0-5.5) and synaptic vesicles (pH $\approx$ 5.6) display acidic pH values [252, 253, 156, 157]. In order to analyze the functional relevance of high proton concentrations for transport processes and organelle-specific enzymes, a proton-selective ChR would be useful. DChR constitues a highly proton-selective variant, but its use for optogenetics has been hampered due to its low expression level in mammalian cells [26]. An improved DChR variant could be obtained by creation of chimeric ChRs that combine the ion-permeation pathway of DChR with the higher expression level of other ChRs. Alternatively, introduction of stabilizing mutations e.g. the corresponding exchanges to H134R and T159C may enhance DChR applicability. By transfer of the DChR counterion residue A178 to C2, a C2 mutant featuring an increased proton-selectivity has been generated (C2 E123A) [224, 100]. In the future, combination of proton-selective ChRs with organelle-specific targeting sequences, may allow for light-activated pH increase in

acidic organelles.

While ChRs present potent tools for membrane depolarization, a hyperpolarizing ChR would also be of great usefulness. In contrast to microbial proton and chloride pumps, ChRs transport several charges per absorbed photon and thus show an enhanced light sensitivity. A hyperpolarizing ChR would exhibit a reversal potential close to the resting potential or lower, thereby suppressing the initial depolarization required for action potential firing. Both a K^+ or a Cl^--selective ChR would provide the necessary light activity. Although several ChR mutants e.g. C2 T159M and C2 Q117E/R display negatively shifted reversal potentials due to enhanced K^+ selectivity, none of the mutants has been succesfully applied to suppress neuronal activity [224, 254]. Moreover, despite extensive mutational screening, no highly K^+-selective ChR variant could be obtained. An alternative approach to inhibit neuronal activity combines light-activated pumps with secondary proton-activated K^+ or Cl^- channels (personal communication with Kyoko Tsunoda and Johannes Vierock). These systems may allow for current amplification of the primary light-induced hyperpolarizing current.

Taken together, many potent ChR variants with altered cation selectivity have been reported and should be considered for specific applications. But, ChRs lack a "real" selectivity filter which would provide for high substrate specificity. The knowlegde of an open state ChR structure featuring the positions of bound cations may allow for the directed design of ChRs with shifted selectivitites that will potentially increase the repertoire of optogenetic experiments using ChRs.

6.3. Vesicular acidification using pHoenix

Neurons represent highly structured cells consisting of a dendritic tree, a single axon and a soma featuring the nucleus as well as the protein synthesis machinery. Both dendrites and soma receive and process synaptic inputs from neighboring cells. When integration of the incoming signals results in a threshold depolarization at the axon initial segment, an action potential (AP) is triggered that propagates to the axonal presynaptic terminals. At the presynaptic side of chemical synapses, the AP-induced transient depolarization opens voltage-gated Ca^{2+} channels, thereby initiating neurotransmitter release. Postsynaptic receptors sense the transient elevation of neurotransmitter concentration in the synaptic cleft and in turn activate postsynaptic ion channels or intracellular signaling cascades (Figure 3.8).

Given the functional compartimentalization of neuronal cells, specific manipulation of these subcellular structures are of great interest. Spatially defined activation of small neuronal compartments - mostly spines and dendrites - has been achieved by light-induced uncaging of neurotransmitters such as glutamate [255]. But irreversible glutamate uncaging exhibits the common drawbacks of chemical approaches such as compound synthesis, delivery and cell-type unspecificity. Using chemo-optogenetics, light-induced neurotransmitter binding to engineered receptors allows for reversible activation of specific postsynaptic responses. The genetically modified receptors contain an exposed cysteine residue that covalently binds a photoswitchable azobenzene linked

to the respective ligand [256]. Thus, depending on the nature of the used azobenzene and the geometry of the ligand binding site, light activation at a certain wavelength favors either the activated or the inactivated receptor state. Chemo-optogenetically targeted receptors include ionotropic and metabotropic glutamate receptors (LiGluR and LimGluR) and nicotinic acetylcholine receptors [256, 257, 258, 259].

Purely optogenetic aproaches offer an alternative for subcellular neuronal activation. By fusion of microbial rhodopsin genes with specific targeting sequences, rhodopsins have been preferentially expressed in the somatodendritic compartment, the postsynaptic membrane or the axon initial segment (see section 3.5.5) allowing for spatially-defined membrane depolarization/hyperpolarization [166, 167, 168]. Despite these advances in subcellular neuronal activation, direct and specific manipulation of the axonal and presynaptic compartment has not yet been reported. In the present work, an optogenetic actuator allowing for presynaptic activation by synaptic vesicle acidification was developed. Since presynaptic vesicles have been successfully targeted by fluorescent indicators to visualize vesicular pH changes as well as presynaptic Ca^{2+} influx [156, 172, 173, 161], a similar targeting strategy was followed for the tested optogenetic actuators.

6.3.1. Performance of available constructs

Four fusion proteins that combine the vesicular pH indicators Syphy/SyphTomato with either Arch3, C_vRh T146N, C2 E123A T159C or N_pHR as well as a second fluorescent protein were created and tested in HEK cells and cultured neurons. Both Arch3 and the voltage-independent C_vRh mutant T46N were chosen for vesicular acidification by light-induced proton pumping. In contrast, the proton-selective C2 mutant was supposed to reduce the pH gradient over the vesicular membrane. To distinguish effects of vesicular membrane potential and pH, the microbial proton pumps were replaced by N_pHR.

Out of the four tested fusion proteins, Syphy-Arch3-mKate (pHoenix), Syphy-C_vRh T46N-mKate and Syphy-N_pHR-mKate show small outward-directed currents when expressed in HEK cells. While proper targeting of the respective proteins to the plasmamembrane is weak and most of the fluorescence is located at intracellular membranes e.g. at the endoplasmic reticulum, the fusion proteins are properly folded allowing for light-induced pumping activity. Despite a similar molecular composition, SypHTomato-C2 E123A T159C-eGFP displays very weak fluorescence and photocurrents are absent even after extended expression times and upon addition of excess retinal. The unfunctionality of the C2-derived variant might be explained by hampered dimer formation in the complex fusion protein. Notably, light-driven proton and chloride pumps typically form trimers, whereas archearhodopsin one and two have also been crystallized as dimers [260, 261, 262]. On the other hand, synaptophysin has been reported to form homodimers or heterodimers in conjunction with synaptobrevin [263]. Thus, the oligomeric state of the fusion proteins remains to be investigated.

Being expressed in cultured hippocampal neurons, pHoenix again triggers very low somatic photocurrents that are 260-fold reduced when compared to untargeted Arch3 currents (Figure 5.33F). Moreover, pHoenix accumulates in presynaptic terminals as

has been shown by colocalization with vGlut1 in glutamatergic neurons. Contrarily, Syphy-C_vRh T46N-mKate does not exhibit light-activated currents in neurons, despite higher performance compared to pHoenix in HEK cells. The molecular explanation for unfunctionality of both targeted and untargeted C_vRh in cultured neurons remains to be determined. Currently, Arend Vogt and Benjamin Rost are testing human codon-adapted C_vRh that may provide activity in neuronal cells. Syphy-N_pHR-mKate has not yet been tested for somatic currents in neurons, but is supposed to be funtional based on its activity in HEK cells and functionality of untargeted N_pHR in neurons [143, 70].

6.3.2. pHoenix activation for analysis of vesicular release properties

pHoenix enables green light-induced acidification of synaptic vesicles and can thus be applied to analyze the influence of vesicular pH on evoked and spontaneous transmitter release. Following light application for two minutes, EPSC amplitudes of pHoenix-expressing glutamatergic neurons are enhanced by $(11 \pm 2)\,\%$. Based on the currently available data, it cannot be distinguished if the increased amplitude is caused by an "overfilling" of single vesicles that would result in an increased mEPSC amplitude or if a decrease in vesicular pH enhances the vesicular release propability. Both analysis of the paired-pulse ratio as well as amplitude and frequency determination of single events are necessary to understand the underlying effects. Although these experiments demand for careful analysis due to low changes of the expected signals, they will be addressed in the near future. Together, the data may indicate how vesicle release is influenced by the neurotransmitter filling state of single vesicles.

In the following, pHoenix activation was analyzed in neurons that had been treated with bafilomycin, a specific blocker of the V-type ATPase that naturally acidifies synaptic vesicles following vesicle formation [235, 236]. After two hours of drug treatment, neurons exhibit only very low or no detectable EPSCs as almost all neurotransmitter-filled vesicles have been depleted and newly-formed vesicles have not been refilled. Light-induced pHoenix activation for two minutes restores full EPSC amplitudes in bafilomycin-treated glutamatergic neurons. This indicates that pHoenix-mediated vesicular acidification is sufficient for activation of vesicular glutamate transporters, whereas activation of untargeted Arch does not affect vesicle filling. Reduction of the intensity of the applied light to 25 % ($\approx 1.7 \times 10^{22}$ photons $m^{-2}s^{-1}$) does not reduce somatic Arch3 photocurrents in neurons. Similarly, pHoenix currents in HEK cells are only reduced by 17 % using 25 % light intensity. However, reduced light intensity decelerates EPSC recovery in bafilomycin-treated neurons, indicating that proton pumping is one of the rate-limiting steps of the EPSC recovery kinetics. In natural systems employing the V-type ATPase, proton pumping has been reported to be relatively fast (0.5 s to 5 s) when compared to neurotransmitter uptake (15 s in the case of glutamate) [176, 198].

Application of a two-pulse protocol at 25 % light intensity ($\approx 1.7 \times 10^{22}$ photons $m^{-2}s^{-1}$) allowed to further analyze release properties of partially filled vesicles. After 30 s of pHoenix activation EPSCs exhibit an intermediate amplitude that is stable as soon as light is turned off. Hence, glutamate uptake following acidification is faster than our

protocol-inherent time resolution of 5 s. Higher frequencies of EPSC monotoring may allow for determination of the phase lag between acidification and neurotransmitter uptake. Additional pHoenix activation for 90 s results in a saturated, 2.5-fold enhanced EPSC amplitude. Based on the different EPSC amplitudes vesicles are classified as "intermediate filled" or "full". The EPSC paired-pulse ratio in the full state is slightly reduced ($(6.2 \pm 2.8)\,\%$) when compared to the intermediate state, which can be interpreted as an increased release propability of the "full" vesicles. Moreover, both amplitude and frequency of miniature EPSCs, reflecting spontaneous vesicle exocytosis, are increased in the full state. These results confirm earlier findings by Zhou *et al.* who described a decrease in mEPSC/mIPSC amplitude and frequency in cultured bafilomycin-treated neurons when compared to untreated control cells [197]. In our experiments, different mEPSC amplitudes reflect the release of half-filled vesicles of the "intermediate" state, whereas "full" vesicles are maximally loaded with neurotransmitters. The interpretation of the frequency increase is more difficult, because release of empty and sparsely filled vesicles is not detectable using electrical mEPSC recordings. Notably, several earlier studies showed that the propability of vesicle release is independent of the vesicular filling level [264, 197]. But, since our experiments also reveal a reduced PPR of the full state, the increase in mEPSC frequency may at least partially be caused by a higher release propability of full vesicles. In order to clarify the influence of the filling state on vesicle-pool size and release propability, experiments combining step-wise pHoenix activation with application of hypertonic solutions might be helpful [265]. In summary, the presented experimental findings show that pHoenix is exceptionally well suited to analyze the influence of intravesicular pH on the neurotransmitter contents and the related release properties of synaptic vesicles. Moreover, our results propose that synaptic release propability indeed depends on the vesicular filling state, however this hypothesis needs further experimental validation.

6.3.3. Energetics of vesicular glutamate uptake

The driving forces for uptake of different neurotransmitters have been controversially discussed. In a recent review Omote *et al.* state that both glutamate and GABA uptake is predominantly driven by membrane potential differences $\Delta\psi$ whereas uptake of monoamines and acetylcholine relies on an additional pH gradient allowing for proton-neurotransmitter antiport [195]. The $\Delta\psi$ hypothesis for glutamate uptake is supported by the finding that exchange of vesicular protons by K^+ promotes vesicular glutamate transport [266]. In addition, computation of glutamate accumulation under the assumption that the electrical potential is the only driving force yields reasonable glutamate distributions reflecting measured values of $[glutamate]_{\text{vesicle}} / [glutamate]_{\text{cytosol}} \approx 10$ [195, 267]. Nevertheless, the intravesicular pH strongly affects VGlut transport activity as was pointed out in several other studies [196, 191].

To discriminate between $\Delta\psi$ and ΔpH-induced glutamate uptake, light-induced vesicle acidification using pHoenix was compared to light-driven Cl^- export mediated by Syphy-N_pHR-mKate. While pHoenix activation evokes increased EPSCs in both un-

treated and bafilomycin-treated neurons, Syphy-N_pHR-mKate activation did not influence EPSCs in our hands (data not shown). Notably, due to the preliminary state of our data, further control experiments are indispensable. Our results suggest that $\Delta\psi$ changes alone - as anticipated for Syphy-N_pHR-mKate activation - are insufficient to drive glutamate uptake. However, Cl^- itself has been suggested to directly bind VGluts, thereby activating glutamate transport and an intrinsic Cl^- conductance has been proposed for VGlut1 [268, 196]. Besides direct interactions with the transporters, decrease in intravesicular Cl^- concentration also results in increased vesicular pH [196, 195]. Thus, Cl^--induced changes in membrane potentials might be counteracted by other Cl^- -related effects. Whereas light-induced proton and Cl^- pumping equally modulate the electrical membrane potential, the induced changes in the respective chemical potentials are considerably different. Newly formed synaptic vesicles reflect the extracellular ionic composition and contain low amounts of protons ($< 1\,\mu M$) compared to high amounts of Cl^- ($\approx 125\,mM$). Therefore, significant acidification of synaptic vesicles is already achieved by few transported protons. Interestingly, an intravesicular pH of 6 corresponds to less than one free proton per vesicle [269]. In contrast, high vesicular chloride concentrations together with cytosolic chloride concentrations in the 10 mM range prevent significant N_pHR-mediated changes in the chemical potential for Cl^-. Thus, the abscence of changes in chemical potentials may account for the unfunctionalilty of Syphy-N_pHR-mKate to trigger glutamate uptake and changes in EPSC amplitudes. Taken together, our so-far available results do not support the common hypothesis of purely $\Delta\psi$-driven glutamate uptake. The presented experiments show how combinational application of different optogenetic actuators enables directed manipulation of cellular parameters in living cells. The interplay of light-activated manipulation and physiological read-outs may help to understand the complexitiy of cellular responses.

6.3.4. Outlook on presynaptic optogenetics

The first desribed presynaptic optogenetic tools encompass the pH indicators pHluorin, Syphy and pHTomato and the Ca^{2+} indicator SyGCamp [156, 172, 173, 161]. In the present study combination of Syphy with Arch3 yielded pHoenix, a green light-activated proton pump targeted to synaptic vesicles. Using electrical recordings on cultured, autapic neurons facilitates analysis of light-induced changes in postsynaptic currents. Additionally, pHoenix also allows for intravesicular pH imaging using the pH sensitivity of the superecliptic pHlourin fluorescence. In the next step, pH imaging will be used for direct visualization of Arch-induced vesicle acidification. Since pHlourin shows maximal activation using blue light and Arch is activated by green/yellow light, both fluorescence readout and Arch activation can be independently performed in priciple. However, independent activation demands for careful adjustment of the applied light intensities and activation of the characteristic β-band of rhodopsin absorption may result in minor Arch activation with blue light. To circumvent crosstalk of the actinic light sources, the use of a modified pHoenix variant that implies either a blue-shifted pHlourin (e.g. T-Sapphire) or a red-shifted Arch mutant might be useful [158]. Sequence comparison of Arch with

color-shifted proteorhodopsin mutants may facilitate the design of a red-shifted Arch variant. Alternatively, the use of an inverse pHoenix variant that contains a blue-shifted Arch e.g. Arch M126A S149A A223T combined with pHTomato should be considered to prevent β-band activation [240, 161]. Once experimentally implemented simultaneous pH imaging and electrical recordings will allow for correlation of intravesicular pH changes with postsynaptic reponses. Accordingly, the kinetics of vesicle acidification can be compared to the kinetics of consecutive processes of neurotransmitter uptake and vesicle priming.

Based on synaptophysin targeting, pHoenix is localized on synaptic vesicle membranes in mammalian neurons. Replacement of synaptophysin by the *C. elegans* protein synaptogyrin yielded synaptogyrin-pHoenix, potentially targeting to synaptic vesicles in nematodes. Due to their simple genetic manipulation and the mapping of the entire connectome of all 302 neurons, *C. elegans* represents one of the top model organisms to study synaptic transmission [270, 271]. Furthermore, *C. elegans* was the first eucaryotic organism that heterologously expressed the green-fluorescent protein GFP and represents the first transgenic animal expressing channelrhodopsin C2 H134R [272, 101]. Synaptogyrin-pHoenix functionally expresses in HEK cells and exhibits small light-induced currents indicating intracellular accumulation. In the future, synaptogyrin-pHoenix will be tested for light-induced vesicle acidification in living nematodes. Moreover, the fusion protein might be applied to compensate for developmental deficits in V-type ATPase-knockout animals [273].

Here, we demonstrate the first optogenetic application that specifically modulates presynaptic activity. However, the complex interplay of presynaptic proteins exposes diverse other targets for optogenetic manipulations. For example, optical control of protein interactions e.g. formation of SNARE complexes or nucleation of clathrin-mediated pits using light-activated dimerization systems might be complex, but highly interesting approaches [122, 123, 274]. In the same direction, presynaptically targeted, Ca^{2+}-selective ChRs (e.g. Catch+) may facilitate light activation of presynaptic vesicle release. Complementary, presynaptic expression of G-protein-coupled rhodopsins may allow to analyze presynaptic regulatory mechanisms [115, 116, 117, 275]. Similarly, presynaptic targeting of light-activated enzymes such as cAMP/cGMP cyclases might enable interrogation of the corresponding signaling cascades [126, 127]. Taken together, in conjunction with classical neurophysiological methods such as electrophysiology and imaging techniques, presynaptic optogenetics has a great potential to unravel principles of synaptic transmission.

Bibliography

[1] P. Hegemann, "Algal sensory photoreceptors.," *Annual review of plant biology*, vol. 59, pp. 167–89, Jan. 2008.

[2] J. Holton, *Encyclopedia of atmospheric sciences*. Amsterdam [u.a.]: Academic Press, 2003.

[3] A. Möglich, X. Yang, R. A. Ayers, and K. Moffat, "Structure and function of plant photoreceptors.," *Annual review of plant biology*, vol. 61, pp. 21–47, Jan. 2010.

[4] M. A. van der Horst and K. J. Hellingwerf, "Photoreceptor proteins, "star actors of modern times": a review of the functional dynamics in the structure of representative members of six different photoreceptor families.," *Accounts of chemical research*, vol. 37, pp. 13–20, Jan. 2004.

[5] M. Ikeuchi and T. Ishizuka, "Cyanobacteriochromes: a new superfamily of tetrapyrrole-binding photoreceptors in cyanobacteria.," *Photochemical & photobiological sciences : Official journal of the European Photochemistry Association and the European Society for Photobiology*, vol. 7, pp. 1159–67, Oct. 2008.

[6] R. Narikawa, T. Ishizuka, N. Muraki, T. Shiba, G. Kurisu, and M. Ikeuchi, "Structures of cyanobacteriochromes from phototaxis regulators AnPixJ and TePixJ reveal general and specific photoconversion mechanism.," *Proceedings of the National Academy of Sciences of the United States of America*, vol. 110, pp. 918–23, Jan. 2013.

[7] N. C. Rockwell, R. Ohlendorf, and A. Möglich, "Cyanobacteriochromes in full color and three dimensions.," *Proceedings of the National Academy of Sciences of the United States of America*, vol. 110, pp. 806–7, Jan. 2013.

[8] S. O. Mast, "The process of orientation in the colonial organism, Gonium pectorale, and a study of the structure and function of the eye-spot," *Journal of Experimental Zoology*, vol. 20, pp. 1–17, Jan. 1916.

[9] K. W. Foster and R. D. Smyth, "Light Antennas in phototactic algae.," *Microbiological reviews*, vol. 44, pp. 572–630, Dec. 1980.

[10] K. W. Foster, J. Saranak, N. Patel, G. Zarilli, M. Okabe, T. Kline, and K. Nakanishi, "A rhodopsin is the functional photoreceptor for phototaxis in the unicellular eukaryote Chlamydomonas.," *Nature*, vol. 311, no. 5988, pp. 756–9, 1984.

[11] M. Beckmann and P. Hegemann, "In vitro identification of rhodopsin in the green alga Chlamydomonas.," *Biochemistry*, vol. 30, pp. 3692–7, Apr. 1991.

[12] W. Deininger, P. Kröger, U. Hegemann, F. Lottspeich, and P. Hegemann, "Chlamyrhodopsin represents a new type of sensory photoreceptor.," *The EMBO journal*, vol. 14, pp. 5849–58, Dec. 1995.

[13] P. Hegemann, M. Fuhrmann, and S. Kateriya, "Algal Sensory Photoreceptors," *Journal of Phycology*, vol. 37, pp. 668–676, Oct. 2001.

[14] M. Fuhrmann, W. Deininger, S. Kateriya, and P. Hegemann, "Rhodopsin-related proteins, Cop1, Cop2 and Chop1, in Chlamydomonas reinhardtii," in *Photoreceptors and Light Signalling* (A. Batschauer, ed.), ch. 4, pp. 124–135, Royal Society of Chemistry, 2003.

[15] M. Calenberg, "Light- and Ca2+-Modulated Heterotrimeric GTPases in the Eyespot Apparatus of a Flagellate Green Alga," *The Plant Cell Online*, vol. 10, pp. 91–104, Jan. 1998.

[16] O. A. Sineshchekov, K.-H. Jung, and J. L. Spudich, "Two rhodopsins mediate phototaxis to low- and high-intensity light in Chlamydomonas reinhardtii.," *Proceedings of the National Academy of Sciences of the United States of America*, vol. 99, pp. 8689–94, June 2002.

[17] G. Nagel, D. Ollig, M. Fuhrmann, S. Kateriya, A. M. Musti, E. Bamberg, and P. Hegemann, "Channelrhodopsin-1: a light-gated proton channel in green algae.," *Science (New York, N.Y.)*, vol. 296, pp. 2395–8, June 2002.

[18] G. Nagel, T. Szellas, W. Huhn, S. Kateriya, N. Adeishvili, P. Berthold, D. Ollig, P. Hegemann, and E. Bamberg, "Channelrhodopsin-2, a directly light-gated cation-selective membrane channel.," *Proceedings of the National Academy of Sciences of the United States of America*, vol. 100, pp. 13940–5, Nov. 2003.

[19] T. Suzuki, K. Yamasaki, S. Fujita, K. Oda, M. Iseki, K. Yoshida, M. Watanabe, H. Daiyasu, H. Toh, E. Asamizu, S. Tabata, K. Miura, H. Fukuzawa, S. Nakamura, and T. Takahashi, "Archaeal-type rhodopsins in Chlamydomonas: model structure and intracellular localization," *Biochemical and Biophysical Research Communications*, vol. 301, pp. 711–717, Feb. 2003.

[20] H. Harz and P. Hegemann, "Rhodopsin-regulated calcium currents in Chlamydomonas," *Nature*, vol. 351, pp. 489–491, June 1991.

[21] S. Ehlenbeck, D. Gradmann, F.-J. Braun, and P. Hegemann, "Evidence for a light-induced H(+) conductance in the eye of the green alga Chlamydomonas reinhardtii.," *Biophysical journal*, vol. 82, pp. 740–51, Feb. 2002.

[22] F. J. Braun and P. Hegemann, "Two light-activated conductances in the eye of the green alga Volvox carteri.," *Biophysical journal*, vol. 76, pp. 1668–78, Mar. 1999.

[23] S. Kateriya, ""Vision" in Single-Celled Algae," *News in Physiological Sciences*, vol. 19, pp. 133–137, June 2004.

[24] B. Zorin, Y. Lu, I. Sizova, and P. Hegemann, "Nuclear gene targeting in Chlamydomonas as exemplified by disruption of the PHOT gene.," *Gene*, vol. 432, pp. 91–6, Mar. 2009.

[25] I. Sizova, A. Greiner, M. Awasthi, S. Kateriya, and P. Hegemann, "Nuclear gene targeting in Chlamydomonas using engineered zinc-finger nucleases.," *The Plant journal : for cell and molecular biology*, Nov. 2012.

[26] F. Zhang, J. Vierock, O. Yizhar, L. E. Fenno, S. Tsunoda, A. Kianianmomeni, M. Prigge, A. Berndt, J. Cushman, J. Polle, J. Magnuson, P. Hegemann, and K. Deisseroth, "The microbial opsin family of optogenetic tools.," *Cell*, vol. 147, pp. 1446–57, Dec. 2011.

[27] M. Luck, T. Mathes, S. Bruun, R. Fudim, R. Hagedorn, T. M. Tran Nguyen, S. Kateriya, J. T. M. Kennis, P. Hildebrandt, and P. Hegemann, "A photochromic histidine kinase rhodopsin (HKR1) that is bimodally switched by ultraviolet and blue light.," *The Journal of biological chemistry*, vol. 287, pp. 40083–90, Nov. 2012.

[28] K. Huang and C. F. Beck, "Phototropin is the blue-light receptor that controls multiple steps in the sexual life cycle of the green alga Chlamydomonas reinhardtii.," *Proceedings of the National Academy of Sciences of the United States of America*, vol. 100, pp. 6269–74, May 2003.

[29] K. Huang, T. Kunkel, and C. F. Beck, "Localization of the blue-light receptor phototropin to the flagella of the green alga Chlamydomonas reinhardtii.," *Molecular biology of the cell*, vol. 15, pp. 3605–14, Aug. 2004.

[30] C.-S. Im, S. Eberhard, K. Huang, C. F. Beck, and A. R. Grossman, "Phototropin involvement in the expression of genes encoding chlorophyll and carotenoid biosynthesis enzymes and LHC apoproteins in Chlamydomonas reinhardtii.," *The Plant journal : for cell and molecular biology*, vol. 48, pp. 1–16, Oct. 2006.

[31] E. V. Ermilova, Z. M. Zalutskaya, K. Huang, and C. F. Beck, "Phototropin plays a crucial role in controlling changes in chemotaxis during the initial phase of the sexual life cycle in Chlamydomonas.," *Planta*, vol. 219, pp. 420–7, July 2004.

[32] J. Trippens, A. Greiner, J. Schellwat, M. Neukam, T. Rottmann, Y. Lu, S. Kateriya, P. Hegemann, and G. Kreimer, "Phototropin influence on eyespot development and regulation of phototactic behavior in Chlamydomonas reinhardtii.," *The Plant Cell*, vol. 24, pp. 4687–702, Nov. 2012.

[33] N. A. Reisdorph and G. D. Small, "The CPH1 gene of Chlamydomonas reinhardtii encodes two forms of cryptochrome whose levels are controlled by light-induced proteolysis.," *Plant physiology*, vol. 134, pp. 1546–54, Apr. 2004.

[34] B. Beel, K. Prager, M. Spexard, S. Sasso, D. Weiss, N. Müller, M. Heinnickel, D. Dewez, D. Ikoma, A. R. Grossman, T. Kottke, and M. Mittag, "A flavin binding cryptochrome photoreceptor responds to both blue and red light in Chlamydomonas reinhardtii.," *The Plant Cell*, vol. 24, pp. 2992–3008, July 2012.

[35] D. L. Kirk, *Volvox: A Search for the Molecular and Genetic Origins of Multicellularity and Cellular Differentiation*. Cambridge University Press, 2005.

[36] O. P. Ernst, P. A. Sánchez Murcia, P. Daldrop, S. P. Tsunoda, S. Kateriya, and P. Hegemann, "Photoactivation of channelrhodopsin.," *The Journal of biological chemistry*, vol. 283, pp. 1637–43, Jan. 2008.

[37] F. Zhang, M. Prigge, F. Beyrière, S. P. Tsunoda, J. Mattis, O. Yizhar, P. Hegemann, and K. Deisseroth, "Red-shifted optogenetic excitation: a tool for fast neural control derived from Volvox carteri.," *Nature neuroscience*, vol. 11, pp. 631–3, June 2008.

[38] A. Kianianmomeni, K. Stehfest, G. Nematollahi, P. Hegemann, and A. Hallmann, "Channelrhodopsins of Volvox carteri are photochromic proteins that are specifically expressed in somatic cells under control of light, temperature, and the sex inducer.," *Plant physiology*, vol. 151, pp. 347–66, Sept. 2009.

[39] E. Ebnet, "Volvoxrhodopsin, a Light-Regulated Sensory Photoreceptor of the Spheroidal Green Alga Volvox carteri," *The Plant Cell Online*, vol. 11, pp. 1473–1484, Aug. 1999.

[40] S. E. Prochnik, J. Umen, A. M. Nedelcu, A. Hallmann, S. M. Miller, I. Nishii, P. Ferris, A. Kuo, T. Mitros, L. K. Fritz-Laylin, U. Hellsten, J. Chapman, O. Simakov, S. A. Rensing, A. Terry, J. Pangilinan, V. Kapitonov, J. Jurka, A. Salamov, H. Shapiro, J. Schmutz, J. Grimwood, E. Lindquist, S. Lucas, I. V. Grigoriev, R. Schmitt, D. Kirk, and D. S. Rokhsar, "Genomic analysis of organismal complexity in the multicellular green alga Volvox carteri.," *Science (New York, N.Y.)*, vol. 329, pp. 223–6, July 2010.

[41] J. L. Spudich, C. S. Yang, K. H. Jung, and E. N. Spudich, "Retinylidene proteins: structures and functions from archaea to humans.," *Annual review of cell and developmental biology*, vol. 16, pp. 365–92, Jan. 2000.

[42] J. K. Lanyi and B. Schobert, "Structural changes in the L photointermediate of bacteriorhodopsin.," *Journal of molecular biology*, vol. 365, pp. 1379–92, Feb. 2007.

[43] H. J. de Groot, G. S. Harbison, J. Herzfeld, and R. G. Griffin, "Nuclear magnetic resonance study of the Schiff base in bacteriorhodopsin: counterion effects on the 15N shift anisotropy.," *Biochemistry*, vol. 28, pp. 3346–53, Apr. 1989.

[44] R. Needleman, M. Chang, B. Ni, G. Varo, J. Fornes, S. White, and J. Lanyi, "Properties of Asp212—-Asn bacteriorhodopsin suggest that Asp212 and Asp85 both participate in a counterion and proton acceptor complex near the Schiff base," *J. Biol. Chem.*, vol. 266, pp. 11478–11484, June 1991.

[45] T. Marti, S. J. Rösselet, H. Otto, M. P. Heyn, and H. G. Khorana, "The retinylidene Schiff base counterion in bacteriorhodopsin.," *The Journal of biological chemistry*, vol. 266, pp. 18674–83, Oct. 1991.

[46] M. S. Braiman, T. Mogi, T. Marti, L. J. Stern, H. G. Khorana, and K. J. Rothschild, "Vibrational spectroscopy of bacteriorhodopsin mutants: light-driven proton transport involves protonation changes of aspartic acid residues 85, 96, and 212.," *Biochemistry*, vol. 27, pp. 8516–20, Nov. 1988.

[47] K. Gerwert, B. Hess, J. Soppa, and D. Oesterhelt, "Role of aspartate-96 in proton translocation by bacteriorhodopsin.," *Proceedings of the National Academy of Sciences of the United States of America*, vol. 86, pp. 4943–7, July 1989.

[48] K. Gerwert, G. Souvignier, and B. Hess, "Simultaneous monitoring of light-induced changes in protein side-group protonation, chromophore isomerization, and backbone motion of bacteriorhodopsin by time-resolved Fourier-transform infrared spectroscopy.," *Proceedings of the National Academy of Sciences of the United States of America*, vol. 87, pp. 9774–8, Dec. 1990.

[49] S. O. Smith, J. Lugtenburg, and R. A. Mathies, "Determination of retinal chromophore structure in bacteriorhodopsin with resonance Raman spectroscopy," *The Journal of Membrane Biology*, vol. 85, pp. 95–109, June 1985.

[50] J. Sasaki and J. L. Spudich, "Signal transfer in haloarchaeal sensory rhodopsin- transducer complexes.," *Photochemistry and photobiology*, vol. 84, no. 4, pp. 863–8, 2008.

[51] D. Oesterhelt and W. Stoeckenius, "Rhodopsin-like Protein from the Purple Membrane of Halobacterium halobium," *Nature*, vol. 233, pp. 149–152, Sept. 1971.

[52] O. Béjà, L. Aravind, E. V. Koonin, M. T. Suzuki, A. Hadd, L. P. Nguyen, S. B. Jovanovich, C. M. Gates, R. A. Feldman, J. L. Spudich, E. N. Spudich, and E. F. DeLong, "Bacterial rhodopsin: evidence for a new type of phototrophy in the sea.," *Science (New York, N.Y.)*, vol. 289, pp. 1902–6, Sept. 2000.

[53] S. P. Balashov, E. S. Imasheva, V. A. Boichenko, J. Antón, J. M. Wang, and J. K. Lanyi, "Xanthorhodopsin: a proton pump with a light-harvesting carotenoid antenna.," *Science (New York, N.Y.)*, vol. 309, pp. 2061–4, Sept. 2005.

[54] R. H. Lozier, R. A. Bogomolni, and W. Stoeckenius, "Bacteriorhodopsin: a light-driven proton pump in Halobacterium Halobium.," *Biophysical journal*, vol. 15, pp. 955–62, Sept. 1975.

[55] J. K. Lanyi, "Bacteriorhodopsin.," *Annual review of physiology*, vol. 66, pp. 665–88, Jan. 2004.

[56] L. Drachev, A. Kaulen, and V. Skulachev, "Correlation of photochemical cycle, H+ release and uptake, and electric events in bacteriorhodopsin," *FEBS Letters*, vol. 178, pp. 331–335, Dec. 1984.

[57] S. Grzesiek and N. A. Dencher, "Time-course and stoichiometry of light-induced proton release and uptake during the photocycle of bacteriorhodopsin," *FEBS Letters*, vol. 208, pp. 337–342, Nov. 1986.

[58] Y. Cao, G. Váró, M. Chang, B. F. Ni, R. Needleman, and J. K. Lanyi, "Water is required for proton transfer from aspartate-96 to the bacteriorhodopsin Schiff base.," *Biochemistry*, vol. 30, pp. 10972–9, Nov. 1991.

[59] A. K. Dioumaev, L. S. Brown, R. Needleman, and J. K. Lanyi, "Coupling of the reisomerization of the retinal, proton uptake, and reprotonation of Asp-96 in the N photointermediate of bacteriorhodopsin.," *Biochemistry*, vol. 40, pp. 11308–17, Sept. 2001.

[60] A. Wand, N. Friedman, M. Sheves, and S. Ruhman, "Ultrafast photochemistry of light-adapted and dark-adapted bacteriorhodopsin: effects of the initial retinal configuration.," *The journal of physical chemistry. B*, vol. 116, pp. 10444–52, Sept. 2012.

[61] G. Nagel, T. Szellas, S. Kateriya, N. Adeishvili, P. Hegemann, and E. Bamberg, "Channelrhodopsins: directly light-gated cation channels.," *Biochemical Society transactions*, vol. 33, pp. 863–6, Aug. 2005.

[62] O. Béjà, E. N. Spudich, J. L. Spudich, M. Leclerc, and E. F. DeLong, "Proteorhodopsin phototrophy in the ocean.," *Nature*, vol. 411, pp. 786–9, June 2001.

[63] D. Man, W. Wang, G. Sabehi, L. Aravind, A. F. Post, R. Massana, E. N. Spudich, J. L. Spudich, and O. Béjà, "Diversification and spectral tuning in marine proteorhodopsins.," *The EMBO journal*, vol. 22, pp. 1725–31, Apr. 2003.

[64] J. P. Bielawski, K. A. Dunn, G. Sabehi, and O. Béjà, "Darwinian adaptation of proteorhodopsin to different light intensities in the marine environment.," *Proceedings of the National Academy of Sciences of the United States of America*, vol. 101, pp. 14824–9, Oct. 2004.

[65] H. Luecke, B. Schobert, J. K. Lanyi, E. N. Spudich, and J. L. Spudich, "Crystal structure of sensory rhodopsin II at 2.4 angstroms: insights into color tuning and transducer interaction.," *Science (New York, N.Y.)*, vol. 293, pp. 1499–503, Aug. 2001.

[66] A. Matsuno-Yagi and Y. Mukohata, "Two possible roles of bacteriorhodopsin; a comparative study of strains of Halobacterium halobium differing in pigmentation," *Biochemical and Biophysical Research Communications*, vol. 78, pp. 237–243, Sept. 1977.

[67] B. Schobert and J. K. Lanyi, "Halorhodopsin is a light-driven chloride pump.," *The Journal of biological chemistry*, vol. 257, pp. 10306–13, Sept. 1982.

[68] I. Chizhov and M. Engelhard, "Temperature and halide dependence of the photocycle of halorhodopsin from Natronobacterium pharaonis.," *Biophysical journal*, vol. 81, pp. 1600–12, Sept. 2001.

[69] L.-O. Essen, "Halorhodopsin: light-driven ion pumping made simple?," *Current Opinion in Structural Biology*, vol. 12, pp. 516–522, Aug. 2002.

[70] F. Zhang, L.-P. Wang, M. Brauner, J. F. Liewald, K. Kay, N. Watzke, P. G. Wood, E. Bamberg, G. Nagel, A. Gottschalk, and K. Deisseroth, "Multimodal fast optical interrogation of neural circuitry.," *Nature*, vol. 446, pp. 633–9, Apr. 2007.

[71] A. Seki, S. Miyauchi, S. Hayashi, T. Kikukawa, M. Kubo, M. Demura, V. Ganapathy, and N. Kamo, "Heterologous Expression of Pharaonis Halorhodopsin in Xenopus laevis Oocytes and Electrophysiological Characterization of Its Light-Driven Cl^- Pump Activity," *Biophysical Journal*, vol. 92, no. 7, pp. 2559–2569, 2007.

[72] E. G. Govorunova, E. N. Spudich, C. E. Lane, O. A. Sineshchekov, and J. L. Spudich, "New channelrhodopsin with a red-shifted spectrum and rapid kinetics from Mesostigma viride.," *mBio*, vol. 2, pp. e00115–11, Jan. 2011.

[73] S.-Y. Hou, E. G. Govorunova, M. Ntefidou, C. E. Lane, E. N. Spudich, O. A. Sineshchekov, and J. L. Spudich, "Diversity of Chlamydomonas channelrhodopsins.," *Photochemistry and photobiology*, vol. 88, no. 1, pp. 119–28, 2011.

[74] H. E. Kato, F. Zhang, O. Yizhar, C. Ramakrishnan, T. Nishizawa, K. Hirata, J. Ito, Y. Aita, T. Tsukazaki, S. Hayashi, P. Hegemann, A. D. Maturana, R. Ishitani, K. Deisseroth, and O. Nureki, "Crystal structure of the channelrhodopsin light-gated cation channel.," *Nature*, vol. 482, pp. 369–74, Feb. 2012.

[75] H. C. Watanabe, K. Welke, F. Schneider, S. Tsunoda, F. Zhang, K. Deisseroth, P. Hegemann, and M. Elstner, "Structural model of channelrhodopsin.," *The Journal of Biological Chemistry*, vol. 287, no. 10, pp. 7456–7466, 2012.

[76] N. Klapoetke, B. Y. Chow, E. Boyden, G. K.-S. Wong, and Y. P. Cho, "Channelrhodopsins for optical control of cells," May 2013.

[77] M. Müller, C. Bamann, E. Bamberg, and W. Kühlbrandt, "Projection structure of channelrhodopsin-2 at 6 Å resolution by electron crystallography.," *Journal of molecular biology*, vol. 414, pp. 86–95, Nov. 2011.

[78] H. Wang, Y. Sugiyama, T. Hikima, E. Sugano, H. Tomita, T. Takahashi, T. Ishizuka, and H. Yawo, "Molecular determinants differentiating photocurrent properties of two channelrhodopsins from chlamydomonas.," *The Journal of biological chemistry*, vol. 284, pp. 5685–96, Mar. 2009.

[79] S. P. Tsunoda and P. Hegemann, "Glu 87 of channelrhodopsin-1 causes pH-dependent color tuning and fast photocurrent inactivation.," *Photochemistry and photobiology*, vol. 85, no. 2, pp. 564–9, 2009.

[80] J. Y. Lin, M. Z. Lin, P. Steinbach, and R. Y. Tsien, "Characterization of engineered channelrhodopsin variants with improved properties and kinetics.," *Biophysical journal*, vol. 96, pp. 1803–14, Mar. 2009.

[81] E. Neher, B. Sakmann, and J. H. Steinbach, "The extracellular patch clamp: a method for resolving currents through individual open channels in biological membranes.," *Pflügers Archiv : European journal of physiology*, vol. 375, pp. 219–28, July 1978.

[82] E. Neher and B. Sakmann, "The patch clamp technique.," *Scientific American*, vol. 266, pp. 44–51, Mar. 1992.

[83] K. Feldbauer, D. Zimmermann, V. Pintschovius, J. Spitz, C. Bamann, and E. Bamberg, "Channelrhodopsin-2 is a leaky proton pump.," *Proceedings of the National Academy of Sciences of the United States of America*, vol. 106, pp. 12317–22, July 2009.

[84] P. Hegemann, S. Ehlenbeck, and D. Gradmann, "Multiple photocycles of channelrhodopsin.," *Biophysical journal*, vol. 89, pp. 3911–8, Dec. 2005.

[85] K. Nikolic, N. Grossman, M. S. Grubb, J. Burrone, C. Toumazou, and P. Degenaar, "Photocycles of channelrhodopsin-2.," *Photochemistry and photobiology*, vol. 85, no. 1, pp. 400–11, 2009.

[86] A. Berndt, M. Prigge, D. Gradmann, and P. Hegemann, "Two open states with progressive proton selectivities in the branched channelrhodopsin-2 photocycle.," *Biophysical journal*, vol. 98, pp. 753–61, Mar. 2010.

[87] M. Prigge, F. Schneider, S. P. Tsunoda, C. Shilyansky, J. Wietek, K. Deisseroth, and P. Hegemann, "Color-tuned Channelrhodopsins for Multiwavelength Optogenetics.," *The Journal of biological chemistry*, 2012.

[88] F. Schneider, *Modifikationen an Volvox-Kanalrhodopsin 1 zur Verbesserung von Expression und Farbverschiebung*. Diploma thesis, Humboldt Universität zu Berlin, 2009.

[89] E. Ritter, K. Stehfest, A. Berndt, P. Hegemann, and F. J. Bartl, "Monitoring light-induced structural changes of Channelrhodopsin-2 by UV-visible and Fourier transform infrared spectroscopy.," *The Journal of biological chemistry*, vol. 283, pp. 35033–41, Dec. 2008.

[90] M.-K. Verhoefen, C. Bamann, R. Blöcher, U. Förster, E. Bamberg, and J. Wachtveitl, "The photocycle of channelrhodopsin-2: ultrafast reaction dynamics and subsequent reaction steps.," *Chemphyschem : a European journal of chemical physics and physical chemistry*, vol. 11, pp. 3113–22, Oct. 2010.

[91] V. A. Lórenz-Fonfría, T. Resler, N. Krause, M. Nack, M. Gossing, G. Fischer von Mollard, C. Bamann, E. Bamberg, R. Schlesinger, and J. Heberle, "Transient protonation changes in channelrhodopsin-2 and their relevance to channel gating.," *Proceedings of the National Academy of Sciences of the United States of America*, vol. 110, pp. E1273–81, Apr. 2013.

[92] C. Bamann, T. Kirsch, G. Nagel, and E. Bamberg, "Spectral characteristics of the photocycle of channelrhodopsin-2 and its implication for channel function.," *Journal of molecular biology*, vol. 375, pp. 686–94, Jan. 2008.

[93] K. Stehfest and P. Hegemann, "Evolution of the channelrhodopsin photocycle model.," *Chemphyschem : a European journal of chemical physics and physical chemistry*, vol. 11, pp. 1120–6, Apr. 2010.

[94] K. Eisenhauer, J. Kuhne, E. Ritter, A. Berndt, S. Wolf, E. Freier, F. Bartl, P. Hegemann, and K. Gerwert, "In channelrhodopsin-2 Glu-90 is crucial for ion selectivity and is deprotonated during the photocycle.," *The Journal of biological chemistry*, vol. 287, pp. 6904–11, Feb. 2012.

[95] K. Stehfest, E. Ritter, A. Berndt, F. Bartl, and P. Hegemann, "The branched photocycle of the slow-cycling channelrhodopsin-2 mutant C128T.," *Journal of molecular biology*, vol. 398, pp. 690–702, May 2010.

[96] I. Radu, C. Bamann, M. Nack, G. Nagel, E. Bamberg, and J. Heberle, "Conformational changes of channelrhodopsin-2.," *Journal of the American Chemical Society*, vol. 131, pp. 7313–9, June 2009.

[97] E. Ritter, P. Piwowarski, P. Hegemann, and F. J. Bartl, "Light-dark adaptation of channelrhodopsin C128T mutant.," *The Journal of biological chemistry*, vol. 288, pp. 10451–8, Apr. 2013.

[98] L. A. Gunaydin, O. Yizhar, A. Berndt, V. S. Sohal, K. Deisseroth, and P. Hegemann, "Ultrafast optogenetic control.," *Nature neuroscience*, vol. 13, pp. 387–92, Mar. 2010.

[99] A. Berndt, P. Schoenenberger, J. Mattis, K. M. Tye, K. Deisseroth, P. Hegemann, and T. G. Oertner, "High-efficiency channelrhodopsins for fast neuronal stimulation at low light levels," *Proc Natl Acad Sci U S A*, vol. 108, no. 18, pp. 7595–7600, 2011.

[100] D. Gradmann, A. Berndt, F. Schneider, and P. Hegemann, "Rectification of the channelrhodopsin early conductance.," *Biophysical journal*, vol. 101, pp. 1057–68, Sept. 2011.

[101] G. Nagel, M. Brauner, J. F. Liewald, N. Adeishvili, E. Bamberg, and A. Gottschalk, "Light activation of channelrhodopsin-2 in excitable cells of Caenorhabditis elegans triggers rapid behavioral responses.," *Current biology : CB*, vol. 15, pp. 2279–84, Dec. 2005.

[102] A. Berndt, O. Yizhar, L. A. Gunaydin, P. Hegemann, and K. Deisseroth, "Bi-stable neural state switches.," *Nature neuroscience*, vol. 12, pp. 229–34, Feb. 2009.

[103] C. Bamann, R. Gueta, S. Kleinlogel, G. Nagel, and E. Bamberg, "Structural guidance of the photocycle of channelrhodopsin-2 by an interhelical hydrogen bond.," *Biochemistry*, vol. 49, pp. 267–78, Jan. 2010.

[104] S. Bruun, H. Naumann, U. Kuhlmann, C. Schulz, K. Stehfest, P. Hegemann, and P. Hildebrandt, "The chromophore structure of the long-lived intermediate of the C128T channelrhodopsin-2 variant.," *FEBS letters*, vol. 585, pp. 3998–4001, Dec. 2011.

[105] M. Nack, I. Radu, C. Bamann, E. Bamberg, and J. Heberle, "The retinal structure of channelrhodopsin-2 assessed by resonance Raman spectroscopy.," *FEBS letters*, vol. 583, pp. 3676–80, Nov. 2009.

[106] H. Luecke, B. Schobert, H. T. Richter, J. P. Cartailler, and J. K. Lanyi, "Structure of bacteriorhodopsin at 1.55 A resolution.," *Journal of molecular biology*, vol. 291, pp. 899–911, Aug. 1999.

[107] H. C. Watanabe, K. Welke, D. J. Sindhikara, P. Hegemann, and M. Elstner, "Towards an understanding of Channelrhodopsin function: Simulations lead to novel insights of the channel mechanism.," *Journal of molecular biology*, Jan. 2013.

[108] O. Yizhar, L. E. Fenno, M. Prigge, F. Schneider, T. J. Davidson, D. J. O'Shea, V. S. Sohal, I. Goshen, J. Finkelstein, J. T. Paz, K. Stehfest, R. Fudim, C. Ramakrishnan, J. R. Huguenard, P. Hegemann, and K. Deisseroth, "Neocortical excitation/inhibition balance in information processing and social dysfunction.," *Nature*, vol. 477, no. 7363, pp. 171–178, 2011.

[109] S. Ullrich, R. Gueta, and G. Nagel, "Degradation of channelopsin-2 in the absence of retinal and degradation resistance in certain mutants.," *Biological chemistry*, Nov. 2012.

[110] S. Kleinlogel, K. Feldbauer, R. E. Dempski, H. Fotis, P. G. Wood, C. Bamann, and E. Bamberg, "Ultra light-sensitive and fast neuronal activation with the Ca^{2+}-permeable channelrhodopsin CatCh.," *Nature neuroscience*, vol. 14, pp. 513–8, Apr. 2011.

[111] L. Wen, H. Wang, S. Tanimoto, R. Egawa, Y. Matsuzaka, H. Mushiake, T. Ishizuka, and H. Yawo, "Opto-Current-Clamp Actuation of Cortical Neurons Using a Strategically Designed Channelrhodopsin," *PLoS ONE*, vol. 5, p. e12893, Sept. 2010.

[112] K. Deisseroth, G. Feng, A. K. Majewska, G. Miesenböck, A. Ting, and M. J. Schnitzer, "Next-generation optical technologies for illuminating genetically targeted brain circuits.," *The Journal of neuroscience : the official journal of the Society for Neuroscience*, vol. 26, pp. 10380–6, Oct. 2006.

[113] G. Miesenböck, "The optogenetic catechism.," *Science (New York, N.Y.)*, vol. 326, pp. 395–9, Oct. 2009.

[114] E. Pastrana, "Optogenetics: controlling cell function with light," *Nature Methods*, vol. 8, pp. 24–25, Dec. 2010.

[115] B. V. Zemelman, G. A. Lee, M. Ng, and G. Miesenböck, "Selective photostimulation of genetically chARGed neurons.," *Neuron*, vol. 33, pp. 15–22, Jan. 2002.

[116] J.-M. Kim, J. Hwa, P. Garriga, P. J. Reeves, U. L. RajBhandary, and H. G. Khorana, "Light-driven activation of beta 2-adrenergic receptor signaling by a chimeric rhodopsin containing the beta 2-adrenergic receptor cytoplasmic loops.," *Biochemistry*, vol. 44, pp. 2284–92, Mar. 2005.

[117] R. D. Airan, K. R. Thompson, L. E. Fenno, H. Bernstein, and K. Deisseroth, "Temporally precise in vivo control of intracellular signalling," *Nature*, vol. 458, pp. 1025–1029, Mar. 2009.

[118] D. Strickland, K. Moffat, and T. R. Sosnick, "Light-activated DNA binding in a designed allosteric protein.," *Proceedings of the National Academy of Sciences of the United States of America*, vol. 105, pp. 10709–14, Aug. 2008.

[119] Y. I. Wu, D. Frey, O. I. Lungu, A. Jaehrig, I. Schlichting, B. Kuhlman, and K. M. Hahn, "A genetically encoded photoactivatable Rac controls the motility of living cells.," *Nature*, vol. 461, pp. 104–8, Sept. 2009.

[120] A. Möglich, R. A. Ayers, and K. Moffat, "Design and signaling mechanism of light-regulated histidine kinases.," *Journal of molecular biology*, vol. 385, pp. 1433–44, Mar. 2009.

[121] S. Shimizu-Sato, E. Huq, J. M. Tepperman, and P. H. Quail, "A light-switchable gene promoter system.," *Nature biotechnology*, vol. 20, pp. 1041–4, Oct. 2002.

[122] M. Yazawa, A. M. Sadaghiani, B. Hsueh, and R. E. Dolmetsch, "Induction of protein-protein interactions in live cells using light.," *Nature biotechnology*, vol. 27, pp. 941–5, Oct. 2009.

[123] A. Levskaya, O. D. Weiner, W. A. Lim, and C. A. Voigt, "Spatiotemporal control of cell signalling using a light-switchable protein interaction.," *Nature*, vol. 461, pp. 997–1001, Oct. 2009.

[124] M. J. Kennedy, R. M. Hughes, L. A. Peteya, J. W. Schwartz, M. D. Ehlers, and C. L. Tucker, "Rapid blue-light-mediated induction of protein interactions in living cells.," *Nature methods*, vol. 7, pp. 973–5, Dec. 2010.

[125] D. Strickland, Y. Lin, E. Wagner, C. M. Hope, J. Zayner, C. Antoniou, T. R. Sosnick, E. L. Weiss, and M. Glotzer, "TULIPs: tunable, light-controlled interacting protein tags for cell biology.," *Nature methods*, vol. 9, pp. 379–84, May 2012.

[126] S. Schröder-Lang, M. Schwärzel, R. Seifert, T. Strünker, S. Kateriya, J. Looser, M. Watanabe, U. B. Kaupp, P. Hegemann, and G. Nagel, "Fast manipulation of cellular cAMP level by light in vivo.," *Nature methods*, vol. 4, pp. 39–42, Jan. 2007.

[127] M. Stierl, P. Stumpf, D. Udwari, R. Gueta, R. Hagedorn, A. Losi, W. Gärtner, L. Petereit, M. Efetova, M. Schwarzel, T. G. Oertner, G. Nagel, and P. Hegemann, "Light modulation of cellular cAMP by a small bacterial photoactivated adenylyl cyclase, bPAC, of the soil bacterium Beggiatoa.," *The Journal of biological chemistry*, vol. 286, pp. 1181–8, Jan. 2011.

[128] H. G. Khorana, B. E. Knox, E. Nasi, R. Swanson, and D. A. Thompson, "Expression of a bovine rhodopsin gene in Xenopus oocytes: demonstration of light-dependent ionic currents.," *Proceedings of the National Academy of Sciences of the United States of America*, vol. 85, pp. 7917–21, Nov. 1988.

[129] E. S. Boyden, F. Zhang, E. Bamberg, G. Nagel, and K. Deisseroth, "Millisecond-timescale, genetically targeted optical control of neural activity.," *Nature neuroscience*, vol. 8, pp. 1263–8, Sept. 2005.

[130] T. Ishizuka, M. Kakuda, R. Araki, and H. Yawo, "Kinetic evaluation of photosensitivity in genetically engineered neurons expressing green algae light-gated channels.," *Neuroscience research*, vol. 54, pp. 85–94, Feb. 2006.

[131] F. Zhang, A. M. Aravanis, A. Adamantidis, L. de Lecea, and K. Deisseroth, "Circuit-breakers: optical technologies for probing neural signals and systems.," *Nature reviews. Neuroscience*, vol. 8, pp. 577–81, Aug. 2007.

[132] L. Petreanu, D. Huber, A. Sobczyk, and K. Svoboda, "Channelrhodopsin-2-assisted circuit mapping of long-range callosal projections.," *Nature neuroscience*, vol. 10, pp. 663–8, May 2007.

[133] X. Li, D. V. Gutierrez, M. G. Hanson, J. Han, M. D. Mark, H. Chiel, P. Hegemann, L. T. Landmesser, and S. Herlitze, "Fast noninvasive activation and inhibition of neural and network activity by vertebrate rhodopsin and green algae channelrhodopsin.," *Proceedings of the National Academy of Sciences of the United States of America*, vol. 102, pp. 17816–21, Dec. 2005.

[134] C. Schroll, T. Riemensperger, D. Bucher, J. Ehmer, T. Völler, K. Erbguth, B. Gerber, T. Hendel, G. Nagel, E. Buchner, and A. Fiala, "Light-induced activation of distinct modulatory neurons triggers appetitive or aversive learning in Drosophila larvae.," *Current biology : CB*, vol. 16, pp. 1741–7, Oct. 2006.

[135] B. R. Arenkiel, J. Peca, I. G. Davison, C. Feliciano, K. Deisseroth, G. J. Augustine, M. D. Ehlers, and G. Feng, "In vivo light-induced activation of neural circuitry in transgenic mice expressing channelrhodopsin-2.," *Neuron*, vol. 54, pp. 205–18, Apr. 2007.

[136] A. Bi, J. Cui, Y.-P. Ma, E. Olshevskaya, M. Pu, A. M. Dizhoor, and Z.-H. Pan, "Ectopic expression of a microbial-type rhodopsin restores visual responses in mice with photoreceptor degeneration.," *Neuron*, vol. 50, pp. 23–33, May 2006.

[137] V. Gradinaru, M. Mogri, K. R. Thompson, J. M. Henderson, and K. Deisseroth, "Optical deconstruction of parkinsonian neural circuitry.," *Science (New York, N.Y.)*, vol. 324, pp. 354–9, Apr. 2009.

[138] T. Shimano, B. Fyk-Kolodziej, N. Mirza, M. Asako, K. Tomoda, S. Bledsoe, Z.-H. Pan, S. Molitor, and A. G. Holt, "Assessment of the AAV-mediated expression of channelrhodopsin-2 and halorhodopsin in brainstem neurons mediating auditory signaling.," *Brain research*, vol. 1511, pp. 138–52, May 2013.

[139] A. B. Arrenberg, D. Y. R. Stainier, H. Baier, and J. Huisken, "Optogenetic control of cardiac function.," *Science (New York, N.Y.)*, vol. 330, pp. 971–4, Nov. 2010.

[140] T. Bruegmann, D. Malan, M. Hesse, T. Beiert, C. J. Fuegemann, B. K. Fleischmann, and P. Sasse, "Optogenetic control of heart muscle in vitro and in vivo.," *Nature methods*, vol. 7, pp. 897–900, Dec. 2010.

[141] A. N. Yaroslavsky, P. C. Schulze, I. V. Yaroslavsky, R. Schober, F. Ulrich, and H.-J. Schwarzmaier, "Optical properties of selected native and coagulated human brain tissues in vitro in the visible and near infrared spectral range," *Physics in Medicine and Biology*, vol. 47, pp. 2059–2073, June 2002.

[142] S. L. Jacques, "Optical properties of biological tissues: a review.," *Physics in medicine and biology*, vol. 58, pp. R37–61, June 2013.

[143] X. Han and E. S. Boyden, "Multiple-color optical activation, silencing, and desynchronization of neural activity, with single-spike temporal resolution.," *PloS one*, vol. 2, p. e299, Jan. 2007.

[144] V. Gradinaru, K. R. Thompson, and K. Deisseroth, "eNpHR: a Natronomonas halorhodopsin enhanced for optogenetic applications.," *Brain cell biology*, vol. 36, pp. 129–39, Aug. 2008.

[145] H. Baier and E. K. Scott, "Genetic and optical targeting of neural circuits and behavior–zebrafish in the spotlight.," *Current opinion in neurobiology*, vol. 19, pp. 553–60, Oct. 2009.

[146] A. B. Arrenberg, F. Del Bene, and H. Baier, "Optical control of zebrafish behavior with halorhodopsin.," *Proceedings of the National Academy of Sciences of the United States of America*, vol. 106, pp. 17968–73, Oct. 2009.

[147] I. Diester, M. T. Kaufman, M. Mogri, R. Pashaie, W. Goo, O. Yizhar, C. Ramakrishnan, K. Deisseroth, and K. V. Shenoy, "An optogenetic toolbox designed for primates.," *Nature neuroscience*, vol. 14, pp. 387–97, Mar. 2011.

[148] J. Tonnesen, A. T. Sorensen, K. Deisseroth, C. Lundberg, and M. Kokaia, "Optogenetic control of epileptiform activity.," *Proceedings of the National Academy of Sciences of the United States of America*, vol. 106, pp. 12162–7, July 2009.

[149] Y. Zhang, E. Ivanova, A. Bi, and Z.-H. Pan, "Ectopic expression of multiple microbial rhodopsins restores ON and OFF light responses in retinas with photoreceptor degeneration.," *The Journal of neuroscience : the official journal of the Society for Neuroscience*, vol. 29, pp. 9186–96, July 2009.

[150] V. Busskamp, J. Duebel, D. Balya, M. Fradot, T. J. Viney, S. Siegert, A. C. Groner, E. Cabuy, V. Forster, M. Seeliger, M. Biel, P. Humphries, M. Paques, S. Mohand-Said, D. Trono, K. Deisseroth, J. A. Sahel, S. Picaud, and B. Roska, "Genetic reactivation of cone photoreceptors restores visual responses in retinitis pigmentosa.," *Science (New York, N.Y.)*, vol. 329, pp. 413–7, July 2010.

[151] B. Y. Chow, X. Han, A. S. Dobry, X. Qian, A. S. Chuong, M. Li, M. A. Henninger, G. M. Belfort, Y. Lin, P. E. Monahan, and E. S. Boyden, "High-performance genetically targetable optical neural silencing by light-driven proton pumps.," *Nature*, vol. 463, pp. 98–102, Jan. 2010.

[152] X. Han, B. Y. Chow, H. Zhou, N. C. Klapoetke, A. Chuong, R. Rajimehr, A. Yang, M. V. Baratta, J. Winkle, R. Desimone, and E. S. Boyden, "A high-light sensitivity optical neural silencer: development and application to optogenetic control of non-human primate cortex.," *Frontiers in systems neuroscience*, vol. 5, p. 18, Jan. 2011.

[153] S. J. Husson, J. F. Liewald, C. Schultheis, J. N. Stirman, H. Lu, and A. Gottschalk, "Microbial light-activatable proton pumps as neuronal inhibitors to functionally dissect neuronal networks in C. elegans.," *PloS one*, vol. 7, p. e40937, Jan. 2012.

[154] W. W. Ward, H. J. Prentice, A. F. Roth, C. W. Cody, and S. C. Reeves, "Spectral pertubations of the Aequorea green-fluorescent protein," *Photochemistry and Photobiology*, vol. 35, pp. 803–808, June 1982.

[155] R. Heim, D. C. Prasher, and R. Y. Tsien, "Wavelength mutations and posttranslational autoxidation of green fluorescent protein.," *Proceedings of the National Academy of Sciences of the United States of America*, vol. 91, pp. 12501–4, Dec. 1994.

[156] G. Miesenböck, D. A. De Angelis, and J. E. Rothman, "Visualizing secretion and synaptic transmission with pH-sensitive green fluorescent proteins.," *Nature*, vol. 394, pp. 192–5, July 1998.

[157] S. Sankaranarayanan, D. De Angelis, J. E. Rothman, and T. A. Ryan, "The use of pHluorins for optical measurements of presynaptic activity.," *Biophysical journal*, vol. 79, pp. 2199–208, Oct. 2000.

[158] O. Zapata-Hommer and O. Griesbeck, "Efficiently folding and circularly permuted variants of the Sapphire mutant of GFP.," *BMC biotechnology*, vol. 3, p. 5, May 2003.

[159] N. C. Shaner, P. A. Steinbach, and R. Y. Tsien, "A guide to choosing fluorescent proteins," *Nature Methods*, vol. 2, pp. 905–909, Dec. 2005.

[160] M. Tantama, Y. P. Hung, and G. Yellen, "Imaging intracellular pH in live cells with a genetically encoded red fluorescent protein sensor.," *Journal of the American Chemical Society*, vol. 133, pp. 10034–7, July 2011.

[161] Y. Li and R. W. Tsien, "pHTomato, a red, genetically encoded indicator that enables multiplex interrogation of synaptic activity.," *Nature neuroscience*, vol. 15, pp. 1047–53, July 2012.

[162] F. Zhang, L.-P. Wang, E. S. Boyden, and K. Deisseroth, "Channelrhodopsin-2 and optical control of excitable cells.," *Nature methods*, vol. 3, pp. 785–92, Oct. 2006.

[163] J. A. Cardin, M. Carlén, K. Meletis, U. Knoblich, F. Zhang, K. Deisseroth, L.-H. Tsai, and C. I. Moore, "Driving fast-spiking cells induces gamma rhythm and controls sensory responses.," *Nature*, vol. 459, pp. 663–7, July 2009.

[164] H. Wang, J. Peca, M. Matsuzaki, K. Matsuzaki, J. Noguchi, L. Qiu, D. Wang, F. Zhang, E. Boyden, K. Deisseroth, H. Kasai, W. C. Hall, G. Feng, and G. J. Augustine, "High-speed mapping of synaptic connectivity using photostimulation in Channelrhodopsin-2 transgenic mice.," *Proceedings of the National Academy of Sciences of the United States of America*, vol. 104, pp. 8143–8, May 2007.

[165] V. Gradinaru, F. Zhang, C. Ramakrishnan, J. Mattis, R. Prakash, I. Diester, I. Goshen, K. R. Thompson, and K. Deisseroth, "Molecular and cellular approaches for diversifying and extending optogenetics.," *Cell*, vol. 141, pp. 154–65, May 2010.

[166] T. L. Lewis, T. Mao, K. Svoboda, and D. B. Arnold, "Myosin-dependent targeting of transmembrane proteins to neuronal dendrites.," *Nature neuroscience*, vol. 12, pp. 568–76, May 2009.

[167] V. Gradinaru, K. R. Thompson, F. Zhang, M. Mogri, K. Kay, M. B. Schneider, and K. Deisseroth, "Targeting and readout strategies for fast optical neural control in vitro and in vivo.," *The Journal of neuroscience : the official journal of the Society for Neuroscience*, vol. 27, pp. 14231–8, Dec. 2007.

[168] M. S. Grubb and J. Burrone, "Channelrhodopsin-2 localised to the axon initial segment.," *PloS one*, vol. 5, p. e13761, Jan. 2010.

[169] C. Wu, E. Ivanova, J. Cui, Q. Lu, and Z.-H. Pan, "Action potential generation at an axon initial segment-like process in the axonless retinal AII amacrine cell.," *The Journal of neuroscience : the official journal of the Society for Neuroscience*, vol. 31, pp. 14654–9, Oct. 2011.

[170] K. P. Greenberg, A. Pham, and F. S. Werblin, "Differential targeting of optical neuromodulators to ganglion cell soma and dendrites allows dynamic control of center-surround antagonism.," *Neuron*, vol. 69, pp. 713–20, Feb. 2011.

[171] L. Petreanu, T. Mao, S. M. Sternson, and K. Svoboda, "The subcellular organization of neocortical excitatory connections.," *Nature*, vol. 457, pp. 1142–5, Feb. 2009.

[172] B. Granseth, B. Odermatt, S. J. Royle, and L. Lagnado, "Clathrin-mediated endocytosis is the dominant mechanism of vesicle retrieval at hippocampal synapses.," *Neuron*, vol. 51, pp. 773–86, Oct. 2006.

[173] E. Dreosti, B. Odermatt, M. M. Dorostkar, and L. Lagnado, "A genetically encoded reporter of synaptic activity in vivo.," *Nature methods*, vol. 6, pp. 883–9, Dec. 2009.

[174] J. Akerboom, T.-W. Chen, T. J. Wardill, L. Tian, J. S. Marvin, S. Mutlu, N. C. Calderón, F. Esposti, B. G. Borghuis, X. R. Sun, A. Gordus, M. B. Orger, R. Portugues, F. Engert, J. J. Macklin, A. Filosa, A. Aggarwal, R. A. Kerr, R. Takagi, S. Kracun, E. Shigetomi, B. S. Khakh, H. Baier, L. Lagnado, S. S.-H. Wang, C. I. Bargmann, B. E. Kimmel, V. Jayaraman, K. Svoboda, D. S. Kim, E. R. Schreiter, and L. L. Looger, "Optimization of a GCaMP calcium indicator for neural activity imaging.," *The Journal of neuroscience : the official journal of the Society for Neuroscience*, vol. 32, pp. 13819–40, Oct. 2012.

[175] S. M. Voglmaier, K. Kam, H. Yang, D. L. Fortin, Z. Hua, R. A. Nicoll, and R. H. Edwards, "Distinct endocytic pathways control the rate and extent of synaptic vesicle protein recycling.," *Neuron*, vol. 51, pp. 71–84, July 2006.

[176] S. P. Gandhi and C. F. Stevens, "Three modes of synaptic vesicular recycling revealed by single-vesicle imaging.," *Nature*, vol. 423, pp. 607–13, June 2003.

[177] K. L. Budzinski, M. Zeigler, B. S. Fujimoto, S. M. Bajjalieh, and D. T. Chiu, "Measurements of the acidification kinetics of single SynaptopHluorin vesicles.," *Biophysical journal*, vol. 101, pp. 1580–9, Oct. 2011.

[178] B. Granseth, B. Odermatt, S. J. Royle, and L. Lagnado, "Clathrin-mediated endocytosis: the physiological mechanism of vesicle retrieval at hippocampal synapses.," *The Journal of physiology*, vol. 585, pp. 681–6, Dec. 2007.

[179] C. Zhao, E. Dreosti, and L. Lagnado, "Homeostatic synaptic plasticity through changes in presynaptic calcium influx.," *The Journal of neuroscience : the official journal of the Society for Neuroscience*, vol. 31, pp. 7492–6, May 2011.

[180] T. Rose, P. Schoenenberger, K. Jezek, and T. G. Oertner, "Developmental refinement of vesicle cycling at Schaffer collateral synapses.," *Neuron*, vol. 77, pp. 1109–21, Mar. 2013.

[181] N. A. Ramakrishnan, M. J. Drescher, and D. G. Drescher, "The SNARE complex in neuronal and sensory cells.," *Molecular and cellular neurosciences*, vol. 50, pp. 58–69, May 2012.

[182] A. J. Groffen, S. Martens, R. Díez Arazola, L. N. Cornelisse, N. Lozovaya, A. P. H. de Jong, N. A. Goriounova, R. L. P. Habets, Y. Takai, J. G. Borst, N. Brose, H. T. McMahon, and M. Verhage, "Doc2b is a high-affinity Ca2+ sensor for spontaneous neurotransmitter release.," *Science (New York, N.Y.)*, vol. 327, pp. 1614–8, Mar. 2010.

[183] J.-P. Pin and R. Duvoisin, "The metabotropic glutamate receptors: Structure and functions," *Neuropharmacology*, vol. 34, no. 1, pp. 1–26, 1995.

[184] M. F. Bear, B. W. Connors, and M. A. Paradiso, *Neurowissenschaften: Ein grundlegendes Lehrbuch für Biologie, Medizin und Psychologie*. 2008.

[185] Y. Saheki and P. De Camilli, "Synaptic vesicle endocytosis.," *Cold Spring Harbor perspectives in biology*, vol. 4, p. a005645, Sept. 2012.

[186] J. E. Heuser and T. S. Reese, "Evidence for recycling of synaptic vesicle membrane during transmitter release at the frog neuromuscular junction.," *The Journal of cell biology*, vol. 57, pp. 315–44, May 1973.

[187] R. Guan, H. Dai, D. Han, S. C. Harrison, and T. Kirchhausen, "Structure of the PTEN-like region of auxilin, a detector of clathrin-coated vesicle budding.," *Structure (London, England : 1993)*, vol. 18, pp. 1191–8, Sept. 2010.

[188] T. M. Miller, "Endocytosis of synaptic vesicle membrane at the frog neuromuscular junction," *The Journal of Cell Biology*, vol. 98, pp. 685–698, Feb. 1984.

[189] B. Ceccarelli, "Turnover of transmitter and synaptic vesicles at the frog neuromuscular junction," *The Journal of Cell Biology*, vol. 57, pp. 499–524, May 1973.

[190] S. Takamori, M. Holt, K. Stenius, E. A. Lemke, M. Gronborg, D. Riedel, H. Urlaub, S. Schenck, B. Brügger, P. Ringler, S. A. Müller, B. Rammner, F. Gräter, J. S. Hub, B. L. De Groot, G. Mieskes, Y. Moriyama, J. Klingauf, H. Grubmüller, J. Heuser, F. Wieland, and R. Jahn, "Molecular anatomy of a trafficking organelle.," *Cell*, vol. 127, pp. 831–46, Nov. 2006.

[191] E. E. Bellocchio, R. J. Reimer, R. T. Fremeau, and R. H. Edwards, "Uptake of glutamate into synaptic vesicles by an inorganic phosphate transporter.," *Science (New York, N.Y.)*, vol. 289, pp. 957–60, Aug. 2000.

[192] S. Takamori, J. S. Rhee, C. Rosenmund, and R. Jahn, "Identification of a vesicular glutamate transporter that defines a glutamatergic phenotype in neurons.," *Nature*, vol. 407, pp. 189–94, Sept. 2000.

[193] S. Takamori, J. S. Rhee, C. Rosenmund, and R. Jahn, "Identification of differentiation-associated brain-specific phosphate transporter as a second vesicular glutamate transporter (VGLUT2).," *The Journal of neuroscience : the official journal of the Society for Neuroscience*, vol. 21, p. RC182, Nov. 2001.

[194] S. Takamori, P. Malherbe, C. Broger, and R. Jahn, "Molecular cloning and functional characterization of human vesicular glutamate transporter 3.," *EMBO reports*, vol. 3, pp. 798–803, Aug. 2002.

[195] H. Omote, T. Miyaji, N. Juge, and Y. Moriyama, "Vesicular neurotransmitter transporter: bioenergetics and regulation of glutamate transport.," *Biochemistry*, vol. 50, pp. 5558–65, June 2011.

[196] S. Schenck, S. M. Wojcik, N. Brose, and S. Takamori, "A chloride conductance in VGLUT1 underlies maximal glutamate loading into synaptic vesicles.," *Nature neuroscience*, vol. 12, pp. 156–62, Feb. 2009.

[197] Q. Zhou, C. C. Petersen, and R. A. Nicoll, "Effects of reduced vesicular filling on synaptic transmission in rat hippocampal neurones.," *The Journal of physiology*, vol. 525 Pt 1, pp. 195–206, May 2000.

[198] T. Hori and T. Takahashi, "Kinetics of synaptic vesicle refilling with neurotransmitter glutamate.," *Neuron*, vol. 76, pp. 511–7, Nov. 2012.

[199] G. Liu and R. W. Tsien, "Properties of synaptic transmission at single hippocampal synaptic boutons.," *Nature*, vol. 375, pp. 404–8, June 1995.

[200] S. O. Rizzoli and W. J. Betz, "Synaptic vesicle pools.," *Nature reviews. Neuroscience*, vol. 6, pp. 57–69, Jan. 2005.

[201] V. N. Murthy, T. Schikorski, C. F. Stevens, and Y. Zhu, "Inactivity produces increases in neurotransmitter release and synapse size.," *Neuron*, vol. 32, pp. 673–82, Nov. 2001.

[202] T. Schikorski and C. F. Stevens, "Morphological correlates of functionally defined synaptic vesicle populations.," *Nature neuroscience*, vol. 4, pp. 391–5, Apr. 2001.

[203] V. P. Whittaker, I. A. Michaelson, and R. J. Kirkland, "The separation of synaptic vesicles from nerve-ending particles ('synaptosomes').," *The Biochemical journal*, vol. 90, pp. 293–303, Feb. 1964.

[204] H. Zimmermann and V. P. Whittaker, "Effect of electrical stimulation on the yield and composition of synaptic vesicles from the cholinergic synapses of the electric organ of topedo: a combined biochemical, electrophysiological and morphological study," *Journal of Neurochemistry*, vol. 22, pp. 435–450, Mar. 1974.

[205] E. G. Gray and V. P. Whittaker, "The isolation of nerve endings from brain: an electron-microscopic study of cell fragments derived by homogenization and centrifugation.," *Journal of anatomy*, vol. 96, pp. 79–88, Jan. 1962.

[206] R. Llinás, I. Z. Steinberg, and K. Walton, "Relationship between presynaptic calcium current and postsynaptic potential in squid giant synapse.," *Biophysical journal*, vol. 33, pp. 323–51, Mar. 1981.

[207] G. Váró, R. Needleman, and J. K. Lanyi, "Light-driven chloride ion transport by halorhodopsin from Natronobacterium pharaonis. 2. Chloride release and uptake, protein conformation change, and thermodynamics.," *Biochemistry*, vol. 34, pp. 14500–7, Nov. 1995.

[208] G. E. Shull, "cDNA cloning of the beta-subunit of the rat gastric H,K-ATPase.," *The Journal of biological chemistry*, vol. 265, pp. 12123–6, July 1990.

[209] S. Geibel, T. Friedrich, P. Ormos, P. G. Wood, G. Nagel, and E. Bamberg, "The voltage-dependent proton pumping in bacteriorhodopsin is characterized by optoelectric behavior.," *Biophysical journal*, vol. 81, pp. 2059–68, Oct. 2001.

[210] S. Kleinlogel, U. Terpitz, B. Legrum, D. Gökbuget, E. S. Boyden, C. Bamann, P. G. Wood, and E. Bamberg, "A gene-fusion strategy for stoichiometric and co-localized expression of light-gated membrane proteins.," *Nature methods*, vol. 8, pp. 1083–8, Dec. 2011.

[211] M. Mandel and A. Higa, "Calcium-dependent bacteriophage DNA infection.," *Journal of molecular biology*, vol. 53, pp. 159–62, Oct. 1970.

[212] R. M. Horton, H. D. Hunt, S. N. Ho, J. K. Pullen, and L. R. Pease, "Engineering hybrid genes without the use of restriction enzymes: gene splicing by overlap extension.," *Gene*, vol. 77, pp. 61–8, Apr. 1989.

[213] E. J. Furshpan, P. R. MacLeish, P. H. O'Lague, and D. D. Potter, "Chemical transmission between rat sympathetic neurons and cardiac myocytes developing in microcultures: evidence for cholinergic, adrenergic, and dual-function neurons.," *Proceedings of the National Academy of Sciences of the United States of America*, vol. 73, pp. 4225–9, Nov. 1976.

[214] J. M. Bekkers and C. F. Stevens, "Excitatory and inhibitory autaptic currents in isolated hippocampal neurons maintained in cell culture.," *Proceedings of the National Academy of Sciences of the United States of America*, vol. 88, pp. 7834–8, Sept. 1991.

[215] S. J. Pyott and C. Rosenmund, "The effects of temperature on vesicular supply and release in autaptic cultures of rat and mouse hippocampal neurons.," *The Journal of physiology*, vol. 539, pp. 523–35, Mar. 2002.

[216] B. R. Rost, *Presynaptic Inhibition of Transmitter Release by G-protein coupled Receptors in the Hippocampal Formation*. Phd thesis, Charité Universitätsmedizin Berlin, 2012.

[217] C. Lois, E. J. Hong, S. Pease, E. J. Brown, and D. Baltimore, "Germline transmission and tissue-specific expression of transgenes delivered by lentiviral vectors.," *Science (New York, N.Y.)*, vol. 295, pp. 868–72, Feb. 2002.

[218] M. Xue, Y. Q. Lin, H. Pan, K. Reim, H. Deng, H. J. Bellen, and C. Rosenmund, "Tilting the balance between facilitatory and inhibitory functions of mammalian and Drosophila Complexins orchestrates synaptic vesicle exocytosis.," *Neuron*, vol. 64, pp. 367–80, Nov. 2009.

[219] M. Prigge, *Über die elektrophysiologische Untersuchung und Entwicklung von farbverschobenen Kanalrhodopsinchimären aus der Grünalge Volvox carteri*. PhD thesis, Humboldt Universität zu Berlin, 2012.

[220] J. Wietek, *Elektrophysiologische Charakterisisierung von Gloeobacter Rhodopsin -Jenseits des Grenzbereins einer Protonenpumpe-*. Master thesis, Humboldt Universität zu Berlin, 2012.

[221] B. Hille, *Ion Channels of Excitable Membrane*. Sunderland, MA: Sinauer associates, Inc., third edit ed., 2001.

[222] S. Y. Kim, S. A. Waschuk, L. S. Brown, and K.-H. Jung, "Screening and characterization of proteorhodopsin color-tuning mutations in Escherichia coli with endogenous retinal synthesis.," *Biochimica et biophysica acta*, vol. 1777, pp. 504–13, June 2008.

[223] Y. Sugiyama, H. Wang, T. Hikima, M. Sato, J. Kuroda, T. Takahashi, T. Ishizuka, and H. Yawo, "Photocurrent attenuation by a single polar-to-nonpolar point mutation of channelrhodopsin-2.," *Photochemical & photobiological sciences : Official journal of the European Photochemistry Association and the European Society for Photobiology*, vol. 8, pp. 328–36, Mar. 2009.

[224] A. Berndt, *Mechanismus und anwendungsbezogene Optimierung von Channelrhodopsin-2*. Doktorarbeit, Humboldt-Universität zu Berlin, 2011.

[225] K. Ruffert, B. Himmel, D. Lall, C. Bamann, E. Bamberg, H. Betz, and V. Eulenburg, "Glutamate residue 90 in the predicted transmembrane domain 2 is crucial for cation flux through channelrhodopsin 2.," *Biochemical and biophysical research communications*, vol. 410, pp. 737–43, July 2011.

[226] A. P. Plazzo, N. De Franceschi, F. Da Broi, F. Zonta, M. F. Sanasi, F. Filippini, and M. Mongillo, "Bioinformatic and mutational analysis of channelrhodopsin-2 protein cation-conducting pathway.," *The Journal of biological chemistry*, vol. 287, pp. 4818–25, Feb. 2012.

[227] Z. Lu, "Mechanism of rectification in inward-rectifier K+ channels.," *Annual review of physiology*, vol. 66, pp. 103–29, Jan. 2004.

[228] E. Holland, F. Braun, C. Nonnengässer, H. Harz, and P. Hegemann, "The nature of rhodopsin-triggered photocurrents in Chlamydomonas. I. Kinetics and influence of divalent ions," *Biophysical Journal*, vol. 70, no. 2, pp. 924–931, 1996.

[229] F. Schneider, D. Gradmann, and P. Hegemann, "Ion Selectivity and Competition in Channelrhodopsins," *Biophysical Journal*, vol. 105, pp. 91–100, July 2013.

[230] H. G. Klieber and D. Gradmann, "Enzyme kinetics of the prime K+ channel in the tonoplast of Chara: selectivity and inhibition.," *The Journal of membrane biology*, vol. 132, pp. 253–65, Mar. 1993.

[231] I. V. Kalaidzidis, Y. L. Kalaidzidis, and A. D. Kaulen, "Flash-induced voltage changes in halorhodopsin from Natronobacterium pharaonis.," *FEBS letters*, vol. 427, pp. 59–63, May 1998.

[232] M. L. Nonet, "Visualization of synaptic specializations in live C. elegans with synaptic vesicle protein-GFP fusions," *Journal of Neuroscience Methods*, vol. 89, pp. 33–40, July 1999.

[233] G. Werner, H. Hagenmaier, H. Drautz, A. Baumgartner, and H. Zähner, "Metabolic products of microorganisms. 224. Bafilomycins, a new group of macrolide antibiotics. Production, isolation, chemical structure and biological activity.," *The Journal of antibiotics*, vol. 37, pp. 110–7, Feb. 1984.

[234] E. J. Bowman, A. Siebers, and K. Altendorf, "Bafilomycins: a class of inhibitors of membrane ATPases from microorganisms, animal cells, and plant cells.," *Proceedings of the National Academy of Sciences of the United States of America*, vol. 85, pp. 7972–6, Nov. 1988.

[235] J. R. Haigh, K. Noremberg, and S. M. Parsons, "Acetylcholine active transport by rat brain synaptic vesicles.," *Neuroreport*, vol. 5, pp. 773–6, Mar. 1994.

[236] S. Roseth, E. M. Fykse, and F. Fonnum, "Uptake of L-glutamate into rat brain synaptic vesicles: effect of inhibitors that bind specifically to the glutamate transporter.," *Journal of neurochemistry*, vol. 65, pp. 96–103, July 1995.

[237] S. G. Olenych, N. S. Claxton, G. K. Ottenberg, and M. W. Davidson, "The fluorescent protein color palette.," *Current protocols in cell biology / editorial board, Juan S. Bonifacino ... [et al.]*, vol. Chapter 21, p. Unit 21.5, Sept. 2007.

[238] A. A. Pakhomov and V. I. Martynov, "GFP family: structural insights into spectral tuning.," *Chemistry & biology*, vol. 15, pp. 755–64, Aug. 2008.

[239] D. M. Shcherbakova and V. V. Verkhusha, "Near-infrared fluorescent proteins for multicolor in vivo imaging.," *Nature methods*, vol. 10, pp. 751–4, Aug. 2013.

[240] Y. Sudo, A. Okazaki, H. Ono, J. Yagasaki, S. Sugo, M. Kamiya, L. Reissig, K. Inoue, K. Ihara, H. Kandori, S. Takagi, and S. Hayashi, "A Blue-shifted Light-driven Proton Pump for Neural Silencing.," *The Journal of biological chemistry*, vol. 288, pp. 20624–32, July 2013.

[241] W. Wang, Z. Nossoni, T. Berbasova, C. T. Watson, I. Yapici, K. S. S. Lee, C. Vasileiou, J. H. Geiger, and B. Borhan, "Tuning the electronic absorption of protein-embedded all-trans-retinal.," *Science (New York, N.Y.)*, vol. 338, pp. 1340–3, Dec. 2012.

[242] S. Reckel, D. Gottstein, J. Stehle, F. Löhr, M.-K. Verhoefen, M. Takeda, R. Silvers, M. Kainosho, C. Glaubitz, J. Wachtveitl, F. Bernhard, H. Schwalbe, P. Güntert, and V. Dötsch, "Solution NMR structure of proteorhodopsin.," *Angewandte Chemie (International ed. in English)*, vol. 50, pp. 11942–6, Dec. 2011.

[243] C. Grimm, "A Red-activatable Channelrhodopsin - investigating Reach," tech. rep., Humboldt Universität zu Berlin, 2013.

[244] K. Erbguth, M. Prigge, F. Schneider, P. Hegemann, and A. Gottschalk, "Bimodal activation of different neuron classes with the spectrally red-shifted channelrhodopsin chimera C1V1 in Caenorhabditis elegans.," *PloS one*, vol. 7, p. e46827, Jan. 2012.

[245] R. Prakash, O. Yizhar, B. Grewe, C. Ramakrishnan, N. Wang, I. Goshen, A. M. Packer, D. S. Peterka, R. Yuste, M. J. Schnitzer, and K. Deisseroth, "Two-photon optogenetic toolbox for fast inhibition, excitation and bistable modulation.," *Nature methods*, vol. 9, pp. 1171–9, Dec. 2012.

[246] A. M. Packer, D. S. Peterka, J. J. Hirtz, R. Prakash, K. Deisseroth, and R. Yuste, "Two-photon optogenetics of dendritic spines and neural circuits.," *Nature methods*, vol. 9, pp. 1202–5, Dec. 2012.

[247] J. Y. Lin, P. M. Knutsen, A. Muller, D. Kleinfeld, and R. Y. Tsien, "ReaChR: a red-shifted variant of channelrhodopsin enables deep transcranial optogenetic excitation.," *Nature neuroscience*, Sept. 2013.

[248] D. A. Doyle, "The Structure of the Potassium Channel: Molecular Basis of K+ Conduction and Selectivity," *Science*, vol. 280, pp. 69–77, Apr. 1998.

[249] E. Lörinczi, M.-K. Verhoefen, J. Wachtveitl, A. C. Woerner, C. Glaubitz, M. Engelhard, E. Bamberg, and T. Friedrich, "Voltage- and pH-dependent changes in vectoriality of photocurrents mediated by wild-type and mutant proteorhodopsins upon expression in Xenopus oocytes.," *Journal of molecular biology*, vol. 393, pp. 320–41, Oct. 2009.

[250] A. Vogt, J. Wietek, and P. Hegemann, "Gloeobacter Rhodopsin, Limitation of Proton Pumping at High Electrochemical Load," *Biophysical Journal*, vol. 105, no. 9, pp. 2055–2063, 2013.

[251] O. A. Sineshchekov, E. G. Govorunova, J. Wang, H. Li, and J. L. Spudich, "Intramolecular proton transfer in channelrhodopsins.," *Biophysical journal*, vol. 104, pp. 807–17, Mar. 2013.

[252] J. A. Mindell, "Lysosomal acidification mechanisms.," *Annual review of physiology*, vol. 74, pp. 69–86, Jan. 2012.

[253] L. Taiz, "The Plant Vacuole," *J. Exp. Biol.*, vol. 172, pp. 113–122, Nov. 1992.

[254] O. Gaiko and R. Dempski, "Transmembrane Domain Three Contributes to the Ion Conductance Pathway of Channelrhodopsin-2," *Biophysical Journal*, vol. 104, pp. 1230–1237, Mar. 2013.

[255] E. M. Callaway and L. C. Katz, "Photostimulation using caged glutamate reveals functional circuitry in living brain slices.," *Proceedings of the National Academy of Sciences*, vol. 90, pp. 7661–7665, Aug. 1993.

[256] M. Volgraf, P. Gorostiza, R. Numano, R. H. Kramer, E. Y. Isacoff, and D. Trauner, "Allosteric control of an ionotropic glutamate receptor with an optical switch.," *Nature chemical biology*, vol. 2, pp. 47–52, Jan. 2006.

[257] S. Szobota, P. Gorostiza, F. Del Bene, C. Wyart, D. L. Fortin, K. D. Kolstad, O. Tulyathan, M. Volgraf, R. Numano, H. L. Aaron, E. K. Scott, R. H. Kramer, J. Flannery, H. Baier, D. Trauner, and E. Y. Isacoff, "Remote control of neuronal activity with a light-gated glutamate receptor.," *Neuron*, vol. 54, pp. 535–45, May 2007.

[258] I. Tochitsky, M. R. Banghart, A. Mourot, J. Z. Yao, B. Gaub, R. H. Kramer, and D. Trauner, "Optochemical control of genetically engineered neuronal nicotinic acetylcholine receptors.," *Nature chemistry*, vol. 4, pp. 105–11, Feb. 2012.

[259] J. Levitz, C. Pantoja, B. Gaub, H. Janovjak, A. Reiner, A. Hoagland, D. Schoppik, B. Kane, P. Stawski, A. F. Schier, D. Trauner, and E. Y. Isacoff, "Optical control of metabotropic glutamate receptors.," *Nature neuroscience*, vol. 16, pp. 507–16, Apr. 2013.

[260] T. Kouyama, S. Kanada, Y. Takeguchi, A. Narusawa, M. Murakami, and K. Ihara, "Crystal structure of the light-driven chloride pump halorhodopsin from Natronomonas pharaonis.," *Journal of molecular biology*, vol. 396, pp. 564–79, Feb. 2010.

[261] K. Yoshimura and T. Kouyama, "Structural role of bacterioruberin in the trimeric structure of archaerhodopsin-2.," *Journal of molecular biology*, vol. 375, pp. 1267–81, Feb. 2008.

[262] N. Enami, K. Yoshimura, M. Murakami, H. Okumura, K. Ihara, and T. Kouyama, "Crystal structures of archaerhodopsin-1 and -2: Common structural motif in archaeal light-driven proton pumps.," *Journal of molecular biology*, vol. 358, pp. 675–85, May 2006.

[263] D. Mitter, *Cholesterol und der Synaptophysin-Synaptobrevin-Komplex*. PhD thesis, Humboldt-Universität zu Berlin, 2003.

[264] R. L. Parsons, M. A. Calupca, L. A. Merriam, and C. Prior, "Empty synaptic vesicles recycle and undergo exocytosis at vesamicol-treated motor nerve terminals.," *Journal of neurophysiology*, vol. 81, pp. 2696–700, June 1999.

[265] C. Rosenmund and C. F. Stevens, "Definition of the Readily Releasable Pool of Vesicles at Hippocampal Synapses," *Neuron*, vol. 16, pp. 1197–1207, June 1996.

[266] G. Y. Goh, H. Huang, J. Ullman, L. Borre, T. S. Hnasko, L. O. Trussell, and R. H. Edwards, "Presynaptic regulation of quantal size: K+/H+ exchange stimulates vesicular glutamate transport.," *Nature neuroscience*, vol. 14, pp. 1285–92, Oct. 2011.

[267] P. M. Burger, E. Mehl, P. L. Cameron, P. R. Maycox, M. Baumert, F. Lottspeich, P. De Camilli, and R. Jahn, "Synaptic vesicles immunoisolated from rat cerebral cortex contain high levels of glutamate.," *Neuron*, vol. 3, pp. 715–20, Dec. 1989.

[268] N. Juge, J. A. Gray, H. Omote, T. Miyaji, T. Inoue, C. Hara, H. Uneyama, R. H. Edwards, R. A. Nicoll, and Y. Moriyama, "Metabolic control of vesicular glutamate transport and release.," *Neuron*, vol. 68, pp. 99–112, Oct. 2010.

[269] D. E. Bergles and R. H. Edwards, *Structural And Functional Organization Of The Synapse*. Boston, MA: Springer US, 2008.

[270] S. Brenner, "The genetics of Caenorhabditis elegans.," *Genetics*, vol. 77, pp. 71–94, May 1974.

[271] J. G. White, E. Southgate, J. N. Thomson, and S. Brenner, "The structure of the nervous system of the nematode Caenorhabditis elegans.," *Philosophical transactions of the Royal Society of London. Series B, Biological sciences*, vol. 314, pp. 1–340, Nov. 1986.

[272] M. Chalfie, Y. Tu, G. Euskirchen, W. Ward, and D. Prasher, "Green fluorescent protein as a marker for gene expression," *Science*, vol. 263, pp. 802–805, Feb. 1994.

[273] G. G. Ernstrom, R. Weimer, D. R. L. Pawar, S. Watanabe, R. J. Hobson, D. Greenstein, and E. M. Jorgensen, "V-ATPase V1 sector is required for corpse clearance and neurotransmission in Caenorhabditis elegans.," *Genetics*, vol. 191, pp. 461–75, June 2012.

[274] C. L. Tucker, "Manipulating cellular processes using optical control of protein-protein interactions.," *Progress in brain research*, vol. 196, pp. 95–117, Jan. 2012.

[275] D. A. Brown and T. S. Sihra, "Presynaptic signaling by heterotrimeric G-proteins.," *Handbook of experimental pharmacology*, pp. 207–60, Jan. 2008.

[276] E. L. King and C. Altman, "A Schematic Method of Deriving the Rate Laws for Enzyme-Catalyzed Reactions," *J. Phys. Chem.*, vol. 60, no. 10, pp. 1375–1378, 1956.

A. Appendix

A.1. Abbreviations

AdMLP	adenovirus major late promotor
AIS	axon initial segment
AP	action potential
APS	ammonium persulfate
AR	AMPA (a-amino-3-hydroxy-5-methyl-4-isoxazolepropionic acid) receptor
Arch(3)	*Halorubrum sodomense* archearhodopsin-3
ATP	adenosine triphosphate
BCIP	5-bromo-4-chloro-3-indolyl phosphate
BLUF	blue-light sensors using flavin adenine dinucleotide
BR	bacteriorhodopsin
BTP	bis-tris propane
b/w	black and white
C1	*Chlamydomonas reinhardtii* channelrhodopsin 1
C2	*Chlamydomonas reinhardtii* channelrhodopsin 2
C1C2	chimeric protein composed of helices 1-5 from C1 and helices 6, 7 from C2
C1V1	chimeric protein composed of helices 1, 2 from C1 and helices 3-7 from V1
cAMP	cyclic adenosine monophosphate
Ca_v	voltage-gated Ca^{2+} channel
Catch	Ca^{2+}-transporting channelrhodopsin
CCD	charge-coupled device
Cd1	first closed state
Cd2	second closed state
cGMP	cyclic guanosine monophosphate
CHEF	chimeric protein composed of helices 1-5 from C1 and helices 6, 7 from C2
ChETA	Channelrhodopsin 2 E123T Accelerated
CHIEF	CHEF with additional point mutation V170I
ChR	channelrhodopsin
ChRGR	channelrhodopsin-green receiver
CMV	cytomegalovirus
Cop1	Chlamyopsin 1
Cop2	Chlamyopsin 2
cop3, cop4	genes coding for *Chlamydomonas reinhardtii* channelrhodopsin 1 and 2
Cos cells	immortalized green monkey cells
CP	creatine phosphate
C_vRh	*Chlorella vulgaris* rhodopsin
DChR	*Dunaniella salina* channelrhodopsin
DDM	n-dodecyl β-D-maltopyranoside
DEAE	diethylethanolamine

DMEM	Dulbecco's modified Eagle's medium
DMSO	dimethyl sulfoxide
DNA	desoxyribonucleic acid
dNTPs	deoxyribonucleotide
EBSS	Earle's balanced salt solution
eCFP	enhanced cyan fluorescent protein
EDTA	ethylenediaminetetraacetic acid
EGTA	ethylene glycol tetraacetic acid
eGFP	enhanced green fluorescent protein
EPSC	excitatory postsynatic current
ER	endoplasmic reticulum
eYFP	enhanced yellow fluorescent protein
FAD	flavin adenine dinuclotide
FCS	fetal calf serum
FP	fluorescent protein
FRET	Förster resonance energy transfer
GABA	γ-aminobutyric acid
GTP	guanosine triphosphate
K_{M}	Michaelis constant
HEK cells	human embyronic kidney cells
HKR1	histidine kinase rhodopsin 1
HR	halorhodopsin
I_0	extrapolated initial current at time zero of illumination
$I_{0\mathrm{ref}}$	initial current at standard conditions
IR	infrared
I_{p}	peak current
I_{par}	partial current of respective ion
IPSC	inhibitory postsynaptic current
I_{s}	stationary current
IV	current-voltage
LB	lysogeny broth
LOV	ligh-oxygen-voltage
Mac	*Leptosphaeria maculans* proton pump
MAP kinase	mitogen-activated protein kinases
MBD	myosin binding domain
NBQX	2,3-dihydroxy-6-nitro-7-sulfamoyl-benzoquinoxaline-2,3-dione
NBT	nitro blue tetrazolium
MChR	*Mesostigma viride* channelrhodopsin
mEPSC	miniature excitatory postsynaptic current
mGluR	metabotropic glutamate receptors
mIPSC	miniature inhibitory postsynaptic current
MR	metabotropic glutamate receptor
NMDA	N-Methyl-D-aspartate

NMG	N-methyl-D-glucamine
N_pHR	*Natronomonas pharaonis* halorhodopsin
NR	NMDA (N-methyl-D-aspartate) receptor
O1	first open state
O2	second open state
p	permeability
PPR	paired-pulse ratio
PBS	phosphate buffered saline
PCK	phosphocreatine kinase
PCR	polymerase chain reaction
phot	phototropin
PMSF	phenylmethylsulfonyl fluoride
RFP	red fluorescent protein
RNA	ribonucleic acid
SDS	sodium dodecyl sulfate
SNARE	soluble N-ethylmaleimide-sensitive-factor attachment receptor
SFO	step-function opsin
SSFO	stable step-function opsin
TEMED	tetramethylethylenediamine
TM	transmembrane
TTL	transistor-transistor logic
UV	ultraviolet
V1	*Volvox carteri* channelrhodopsin 1
V2	*Volvox carteri* channelrhodopsin 2
VA	Vacuolar-type (V-type) ATPase
VAMP	vesicle-associated membrane protein
VGlut	vesicular glutamate transporter
vis	visible
Vop1	Volvoxopsin 1
wt	wildtype

A.2. Supplementary methods

A.2.1. Cos cell culturing and transfection

Sources of cell culture materials and reagents are given in Table 4.8 in the method section. Cos cells were used to express and purify ChRs. They were grown as described for HEK cells in section 4.2.2. In preparation for protein expression Cos cells were seeded at a concentration of 1.9×10^4 cells /cm^2 into T75 flasks or roller flasks with a surface area of 850 cm^2. Roller flasks were constantly rotating at a speed of 50 rpm. Prior to transfection the following solutions were prepared:
Cells were transfected three days after seeding. 150 µg plasmid DNA per roller flask was mixed with 6 ml 1 M Tris-HCl pH 7.5. Then, 6 ml DEAE solution and 48 ml transfection

solution	components and concentration	solvent
transfection medium	1 % penicillin/streptomycin	DMEM
standard medium	1 % penicillin/streptomycin, 10 % FCS	DMEM
DEAE solution	2.5 mg ml^{-1} DEAE-dextrane	DMEM
chloroquine solution	1 mM chloroquine	ddH_2O

Table A.1.: Solutions required for transfection of Cos cells.

medium were added. Next, the roller flask medium was replaced by the transfection mixture and cells were incubated for at least 5 h. In the following, the transfection mixture was discarded and 67.5 ml standard medium and 7.5 ml chloroquine solution were added. After incubation for 5 h cells were washed twice with 50 ml PBS. Finally, 200 ml standard medium was added and proteins were expressed for 3 d.

A.2.2. Protein purification from Cos cells

All required chemicals were purchased from Sigma Aldrich (Hamburg, Germany), Carl Roth (Karlsruhe, Germany) and Roche (Basel, Switzerland). The 1D4 antibody was generously supplied by the group of Professor Franz Bartl at the Charité Berlin. Prior to cell harvesting the following solutions were prepared:

solution	components and concentration	solvent
EDTA solution	2 mM EDTA	PBS
protease inhibitor cocktail	1/2 tablet protease inhibitor	5 ml PBS per roller flask
DDM stock solution	10 % DDM	PBS
retinal stock solution	30 mM all-*trans* retinal	100 % ethanol
washing buffer I	0.03 % DDM	PBS
washing buffer II	0.03 % DDM	BTP buffer
elution buffer	0.03 % DDM	5 ml BTP buffer
	40 µl 1D4 peptide	per roller flask

Table A.2.: Solutions required for protein purification from Cos cells.

Roller flasks were removed from the incubator, medium was discarded and cells were washed twice with 50 ml PBS. Afterward, 30 ml of EDTA solution was added and flasks were rotated in the incubator for 10 min. Then, the protease inhibitor cocktail was added and cells from two roller flasks were pelleted in subsequent centrifugation steps in one 50 ml falcon tube. Centrifugation took place at 4 °C and 4000×g for 4 min and was repeated until all cells were unified in one tube. Cells were resuspended in 30 ml supernatant and 30 µl retinal stock solution was supplemented. Retinal reconstitution was performed at 4 °C in the dark and under constant agitation for at least 4 h. Subsequently, cells could be frozen in liquid nitrogen and stored at −80 °C or directly used for protein preparation.

For membrane solubilization the DDM stock solution was added to achieve a final concentration of 1 % DDM and cells were solubilized at 4 °C overnight. The next day, the column material required for protein purification from present cell material was

transferred to a 50 ml tube and washed with PBS. The material was centrifuged at 4 °C and 4000×g for 5 min and the supernatant was carefully removed. In parallel to a second washing step solubilized cells were pelleted. While cell debris stayed in the pellet the supernatant contained glycolipids, membranes and membrane proteins. The supernatant was added to the gel material and gel binding occured at 4 °C in the dark and under constant agitation. Gel material was washed twice with washing buffer I and once with washing buffer II. Next, 1.5 ml elution buffer were added and incubated overnight. Eluted protein found in the supernatant was transferred to a new Eppendorf tube and could be used for further analysis. Protein quality was confirmed in a UV-Vis spectrophotometer (Cary 60, Agilent Technologies GmbH, Böblingen, Germany) by recording absorbance spectra between 260 nm to 650 nm. Protein samples were stored at −20 °C.

A.2.3. Western blot analysis

SDS-Page and western blot analysis were performed to check target protein content in the different fractions of the purification process. Prior to loading, unsoluble fractions such as cell pellets were resuspended in 1 ml BTP buffer supplemented with a spatula tip of DNase and 0.1 % PMSF. The pellet was homogenized using a tiny glass potter and then diluted in 10 ml BTP buffer containing 1 % DDM and 0.1 % PMSF. Samples were mildly agitated at 4 °C for 30 min. 75 µl of homogenized cell solution or 75 µl of soluble fractions were mixed with 25 µl 4x loading buffer. The composition of the loading buffer and all other solutions required for SDS-Page and western blotting are summarized in Table A.3. In preparation of gel electrophoresis pairs of clean, ethanol-polished glasses

solution	components and concentration	solvent
4x loading buffer	200 mM Tris-HCl pH 6.8; 40 % glycerol; 4 % SDS; 400 mM β-mercapto ethanol; 0.01 % bromophenol blue	ddH_2O
SDS running buffer	25 mM Tris-HCl pH 8.8; 192 mM glycine 0.1 % m/V SDS	ddH_2O
blotting buffer	20 mM Tris-HCl pH 8.8; 154 mM glycine 0.08 % m/V SDS; 20 % methanol	ddH_2O
TBS-Tween	5 mM Tris-HCl pH 7.5; 15 mM NaCl; 0.5 % Tween-20	ddH_2O
detection buffer	100 mM Tris-HCl pH 9.5; 100 mM NaCl; 50 mM $MgCl_2$	ddH_2O
BCIP solution	50 mg ml^{-1} 5-bromo-4-chloro-3-indolyl phosphate	dimethylformamide
NBT solution	75 mg ml^{-1} nitrotetrazolium blue chloride	70 % dimethyl-formamide

Table A.3.: Solutions required for SDS-Page and Western-Blot analysis.

and the corresponding spacers were mounted. Separating gel and stacking gel were prepared according to the recipe summarized in Table A.4. The electrophoresis chamber was mounted and filled with SDS running buffer. Then, 12 µl samples and 5 µl of protein ladder mix were loaded and electrophoresis took place at 45 V for 45 min. In parallel

ingredient	separating gel	stacking gel
30 % acrylamide	6.25 ml (12.5 %)	0.833 ml (5 %)
ddH_2O	2.8 ml	3.5 ml
1 M Tris pH 8.9	5.6 ml	/
1 M Tris pH 6.8	/	0.625 ml
10 % SDS	150 µl	50 µl
10 % APS	120 µl	25 µl
TEMED	12 µl	5 µl

Table A.4.: Recipe for preparation of one polyacrylamide gel.

nitrocellulose membrane and filter papers were prepared. The membrane was activated for 20 s in methanol, then washed for 2 min in ddH_2O and finally membrane and filter papers were soaked in blotting buffer. Proteins were blotted at 2.5 mV/cm^2 for 1 h. As a next step, membranes were blocked with 1 g powdered milk in 20 ml PBS-Tween under slow agitation for 1 h. Membranes were washed with PBS-Tween and 1D4 antibody was applied by overnight incubation with 20 ml PBS-Tween supplemented with 0.14 g powdered milk and 20 µl 1D4-antibody. The next morning, membranes were washed with PBS-Tween for 15 min, 5 min and 5 min. In the following 5 µl anti-mouse secondary antibody in 10 ml PBS-Tween was applied and incubated for 2 h. After three additional washing steps, detection took place by applying 8 µl NBT and 30 µl BCIP in detection buffer for 10 min in the dark.

A.3. Enzyme kinetic algorithm

The here presented algorithm was developed by Dietrich Gradmann and is based on earlier work [230][100]. It considers translocation of the four substrates protons (H), Na^+ (M), Mg^{2+} (G) and Ca^{2+} (D) that are unidirectionally transported from the extracellular side (e) to the intracellular side (in the following: cytosolic - c). Moreover, the present model comprises ion transport via both open states O1 and O2 that display distinct ion binding and transport rates. Model equations are described in Schneider et al. [229] as follows:

> To calculate the steady-state currents of the model, the probabilities of the state occupancies p have to be determined. This can be done with the method of King and Altman [276] by forming the relative occupation probabilities $\underline{p}$, that consist of the sum of all products of $n-1$ rate constants in a n-state model. Using the abbreviation $\kappa_S = k_{Sc} + k_{Se}$ (S: H, M, D, or G) for writing economy, these relative occupation probabilities for a given conducting state (O1 or O2) in our six-state model are given by the following equations:

$$\begin{aligned}\underline{p}_e = {} & k_{ec}\kappa_H\kappa_M\kappa_D\kappa_G + k_{eH}k_{He}\kappa_M\kappa_D\kappa_G + k_{eM}k_{Me}\kappa_H\kappa_D\kappa_G \\ & + k_{eD}k_{De}\kappa_H\kappa_M\kappa_G + k_{eG}k_{Ge}\kappa_H\kappa_M\kappa_D,\end{aligned} \tag{A.1}$$

$$\underline{p}_c = \underline{p}_e k_{ce}/k_{ec}, \tag{A.2}$$

$$\begin{aligned}\mathrm{H}: \underline{p}_H = &(k_{ec}k_{cH} + k_{ce}k_{eH} + k_{cH}k_{eH})\kappa_M\kappa_D\kappa_G \\ &+(k_{cH}k_{eD}k_{Dc} + k_{eH}k_{cD}k_{De})\kappa_M\kappa_G \\ &+(k_{cH}k_{eM}k_{Mc} + k_{eH}k_{cM}k_{Me})\kappa_D\kappa_G \\ &+(k_{cH}k_{eG}k_{Gc} + k_{eH}k_{cG}k_{Ge})\kappa_D\kappa_M,\end{aligned} \tag{A.3}$$

$$\begin{aligned}\mathrm{M}: \underline{p}_M = &(k_{ec}k_{cM} + k_{ce}k_{eM} + k_{cM}k_{eM})\kappa_H\kappa_D\kappa_G \\ &+(k_{cM}k_{eD}k_{Dc} + k_{eM}k_{cD}k_{De})\kappa_H\kappa_G \\ &+(k_{cM}k_{eH}k_{Hc} + k_{eM}k_{cH}k_{He})\kappa_D\kappa_G \\ &+(k_{cM}k_{eG}k_{Gc} + k_{eM}k_{cG}k_{Ge})\kappa_D\kappa_H,\end{aligned} \tag{A.4}$$

$$\begin{aligned}\mathrm{D}: \underline{p}_D = &(k_{ec}k_{cD} + k_{ce}k_{eD} + k_{cD}k_{eD})\kappa_H\kappa_M\kappa_G \\ &+(k_{cD}k_{eH}k_{Hc} + k_{eD}k_{cH}k_{He})\kappa_M\kappa_G \\ &+(k_{cD}k_{eM}k_{Mc} + k_{eD}k_{cM}k_{Me})\kappa_H\kappa_G \\ &+(k_{cD}k_{eG}k_{Gc} + k_{eD}k_{cG}k_{Ge})\kappa_M\kappa_H, \text{and}\end{aligned} \tag{A.5}$$

$$\begin{aligned}\mathrm{G}: \underline{p}_G = &(k_{ec}k_{cG} + k_{ce}k_{eG} + k_{cG}k_{eG})\kappa_H\kappa_M\kappa_D \\ &+(k_{cG}k_{eD}k_{Dc} + k_{eG}k_{cD}k_{De})\kappa_M\kappa_H \\ &+(k_{cG}k_{eM}k_{Mc} + k_{eG}k_{cM}k_{Me})\kappa_H\kappa_G \\ &+(k_{cG}k_{eH}k_{Hc} + k_{eG}k_{cH}k_{He})\kappa_M\kappa_D.\end{aligned} \tag{A.6}$$

The absolute probabilities p are obtained by referring the relative ones to their sum:

$$\sum\nolimits_{\underline{p}} = \underline{p}_c + \underline{p}_e + \underline{p}_H + \underline{p}_M + \underline{p}_D + \underline{p}_G, \tag{A.7}$$

yielding

$$\begin{aligned}p_c = \underline{p}_c / \sum\nolimits_{\underline{p}};\ p_e = \underline{p}_e / \sum\nolimits_{\underline{p}};\ p_H = \underline{p}_H / \sum\nolimits_{\underline{p}}; \\ p_M = \underline{p}_M / \sum\nolimits_{\underline{p}};\ p_D = \underline{p}_D / \sum\nolimits_{\underline{p}};\ p_G = \underline{p}_G / \sum\nolimits_{\underline{p}}.\end{aligned} \tag{A.8}$$

The particular ion currents are (e is elementary charge)

$$\mathrm{H}: I_H = e(p_c k_{cH} - p_H k_{Hc}), \tag{A.9}$$

$$\mathrm{M}: I_M = e(p_c k_{cM} - p_M k_{Mc}), \tag{A.10}$$

$$\mathrm{D}: I_D = e(p_c k_{cD} - p_D k_{Dc}), \tag{A.11}$$

$$\mathrm{G}: I_G = e(p_c k_{cG} - p_G k_{Gc}), \tag{A.12}$$

which add up to the total current

$$I = I_H + I_M + I_D + I_G. \tag{A.13}$$

Considering both conducting states O1 and O2 [...], the initial current I0 after a long dark period is exclusively mediated by the conductance of O1

($I_0 = I_{O1}$). Then the conductance via O1 relaxes by equilibration with O2 by a factor R1, until a steady-state current I_s is reached, comprising stationary currents through both open states,

$$I_s = I_{1s} + I_{2s}, \tag{A.14}$$

with $I_{1s} = I_0 R1$. The reorientation of the empty binding site under the assumption of one symmetric barrier is described by the rate constants kce and kec that depend on the reduced voltage $u = EF/RT$, with the transmembrane voltage E and R, T and F having their usual thermodynamic meaning

$$k_{ec} = k^0_{ec}\exp\left(\frac{z_E u}{2}\right),\ k_{ce} = k^0_{ce}\exp\left(\frac{-z_E u}{2}\right), \tag{A.15}$$

where the superscript 0 marks reference conditions ($u = 0$), z_E is the apparent charge number of the empty binding site, and the factor 1/2 in the exponent reflects a symmetric Eyring barrier.

The transfer of ionic substrates S with the charge number z_S via an intermediate binding site (c-S-e) is assumed to occur in two reversible steps in series (two symmetric barriers), which see only the portions d and $1 - d$ of the total voltage, respectively:

$$k_{cS} = k^0_{cS}\,[S]_c \exp\left(\frac{d(z_E + z_S)u}{2}\right), \tag{A.16}$$

$$k_{Sc} = k^0_{Sc}\exp\left(\frac{-d(z_E + z_S)u}{2}\right), \tag{A.17}$$

$$k_{Se} = k^0_{Se}\exp\left(\frac{(1-d)(z_E + z_S)u}{2}\right), \tag{A.18}$$

$$k_{eS} = k^0_{eS}\,[S]_e \exp\left(\frac{(d-1)(z_E + z_S)u}{2}\right). \tag{A.19}$$

The voltage partitioning coefficient d (for the cytoplasmic barrier) is treated as voltage- and substrate-dependent,

$$d = \frac{k_{Se} + k_{eS}}{k_{Se} + k_{eS} + k_{Sc} + k_{cS}}, \tag{A.20}$$

and had to be iteratively determined by [equations A.16 to A.19]. The expressions $k_{Se} + k_{eS}$ and $k_{Sc} + k_{cS}$ [...] are equivalent to conductances in an Ohmic voltage divider. Thus, the potential profile is not considered here as a rigid structural entity, but as an elastic one, depending on the actual voltage and substrate concentrations on both sides.

Model description is reproduced from Schneider et al. [229]. Dietrich Gradmann fitted the experimental data to the model equations applying the fitting strategy according to [100]. He used TurboPascal for all model calculations. The model-retrieved kinetic

parameters for the individual analyzed cells are summarized in Tables A.5, A.6 and A.7.

Cell	$C2_7$	$C2_{10}$	$C2_{17}$		$C2_7$	$C2_{10}$	$C2_{17}$
z_{E1}	1.03	0.92	0.06	z_{E2}	0.79	1.11	0.82
k_{ce1}	5.7×10^2	1.3×10^1	8.7×10^3	k_{ce2}	1.3×10^4	8.6	4.4×10^4
k_{ec1}	1.8×10^5	2.2×10^8	3.4×10^3	k_{ec2}	3.9×10^3	8.9×10^5	2.7×10^3
k_{cH1}	2.2×10^4	2.7×10^6	6.1×10^5	k_{cH2}	3.5×10^5	4.7×10^4	2.6×10^5
k_{Hc1}	2.5×10^1	1.8	1.1	k_{Hc2}	1.3×10^3	9.4×10^2	5.8×10^2
k_{He1}	2.5×10^1	9.6	4.2	k_{He2}	4.4×10^1	1.5×10^2	4.0×10^1
k_{cM1}	5.2×10^3	3.8×10^1	6.2×10^2	k_{cM2}	4.7×10^1	1.5×10^2	1.9×10^1
k_{Mc1}	2.6	5.2×10^1	1.2	k_{Mc2}	2.3×10^3	1.3×10^2	7.6×10^2
k_{Me1}	6.9×10^1	4.8×10^2	3.8	k_{Me2}	4.8×10^1	5.9	3.0×10^1
k_{cD1}	8.9×10^4	1.5×10^1	2.2×10^2	k_{cD2}	5.4×10^3	3.0×10^4	2.0×10^3
k_{De1}	2.3×10^1	3.9×10^1	9.2×10^2	k_{De2}	2.6×10^3	3.3×10^1	3.6×10^3
k_{Dc1}	2.6×10^1	8.1×10^1	3.7×10^1	k_{Dc2}	1.5×10^2	2.9×10^4	1.0×10^1
k_{cG1}	1.5×10^4	4.2×10^1	3.8×10^1	k_{cG2}	7.5×10^3	9.2×10^4	9.1×10^4
k_{Gc1}	1.7×10^2	1.8×10^2	1.1×10^2	k_{Gc2}	1.1×10^3	1.8×10^2	9.9×10^4
k_{Ge1}	8.8×10^1	1.3×10^2	1.5	k_{Ge2}	1.2×10^3	8.6	1.4×10^2
R1	0.088	0.081	0.126	Error	0.057	0.072	0.028

Table A.5.: Model parameters obtained for three selected C2 cells. z_E corresponds to the apparent charge of the empty binding site, indices 1 or 2 indicate first open state O1 and second open state O2, respectively. $k_{ce1/2}$ and $k_{ce1/2}$ are the rate constants for reorientation of the empty binding site from the cytosol to the extracellular side and vice versa in s^{-1}. $k_{cX1/2}$ is the rate constant for cytoplasmic binding and translocation of substrate X^+, $k_{Xc1/2}$ describes the rate constant for translocation and cytoplasmic release and $k_{Xe1/2}$ describes the rate for substrate extracellular release. All rate constants are given for standard conditions (−60 mV, 1 mM internal and cytosolic substrate concentration) and are normalized to I_0 at reference conditions (high Na^+, pH_e 7.2 and NMG, pH_i 9.0). H, M, D and G symbolize protons, Na^+, Ca^{2+} and Mg^{2+}, respectively. R1 is the stationary portion of current via O1 compared to I_0 with $I_s = R1 * I_0 + I_{2s}$.

Cells	$C1V1_1$	$C1V1_5$	$C1V1_{11}$		$C1V1_1$	$C1V1_5$	$C1V1_{11}$
z_{E1}	0.04	0.55	0.70	z_{E2}	1.08	0.54	0.20
k_{ce1}	3.0×10^1	3.1×10^2	2.3×10^3	k_{ce2}	7.5×10^2	3.2×10^3	5.1×10^3
k_{ec1}	4.2×10^3	1.4×10^5	1.1×10^5	k_{ec2}	1.0×10^4	2.9×10^4	1.1×10^4
k_{cH1}	8.1×10^4	9.2×10^4	8.1×10^5	k_{cH2}	4.9×10^4	3.7×10^3	1.9×10^4
k_{Hc1}	8.9×10^1	4.4×10^1	1.8	k_{Hc2}	3.7×10^1	2.7×10^2	6.0
k_{He1}	2.8×10^1	1.3×10^1	1.0×10^1	k_{He2}	3.1×10^1	3.7×10^1	1.9×10^1
k_{cM1}	4.3×10^2	3.0×10^2	1.3×10^2	k_{cM2}	1.2×10^1	8.0×10^2	2.2×10^3
k_{Mc1}	3.0×10^2	7.0	1.0×10^2	k_{Mc2}	6.2×10^1	8.4×10^1	7.3
k_{Me1}	4.1×10^1	5.9×10^1	1.0×10^3	k_{Me2}	1.2	1.2×10^1	5.3×10^1
k_{cD1}	8.3×10^3	2.0×10^2	7.7×10^3	k_{cD2}	9.9×10^4	7.2×10^3	3.0×10^3
k_{De1}	1.2×10^1	1.5×10^1	4.1×10^1	k_{De2}	2.0×10^1	9.1×10^2	6.3×10^2
k_{Dc1}	2.1×10^1	3.3	1.5×10^2	k_{Dc2}	2.6×10^1	6.0×10^1	1.2×10^1
k_{cG1}	1.3×10^2	2.6×10^2	3.3×10^2	k_{cG2}	7.3×10^4	1.1×10^1	4.5×10^4
k_{Gc1}	1.8×10^1	1.2×10^2	3.1×10^2	k_{Gc2}	6.2×10^4	5.0×10^3	1.3×10^2
k_{Ge1}	2.0×10^2	2.3	7.4×10^2	k_{Ge2}	1.2×10^2	1.7×10^1	5.8×10^2
R1	0.373	0.024	0.152	Error	0.116	0.079	0.052

Table A.6.: Model parameters obtained for three selected C1V1 cells. Symbols have the same meaning as described for Table A.5.

Cell	Catch+$_3$	Catch+$_5$	Catch+$_9$		Catch+$_3$	Catch+$_5$	Catch+$_9$
z_{E1}	0.39	0.54	0.23	zE2	0.46	0.71	0.82
k_{ce1}	1.4×10^1	1.0×10^1	3.0×10^3	kce2	2.9×10^2	1.3×10^3	1.6×10^3
k_{ec1}	9.2×10^6	1.1×10^8	5.4×10^4	kec2	5.9×10^5	3.8×10^4	6.3×10^4
k_{cH1}	3.2×10^6	3.3×10^6	4.4×10^4	kcH2	5.0×10^4	8.2×10^3	4.4×10^4
k_{Hc1}	2.3×10^2	2.0×10^2	1.9×10^2	kHc2	6.7×10^1	8.1×10^1	2.1×10^2
k_{He1}	3.4×10^1	3.4×10^1	1.1×10^2	kHe2	1.1	2.3×10^1	3.6×10^1
k_{cM1}	6.5×10^1	2.0×10^1	4.4×10^2	kcM2	3.0×10^2	7.2×10^3	4.5×10^2
k_{Mc1}	2.0×10^2	3.4×10^2	6.0×10^1	kMc2	1.1×10^4	9.7×10^1	8.1×10^1
k_{Me1}	9.4×10^1	1.5×10^1	2.7×10^1	kMe2	3.7×10^2	2.2×10^2	1.4×10^1
k_{cD1}	2.6×10^2	5.7×10^2	1.1×10^2	kcD2	2.2×10^3	5.5×10^1	2.4×10^2
k_{De1}	5.8×10^1	9.6×10^2	1.5×10^1	kDe2	3.2	2.0×10^1	1.4×10^1
k_{Dc1}	1.4×10^1	3.8×10^2	7.0×10^1	kDc2	1.6	7.3×10^4	4.0×10^2
k_{cG1}	3.9×10^2	6.6×10^2	1.9×10^1	kcG2	2.1×10^3	1.0×10^2	8.6×10^2
k_{Gc1}	7.6×10^2	4.1×10^2	2.8×10^2	kGc2	1.3×10^2	7.1×10^3	3.0×10^2
k_{Ge1}	3.7×10^1	1.2×10^1	1.3×10^1	kGe2	2.4×10^2	3.1	5.7×10^2
R1	0.53	0.36	0.007	Error	0.066	0.035	0.029

Table A.7.: Model parameters obtained for three selected Catch+ (C2 L132C T159C) cells. Symbols have the same meaning as described for Table A.5.

A.4. Publication list

1. **F. Schneider**, D. Gradmann, and P. Hegemann, "Ion Selectivity and Competition in Channelrhodopsins," *Biophysical Journal*, vol. 105, pp. 91-100, July 2013.

2. K. Erbguth, M. Prigge, **F. Schneider**, P. Hegemann, and A. Gottschalk, "Bimodal activation of different neuron classes with the spectrally red-shifted channelrhodopsin chimera C1V1 in Caenorhabditis elegans.," *PloS one*, vol. 7, p. e46827, Oct. 2012.

3. M. Prigge*, **F. Schneider***, S. P. Tsunoda, C. Shilyansky, J. Wietek, K. Deisseroth, and P. Hegemann, " Color-tuned Channelrhodopsins for Multiwavelength Optogenetics.," *The Journal of biological chemistry*, Sept. 2012.

4. H. C. Watanabe, K. Welke, **F. Schneider**, S. Tsunoda, F. Zhang, K. Deisseroth, P. Hegemann, and M. Elstner, "Structural model of channelrhodopsin.," *The Journal of Biological Chemistry*, vol. 287, no. 10, pp. 7456-7466, Mar. 2012.

5. D. Gradmann, A. Berndt, **F. Schneider**, and P. Hegemann, "Rectification of the channelrhodopsin early conductance.," *Biophysical journal*, vol. 101, pp. 1057-68, Sept. 2011.

6. O. Yizhar, L. E. Fenno, M. Prigge, **F. Schneider**, T. J. Davidson, D. J. O'Shea, V. S. Sohal, I. Goshen, J. Finkelstein, J. T. Paz, K. Stehfest, R. Fudim, C. Ramakrishnan, J. R. Huguenard, P. Hegemann, and K. Deisseroth, "Neocortical excitation/inhibition balance in information processing and social dysfunction.," *Nature*, vol. 477, no. 7363, pp. 171-178, July 2011.

* equal contribution

A.5. Symposia and meeting contributions

1. F. Schneider, P. Hegemann. "Towards Multi-Color Optogenetics with optimized Channelrhodopsin Variants." *Talk.* Society for Neuroscience Meeting, San Diego 2013

2. F. Schneider, P. Hegemann. "Ion Selectivity and Gating in Channelrhodopsins" *Talk.* Optogenetics and Pharmacogenetics in Neuronal Function and Dysfunction, 7th Brain Research Conference, New Orleans 2012

3. F. Schneider, D. Gradmann and P. Hegemann. "Selectivity and Gating in Channelrhodopsins" *Poster.* Society for Neuroscience Meeting, New Orleans 2012

4. Dahlem Conference on Optogenetics, Berlin 2012, *Participation.*

5. F. Schneider, M. Prigge, S. Tsunoda, O. Yizhar, K. Deisseroth and P. Hegemann: "Ion Selectivity of Multi-Color Channelrhodopsins". *Poster.* Berlin Neuroscience Forum 2012

6. F. Schneider, P. Hegemann: "Gating and Ion Selectivity in Channelrhodopsins." *Talk.* 15th International Conference on the Cell and Molecular Biology of Chlamydomonas, Potsdam 2012

7. F. Schneider, P. Hegemann: "ChR Gating and Ion Selectivity." *Talk.* FOR1279 Meeting, Würzburg 2012

8. F. Schneider, M. Prigge, S. Tsunoda, O. Yizhar, K. Deisseroth and P. Hegemann: "Ion Selectivity of Multi-Color Channelrhodopsins". *Poster.* Biophysical Society Meeting, San Diego 2012

9. F. Schneider, P. Hegemann: "Exploring Ca^{2+} Selectivity of Multi-Color Channelrhodopsins" *Talk.* Leibniz graduate school symposium, Berlin 2011

10. F. Schneider, M. Prigge, S. Tsunoda, O. Yizhar, K. Deisseroth and P. Hegemann: "Yellow Optogenetics with Volvox Channelrhodopsin Variants". *Poster.* 2nd German Neurophysiology PhD Meeting, Tübingen 2011

11. F. Schneider, P. Hegemann: "Color-tuning of Channelrhodopsins". *Talk.* FOR1279 Meeting, München 2011

12. F. Schneider, P. Hegemann: "Engineering and Characterization of Channelrhodopsin Variants" *Talk.* Graduate school symposium 1123, Wandlitz 2010

13. M. Prigge, F. Schneider, S. Tsunoda, P. Hegemann: "Green Optogenetics with Volvox Channelrhodopsin Variants" *Poster.* Optogenetics Meeting, Hiddensee 2010

14. F. Schneider, M. Prigge, S. Tsunoda, T. Korte, A. Herrmann and P. Hegemann: "Color-tuning and improved expression of Volvox Channelrhodopsin 1". *Poster.* Biophysical Society Meeting, San Francisco 2010

A.6. Acknowlegdement

First of all, I would like to thank Professor Peter Hegemann who gave me the opportunity to work on very challenging questions in the field of optogenetics. I am very glad for the many inspiring discussions, covering both scientific and more general topics. Moreover, Peter Hegemann was always open to start new projects and collaborations and allowed me to travel to a number of interesting conferences.

Special thanks goes to Dr. Matthias Prigge (now working at the Weizmann Institute) being my supervisor at the initial phase of my work. He taught me both molecular biology and electrophysiology and allowed me to participate in some of his most fruitful projects. In addition, he encouraged me to develop own experiments and taught me the principles of scientific communication. Also, I would like to acknowlegde Dr. André Berndt (now at Stanford University) for providing the basis of several experiments by his thorough analysis of channelrhodopsin properties.

I am very thankful to the present electrophysiologists in our laboratory, namely Arend Vogt, Jonas Wietek, Johannes Vierock and Christiane Grimm. They were open for daily discussions, helped myself whenever technical problems occured and offered an enjoyable lab atmosphere. Thank you also for proofreading parts of the here presented thesis! Even more important, I would like to thank Altina Klein, Maila Reh, Margrit Michalsky and Jelena Pustogowa for excellent technical assistance! Without you, our research would not be possible! I'm also thankful to Benjamin Krause, Dr. Satoshi Tsunoda (now at Goethe University Frankfurt), Dr. Katja Stehfest, Stefanie Kathe (Albert-Ludwigs University Freiburg) and Christian Herold (UC Berkeley) in our group who helped with diverse scientific and technical questions. In the end, I thank all members of the Hegemann group for providing an agreeable working ambience!

I would like to acknowlegde Professor Dietrich Gradmann (University of Göttingen) for our collaboration on data modelling. He thoroughly analyzed my electrophysiological data and helped me to understand the underlying principles.

It was also a pleasure to collaborate with Dr. Benjamin Rost and Professor Christian Rosenmund from the Charité Berlin with whom we collaborated on subcellular optogenetics. Thank you for introducing me to neurophysiology and for allowing me to experimentate in your laboratory. Thank you also for many stimulating discussions in the cafeteria and for proof-reading the respective parts of this thesis. I am likewise indepted to Annegret Felies, Berit Söhl-Kielczynski, Bettina Brokowski, Katja Pötschke (Rosenmund group) and to Anke Schönherr (group of Dietmar Schmitz) for providing technical assistance at the Charité.

Thanks to our collaboration partners at Stanford university, namely Professor Karl Deisseroth, Professor Ofer Yizhar (now at Weizmann Institute), Lief Fenno and Carrie Shilyansky. They applied our optogenetic tools to answer numerous neurophysiological questions, thereby providing both great motivation and publicity for our work.

I would also like to thank my colleagues within the FOR1279 for inspiring meetings and fruitful collaborations. Special thanks goes to Dr. Hiroshi Watanabe, Kai Welke and Professor Markus Elstner (all KIT Karlsruhe) and to Karen Erbguth and Professor

Alexander Gottschalk for working together on development and application of color-tuned channelrhodopsins. In this context I would also like to acknowlegde the DFG for generous funding (FOR 1279 and SFB 1078 to Peter Hegemann).

All confocal fluorescence images shown in this thesis were recorded in the group of Professor Andreas Herrmann (HU Berlin). I would like to acknowlegde him for letting me work at their sophisticated microscope setups and thank Dr. Thomas Korte for his excellent technical support.

A special thanks to Robert Ohlendorf who carefully read and corrected this thesis. Thank you also for your motivation throughout these last years!

Finally, I like to acknowlegde the reviewers of this thesis for taking their time to evaluate the present work.

Zum Schluss möchte ich meinen Eltern und meinen Schwestern für die langjährige, uneingeschränkte Unterstützung und die vielen tollen Unternehmungen in den letzten Jahren danken! Besonderer Dank geht auch an meine Mitbewohner und meine guten Freunde, die jederzeit zu Gesprächen und Abenteuern bereit waren! Danke für alles!

A.7. Selbstständigkeitserklärung

Hiermit erkläre ich, dass ich die vorliegende Arbeit selbstständig und ausschließlich unter Verwendung der angegebenen Literatur und Hilfsmittel angefertigt habe.

Berlin, 21. November 2013
Franziska Schneider

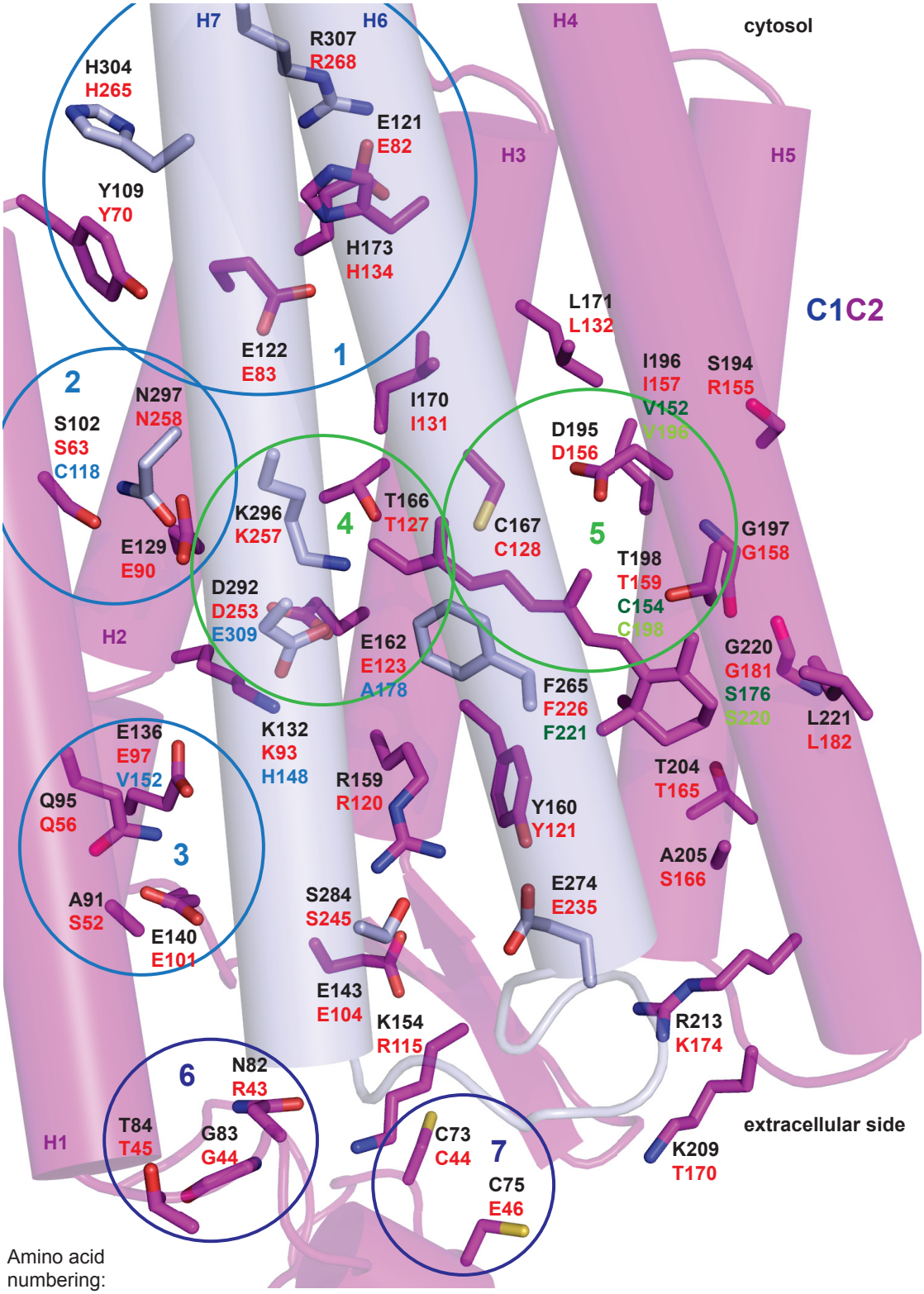

Figure A.1.: Structural model of the C1C2 chimera after Kato et al. [74]. Side chains of all important amino acids described in this thesis are displayed. For glycine residues, main chains are depicted. Circles cluster amino acids according to their function.